Comportement thermo-poro-mécanique d'un ciment pétrolier

Siavash Ghabezloo

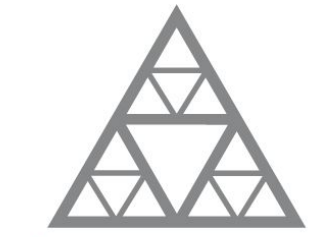

UNIVERSITÉ PARIS-EST

THESE

Présentée et soutenue publiquement pour l'obtention du diplôme de

Docteur de l'École Nationale des Ponts et Chaussées

Discipline : Géotechnique

par

Siavash GHABEZLOO

Comportement thermo-poro-mécanique d'un ciment pétrolier

UR NAVIER/CERMES – LCPC/MSRGI

Soutenue le 26 septembre 2008, devant le jury composé de :

M. Yves GUEGUEN	**Président**
M. Djimedo KONDO	**Rapporteur**
M. Franz-Josef ULM	**Rapporteur**
M. Olivier COUSSY	**Examinateur**
Mme. Sylvine GUEDON	**Examinatrice**
M. Marc MAINGUY	**Examinateur**
M. Ahmad POUYA	**Examinateur**
M. Robert ZIMMERMAN	**Examinateur**
M. Jean SULEM	**Directeur de thèse**

à Sahar

REMERCIEMENTS

Ce travail a été réalisé grâce à une collaboration entre le CERMES (équipe Géotechnique de l'UR Navier) de l'ENPC, la division MSRGI du LCPC et la société TOTAL. Je les remercie de m'avoir accueilli et soutenu pendant ma thèse.

J'adresse tous mes remerciements à Yves Guéguen qui a présidé le jury de thèse, à Djimédo Kondo et Franz-Josef Ulm qui ont accepté d'être rapporteurs ainsi que pour la richesse de leurs commentaires. Je remercie vivement Olivier Coussy, Sylvine Guédon, Marc Mainguy, Ahmad Pouya et Robert Zimmerman qui m'ont fait l'honneur de s'intéresser à mon travail et d'être membres de jury.

Ma profonde reconnaissance et mes vifs remerciements s'adressent à Jean Sulem qui a dirigé cette thèse et qui m'a guidé tout au long de ce parcours passionnant. Je le remercie pour sa disponibilité, ses encouragements, ses précieux conseils scientifiques et pour le plaisir que j'ai eu à travailler avec lui.

Je tiens à remercier vivement Sylvine Guédon qui m'a chaleureusement accueilli au sein de son équipe, et qui m'a généreusement aidé avec son expertise scientifique dans les observations microscopiques.

J'adresse mes vifs remerciements à Ahmad Pouya qui n'a jamais laissé mes questions sans une réponse pertinente. Je le remercie pour sa vaste connaissance en mécanique et pour sa générosité scientifique.

Je remercie chaleureusement Jérémie Saint-Marc et André Garnier de la société TOTAL d'avoir suivi le projet, de m'avoir fait confiance et d'avoir apporté un soutien continu pendant la thèse.

Ce travail expérimental n'aurait pas été possible sans l'aide constante d'une équipe technique performante. Je remercie particulièrement François Martineau pour l'aide précieuse qu'il m'a apportée tout au long de la thèse. J'ai beaucoup appris en travaillant à ses cotés. Je remercie également Emmanuel De Laure, Matthieu Laulom, Louis-Marie Cottineau, Xavier Boulay, Alain Jeandillou, Jérémy Thiriat, Aurélie Maloula et la société Métro-Mesures qui m'ont aidé dans différentes parties du travail expérimental. Je tiens aussi à remercier Myriam Duc pour son aide dans la préparation des solutions chimiques.

Je remercie aussi George Scherer, Hamlin Jennings et Yves Bernabé de m'avoir accordé leur temps pour répondre à mes questions, ainsi que pour les échanges très fructueux que nous avons eus par courrier électronique.

J'adresse toute ma gratitude à Behrouz Gatmiri qui m'a beaucoup aidé pour continuer les études à l'Ecole des Ponts.

Je remercie tous mes amis au LCPC, au CERMES et ailleurs pour leur encouragement, leur soutien et tous les moments très agréables que j'ai eus avec eux. Je souhaite bon courage à mon successeur Manh-Huyen Vu.

Je ne vais pas finir cette page sans remercier ma très chère Sahar, pour son amour, sa patience, et pour tout ce qu'elle a fait pour moi. Nous avons travaillé très dur. Sans elle, tout cela n'aurait pas été possible.

J'adresse également toute ma gratitude à mes parents et mes beaux-parents pour leurs encouragements et leur soutien permanents.

Siavash

« Qu'est-ce qui fait le prix de l'homme? Ce qu'il cherche. »

Djalâl-od-Dîn Rûmî (XIII^e siècle)

Résumé :

Comportement thermo-poro-mécanique d'un ciment pétrolier

Dans un puits pétrolier, une gaine de ciment est coulée entre la roche réservoir et le cuvelage d'acier. Cette gaine de ciment a un rôle primordial dans la stabilité et l'étanchéité des puits pétroliers. Durant les différentes étapes de la vie d'un puits, depuis le forage jusqu'à l'exploitation et finalement l'abandon du puits, le ciment est soumis à différentes sollicitations mécaniques et thermiques. Ces sollicitations peuvent endommager le ciment et dégrader ses propriétés mécaniques et sa perméabilité et par conséquent modifier sa contribution dans la stabilité et l'étanchéité du puits. La connaissance du comportement de ce ciment dans des conditions de fond de puits (hautes températures, fortes pressions) et de son évolution au cours du temps est essentielle pour l'analyse de fonctionnement du puits pendant l'exploitation et aussi pour garantir son étanchéité pour le stockage et la séquestration des gaz à effet de serre dans des réservoirs pétroliers abandonnés. C'est dans ce but qu'est développée cette étude sur la caractérisation du comportement thermo-poro-mécanique des ciments pétroliers sous fortes contraintes pour des températures entre 20 et 90°C. Les paramètres poro-mécaniques du ciment et leurs variations avec l'état de contraintes et la température ont été évalués dans un programme d'essais de compression isotrope drainés, non drainés et sans membrane. Un phénomène de dégradation des propriétés élastiques a été observé dans les essais. Les observations microscopiques ont montré que cette dégradation est provoquée par la microfissuration du matériau y compris sous chargement isotrope. La bonne compatibilité et la cohérence des paramètres poro-mécaniques obtenus montrent que le comportement de ciment peut être décrit dans le cadre de la théorie des milieux poreux.

Les essais poro-mécaniques ont été couplés avec une évaluation de la perméabilité du ciment sous chargement en régime transitoire. Des essais déviatoriques ont été également réalisés pour étudier l'endommagement du matériau sous chargement déviatorique.

Lorsqu'un puits pétrolier est soumis à de rapides variations de températures, les déformations et la surpression interstitielle qui en résultent peuvent porter atteinte à l'intégrité du puits. Ce phénomène de pressurisation thermique induit lors d'un chauffage en conditions non-drainées est dû à la différence entre le coefficient d'expansion thermique du fluide interstitiel et celui de la matrice solide. Une étude préliminaire, théorique et expérimentale a été menée sur un grès. Les effets des déformations mécaniques et thermiques du système de drainage lors d'un essai de chauffage non-drainé ont été analysés et une méthode simple a été développée pour apporter une correction aux valeurs de pressions interstitielles mesurées. Le comportement thermique du ciment a été étudié expérimentalement dans les essais de chauffage drainés et non-drainés et le coefficient de pressurisation thermique ainsi que les coefficients d'expansion thermique drainé et non-drainé du ciment ont été évalués. Le coefficient de pressurisation thermique a été évalué à 0.6 MPa/°C, ce qui montre l'importance des changements de contraintes effectives que peut occasionner un brusque changement de température. L'anomalie du comportement thermique du fluide interstitiel du ciment a été attribuée à son confinement dans les pores de très petite taille et cette anomalie a été étudiée à partir des résultats expérimentaux.

En complément de travail sur le comportement du ciment, une étude expérimentale a été menée sur la loi de contrainte effective qui contrôle la perméabilité d'un calcaire et un modèle conceptuel basé sur la micro-texture du matériau a été proposé.

Abstract:

Thermo-poro-mechanical behaviour of a hardened oil-well cement paste

In oil wells, a cement sheath is placed between the rock and the casing for stability and sealing purpose. The cement lining is submitted to various thermal and mechanical loadings during the life of the well from the drilling phase to the production phase and finally in the abandon phase when the reservoir can be used for storage and sequestration of greenhouse gas. In due course of these solicitations, the cement can be damaged and the mechanical and transport properties can be degraded. This degradation can affect its contribution in the stability and in the sealing of the well. The knowledge of behaviour of this cement in oil-wells conditions (high temperature, high pressure) is essential for the prediction of the well performance during the exploitation and also for the analysis of the well tightness during storage and sequestration as the cement sheath is a possible leakage path.

In this thesis, an experimental study of the thermo-poro-mechanical behaviour of a hardened oil-well cement paste under high stresses and for temperatures between 20°C and 90°C is performed. The poro-mechanical behaviour of hardened cement paste under isotropic loading is studied on the basis of an experimental testing program of drained, undrained and unjacketed compression tests at 20°C and at 90°C. The poroelastic parameters of the material are determined and the effect of stress, pore pressure and temperature on them is evaluated. A phenomenon of degradation of elastic properties is observed in the test results. The microscopic observations showed that this degradation is caused by the microcracking of the material even under isotropic loading. The good compatibility and the consistency of the obtained poromechanical parameters demonstrate that the behaviour of the hardened cement paste can be described within the framework of the theory of porous media.

The poro-mechanical tests are combined with an evaluation of the evolution of permeability of the cement paste under loading using a transient method. Deviatoric loading tests have also been performed to study damage under deviatoric stress.

The effect of undrained heating on volume change and induced pore pressure increase is an important point to properly understand the behaviour and evaluate the integrity of an oil well cement sheath submitted to rapid temperature changes. This thermal pressurization of the pore fluid is due to the discrepancy between the thermal expansion coefficients of the pore fluid and of the solid matrix. A preliminary experimental and theoretical study has been performed on a granular rock. Careful analysis of the effect of mechanical and thermal deformation of the drainage and pressure measurement system has been performed and a simple method has been developed for the correction of the measured pore pressure. Then the effect of undrained heating is studied experimentally for a saturated hardened cement paste. The measured value of the thermal pressurization coefficient is equal to 0.6MPa/°C which shows that the changes in effective stress can be significant when the well is submitted to rapid temperature changes. The drained and undrained thermal expansion coefficients of the hardened cement paste are also measured in the heating tests. The anomalous thermal behaviour of cement pore fluid is back analysed from the results of an undrained heating test and is attributed to its confinement in very small pores.

In addition to this work on the behaviour of cement paste, an experimental study on the effective stress law for the permeability of a limestone is performed and a conceptual model is proposed in relation with the microstructure of the rock.

SOMMAIRE

INTRODUCTION GENERALE

Dans un puits pétrolier, une gaine de ciment est coulée entre la roche réservoir et le cuvelage d'acier. Cette gaine de ciment a un rôle primordial dans la stabilité et l'étanchéité des puits pétroliers. Durant les différentes étapes de la vie d'un puits, depuis le forage jusqu'à l'exploitation et finalement l'abandon du puits, le ciment est soumis à différentes sollicitations mécaniques et thermiques. Ces sollicitations peuvent endommager le ciment et dégrader ses propriétés mécaniques et sa perméabilité et par conséquent modifier sa contribution dans la stabilité et l'étanchéité du puits. La connaissance du comportement de ce ciment dans des conditions de fond de puits (hautes températures, fortes pressions) et de son évolution au cours du temps est essentielle pour l'analyse de fonctionnement du puits pendant l'exploitation et aussi pour garantir son étanchéité pour le stockage et la séquestration des gaz à effet de serre dans des réservoirs pétroliers abandonnés. C'est dans ce but qu'est développée cette étude sur la caractérisation du comportement thermo-poro-mécanique d'un ciment pétrolier sous fortes contraintes pour des températures entre 20 et 90°C. En effet, bien que le ciment soit un matériau de construction très courant, ses propriétés thermo-poro-mécaniques sont encore mal connues. Peu de données expérimentales d'essais poro-mécaniques existent dans la littérature. L'existence de plusieurs échelles de porosité dans la microstructure du ciment fait que l'utilisation de la théorie des milieux poreux pour la description du comportement du ciment est elle-même un sujet de débat. Dans cette étude on essaye de répondre à cette question par une approche expérimentale à l'échelle macroscopique. Le comportement du ciment est étudié dans un programme expérimental avec des essais poromécanique classiques, pour lesquels le protocole d'essai est adapté à la très faible perméabilité du ciment. L'analyse de la compatibilité et de la cohérence des paramètres poromécaniques évalués à partir de ces essais nous permettra d'examiner la possibilité de la description de comportement du ciment dans le cadre de la théorie des milieux poreux.

Ce rapport est présenté sous la forme de cinq chapitres et d'une annexe. Le premier chapitre est consacré à l'étude bibliographique et aux outils de modélisation thermo-poro-mécanique. Etudier le comportement thermo-poro-mécanique du ciment nécessite dans un premier temps une connaissance suffisante de la microstructure de ce matériau. Cela nous permet ensuite de développer un cadre théorique adapté à la microstructure du ciment pour la modélisation thermo-poro-mécanique de son comportement. Un programme expérimental est ensuite défini pour l'évaluation des différents paramètres du modèle développé.

La première étape de l'étude expérimentale de comportement du ciment est la préparation des éprouvettes. Ceci est présenté dans le deuxième chapitre. Pour la préparation des éprouvettes, un ciment pétrolier class G, un rapport d'eau à ciment égal à 0,44, une température d'hydratation de 90°C et une durée minimum d'hydratation de 3 mois ont été choisis et appliqués pour toutes les éprouvettes fabriquées et testées dans cette étude. Le chapitre 2 présente également une description des dispositifs expérimentaux : cellule triaxiale, dispositifs de chargement et de contrôle de la pression interstitielle et de la pression de confinement, instrumentation, ainsi que le protocole de réalisation des différents essais.

Le chapitre 3 présente l'étude de comportement thermo-poro-mécanique du ciment pétrolier sous chargement isotrope. Les paramètres poro-mécaniques du ciment et leurs variations avec l'état de contraintes et la température ont été évalués dans un programme expérimental d'essais de compression drainés, non-drainés et 'sans membrane' à 20°C et à 90°C couplé avec l'observation microscopique des

échantillons avant et après les essais. Le comportement poro-mécanique du ciment à température ambiante est présenté sous la forme d'un article intitulé 'Poromechanical behaviour of hardened cement paste under isotropic loading' publié dans la revue 'Cement and Concrete Research'. Les essais poro-mécaniques ont été couplés avec une évaluation de la perméabilité du ciment sous chargement isotrope en régime transitoire. Une nouvelle méthode est développée pour l'évaluation de la relation perméabilité-porosité à partir d'un seul essai. Ceci est présenté sous la forme d'un article intitulé 'Evaluation of a permeability-porosity relationship in a low-permeability creeping material using a single transient test' qui est publié la revue 'International Journal of Rock Mechanics and Mining Sciences'.

Lorsqu'un puits pétrolier est soumis à de rapides variations de températures, les déformations et la surpression interstitielle qui en résultent peuvent porter atteinte à l'intégrité du puits. Ce phénomène de pressurisation thermique est étudié et présenté dans le chapitre 4. Une étude préliminaire, théorique et expérimentale a été menée sur un grès. Les effets des déformations mécaniques et thermiques du système de drainage lors d'un essai de chauffage non-drainé ont été analysés et une méthode simple a été développée pour apporter une correction aux valeurs de pressions interstitielles mesurées. Cette étude préliminaire est présentée sous la forme d'un article intitulé 'Stress-dependent thermal pressurization of a fluid-saturated rock' qui est publié dans la revue 'Rock Mechanics and Rock Engineering'. Le comportement thermique du ciment a été étudié expérimentalement dans les essais de chauffage drainés et non-drainés et le coefficient de pressurisation thermique ainsi que les coefficients d'expansion thermique drainé et non-drainé du ciment ont été évalués. Ceci est présenté sous la forme d'un article intitulé 'The effect of undrained heating on a fluid saturated hardened cement paste' qui est publié dans à la revue 'Cement and Concrete Research'.

Le chapitre 5 présente une étude préliminaire du comportement poromécanique du ciment sous chargement déviatorique. Cette étude est limitée à trois essais déviatoriques drainés réalisés à 90°C. Elle permet de proposer un modèle simple d'endommagement. Elle comporte aussi une discussion sur l'observation microscopique des échantillons après la rupture.

Les conclusions et les perspectives générales de l'ensemble de l'étude de comportement thermo-poro-mécanique du ciment sont présentées dans le sixième chapitre de ce rapport.

En complément de ce travail sur le comportement du ciment, une étude expérimentale est menée sur la loi de contrainte effective qui contrôle la perméabilité d'un calcaire et un modèle conceptuel basé sur la micro-texture du matériau est proposé. Les résultats de cette étude sont présentés dans l'annexe, sous la forme d'un article intitulé 'Effective stress law for the permeability of a limestone' qui est publié dans la revue 'International Journal of Rock Mechanics and Mining Sciences'.

Les cinq articles de revue sont présentés à l'intérieur des différents chapitres de la thèse, mais sous la forme des documents indépendants pour lesquels la numérotation des sous chapitre, des figures, des tableaux et des équations est indépendante du reste du document. Une partie de la formulation poromécanique ainsi que le processus de préparation des éprouvettes testées décrits dans les chapitres 1 et 2 sont repris dans les différents articles.

CHAPITRE 1. ETUDE BIBLIOGRAPHIQUE ET OUTILS DE MODELISATION THERMO-PORO-MECANIQUE

1.1 Introduction

L'objet de ce chapitre est de présenter une étude bibliographique de la microstructure du ciment et de donner le cadre de la modélisation thermo-poro-mécanique du comportement de ce matériau. La connaissance et la compréhension de la microstructure du ciment est en effet une étape importante dans l'étude du comportement de ce matériau. Ce chapitre est organisée en trois parties; il comporte une étude bibliographique sur la microstructure de la pâte de ciment durcie, la présentation du cadre théorique de la modélisation thermo-poro-mécanique et enfin une étude bibliographique sur le comportement du ciment et sur les valeurs numériques des différents paramètres du modèle thermo-poro-élastique, disponibles dans la littérature.

1.2 Microstructure de pâte de ciment durcie

La prise et le durcissement du ciment sont les résultats des réactions chimiques qui se passent entre la poudre de ciment et l'eau de gâchage. Le rapport entre la masse d'eau de gâchage et la masse de ciment est appelé *rapport eau/ciment* et sera désigné dans le reste du mémoire suivant la terminologie anglo-saxone par w/c. On désigne par *hydratation* ces réactions chimiques et les nouveaux composés qui en résultent sont appelés *produits d'hydratation* ou plus simplement *hydrates*. La composition du ciment est variable selon le clinker utilisé. Le ciment est composé de cinq constituants principaux, alite, bélite, aluminate, ferrite et gypse, pour lesquels les fractions massiques typiques pour un ciment Portland ordinaire et un ciment pétrolier class G sont présentées dans le Tableau 1-1. Les abréviations utilisées sont les notations normalisées de la chimie des ciments : C=CaO, H=H_2O, S=SiO_2, F=Fe_2O_3, A=Al_2O_3, $\overline{S}$=SO_3. Généralement le ciment contient aussi des petites quantités d'oxydes mineurs de calcium, magnésium, potassium, sodium et soufre. Le ciment, lorsqu'il est utilisé dans un puits pétroliers, doit satisfaire à des besoins spécifiques. Le coulis de ciment au cours de sa mise en place dans le puits, peut atteindre une température élevée (jusqu'à 250°C) et une pression de l'ordre de 150MPa. Le coulis doit rester suffisamment fluide pendant l'opération de pompage et doit développer rapidement une résistance à la compression suffisante. Le ciment doit être aussi suffisamment étanche pour isoler les formations et empêcher l'écoulement de fluides (eau, saumure ou gaz) et cela en résistant à l'attaque chimique. Différentes classes du ciment sont définies par l'*American Petroleum Institute (API)* pour l'utilisation dans les puits pétroliers. Les classes G et H, qui sont largement utilisées peuvent se trouver comme MSR (*Moderate Sulfate-Resistant Grade*) ou HSR (*High Sulfate-Resistant Grade*), la différence est leur teneur en C_3A. La concentration en C_3A doit être inférieure à 8% en poids pour un ciment MSR et à 3% pour un HSR. La composition typique du ciment class G est présentée dans le Tableau 1-1.

Composante	Nom	Formule chimique	Notation	% massique (ciment ordinaire)	% massique (ciment class G)
Tricalcium silicate	Alite	$3CaO.SiO_2$	C_3S	50	50
Dicalcium silicate	Bélite	$2CaO.SiO_2$	C_2S	25	30
Tricalcium aluminate	Aluminate	$3CaO.Al_2O_3$	C_3A	12	5
Tetracalcium aluminoferrite	Ferrite	$4CaO.Al_2O_3.Fe_2O_3$	C_4AF	8	12
Calcium sulfate dihydrate	Gypse	$CaSO_4.2H_2O$	$C\bar{S}H_2$	3,5	1,4

Tableau 1-1- Compositions typiques du ciment Portland ordinaire et d'un ciment pétrolier class G (d'après, Michaux *et al*., 1990 ; Jennings *et al*., 2002 ; Mindess *et al*., 2003)

1.2.1 Hydratation du ciment

Une discussion sur la microstructure de la pâte de ciment durcie nécessite une compréhension du processus d'hydratation. Les réactions chimiques de l'hydratation du ciment sont complexes et plusieurs détails sont encore aujourd'hui sujets de débat. Dans ce chapitre uniquement les aspects essentiels de ce processus qui sont en relation avec la discussion principale sur la microstructure de ciment seront présentés. Une description plus détaillée des réactions chimiques est présentée par Taylor (1997). Sur le Tableau 1-1 on peut voir que les silicates de calcium représentent à peu près deux tiers de la composition du ciment. Ces produits réagissent avec l'eau et forment le produit principal d'hydratation, appelé calcium silicate hydrate C-S-H, et l'hydroxyde de calcium CH, appelé Portlandite (Michaux *et al*., 1990):

$$2C_3S + 6H \rightarrow C_3S_2H_3 + 3CH \quad (1\text{-}1)$$

$$2C_2S + 4H \rightarrow C_3S_2H_3 + CH \quad (1\text{-}2)$$

L'hydratation de l'alite (C_3S impur) et de la bélite (C_2S impur) fournit une grande partie de la résistance développée dans la pâte du ciment. Le C-S-H et le CH occupent respectivement environ 50 à 60% et 20 à 25% du volume total des hydrates. La formule $C_3S_2H_3$ n'est qu'une approximation pour le C-S-H, car sa composition varie considérablement selon la composition du ciment, la quantité d'eau dans la pâte, les conditions de cure. Mindess *et al*. (2003) présentent la formule $C_3S_2H_8$ pour le C-S-H. Par conséquent, ces auteurs présentent les équations (1-1) et (1-2) sous des formes légèrement différentes. Le C-S-H est un gel amorphe qui contient des pores, appelés pores de gel, dont le diamètre est de l'ordre de quelques nanomètres. La finesse de la porosité de gel, crée une surface spécifique de quelques centaines de m^2/g. Par conséquent, le C-S-H est responsable de la plupart des propriétés de la pâte de ciment durcie, comme la résistance, la perméabilité, les variations de volume, etc. Une autre conséquence de la porosité très fine et de la surface spécifique très grande est l'association et les interactions significatives entre la phase solide et la phase aqueuse de C-S-H. Par conséquent le C-S-H est souvent décrit dans la littérature comme une structure colloïdale très fine. En plus de l'eau dans les pores de gel, le C-S-H contient une certaine quantité d'eau chimiquement liée. Contrairement au C-S-H, le CH est un matériau cristallin avec une composition fixe. C_3A et C_4AF réagissent avec le gypse et l'eau et produisent l'ettringite, $C_6A\bar{S}_3H_{32}$ (Mindess *et al*., 2003).

$$C_3A + 3C\bar{S}H_2 + 26H \rightarrow C_6A\bar{S}_3H_{32} \quad (1\text{-}3)$$

$$C_4AF + 3C\bar{S}H_2 + 21H \rightarrow C_6(A,F)\bar{S}_3H_{32} + (F,A)H_3 \quad (1\text{-}4)$$

Si les sulfates sont consommés avant l'hydratation complète du C_3A, l'ettringite réagit avec le C_3A et l'eau et forme un autre produit, le monosulfoaluminate. Quand celui-ci est en contact avec de nouvelles sources de sulfates, l'ettringite peut être produite à nouveau. Ce potentiel de production de l'ettringite est la base de l'agression du ciment par les sulfates quand celui-ci est en contact avec une source externe de sulfates. Les ciments qui contiennent une quantité faible de C_3A et une quantité plus importante de C_4AF sont plus résistants à l'agression par les sulfates (Mindess *et al*., 2003), comme on peut voir dans la composition du ciment classe G présentée sur le Tableau 1-1.

A température ambiante, après le mélange du ciment et de l'eau, le coulis préparé reste dans un état relativement fluide jusqu'à 2 à 4 heures et ensuite commence à se solidifier avec une vitesse plus rapide. La phase de prise initiale correspond au temps nécessaire pour que le coulis perde sa fluidité. La résistance de ciment augmente rapidement dans les deux premiers jours et continue à augmenter plus lentement pendant plusieurs mois. Le processus d'hydratation et la formation de la microstructure de la pâte du ciment, schématisés sur la Figure 1-1, commencent par la production des hydrates solides qui naissent à la surface des grains anhydres et remplacent l'espace initialement rempli par l'eau. Ces hydrates, appelés C-S-H de faible densité (*outer product* ou *early product*), forment une matrice continue et relient les grains anhydres. En raison de leur densité plus faible (~2 gr/cm^3 à comparer avec 3,2 gr/cm^3 pour les grains anhydres) ils occupent un volume plus grand que les grains anhydres. Par conséquent, la porosité capillaire qui est initialement remplie par l'eau, diminue progressivement au cours de l'hydratation. Les hydrates de faible densité contiennent des impuretés et ont une porosité élevée, environ 0,37 pour un ciment ordinaire hydraté à température ambiante (Jennings, 2000).

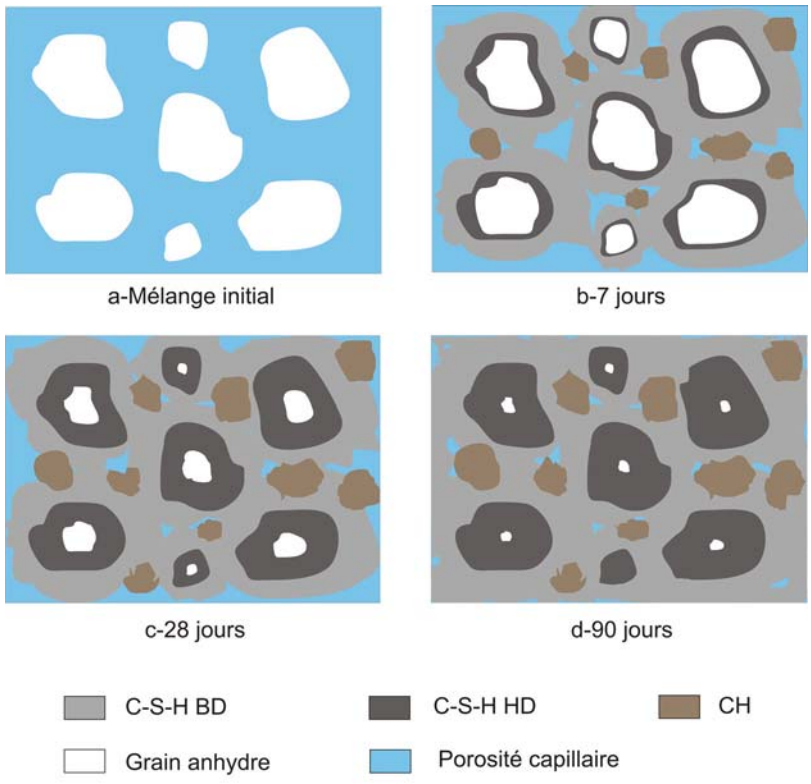

Figure 1-1- Le processus d'hydratation et la formation de la microstructure de la pâte du ciment : (a) Mélange initial ; (b) 7 jours ; (c) 28 jours ; (d) 90 jours

Le processus d'hydratation continue par la formation d'un autre type de C-S-H, appelé C-S-H de haute densité (*inner product* ou *late product*), autour des grains anhydres. Ces hydrates de haute densité forment une coquille autour des grains anhydres qui s'épaissie avec le temps, vers l'intérieur des grains aussi bien que vers l'extérieur (Figure 1-2-b). Comparé au C-S-H de faible densité, le C-S-H de haute densité contient moins d'impuretés et a une porosité plus faible, environ 0,24 pour un ciment ordinaire hydraté à température ambiante (Jennings, 2000). La fraction volumique de C-S-H de haute densité dans un ciment augmente avec la diminution de la quantité d'eau dans le mélange initial. Au cours de l'hydratation, les cristaux d'hydroxyde de calcium, CH, sont formés dans l'espace de la porosité capillaire initialement rempli par l'eau (Figure 1-2-a).

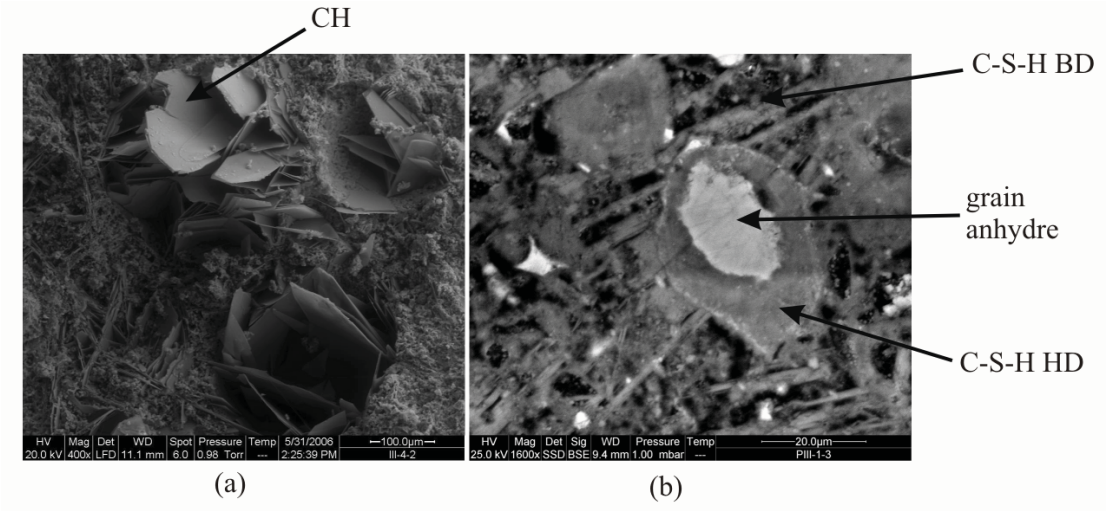

Figure 1-2- Microstructure de la pâte de ciment durcie vue dans une (a) section fracturée, (b) section polie

La chimie d'hydratation du ciment entre 25°C et 100°C ne varie pas essentiellement, mais la température accélère la cinétique d'hydratation et modifie la microstructure du ciment et les fractions volumiques des hydrates (Taylor, 1997). La température d'hydratation a une influence assez significative sur les propriétés mécaniques et la résistance de la pâte durcie. Verbeck et Helmuth (1968) suggèrent que pour les températures élevées l'hydratation rapide de ciment produit une quantité initiale importante d'hydrates. Ces hydrates entourent les grains anhydres et créent une barrière qui limite l'accès de l'eau et par conséquent limite ou retarde la suite du processus d'hydratation. Il en résulte des hydrates qui sont plus poreux et plus hétérogènes. Les ciments hydratés à températures plus élevées ont une porosité totale plus grande et une quantité plus importante de pores de grandes tailles (Kjellsen *et al*., 1990). Ainsi, l'hydratation à température plus élevée augmente la fraction volumique de C-S-H de haute densité dans le ciment. Les modifications de la microstructure du ciment provoquées par la température d'hydratation, influencent ses propriétés mécaniques. Due à l'augmentation de la vitesse d'hydratation avec la température, les ciments hydratés à température plus élevée ont une résistance initiale plus importante. Mais l'hétérogénéité plus importante de la microstructure et la porosité plus élevée de ces ciments conduisent à une résistance à long-terme qui est inférieure à celle des ciments hydratés aux températures plus basses, (Figure 1-3, d'après Mindess *et al*., 2003).

1.2.2 Structure de C-S-H

A cause de son caractère amorphe et la variabilité de sa composition, le C-S-H est un matériau difficile à étudier. La structure colloïdale de C-S-H a été identifiée pour la première fois par Powers et ses collègues à la *Portland Cement Association* (Powers et Brownyard, 1948). Dès lors, plusieurs

modèles conceptuels ont été présentés pour la structure de C-S-H. Afin de donner une idée de la structure de C-S-H, deux modèles sont présentés brièvement dans la suite. Le premier est le modèle présenté par Feldman et Sereda (1968), schématisé sur la Figure 1-4, qui considère le gel de C-S-H comme un assemblage des feuillets de C-S-H qui tendent de former des groupes semi-parallèles de quelques couches et qui entourent des pores. Ce modèle considère l'existence d'un espace interfoliaire contenant l'eau fortement liée et l'eau interfoliaire.

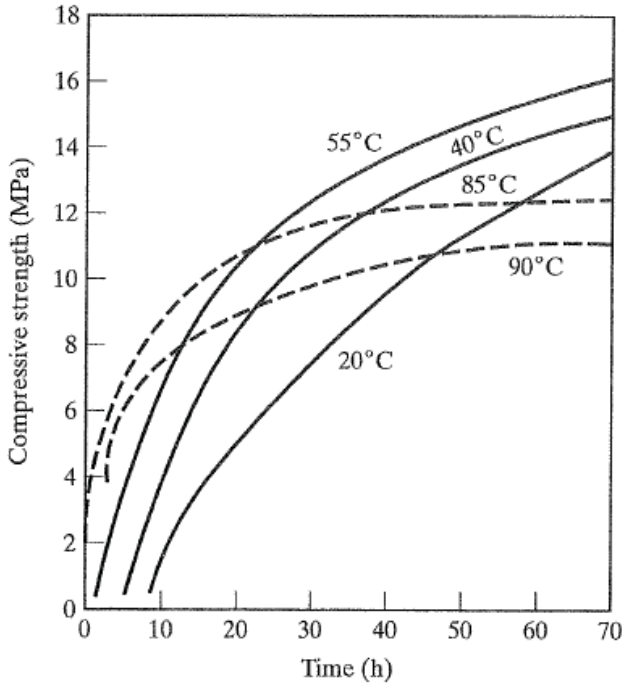

Figure 1-3- Effet de la température d'hydratation sur la résistance en compression (d'après Mindess *et al.*, 2003)

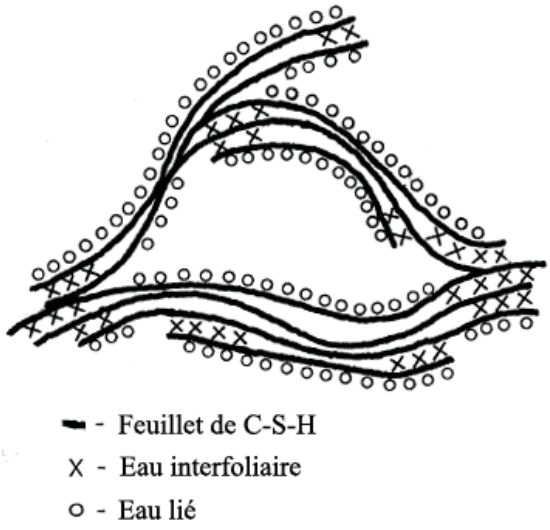

Figure 1-4- Modèle de Feldman et Sereda (1968) pour la structure de C-S-H

Récemment, Jennings (2000, 2008) a proposé un modèle pour la structure colloïdale et amorphe de C-S-H, organisé en éléments, appelés *globules*. Les globules sont composés de feuillets de C-S-H et ont une porosité intra-globule. La structure colloïdale de C-S-H dans le modèle de Jennings (2008) et la structure des globules sont schématisées sur la Figure 1-5. La structure de C-S-H contient des petits pores de gel dans les espaces entre les globules voisins et des grands pores de gel entre les assemblages

de quelques globules. Le modèle de Jennings (2008), ainsi que les études expérimentales et théoriques de Constantinides et Ulm (2007) et DeJong et Ulm (2007) à l'aide des essais de nanoindentation montrent la structure nanogranulaire du C-S-H.

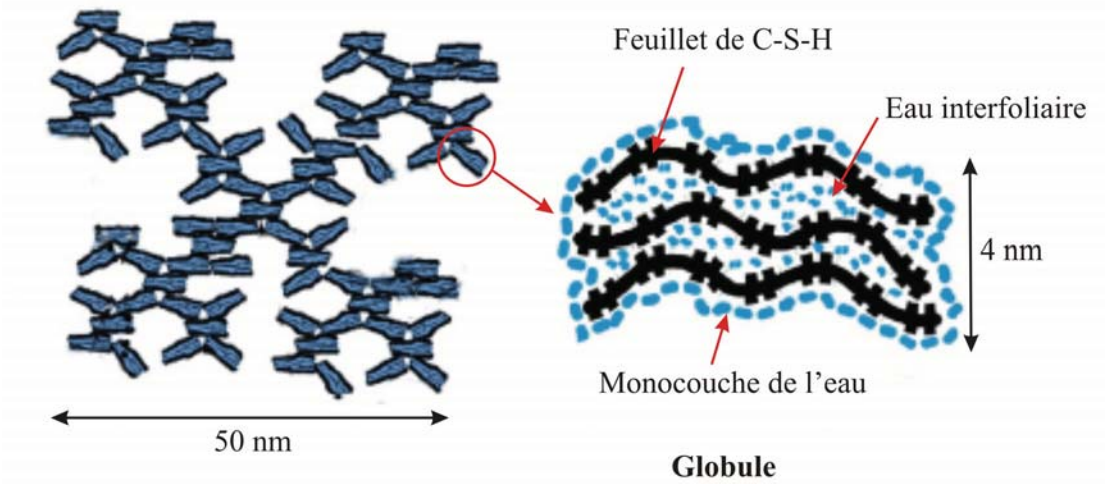

Figure 1-5-Modèle de Jennings (2008) pour la structure de C-S-H

1.2.3 Microstructure simplifiée de la pâte de ciment durcie

Dans une représentation simplifiée, on peut considérer que la microstructure de la pâte de ciment est composée de quatre phases solides principales : grains anhydres, C-S-H HD, C-S-H BD et CH. Pour simplifier, les autres produits d'hydratation comme l'ettringite et les impuretés sont considérés comme une partie de la phase C-S-H. La microstructure simplifiée de la pâte de ciment durcie est schématisée sur la Figure 1-6.

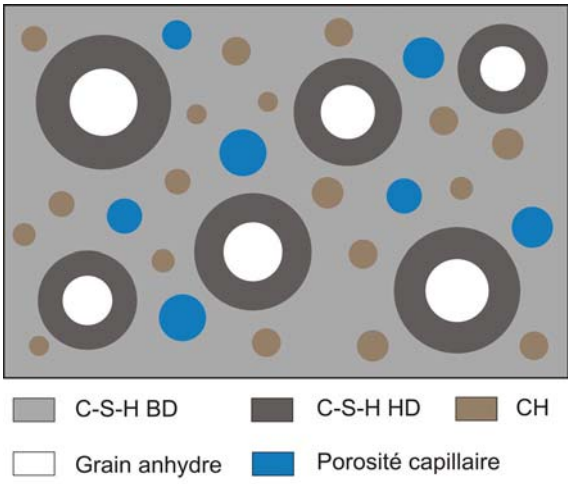

Figure 1-6- Microstructure simplifiée de la pâte de ciment durcie

La fraction volumique approximative de chaque composant peut être estimée à l'aide de modèle de Powers et Brownyard (1948) pour un ciment Portland ordinaire en fonction du rapport w/c et du degré d'hydratation. Pour les autres types de ciment, le modèle de Jennings et Tennis (1994) donne les fractions volumiques des composants en fonction de la composition de ciment, du rapport w/c et du degré d'hydratation. Ces deux modèles sont adaptés pour l'hydratation à température ambiante. Parmi les quatre phases solides, les grains anhydres et le CH peuvent être considérés comme des solides non-poreux tandis que les deux types de C-S-H contiennent une porosité de gel. Les composantes de la

microstructure de la pâte de ciment durcie, schématisée sur la Figure 1-6, ont des propriétés physiques et mécaniques très différentes. Le Tableau 1-2 présente les valeurs de densité, porosité, module d'Young et la fraction volumique de ces composantes (Ulm *et al*., 2004). Les valeurs des modules d'Young sont évaluées à l'aide des essais de nanoindentation. On peut voir les différences considérables entre les propriétés des différentes composantes, et particulièrement pour les modules d'Young.

Composant	**Densité (Saturé) (gr/cm^3)**	**Porosité**	**Indentation modulus $E/(1-\nu^2)$ (GPa)**	**Fraction volumique (w/c=0,5 ; hydratation complète)**
C-S-H BD	1,93	0,37	22	0,57
C-S-H HD	2,13	0,24	29	0,25
CH	2,24	-	38	0,11
Grain anhydre	3,15	-	125-145	0,0[(a)]
Porosité capillaire	-	-	-	0,07

Les valeurs sont présentées pour un ciment ordinaire hydraté à température ambiante
[(a)]En réalité une quantité des grains anhydres restent dans la microstructure même après plusieurs années d'hydratation

Tableau 1-2- Propriétés des composants de la microstructure de la pâte de ciment durcie (d'après Ulm *et al*., 2004)

1.2.4 Porosité

La porosité de gel dans le C-S-H et la porosité capillaire forment la porosité totale de la pâte de ciment durcie. Lorsque le rapport w/c dans une pâte de ciment dépasse une certaine limite (~0,38), les hydrates ne peuvent plus entièrement remplir l'espace disponible initialement occupé par l'eau et par conséquent une porosité avec des pores relativement grands, appelée porosité capillaire, est introduite dans la pâte durcie. Les diamètres des pores dans la porosité de la pâte de ciment couvrent une large gamme, de 0,5nm dans la porosité de gel jusqu'à 10µm dans la porosité capillaire. Dans les micro-photographies de la pâte de ciment, on peut parfois voir aussi des grands pores créés par des bulles d'air au moment de la fabrication de coulis du ciment, qui peuvent atteindre un diamètre de 1,0mm. La porosité totale de ciment peut être évaluée en séchant un échantillon à 105°C. Cette porosité contient une partie de l'eau interfoliaire de la structure de C-S-H. Au cours du séchage de ciment, à partir d'une humidité relative égale à 11%, une partie de l'eau située dans la porosité interfoliaire s'évapore, mais une autre partie liée aux feuillets de C-S-H reste dans la structure de ciment (Jennings, 2008). Par conséquent une autre porosité, appelée porosité de l'eau libre, peut être définie qui ne prend pas en compte l'eau interfoliaire. Cette porosité peut être évaluée en mettant un échantillon en équilibre à 11% d'humidité relative (Taylor, 1997 ; Jennings *et al*., 2002). La Figure 1-7 présente la dépendance de la porosité totale et de la porosité de l'eau libre mesurées pour une pâte de ciment ordinaire durcie en fonction du rapport w/c (d'après Feldman, 1972). La Figure 1-8 présente la relation entre les différentes porosités de la pâte de ciment durcie et le rapport w/c. Dans cette figure les courbes sont calculées à l'aide du modèle de Powers et Brownyard (1948). Les données expérimentales correspondent aux mesures de la porosité totale à l'eau et de la porosité à mercure. On peut voir que pour un rapport w/c inférieur à 0,5 la porosité de l'eau libre peut être approximée par la porosité à mercure. Pour un rapport w/c plus important, la porosité à mercure est inférieure à la porosité de l'eau libre.

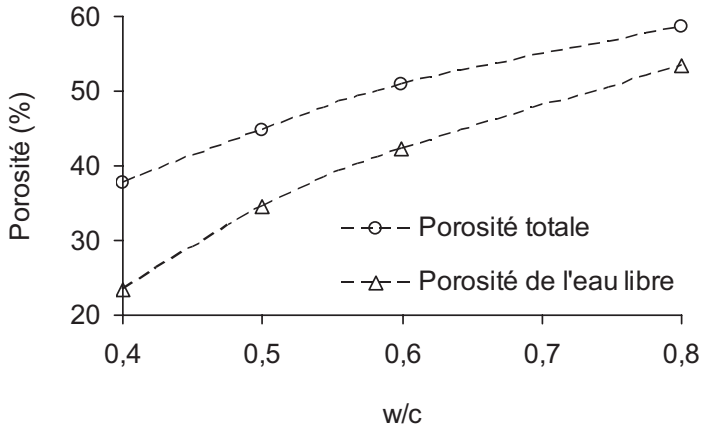

Figure 1-7- Porosité totale et porosité de l'eau libre mesurées pour une pâte de ciment ordinaire durcie (d'après Feldman, 1972)

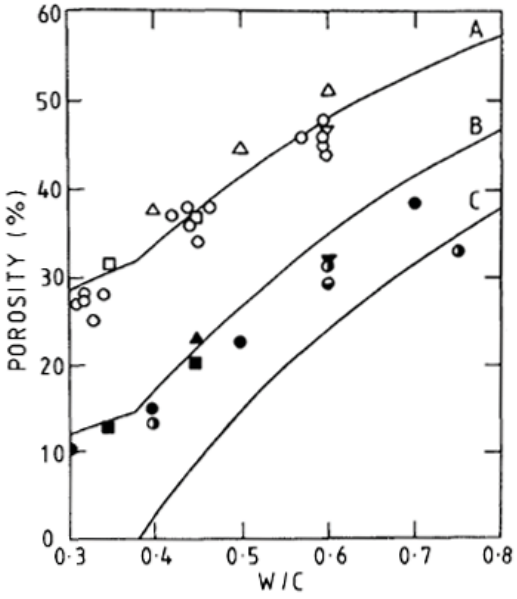

Figure 1-8- Relation entre les porosités d'une pâte de ciment durcie et le rapport w/c. Les courbes sont calculées à l'aide de modèle de Powers et Brownyard (1948) ; A : porosité totale à l'eau, B : porosité de l'eau libre, C : porosité capillaire. Les données expérimentales correspondent à la porosité totale à l'eau (symboles non-remplis) et à la porosité à mercure (symboles remplis) (d'après Taylor, 1990)

1.3 Outils de modélisation thermo-poro-mécanique

Pour étudier le comportement thermo-poro-mécanique du ciment, il est nécessaire de préciser le cadre théorique de la modélisation, d'identifier les paramètres de base du modèle et de définir les essais de laboratoire nécessaires pour les évaluer. La théorie poromécanique est une extension de la théorie de la mécanique des milieux continus solides, à l'étude des matériaux poreux pour lesquels le comportement mécanique est influencé par la présence d'un ou plusieurs fluides interstitiels. Terzaghi (1936) est vraisemblablement le premier qui a identifié le rôle important de la pression interstitielle dans la déformation des sols. Terzaghi a observé que la contrainte totale et la pression interstitielle ont des rôles équivalents, mais inverses, dans la déformation des sols et par conséquent il a attribué les variations de volume et les états limites à la rupture du matériau à une contrainte dite « effective » σ'_{ij}, définie comme la différence entre la contrainte totale σ_{ij} et la pression interstitielle p_f :

$\sigma_{ij}^{'} = \sigma_{ij} - p_f \delta_{ij}$. Cette hypothèse de Terzaghi n'est en réalité correcte que dans certains cas et n'est pas une règle générale pour tous les matériaux poreux. La première théorie de comportement mécanique des milieux poreux est développée par Biot (1941) pour un cas général dans lequel les grains solides sont compressibles et ne sont pas nécessairement isotropes ou homogènes. Biot a présenté une extension des équations de la théorie de l'élasticité pour le cas d'un matériau poreux saturé en introduisant deux paramètres supplémentaires, *H* et *R*. Le paramètre *H* décrit la variation du volume du matériau due à une variation de la pression interstitielle tandis que *R* décrit la variation de la quantité du fluide interstitiel due à une variation de la pression interstitielle. Par conséquent la déformation volumique ε est exprimée en fonction de la contrainte moyenne σ et la pression interstitielle p_f : $\varepsilon = \sigma / K_d + p_f / H$ ou K_d est le module de compression du solide drainé. La variation de la quantité du fluide θ est exprimée en fonction de σ et p_f : $\theta = \sigma / H + p_f / R$. Gassman (1951) a établi les relations entre les propriétés des constituants solide et fluide et les coefficients qui apparaissent dans les équations de Biot pour le cas d'un matériau poreux avec un seul constituant solide. Biot et Willis (1957) ont écrit l'expression d'une contrainte effective plus générale que celle de Terzaghi pour la variation du volume total des matériaux poreux. Geertsma (1957) a réécrit les équations de Biot en termes de variables directement mesurables en laboratoire telles que la pression de confinement, la pression interstitielle, le volume total et le volume poreux pour une matrice solide isotrope et homogène et a défini, pour un matériau homogène et isotrope, la contrainte effective pour la variation du volume total (équivalente à la contrainte effective de Biot) et la contrainte effective pour la variation du volume poreux. Brown et Korringa (1975) ont complété la formulation de Geertsma (1957) en ajoutant un paramètre supplémentaire, pour des matériaux, similaires à ceux considérés par Biot (1941), qui ne satisfont pas nécessairement les conditions de micro-homogénéité ou micro-isotropie. La définition des paramètres poro-élastiques dans Brown et Korringa (1975) est basée sur le choix de deux variables indépendantes: la pression différentielle définie comme la différence entre la contrainte totale moyenne et la pression interstitielle (autrement dit, la contrainte effective de Terzaghi) et la pression interstitielle. Rice et Cleary (1976) ont utilisé une formulation assez semblable à celle de Brown et Korringa (1975) pour la solution de plusieurs problèmes aux limites avec des paramètres de compressibilité constants. La prise en compte de l'effet de la température dans la théorie des milieux poreux est probablement initiée par Palciauskas et Domenico (1982) qui ont présenté une extension de la formulation de Biot en ajoutant le terme de température. McTigue (1986) a ensuite présenté une extension de l'approche de Rice et Cleary (1976) en prenant en compte l'effet de température. Zimmerman *et al*. (1986) ont présenté une formulation pour le comportement volumique poro-élastique d'un matériau poreux composé d'un seul constituant solide. Dans cette formulation les compressibilités varient avec la contrainte et leurs définitions sont basées sur le choix de la pression de confinement et la pression interstitielle comme deux variables indépendantes. Ces auteurs ont également présenté les expressions des coefficients de contrainte effective pour la variation des différentes propriétés physique du matériau et ont présenté aussi des bornes et des inégalités pour les valeurs de compressibilités et les coefficients de contrainte effective. Une approche similaire a été présentée par Berryman (1992) en se basant sur la formulation de Brown et Korringa (1975) pour un cas plus général sans faire d'hypothèse de micro-homogénéité ou micro-isotropie. Coussy (1991, 2004) a présenté un cadre rigoureux pour la théorie poromécanique qui prend en compte plusieurs aspects de thermo-poro-élasticité des milieux poreux saturés et non-saturés, poroplasticité, poro-visco-élasticité, chemo-élasticité.

Le cadre théorique utilisé dans cette étude est une combinaison des formulations de Brown et Korringa (1975) et Rice et Cleary (1976) pour la partie isotherme et les travaux de Palciauskas et

Domenico (1982) et McTigue (1986) pour les aspects thermiques. Trois variables indépendantes ont été choisies pour la définition des paramètres du modèle : la pression différentielle, la pression interstitielle et la température. Cette formulation est développée pour un matériau qui ne satisfait pas nécessairement les conditions de micro-isotropie ou micro-homogénéité, ce qui convient à la microstructure de la pâte de ciment durcie. Le matériau est supposé saturé et la phase fluide est présumée connectée. De plus, on suppose que la pression interstitielle est en équilibre dans les pores. La porosité occlue et le fluide qui remplit cette partie de la porosité sont considérés comme faisant partie de la phase solide. Dans un premier temps on suppose que le matériau et sa phase solide sont élastiques. Une fois la formulation thermo-poro-élastique développée, une extension de cette formulation sera présentée pour prendre en compte les effets des déformations non-élastiques. La formulation développée peut être aisément simplifiée et utilisée pour un matériau poreux idéal qui satisfait les conditions de micro-isotropie et micro-homogénéité. La phase solide d'un tel matériau doit être composée d'un seul constituant sans porosité occlue.

1.3.1 Comportement volumique thermo-poro-élastique

Le matériau poreux saturé est constitué de deux phases: la phase solide et la phase liquide. La phase solide peut être constituée de plusieurs constituants mais la phase fluide est constituée d'un seul fluide. La porosité Eulerienne ϕ est définie comme le rapport du volume de l'espace poreux V_ϕ et le volume total V dans la configuration actuelle (déformée) du système.

$$\phi = \frac{V_\phi}{V} \tag{1-5}$$

Dans un matériau poreux saturé le volume poreux est égal au volume de la phase fluide. On considère un état de contraintes isotrope et on choisit trois variables indépendantes pour caractériser le comportement volumique du matériau poreux : la pression différentielle σ_d, la pression interstitielle p_f et la température T. La pression différentielle qui est équivalente à la contrainte effective de Terzaghi est définie comme la différence entre la contrainte moyenne σ (positive en compression) et la pression interstitielle p_f :

$$\sigma_d = \sigma - p_f \tag{1-6}$$

Les conventions de signe utilisées ici sont celles de la mécanique des sols et des roches qui contrairement aux conventions de la mécanique des milieux continus considèrent les contraintes de compression positives. Les expressions de la variation du volume total V et du volume de la phase fluide V_ϕ sont écrites comme :

$$\frac{dV}{V} = \frac{1}{V}\left(\frac{\partial V}{\partial \sigma_d}\right)_{p_f,T} d\sigma_d + \frac{1}{V}\left(\frac{\partial V}{\partial p_f}\right)_{\sigma_d,T} dp_f + \frac{1}{V}\left(\frac{\partial V}{\partial T}\right)_{p_f,\sigma_d} dT \tag{1-7}$$

$$\frac{dV_\phi}{V_\phi} = \frac{1}{V_\phi}\left(\frac{\partial V_\phi}{\partial \sigma_d}\right)_{p_f,T} d\sigma_d + \frac{1}{V_\phi}\left(\frac{\partial V_\phi}{\partial p_f}\right)_{\sigma_d,T} dp_f + \frac{1}{V_\phi}\left(\frac{\partial V_\phi}{\partial T}\right)_{p_f,\sigma_d} dT \tag{1-8}$$

Les équations (1-7) et (1-8) permettent de définir six paramètres principaux pour caractériser le comportement volumique du matériau poreux. Parmi ces paramètres, quatre sont les modules de

compressions définis en condition isotherme $\left(dT = 0\right)$ et les deux autres sont les coefficients d'expansion thermiques définis pour un état de contraintes et de pression interstitielle constantes $\left(d\sigma_d = dp_f = 0\right)$. Ces six paramètres sont définis dans les équations suivantes :

$$\frac{1}{K_d} = -\frac{1}{V}\left(\frac{\partial V}{\partial \sigma_d}\right)_{p_f,T} \quad , \quad \frac{1}{K_p} = -\frac{1}{V_\phi}\left(\frac{\partial V_\phi}{\partial \sigma_d}\right)_{p_f,T} \tag{1-9}$$

$$\frac{1}{K_s} = -\frac{1}{V}\left(\frac{\partial V}{\partial p_f}\right)_{\sigma_d,T} \quad , \quad \frac{1}{K_\phi} = -\frac{1}{V_\phi}\left(\frac{\partial V_\phi}{\partial p_f}\right)_{\sigma_d,T} \tag{1-10}$$

$$\alpha_d = \frac{1}{V}\left(\frac{\partial V}{\partial T}\right)_{p_f,\sigma_d} \quad , \quad \alpha_\phi = \frac{1}{V_\phi}\left(\frac{\partial V_\phi}{\partial T}\right)_{p_f,\sigma_d} \tag{1-11}$$

L'équation (1-9) décrit un essai de compression isotrope drainé isotherme. Dans cet essai la pression interstitielle et la température sont contrôlées et maintenues constantes et les variations du volume total V et du volume de la phase fluide V_ϕ avec la pression de confinement permettent d'évaluer le module de compression drainée K_d et le module K_p. L'équation (1-10) décrit une situation dans laquelle l'échantillon est immergé dans un réservoir de fluide à pression constante. Pour réaliser cet essai on applique de façon simultanée, des incréments égaux de la pression de confinement et de la pression interstitielle. Dans cette situation la variation de la pression différentielle est nulle. Le module de compression de la phase solide K_s (encore appelée « *module de compression sans membrane* », '*unjacketed compression modulus*' dans la littérature anglo-saxonne) est mesurée dans cet essai à partir des variations du volume total de l'échantillon avec la pression interstitielle. Le module de compression K_ϕ correspond à la variation de volume de la phase fluide dans cet essai. La quantité de fluide échangé entre l'échantillon et le générateur de la pression de fluide peut en principe permettre d'évaluer ce module. Cependant, l'évaluation expérimentale de module K_ϕ est très difficile, car le volume du fluide échangé doit être corrigé pour tenir compte de la compressibilité de système de drainage de la cellule triaxiale et aussi de la compressibilité du générateur de pression pour trouver la variation du volume poreux de l'échantillon, qui doit être en principe un petit volume dans cet essai. Dans le cas d'un matériau poreux idéal, l'échantillon va se déformer dans un essai de compression sans membrane comme si tous les pores étaient remplis du même matériau solide. Le squelette et la phase solide subissent une déformation volumique uniforme sans aucune variation de porosité (Detournay et Cheng, 1993). Pour un tel matériau $K_s = K_\phi = K_m$, ou K_m est le module de compression du seul constituant de la phase solide. Dans le cas plus général d'un matériau poreux constitué de deux ou plusieurs solides, i.e. micro-hétérogène, le module K_s est une certaine moyenne pondérée des modules de compression K_m des différents constituants de la phase solide (Berryman, 1992). Dans le cas général les coefficients de cette moyenne ne sont pas connus, néanmoins dans Ghabezloo et Sulem (2009) (article présenté dans le chapitre 4), en utilisant la formule de la moyenne de Hill (1952) avec les modules de compression et les fractions volumiques des différents constituants de grès de Rothbach, nous avons trouvé une bonne compatibilité entre le module K_s calculé et la valeur mesurée dans un essai de compression 'sans membrane'. Le module K_ϕ d'un matériau poreux micro-hétérogène dépend de façon complexe des propriétés des constituants. Généralement la valeur numérique de ce module n'est pas limitée par celles des modules de compression des constituants et peut même avoir une valeur négative lorsqu'il y a une différence très importante entre les modules de compression des différents constituants (Berge 1995,

Berge et Berryman 1998). Les définitions des modules de compression dans les équations (1-9) et (1-10) ont été présentées par Brown et Korringa (1975).

L'équation (1-11) décrit un essai de chauffage drainé dans lequel la pression de confinement et la pression interstitielle sont contrôlées et maintenues constantes. Le coefficient d'expansion thermique drainé α_d est évalué à partir des mesures de la variation du volume total de l'échantillon avec la température. D'après Palciauskas et Domenico (1982), le coefficient α_d mesuré dans un essai de chauffage drainé peut pratiquement prendre en compte les déformations thermiques non-réversibles qui peuvent être produites par la microfissuration générée en raison de la différence entre les expansions thermique des différents constituants du matériau poreux. Mais l'étude expérimentale de Walsh (1973) a montré que la génération de ces microfissures débute seulement aux températures élevées. Le coefficient α_ϕ doit être en principe évalué à partir des variations de volume de la phase fluide, mais pour les mêmes raisons que celles présentées ci-dessus pour le module K_ϕ, l'évaluation expérimentale de ce coefficient est très difficile et il n'y a aucune mesure directe de ce coefficient dans la littérature. Dans le cas d'un matériau poreux idéal qui satisfait les conditions de micro-isotropie et micro-homogénéité, on a $\alpha_d = \alpha_\phi = \alpha_m$, où α_m est le coefficient d'expansion thermique du constituant de la phase solide. Pour un tel matériau, il n'y a aucune variation de la porosité lors d'un chargement thermique drainé, car une expansion thermique uniforme va générer des variations proportionnelles dans chacune des dimensions linéaires du matériau. En utilisant les définitions des six paramètres présentées dans les équations (1-9) à (1-11), les expressions des déformations volumiques V et V_ϕ, présentées dans les équations (1-7) et (1-8), peuvent être réécrites :

$$\frac{dV}{V} = -\frac{d\sigma_d}{K_d} - \frac{dp_f}{K_s} + \alpha_d dT \tag{1-12}$$

$$\frac{dV_\phi}{V_\phi} = -\frac{d\sigma_d}{K_p} - \frac{dp_f}{K_\phi} + \alpha_\phi dT \tag{1-13}$$

L'expression de la déformation volumique incrémentale $d\varepsilon = -dV/V$ s'écrit donc:

$$d\varepsilon = \frac{d\sigma_d}{K_d} + \frac{dp_f}{K_s} - \alpha_d dT \tag{1-14}$$

En utilisant le théorème de réciprocité de Betti, on peut trouver une relation entre les modules de compression K_p, K_d et K_s (Brown et Korringa, 1975 ; Zimmerman *et al*., 1984). Selon ce théorème, si un corps élastique est soumis à deux ensembles d'efforts, F_1 et F_2, le travail w_{12} de F_1 dans le champ de déplacement généré par F_2 est égal au travail w_{21} de F_2 dans le champ de déplacement généré par F_1. On choisit la pression de confinement appliquée sur la surface extérieure de l'échantillon comme le premier ensemble des efforts, $F_1 = (d\sigma, 0)$ et la pression interstitielle appliquée sur la totalité de la surface des pores comme le deuxième ensemble des efforts, $F_2 = (0, dp_f)$. A l'aide des équations (1-6), (1-12) et (1-13), on écrit les expressions du travail de la pression de confinement dans la variation du volume total causée par la pression interstitielle et réciproquement le travail de la pression interstitielle dans la variation du volume poreux causée par la pression de confinement :

$$w_{12} = -d\sigma\left[dV\left(0, dp_f\right)\right] = -d\sigma\left[V\left(\frac{1}{K_d} - \frac{1}{K_s}\right)dp_f\right] \tag{1-15}$$

$$w_{21} = dp_f \left[dV_\phi \left(d\sigma, 0 \right) \right] = dp_f \left[V_\phi \left(-\frac{1}{K_p} \right) d\sigma \right] \tag{1-16}$$

Le signe négatif dans l'équation (1-15) est mis pour prendre en compte le fait qu'une variation positive de la pression de confinement (compression) entraîne une variation négative du volume total, tandis que dans l'équation (1-16) une variation positive de la pression interstitielle entraîne une variation positive du volume poreux. Selon le théorème de réciprocité de Betti on doit avoir $w_{12} = w_{21}$. En remplaçant les équations (1-15) et (1-16) dans cette égalité et à l'aide de l'équation (1-5) on obtient la relation suivante entre les modules de compressions:

$$\frac{1}{K_p} = \frac{1}{\phi} \left(\frac{1}{K_d} - \frac{1}{K_s} \right) \tag{1-17}$$

Zimmerman *et al*. (1986) soulignent que l'utilisation du théorème de réciprocité dans ce contexte ne présuppose pas que les pores sont bien séparés ou distincts et non-connectés. En utilisant l'équation (1-17), le nombre des paramètres nécessaires pour décrire le comportement volumique est réduit à cinq, dont deux (K_ϕ et α_ϕ) sont difficiles à mesurer expérimentalement comme on l'a mentionné plus haut.

A l'aide de la définition de la porosité présentée dans l'équation (1-5) on peut écrire l'expression de la variation de la porosité :

$$\frac{d\phi}{\phi} = \frac{dV_\phi}{V_\phi} - \frac{dV}{V} \tag{1-18}$$

En remplaçant les équations (1-12), (1-13) et (1-17) dans l'équation (1-18) on obtient l'expression suivante pour la variation de la porosité:

$$\frac{d\phi}{\phi} = -\frac{1}{\phi} \left(\frac{1-\phi}{K_d} - \frac{1}{K_s} \right) d\sigma_d + \left(\frac{1}{K_s} - \frac{1}{K_\phi} \right) dp_f - \left(\alpha_d - \alpha_\phi \right) dT \tag{1-19}$$

La condition non-drainée est définie comme une condition dans laquelle la variation de la masse de fluide est nulle ($dm_f = 0$). Sous cette condition, on choisit deux variables indépendantes : la contrainte moyenne σ et la température T. Les deux quantités à mesurer sont le volume total V et la pression interstitielle p_f. Les variations de V et p_f avec σ et T sont écrites de la façon suivante :

$$\frac{dV}{V} = \frac{1}{V} \left(\frac{\partial V}{\partial \sigma} \right)_{m_f, T} d\sigma + \frac{1}{V} \left(\frac{\partial V}{\partial T} \right)_{m_f, \sigma} dT \tag{1-20}$$

$$dp_f = \left(\frac{\partial p_f}{\partial \sigma} \right)_{m_f, T} d\sigma + \left(\frac{\partial p_f}{\partial T} \right)_{m_f, \sigma} dT \tag{1-21}$$

Les équations (1-20) et (1-21) permettent de définir quatre autres paramètres correspondant à la condition non-drainée.

$$\frac{1}{K_u} = -\frac{1}{V} \left(\frac{\partial V}{\partial \sigma} \right)_{m_f, T} \quad , \quad B = \left(\frac{\partial p_f}{\partial \sigma} \right)_{m_f, T} \tag{1-22}$$

$$\alpha_u = \frac{1}{V}\left(\frac{\partial V}{\partial T}\right)_{m_f,\sigma} \quad , \quad \Lambda = \left(\frac{\partial p_f}{\partial T}\right)_{m_f,\sigma} \tag{1-23}$$

L'équation (1-22) décrit un essai de compression isotrope non-drainé isotherme dans lequel la masse de fluide et la température sont contrôlées et maintenues constantes et où l'on mesure la variation de volume total V et la surpression interstitielle p_f avec la variation de la pression de confinement. B est le coefficient de Skempton (1954) et K_u est le module de compression non-drainé. L'équation (1-23) décrit un essai de chauffage non-drainé à l'état de contrainte constante. Dans cet essai les mesures de la variation du volume total V et de la surpression interstitielle p_f avec la température permettent d'évaluer le coefficient d'expansion thermique non-drainée α_u et le coefficient de pressurisation thermique Λ. En remplaçant les équations (1-22) et (1-23) dans les équations (1-20) et (1-21), on réécrit les expressions des variations du volume total et de la pression interstitielle :

$$\frac{dV}{V} = \frac{d\sigma}{K_u} + \alpha_u dT \tag{1-24}$$

$$dp_f = Bd\sigma + \Lambda dT \tag{1-25}$$

La conservation de la masse de fluide en condition non-drainée ($dm_f = 0$), donne la variation du volume poreux en fonction du module de compression K_f et du coefficient d'expansion thermique α_f du fluide :

$$-\frac{dV_\phi}{V_\phi} = \frac{dp_f}{K_f} - \alpha_f dT \tag{1-26}$$

En utilisant les équations (1-6), (1-13) et (1-17) on peut réécrire l'équation (1-26) de la façon suivante:

$$dp_f = \frac{\left(1/K_d - 1/K_s\right)}{\left(1/K_d - 1/K_s\right) + \phi\left(1/K_f - 1/K_\phi\right)} d\sigma + \frac{\phi\left(\alpha_f - \alpha_\phi\right)}{\left(1/K_d - 1/K_s\right) + \phi\left(1/K_f - 1/K_\phi\right)} dT \tag{1-27}$$

La comparaison des équations (1-25) et (1-27) permet d'identifier le coefficient de Skempton B et le coefficient de pressurisation thermique Λ :

$$B = \frac{\left(1/K_d - 1/K_s\right)}{\left(1/K_d - 1/K_s\right) + \phi\left(1/K_f - 1/K_\phi\right)} \tag{1-28}$$

$$\Lambda = \frac{\phi\left(\alpha_f - \alpha_\phi\right)}{\left(1/K_d - 1/K_s\right) + \phi\left(1/K_f - 1/K_\phi\right)} \tag{1-29}$$

En utilisant les équations (1-6) et (1-25) on réécrit l'équation (1-12) pour la condition non-drainée :

$$\frac{dV}{V} = -\left[\frac{1 - B\left(1 - K_d/K_s\right)}{K_d}\right] d\sigma + \left[\alpha_d + \Lambda\left(1/K_d - 1/K_s\right)\right] dT \tag{1-30}$$

La comparaison des équations (1-24) et (1-30) permet d'identifier les expressions du module de compression non-drainé K_u et du coefficient d'expansion thermique non-drainé α_u :

$$K_u = \frac{K_d}{1 - B\left(1 - K_d / K_s\right)} \tag{1-31}$$

$$\alpha_u = \alpha_d + \Lambda\left(1/K_d - 1/K_s\right) \tag{1-32}$$

En utilisant les équations (1-28) et (1-29) dans l'équation (1-32) on obtient une autre relation pour le coefficient d'expansion thermique non-drainé.

$$\alpha_u = \alpha_d + \phi B\left(\alpha_f - \alpha_\phi\right) \tag{1-33}$$

Comme on l'a déjà mentionné, les paramètres K_ϕ et α_ϕ sont difficiles à mesurer expérimentalement. Les paramètres poro-élastiques mesurés en condition non-drainée et les équations présentées ci-dessus permettent d'évaluer indirectement ces deux paramètres. Les équations (1-34) et (1-35), obtenues en utilisant les équations présentées ci-dessus, expriment les paramètres K_ϕ et α_ϕ en fonction des différents paramètres plus simples à mesurer expérimentalement.

$$\frac{1}{K_\phi} = \begin{cases} \dfrac{1}{K_f} - \dfrac{\left(1/K_d - 1/K_s\right)\left(1/K_u - 1/K_s\right)}{\phi\left(1/K_d - 1/K_u\right)} & \text{(a)} \\ \dfrac{1}{K_f} - \dfrac{\left(1-B\right)\left(1/K_d - 1/K_s\right)}{\phi B} & \text{(b)} \\ \dfrac{1}{K_f} - \dfrac{1/K_u - 1/K_s}{\phi B} & \text{(c)} \\ \dfrac{1}{K_f} - \dfrac{\left(1-B\right)\left(1/K_d - 1/K_u\right)}{\phi B^2} & \text{(d)} \end{cases} \tag{1-34}$$

$$\alpha_\phi = \begin{cases} \alpha_f - \dfrac{\alpha_u - \alpha_d}{\phi B} & \text{(a)} \\ \alpha_f - \dfrac{\Lambda\left(1/K_d - 1/K_s\right)^2}{\phi\left(1/K_d - 1/K_u\right)} & \text{(b)} \\ \alpha_f - \dfrac{\left(\alpha_u - \alpha_d\right)\left(1/K_d - 1/K_s\right)}{\phi\left(1/K_d - 1/K_u\right)} & \text{(c)} \\ \alpha_f - \dfrac{\Lambda\left(1/K_d - 1/K_s\right)}{B} & \text{(d)} \end{cases} \tag{1-35}$$

1.3.1.1 Effets des déformations volumiques non-élastiques

Le cadre théorique décrit ci-dessus peut être généralisé pour prendre en compte les effets des déformations non-élastiques. Ces déformations peuvent être d'origine plastique, viscoélastique ou viscoplastique. Les variations non-élastiques du volume total, du volume poreux et du volume de solide sont définies comme la différence entre la totalité de la variation de volume et sa partie élastique :

$$dV^{ne} = dV - dV^e \; ; \; dV_\phi^{ne} = dV_\phi - dV_\phi^e \; ; \; dV_s^{ne} = dV_s - dV_s^e \tag{1-36}$$

La partie élastique des variations de volume dans l'équation (1-36), dV^e et dV_ϕ^e, sont données respectivement par les équations (1-12) et (1-13). En utilisant les relations $V_\phi = V - V_s$, $d\varepsilon = -dV/V$ et $d\varepsilon_s = -dV_s/V_s$, ou $d\varepsilon_s$ est la déformation volumique de la phase solide, la variation non-élastique du volume poreux est écrite de la façon suivante:

$$dV_\phi^{ne} = dV_\phi - dV_\phi^e = \left(dV - dV_s\right) - \left(dV^e - dV_s^e\right) = V\left[-d\varepsilon^{ne} + (1-\phi)d\varepsilon_s^{ne}\right] \tag{1-37}$$

A partir de l'équation (1-37) on peut écrire :

$$\frac{dV_\phi^{ne}}{V_\phi} = \frac{-1}{\phi}\left[d\varepsilon^{ne} - (1-\phi)d\varepsilon_s^{ne}\right] \tag{1-38}$$

En présence de déformations volumiques non-élastiques les équations (1-12) et (1-13) sont ré-écrites sous la forme suivante :

$$-\frac{dV}{V} = \frac{d\sigma_d}{K_d} + \frac{dp_f}{K_s} - \alpha_d dT + d\varepsilon^{ne} \tag{1-39}$$

$$-\frac{dV_\phi}{V_\phi} = \frac{d\sigma_d}{K_p} + \frac{dp_f}{K_\phi} - \alpha_\phi dT + \frac{d\varepsilon^{ne}}{\phi} - \frac{1-\phi}{\phi} d\varepsilon_s^{ne} \tag{1-40}$$

En utilisant les équations (1-39) et (1-40) dans l'équation (1-18) la relation suivante est obtenue pour la variation de la porosité :

$$\frac{d\phi}{\phi} = -\frac{1}{\phi}\left(\frac{1-\phi}{K_d} - \frac{1}{K_s}\right)d\sigma_d + \left(\frac{1}{K_s} - \frac{1}{K_\phi}\right)dp_f - \left(\alpha_d - \alpha_\phi\right)dT - \frac{1-\phi}{\phi}\left(d\varepsilon^{ne} - d\varepsilon_s^{ne}\right) \tag{1-41}$$

En remplaçant l'équation (1-26) dans l'équation (1-40) pour la condition non-drainée et en utilisant les équations (1-28) et (1-29), on obtient l'expression suivante qui décrit l'effet des déformations non-élastiques sur la surpression interstitielle générée en condition de chargement non-drainé:

$$dp_f = Bd\sigma + \Lambda dT + \frac{d\varepsilon^{ne} - \left(1-\phi\right)d\varepsilon_s^{ne}}{\left(1/K_d - 1/K_s\right) + \phi\left(1/K_f - 1/K_\phi\right)} \tag{1-42}$$

L'équation (1-42) montre que les déformations volumiques non-élastiques contractantes provoquent une augmentation supplémentaire de la pression interstitielle en condition non-drainée. Dans le cas d'un matériau poreux pour lequel la phase solide est élastique ($d\varepsilon_s^{ne} = 0$), les déformations non-élastiques sont dues au déplacement irréversible des grains ou à la création de microfissures dans la matrice solide, et donc l'équation (1-42) est réduite à la forme suivante :

$$dp_f = Bd\sigma + \Lambda dT + \frac{d\varepsilon^{ne}}{\left(1/K_d - 1/K_s\right) + \phi\left(1/K_f - 1/K_\phi\right)} \tag{1-43}$$

1.3.2 Comportement déviatorique

L'expression de déformation volumique présentée dans la section précédente, équation (1-12), peut être généralisée pour prendre en compte de comportement déviatorique (Palciauskas et Domenico, 1982 ; McTigue, 1986 ; Coussy, 2004) :

$$d\varepsilon_{ij} = \frac{d\sigma_{ij}}{2G} - \left(\frac{1}{6G} - \frac{1}{9K_d}\right)\delta_{ij} d\sigma_{kk} + \frac{1}{3}\left(\frac{1}{K_d} - \frac{1}{K_s}\right)\delta_{ij} dp_f - \frac{\alpha_d}{3}\delta_{ij} dT \tag{1-44}$$

$$d\sigma_{ij} = 2G d\varepsilon_{ij} + \left(K_d - \frac{2G}{3}\right)\delta_{ij} d\varepsilon_{kk} - \left(1 - \frac{K_d}{K_s}\right)\delta_{ij} dp_f - K_d \alpha_d \delta_{ij} dT \tag{1-45}$$

où G est le module de cisaillement. De façon équivalente, les relations (1-44) et (1-45), peuvent être écrites en fonction des invariants des tenseurs de contrainte et de déformation. On définit la contrainte moyenne $p = \sigma_{kk}/3$ et le second invariant du déviateur des contraintes $\tau = \sqrt{s_{ij} s_{ij}/2}$, où $s_{ij} = \sigma_{ij} - p\delta_{ij}$ est le déviateur des contraintes ainsi que la déformation volumique $\varepsilon = \varepsilon_{kk}$ et l'intensité du déviateur du tenseur de déformation $\gamma = \sqrt{2 e_{ij} e_{ij}}$, où $e_{ij} = \varepsilon_{ij} - \varepsilon_{kk}\delta_{ij}/3$ est le déviateur des contraintes. Dans les expressions précédentes, la répétition des indices indique la sommation. Les équations (1-44) et (1-45) s'expriment de façon équivalente comme suit:

$$\begin{aligned} d\varepsilon &= \frac{1}{K_d} dp + \left(\frac{1}{K_d} - \frac{1}{K_s}\right) dp_f - \alpha_d dT \\ d\gamma &= \frac{1}{G} d\tau \end{aligned} \tag{1-46}$$

$$\begin{aligned} dp &= K_d d\varepsilon - \left(1 - \frac{K_d}{K_s}\right) dp_f - K_d \alpha_d dT \\ d\tau &= G d\gamma \end{aligned} \tag{1-47}$$

1.3.3 Notion de la contrainte effective

La notion de contrainte effective est couramment utilisée en mécanique des sols et des roches sous la forme de la contrainte effective de Terzaghi (dans le cas de constituants solides incompressibles) ou de Biot (dans le cas de constituants solides compressibles). Cette contrainte effective contrôle les variations de volume total d'un matériau poreux. Si l'on considère maintenant la variation d'une autre propriété physique Q d'un matériau poreux comme par exemple le volume poreux ou la perméabilité, on peut tenter de généraliser cette notion de contrainte effective. Pour ce faire, on définit une quantité σ' ayant la dimension d'une contrainte qui est une fonction de la contrainte totale σ et de la pression interstitielle p_f et qui peut être utilisée comme variable unique pour exprimer les variations de la propriété Q du matériau poreux provoquées par les changements indépendants de la contrainte totale et de la pression interstitielle:

$$Q = Q(\sigma, p_f) = Q(\sigma') \tag{1-48}$$

Par conséquent, si la contrainte totale et la pression interstitielle changent de telle manière que la contrainte effective reste constante, aucune variation de la propriété correspondante n'est attendue. Donc

l'expression de la contrainte effective correspondant à la propriété Q peut être obtenue à partir des isovaleurs de Q. Diminuer le nombre de variables indépendantes de deux à une en employant le concept de la contrainte effective simplifie considérablement l'analyse de la dépendance en contrainte totale et en pression interstitielle des propriétés physiques des matériaux poreux.

Puisque les différentes propriétés du matériau peuvent dépendre de la contrainte totale et de la pression interstitielle de différentes manières, il n'y a pas une contrainte effective unique qui serait appropriée à toutes les propriétés du matériau et par conséquent différentes expressions de la contrainte effective doivent être définies pour les différentes propriétés.

La variation de la propriété Q peut être écrite dans la forme suivante :

$$dQ = \frac{\partial Q}{\partial \sigma} d\sigma + \frac{\partial Q}{\partial p_f} dp_f \tag{1-49}$$

On peut réécrire cette équation sous la forme suivante :

$$dQ = \frac{\partial Q}{\partial \sigma}\left[d\sigma - \left(-\frac{\partial Q/\partial p_f}{\partial Q/\partial \sigma} \right) dp_f \right] \tag{1-50}$$

Cette équation montre que la variation de la propriété Q peut être écrite en fonction d'une seule variable incrémentale $d\sigma'$:

$$dQ = \frac{\partial Q}{\partial \sigma} d\sigma' \tag{1-51}$$

où $d\sigma'$ est défini par :

$$d\sigma' = d\sigma - n_Q dp_f \tag{1-52}$$

avec

$$n_Q\left(\sigma, p_f\right) = -\frac{\partial Q/\partial p_f}{\partial Q/\partial \sigma} \tag{1-53}$$

En choisissant la propriété Q comme une fonction de la pression différentielle σ_d et la pression interstitielle p_f on peut obtenir une expression équivalente pour le coefficient n_Q :

$$n_Q\left(\sigma_d, p_f\right) = 1 - \frac{\partial Q/\partial p_f}{\partial Q/\partial \sigma_d} \tag{1-54}$$

Les isovaleurs de Q sont obtenues à partir de la solution de l'équations différentielle suivante :

$$d\sigma' = 0 \tag{1-55}$$

Dans la proximité d'un état de contraintes donné $\left(\sigma_d, p_f\right)$, les isovaleurs de Q sont généralement approximées par des droites parallèles (Bernabé, 1986), ce qui est équivalent à l'hypothèse de n_Q constant. Avec cette hypothèse on peut facilement intégrer l'équation (1-52) et obtenir l'expression linéaire de la contrainte effective :

$$\sigma' = \sigma - n_Q p_f \tag{1-56}$$

Le paramètre n_Q est le coefficient de la contrainte effective correspondant à la variation de la propriété Q. n_Q est égal à l'unité dans la définition de Terzaghi, ce qui signifie que la contrainte totale et la pression interstitielle ont les effets semblables, mais opposés, sur la variation de la propriété Q. Une valeur du coefficient n_Q plus petite (respectivement plus grand) que l'unité signifie que l'effet du changement de la pression interstitielle sur la variation de la propriété Q est moins (respectivement plus) important que l'effet d'un changement de la contrainte totale. L'expression de coefficient de contrainte effective exprimée dans l'équation (1-54) est présentée pour la première fois par Todd et Simmons (1972). Zimmerman *et al*. (1986), Zimmerman (1991) et Berryman (1992) ont présenté les expressions des coefficients de contrainte effective correspondant aux différentes propriétés physiques des matériaux poreux avec quelques bornes et inégalités entre ces coefficients. Dans Ghabezloo *et al.* (2009) (article présenté dans l'annexe 1) nous avons étudié le coefficient de la contrainte effective pour la variation de la perméabilité d'un calcaire.

Si on remplace la propriété Q dans l'équation (1-54) par la déformation volumique incrémentale $d\varepsilon = -dV/V$, en utilisant les définitions de K_d et K_s données par les équations (1-9) et (1-10), on identifie l'expression de coefficient α de la contrainte effective de Biot (Biot et Willis, 1957) pour la variation du volume total d'un matériau poreux:

$$\alpha = 1 - \frac{K_d}{K_s} \tag{1-57}$$

On définit la contrainte effective de Biot σ'_b comme suit :

$$\sigma'_b = \sigma - \alpha\, p_f \tag{1-58}$$

De la même façon, en remplaçant la propriété Q dans l'équation (1-54) par $-dV_\phi/V_\phi$ et en utilisant les définitions de K_p et K_ϕ données par les équations (1-9) et (1-10), on trouve l'expression de coefficient β de la contrainte effective correspondant à la variation du volume poreux V_ϕ :

$$\beta = 1 - \frac{K_p}{K_\phi} = 1 - \frac{\phi}{K_\phi\left(1/K_d - 1/K_s\right)} \tag{1-59}$$

On observe que ce coefficient est différent du coefficient de Biot présenté dans l'équation (1-57) correspondant à la variation du volume total. On peut également définir, le coefficient χ de la contrainte effective pour la variation de la porosité ϕ en réécrivant l'équation (1-19):

$$d\phi = -\left(\frac{1-\phi}{K_d} - \frac{1}{K_s}\right)\left(d\sigma - \chi dp_f\right) \tag{1-60}$$

avec

$$\chi = 1 - \frac{\phi\left(1/K_\phi - 1/K_s\right)}{\left(1-\phi\right)/K_d - 1/K_s} \tag{1-61}$$

Pour un matériau poreux idéal ($K_\phi = K_s$), on trouve $\chi = 1$ et donc la porosité varie avec la contrainte effective de Terzaghi.

En utilisant l'équation (1-5) on obtient la relation suivante pour la variation du volume de la phase solide $V_s = V - V_\phi$:

$$-\frac{dV_s}{V_s} = \frac{dV}{V} - \frac{d\phi}{1-\phi} \tag{1-62}$$

En remplaçant les équations (1-12) et (1-19) pour la condition isotherme dans l'équation (1-62) et en réécrivant l'expression qui en résulte, on peut identifier le coefficient κ de la contrainte effective pour la variation de volume de la phase solide :

$$\kappa = \frac{\phi K_s}{K_\phi} \tag{1-63}$$

Berryman (1992) a montré que les coefficients de la contrainte effective pour la variation des différentes propriétés physiques du matériau, présentés ci-dessus, vérifient l'inégalité suivante :

$$\kappa \le \alpha \le \beta \le \chi \tag{1-64}$$

Berryman souligne que l'inégalité $\alpha \le \chi$ est obtenu en considérant l'inégalité empirique $\phi \le \alpha$.

1.3.3.1 Contrainte effective pour le module de compression drainé

On considère la compressibilité drainée $c_d = 1/K_d$ comme la propriété Q dans l'équation (1-53) et on obtient l'expression suivante pour le coefficient θ de contrainte effective :

$$\theta = -\frac{\partial\left(1/K_d\right)/\partial p_f}{\partial\left(1/K_d\right)/\partial\sigma} \tag{1-65}$$

En utilisant l'équation (1-6) on réécrit l'équation (1-12) pour une condition isotherme sous la forme suivante :

$$d\varepsilon = -\frac{dV}{V} = \frac{d\sigma}{K_d} + \left(\frac{1}{K_s} - \frac{1}{K_d}\right)dp_f \tag{1-66}$$

Dans les matériaux hyperélastiques, l'existence d'un potentiel élastique garantit que la déformation volumique est indépendante du chemin de chargement. La condition d'existence d'un potentiel élastique s'exprime par la condition d'égalité des dérivées croisées dans l'équation (1-66):

$$\frac{\partial\left(1/K_d\right)}{\partial p_f} = \frac{\partial\left(1/K_s - 1/K_d\right)}{\partial\sigma} \tag{1-67}$$

En remplaçant l'équation (1-67) dans l'équation (1-65) on trouve l'expression suivante pour le coefficient de la contrainte effective pour la compressibilité drainée:

$$\theta = 1 - \frac{\partial\left(1/K_s\right)/\partial\sigma}{\partial\left(1/K_d\right)/\partial\sigma} \tag{1-68}$$

Cette expression montre que pour un matériau avec un module K_s constant, le module de compression drainé K_d est une fonction de la contrainte effective de Terzaghi $K_d = f(\sigma_d)$. Différentes démonstrations théoriques de cette conclusion sont présentées par Zimmerman (1991), Berryman (1992) et Gurevich (2004) et d'un point de vue micromécanique par Dormieux *et al*. (2002). Boutéca *et al*. (1994) en ont présenté la vérification expérimentale pour deux types de grès.

1.3.4 Modules tangent et sécant

Les variations de volume d'un matériau poreux peuvent être exprimées en terme de modules tangents ou de modules sécants. Les définitions de ces deux modules sont présentées dans la Figure 1-9. Les modules définis dans les équations (1-9) et (1-10) sont les modules tangents. Les relations suivantes expriment les modules sécants en fonction des modules tangents :

$$\frac{1}{K_d^{\sec}} = \frac{1}{\sigma_d}\int \frac{d\sigma_d}{K_d} \tag{1-69}$$

$$\frac{1}{K_s^{\sec}} = \frac{1}{p_f}\int \frac{dp_f}{K_s} \tag{1-70}$$

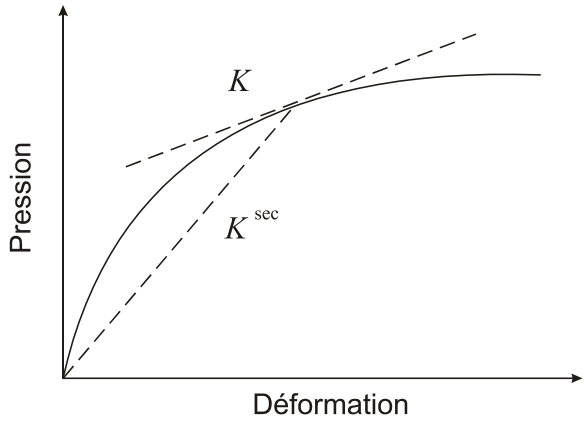

Figure 1-9- Définition des modules de compression tangent et sécant

Le module sécant peut être interprété comme une moyenne des modules tangents dans une gamme de pression. Si le module K_d est une fonction de σ_d et le module K_s est constant, ce qui est le cas pour le plupart des géomatériaux, l'équation (1-14) peut être intégrée et la déformation volumique peut être exprimée en fonction des modules sécants. Cette hypothèse est similaire à celle utilisée par Zimmerman *et al*. (1984) et va être justifiée dans le chapitre 3 pour le matériau étudié.

$$\varepsilon = \frac{\sigma_d}{K_d^{\sec}} + \frac{p_f}{K_s^{\sec}} \tag{1-71}$$

A l'aide de l'équation (1-6) on réécrit l'équation (1-71) pour trouver l'expression de coefficient sécant α^{sec} de la contrainte effective de Biot pour la variation du volume total :

$$\varepsilon = \frac{1}{K_d^{\sec}}\left(\sigma - \alpha^{\sec} p_f\right) \tag{1-72}$$

avec

$$\alpha^{\text{sec}} = 1 - \frac{K_d^{\text{sec}}}{K_s^{\text{sec}}} \tag{1-73}$$

1.4 Propriétés thermo-poro-mécanique du ciment

Après avoir défini le cadre théorique de cette étude, on présente dans cette partie une synthèse bibliographique sur les propriétés thermo-poro-mécanique du ciment, tel qu'on les a définies dans la section 1.3. Peu de résultats expérimentaux d'essais poromécaniques classiques, comme les essais de compression isotrope drainés, non-drainés ou 'sans-membrane', sur le ciment existent dans la littérature. On peut citer les travaux de Heukamp *et al* (2001, 2003) pour l'étude de l'effet de dégradation chimique sur les propriétés mécaniques du ciment. Les propriétés mécaniques de la pâte de ciment durcie varient avec les caractéristiques du ciment, le rapport w/c, les conditions d'hydratation, degré d'hydratation et la condition de saturation. Parmi les paramètres mécaniques, la résistance en compression simple est le paramètre le plus couramment étudié. Taylor (1997) présente une synthèse des résultats rapportés dans la littérature sur différentes relations empiriques qui décrivent la résistance du ciment en fonction de sa porosité. Ces relations exprimées par des fonctions puissance, exponentielle, logarithmique, etc. Toutes ces relations montrent la diminution de la résistance avec l'augmentation de la porosité. Les résultats des essais de compressions uniaxiales dépendent de la vitesse de chargement, ce qui rend difficile la comparaison des résultats publiés lorsque la vitesse n'est pas précisée. De plus, ces essais sont souvent réalisés dans des conditions de drainage ou de saturation qui ne sont pas bien définies ou contrôlées. Par conséquent, les modules d'élastiques obtenus dans ces essais se situent quelque part entre le module drainé et le module non-drainé. Les modules élastiques peuvent être aussi évalués à l'aide des essais non-destructifs. Ulm *et al*. (2004) ont utilisé deux méthodes non-destructives pour évaluer le module élastique d'une pâte de ciment durcie avec w/c=0,5 : la mesure de la vitesse d'impulsion ultrasonore et celle de la fréquence de résonance. Dans le premier essai le module est évalué égal à 22,8GPa en mesurant la vitesse de traversée d'une onde à travers l'échantillon ; ce module est considéré comme équivalent du module d'Young non-drainé. Dans la méthode de fréquence de résonance, un échantillon est mis à vibration et le module est évalué à partir de la fréquence de réponse de l'échantillon. Ce module, évalué égal à 21,7GPa, est considéré comme équivalent au module d'Young drainé. Ces deux modules dynamiques sont plus grands que le module statique mesuré dans la partie décharge d'un essai de compression uniaxiale et égal à 18,6GPa. A partir de méthodes dynamiques, Helmuth et Turk (1966) ont trouvé la relation suivante entre le module élastique de la pâte de ciment et sa porosité :

$$E = E_0 \left(1 - \phi_c\right)^3 \tag{1-74}$$

où ϕ_c est la porosité capillaire, E est le module d'Young et E_0 est son extrapolation à porosité nulle. Le module initial E_0 est trouvé environ égal à 30GPa. La même relation peut être utilisée pour le module de cisaillement G avec une valeur de G_0 environ égale à 12GPa (Mindess *et al*., 2003). Par conséquent on peut aussi utiliser la relation (1-74) pour le module de compression drainé K_d. Dans ce cas le module initial à porosité nulle est égal au module de compression des grains solides K_s.

Scherer (2006) et Grasley *et al*. (2007) ont évalué le module 'sans membrane' K_s et le module drainé K_d d'un ciment type III lors d'essais de pressurisation dynamique, originalement réalisés pour l'évaluation de la perméabilité du ciment. Dans cet essai, un échantillon saturé est placé dans un réservoir de fluide et ensuite la pression du réservoir est augmentée instantanément. Il en résulte une contraction instantanée suivie par une dilatation différée de l'échantillon à cause d'infiltration du fluide

vers l'intérieur de l'échantillon. La perméabilité est évaluée en analysant la réponse en déformation de l'échantillon. Les résultats de cet essai permettent également d'évaluer les modules K_s et K_d. Les résultats obtenus pour un ciment avec w/c=0,5 en fonction de l'âge du ciment sont présentés sur la Figure 1-10.

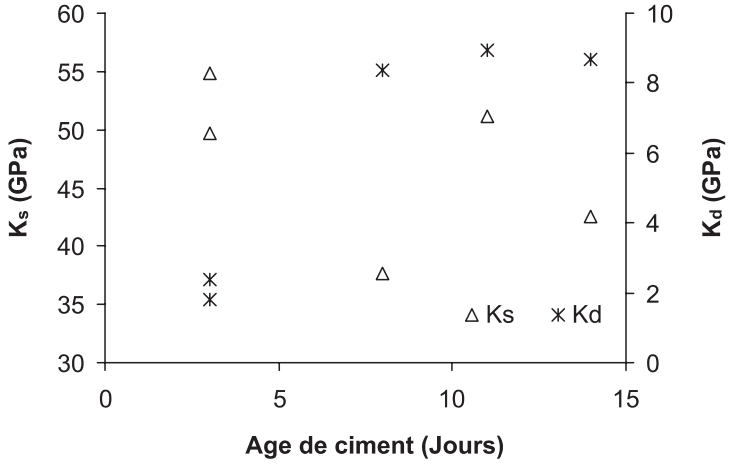

Figure 1-10- Evaluation des module K_d et K_s dans les essais de pressurisation dynamique pour un ciment type III avec w/c=0,5 en fonction de l'age de ciment (d'après Grasley *et al*., 2007)

Sur la Figure 1-10 on observe l'augmentation du module drainé K_d et la diminution du module sans membrane K_s avec le temps et la progression du processus d'hydratation. L'augmentation de K_d est due à la formation du squelette solide du ciment et la diminution de la porosité capillaire avec l'hydratation. Comme on l'a déjà mentionné, le module K_s est une moyenne pondérée des modules de compression des différents constituants solides du ciment. Sur le Tableau 1-2 on peut voir que le module élastique des grains anhydres est considérablement plus grand que celui des hydrates. Au cours de l'hydratation, les grains anhydres réagissent avec l'eau et forment les hydrates. Par conséquent, la diminution du module K_s est due à la diminution de la quantité des grains anhydres au cours de l'hydratation. Xi et Jennings (1997) ont évalué le module K_s pour un ciment type I à l'âge de 30 jours à l'aide d'un modèle d'homogénéisation multi-échelle pour le retrait de la pâte de ciment durcie. En utilisant les données expérimentales de Anson et Newman (1966) pour les ciments préparés avec w/c entre 0,3 et 0,5, ces auteurs évaluent un module K_s entre 24 et 26 GPa et montrent qu'il est très peu sensible au rapport w/c.

Récemment, l'avancée des techniques des essais micromécaniques, notamment la nanoindentation, a donné accès aux propriétés mécaniques des constituants de la pâte de ciment (Monteiro et Chang, 1995; Acker, 2001; Le Bellego, 2001; Velez *et al*., 2001; Constantinides et Ulm, 2004, 2007) et a permis le développement et l'utilisation des méthodes d'homogénéisation pour l'évaluation des propriétés poromécaniques du ciment (Constantinides et Ulm, 2004; Ulm *et al*., 2004; Haecker *et al*., 2005; Sanahuja *et al*. 2007). Un avantage considérable de ces modélisations micromécaniques est la possibilité de produire des résultats pour des pâtes préparées avec différents ciments, différents rapports w/c ou différents degrés d'hydratation, ce qui est très difficile dans les études expérimentales. Un exemple des résultats de modélisation micromécanique multi-échelle, présenté par Ulm *et al*. (2004) est donné sur le Tableau 1-3. Les propriétés mécaniques et les fractions volumiques des constituants du ciment sont présentées sur le Tableau 1-2.

Le coefficient d'expansion thermique de la pâte de ciment durcie a été évalué dans plusieurs études expérimentales, mais comme pour les essais mécaniques, dans la plupart des études les conditions de

saturation et la pression interstitielle ne sont pas bien définies ou contrôlées. Généralement le coefficient d'expansion thermique du ciment varie avec le rapport w/c, l'âge du ciment et le degré de saturation. Mindess *et al*. (2003) donnent des valeurs entre $54\times10^{-6}(°C)^{-1}$ et $60\times10^{-6}(°C)^{-1}$ pour les ciments saturés avec w/c entre 0,4 et 0,6. Quelques autres valeurs présentées dans la littérature pour les ciments saturés sont : $35\times10^{-6}(°C)^{-1}$ pour w/c=0,4 (Helmuth, 1960), $55\times10^{-6}(°C)^{-1}$ pour w/c=0,47 (Sabri et Illston, 1982), $36\times10^{-6}(°C)^{-1}$ pour w/c=0,4 (Sellevold et Bjøntegaard, 2006).

K_d (GPa)	K_u (GPa)	B	α	G (GPa)
13,9	16,9	0,22	0,69	8,7

Tableau 1-3-Propriétés poromécaniques d'une pâte de ciment durcie avec w/c=0,5 obtenues à l'aide d'un modèle micromécanique multi-échelle (d'après Ulm *et al*., 2004)

CHAPITRE 2. MATERIAU ETUDIE ET TECHNIQUES EXPERIMENTALES

2.1 Introduction

Dans ce chapitre, nous décrivons le processus de fabrication des éprouvettes de ciment et nous présentons les dispositifs expérimentaux utilisés : cellule triaxiale, dispositifs de chargement et de contrôle de la pression interstitielle et de la pression de confinement, instrumentation.

2.2 Fabrication des éprouvettes de ciment

2.2.1 Fabrication de coulis

Le coulis est préparé en utilisant un ciment pétrolier de classe G avec un rapport d'eau à ciment, w/c=0,44. La composition du ciment est présentée dans le Tableau 2-1. La densité du ciment est de 3,21g/cm^3.

Composant	C_3S	C_2S	C_3A	C_4AF
%	63	14	2	13

Tableau 2-1- Composition du ciment classe G utilisé dans cette étude

Deux adjuvants anti-mousse et dispersant ont aussi été ajoutés dans le coulis. Une composition typique pour 8 litres de pâte de ciment, fournie par la Société *TOTAL*, est présentée sur le Tableau 2-2.

Composant	Masse (g)
Ciment	10448
Eau	4660
Anti-mousse	41,23
Dispersant	38,70

Tableau 2-2- Composition de pâte de ciment (8 litres)

Après le mélange des composants du coulis dans un malaxeur, celui-ci est vibré sur une table vibrante afin d'expulser les bulles d'air. La qualité de la pâte fraîche est contrôlée par les mesures de la densité apparente et de la viscosité. La densité apparente est mesurée en utilisant la balance pressurisée *TOTAL*. Les mesures effectuées avant et après la vibration du coulis montrent une augmentation de 1,82g/cm^3 à 1,91g/cm^3 due à l'expulsion des bulles d'air par la vibration. Les mesures de la viscosité ont été faites par le viscosimètre FANN 35. D'après les spécifications de *TOTAL* pour la qualité des produits, en considérant le modèle plastique de Bingham, la viscosité dynamique pour le coulis avec w/c=0,44 mesurée à la température ambiante doit être inférieure à 40cP et la contrainte d'écoulement doit être inférieure à 45lbs/100ft^2. Les viscosités mesurées sont entre 29 et 38cP, avec une moyenne de 33cP. Les contraintes d'écoulements mesurées sont entre 23 et 30lbs/100ft^2 avec une moyenne de 26lbs/100ft^2 et donc les résultats obtenus sont dans les limites spécifiées par *TOTAL*.

2.2.2 Fabrication et conservation des éprouvettes

Après le coulage, la pâte fraîche est mise dans les moules cubiques de 14cm de côté. Les moules sont placés dans des bacs remplis d'eau saturé en chaux. La température de l'eau dans le bac est maintenue constante à 90°C à l'aide d'une pompe thermostatée pendant 4 jours pour la prise initiale du ciment. Un couvercle en polystyrène a été placé sur la surface des bacs pour diminuer l'évaporation de l'eau. Après cette période, la température de l'eau est diminuée lentement afin d'éviter la fissuration des blocs de ciment et ensuite les blocs sont démoulés. Le carottage des échantillons est réalisé à l'aide d'un carottier de diamètre interne 38mm pour obtenir 9 éprouvettes cylindriques par bloc. Après le carottage, les éprouvettes ont été sciées et rectifiées pour obtenir une longueur de 76mm et des surfaces parallèles.

Après la préparation, l'homogénéité des éprouvettes est contrôlée en réalisant des mesures de la densité apparente ρ, de la vitesse des ondes longitudinales V_p et du module d'élasticité dynamique E_d par mesure de la fréquence de résonance. Ces mesures sont réalisées sur toutes les éprouvettes et montrent la bonne homogénéité des éprouvettes préparées. Les résultats obtenus sont résumés dans le Tableau 2-3.

Mesure	ρ (g/cm^3)	V_p (m/s)	E_d (GPa)
Min	1,89	2990	14,1
Max	1,93	3330	15,0
Moyenne	1,91	3185	14,7
Incertitude de mesure	±0,007	±288	±0,26

Tableau 2-3- Mesures réalisées sur les éprouvettes 4 jours après le coulage de ciment

Une mesure du retrait/gonflement a été effectuée entre 4 jours et 11 jours après le coulage. Les mesures ont été faites à l'aide d'un comparateur sur des éprouvettes prismatiques de taille 4×4×16 cm avec un plot de retrait à chaque extrémité. Les résultats montrent un faible gonflement d'environ 0,03%.

L'ensemble des opérations de carottage des blocs, sciage et rectification des éprouvettes et les essais non-destructifs sont réalisés à température ambiante pendant environ une demi-journée. Les éprouvettes préparées ont passé la suite de la durée d'hydratation jusqu'au moment de leur utilisation pour l'expérimentation dans un fluide qui est neutre vis-à-vis du fluide interstitiel du ciment et donc ne réagit pas avec le ciment. La composition du fluide neutre, fournie par *TOTAL*, est présentée dans le Tableau 2-4.

Matériau		**Quantité (g)**
Gibbsite	$Al(OH)_3$	7,8
Portlandite	$Ca(OH)_2$	7,4
Sel	NaCl	0,3
Soude	NaOH	5,93
Thenardite	Na_2SO_4	7,6
Silice	SiO_2	1,2
pH ≈		**13**

Tableau 2-4- Composition du fluide 'neutre' pour 1 kg d'eau pure (T=25°C)

Le mode de conservation des éprouvettes pendant la durée d'hydratation est représenté sur la Figure 2-1. Les éprouvettes ont été conservées dans le fluide neutre à 90°C. Un bain thermostaté a été utilisé pour contrôler la température de l'eau du bain-marie.

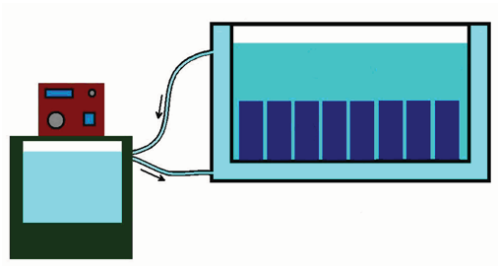

Figure 2-1- Schéma du système de conservation pour la durée d'hydratation

Les éprouvettes sont conservées dans ces conditions pendant au moins trois mois avant d'être utilisées pour les essais. Lorsqu'une éprouvette doit être utilisée pour un essai, elle est sortie du système de conservation et elle est placée immédiatement dans un petit récipient rempli de fluide neutre à 90°C. La température de ce récipient est ensuite diminuée lentement jusqu'à la température ambiante afin d'éviter la fissuration de l'éprouvette que pourrait occasionner un choc thermique. Cette phase de refroidissement prend environ 5 heures.

2.3 Protocole expérimental pour les essais triaxiaux dans la cellule GEODESIGN

2.3.1 Description des dispositifs

La cellule utilisée, schématisée sur la Figure 2-2 et présentée sur la Figure 2-3, est une cellule triaxiale haute pression de la société *GEODESIGN*. La cellule est équipée d'un système hydraulique de chambre d'auto-compensation qui communique avec la chambre de confinement par l'intermédiaire d'un conduit présent au centre du piston, et par conséquent la contrainte déviatorique est appliquée directement sur la face supérieure de l'échantillon. L'embase inférieure de la cellule comprend le circuit hydraulique pour la circulation du fluide de confinement, du fluide interstitiel ainsi que les passages étanches des fils électriques pour la sortie des signaux de l'instrumentation (mesures de déplacement, mesure de température). Un micro-capteur de pression est inséré dans l'embase inférieure pour mesurer la pression interstitielle au voisinage immédiat de l'échantillon. Il faut noter que ce capteur a été utilisé seulement pour certains essais, notamment pour les essais d'évaluation de la perméabilité. Par suite d'une défaillance de ce capteur, un capteur de pression externe a été utilisé pour les autres essais. La chambre de confinement de la cellule a un diamètre intérieur de 140mm et peut recevoir une paire de colliers pour de capteurs de déplacement du type LVDT.

Le système de chauffage conçu par la société *Métro Mesures* est composé d'un collier de résistance chauffante placée autour de la chambre de confinement qui peut appliquer un changement de température avec un taux donné et régler une température constante, et un thermocouple *TCK* qui mesure la température de l'élément chauffant. Afin de limiter la perte de température une mousse thermo isolante est placée entre la résistance chauffante et la paroi extérieure de la cellule. Afin de limiter les échanges de température entre la cellule et la table métallique en dessous, un autre élément thermo isolant composé d'une plaque de forte résistance mécanique, est placé en dessous de la cellule. L'ensemble cellule, huile, éprouvette est donc soumis à la même température. Ce système à l'avantage de fournir une grande inertie ce qui facilite la régulation, mais nécessite une forte puissance de chauffage. Un boîtier de régulation permet de définir une rampe de montée en température ainsi que le maintien de celle ci. Un thermocouple *TCK* mesure la température de l'élément chauffant et une sonde de température *PT100* est installée à l'intérieur de la cellule à proximité de l'éprouvette. La température

mesurée par cette sonde est considérée comme la température de l'éprouvette pour analyser les résultats. Le système de chauffage de la cellule triaxiale a été développé et utilisé pendant la thèse de Lazar (2006). Pour un essai à température constante, la précision du système de chauffage et de réglage de température observée pendant la durée d'un essai est en moyenne ±0,5°C.

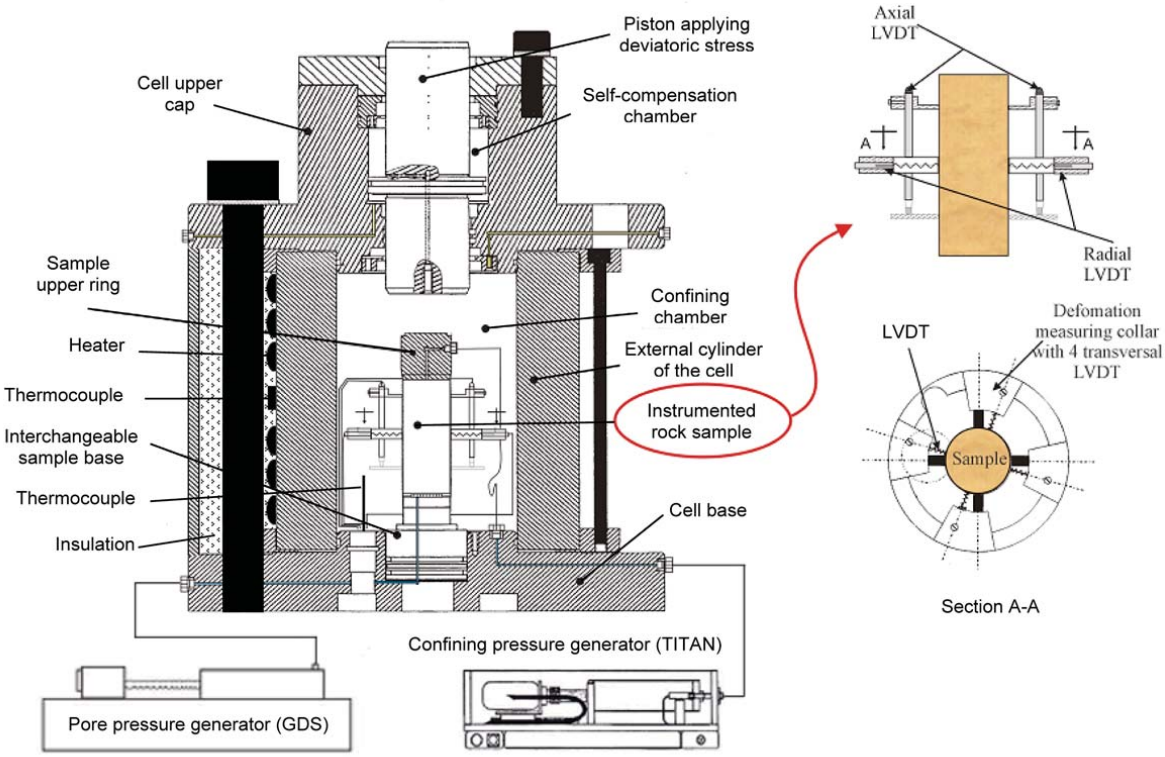

Figure 2-2- Cellule triaxiale et l'instrumentation de l'éprouvette

2.3.1.1 Système de chargement axial

Le système de chargement axial (Figure 2-4) construit par la société *Métro Mesures* est composé d'un bâti quatre colonnes équipé d'un piston à double effet d'une capacité de 50 tonnes, d'une servo-valve montée près du vérin assurant un meilleur temps de réponse, d'un groupe hydraulique et d'un logiciel de commande. La course du piston est de 50mm.

Figure 2-3- (a) Vue de l'extérieur de la cellule triaxiale ; (b) La partie inférieure de la cellule ; (c) Vue d'une éprouvette avec l'installation des anneaux et les instrumentations

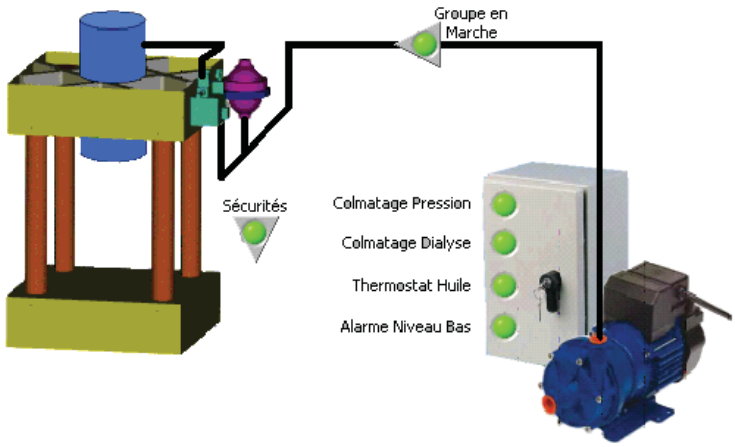

Figure 2-4- Le système de chargement axial

2.3.1.2 Contrôleur de pression de confinement *TITAN*

La pression de confinement de la cellule triaxiale est appliquée et contrôlée par un contrôleur de pression, appelé *TITAN,* fabriqué par la société *GEODESIGN*. Ce générateur de pression est une pompe hydraulique mono corps, qui permet d'effectuer d'une façon précise le contrôle et la mesure de la variation du volume du fluide, et de l'asservir à partir de la pression interne de la pompe (Figure 2-5). Un capteur de pression 0-60 MPa est connecté sur la sortie hydraulique et un autre capteur intégré au moteur permet de déterminer la variation de volume du fluide à l'intérieur du piston. Les caractéristiques de TITAN sont présentées dans le Tableau 2-5.

Figure 2-5- Contrôleur de pression de confinement *TITAN*

2.3.1.3 Contrôleur de pression interstitielle *GDS*

La pression interstitielle est appliquée et contrôlée par un contrôleur de pression de la Société *GDS*. Le principe de fonctionnement du *GDS*, présenté dans la Figure 2-6, est semblable à celui du *TITAN*. Il est composé d'une vis à billes assurant le déplacement du piston à l'intérieur du cylindre via un dispositif de guidage, l'ensemble est asservi par un moteur pas à pas en boucle fermée en consigne imposée ou en rampe de variation linéaire. Pour les essais sur le ciment, le *GDS* est rempli par le fluide neutre. Pour certains essais comme les essais de compression 'sans-membrane', un *GDS* haute pression avec une capacité de 60MPa est utilisé pour le contrôle et l'application de la pression interstitielle. Les principales caractéristiques de ces systèmes sont présentées dans le Tableau 2-5.

Générateurs de pression	Fluide	Pression max	Volume	Résolution
TITAN (Confinement)	Huile hydraulique	60 MPa	300 cm^3	0,1 mm^3
GDS (Drainage)	Fluide neutre	3 MPa	200 cm^3	1 kPa ; 1 mm^3
GDS (Drainage)	Fluide neutre	60 MPa	200 cm^3	1 kPa ; 1 mm^3

Tableau 2-5- Caractéristiques des contrôleurs de pression

Figure 2-6- Contrôleur de pression interstitielle *GDS*

2.3.1.4 Instrumentation

Les déformations axiales et radiales de l'échantillon sont mesurées par des capteurs type LVDT. Ces capteurs ont l'avantage d'offrir moins de sensibilité à la variation de la pression et de la température. Ces capteurs offrent aussi de larges possibilités en terme de course et sont moins affectés par la nuisance

électrique. Le dispositif de mesure des déformations a été développé pendant la thèse de Ouffroukh (2004). Un anneau en aluminium, fixé au milieu de l'échantillon supporte 4 capteurs LVDT, pour la mesure des déformations radiales, et deux anneaux en aluminium (Figure 2-7) qui sont fixés en bas et en haut de l'échantillon supportent les deux capteurs LVDT pour la mesure des déformations axiales. Une photo de l'échantillon avec l'instrumentation installée est présentée sur la Figure 2-3-b.

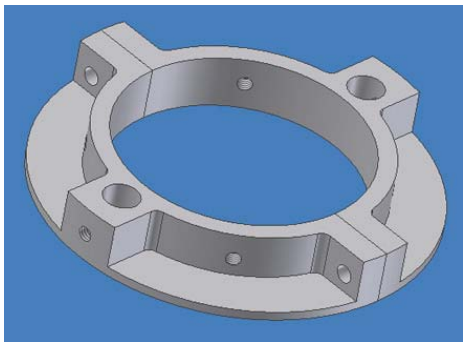

Figure 2-7- Schéma de l'anneau en aluminium supportant les LVDTs axiaux

2.3.2 Protocole d'essai

2.3.2.1 Choix de la membrane

A l'intérieur de la cellule triaxiale, l'échantillon est placé dans une membrane qui l'isole du fluide de confinement. Cette membrane doit résister aux fortes températures appliquées et à la corrosion due au fluide neutre de saturation. Des essais préliminaires sur la tenue des membranes ont été réalisés. Pour les essais à température ambiante, on utilise une membrane en néoprène de 1,2mm d'épaisseur. Pour les essais à haute température, on utilise une membrane en Viton de 1,0mm d'épaisseur.

2.3.2.2 Montage de l'éprouvette dans la cellule

Avant de mettre l'éprouvette dans la membrane, une couche de graisse est mise à l'intérieur de la membrane. Cette couche de graisse a pour but d'empêcher l'infiltration du fluide entre l'éprouvette et la membrane. Avant d'installer l'éprouvette sur l'embase inférieure de la cellule, les circuits de drainage et les pierres poreuses sont saturés. Une couche très fine de graisse anti-frettage est mise sur l'embase autour des pierres poreuses et un papier filtre déjà saturé est mis sur l'embase. Une couche de graisse est aussi mise autour de l'embase, sur la surface en contact avec la membrane, afin de limiter le passage du fluide interstitiel et de l'huile de confinement. Après l'installation de l'éprouvette, les anneaux d'aluminium et ensuite les capteurs LVDT sont installés sur l'éprouvette.

2.3.2.3 Saturation de l'éprouvette

Au cours de la phase de vieillissement, les échantillons sont conservés dans le fluide neutre (voir Tableau 2-4) pendant au moins 3 mois, et donc ils peuvent être considérés saturés. Avant d'être placée dans la membrane, l'éprouvette est toujours conservée dans le fluide. Néanmoins la mise en place de l'échantillon dans la cellule triaxiale peut occasionner une désaturation partielle du matériau, et il est nécessaire de procéder à une phase de saturation à l'intérieur de la cellule. Celle-ci s'effectue sous une pression de confinement de 1,2MPa et une contre-pression fluide de 1,0MPa. Un double drainage de l'échantillon par les deux extrémités est mis en place durant 7 jours. Pendant la durée de la phase de saturation, la variation de volume mesuré par le GDS (volume du fluide entrant dans l'échantillon) est mesurée.

2.3.2.4 Vitesse de chargement

Dans les essais drainés la vitesse de chargement doit être suffisamment lente pour que la surpression interstitielle provoquée par le chargement ait le temps pour se dissiper. Pour déterminer cette vitesse, une étude préliminaire a été réalisée. Dans un essai de compression isotrope sous condition de drainage simple à une extrémité de l'échantillon, le chargement a été appliqué avec différentes vitesses (0,1MPa/mn, 0,075MPa/mn, 0,05MPa/mn, 0,02MPa/mn) et la surpression interstitielle provoquée par le chargement a été mesurée à l'autre extrémité de l'échantillon. On a observé que les vitesses de chargement supérieures à 0,02MPa/mn provoquaient des surpressions interstitielles non négligeables alors que pour la vitesse de 0,02MPa/mn la surpression interstitielle était quasiment nulle. Pour assurer le drainage complet de l'échantillon, le choix s'est porté sur une vitesse de chargement de 0,025MPa/mn en condition de double drainage.

Pour les essais non drainés, la vitesse de chargement peut être supérieure mais l'on doit assurer l'homogénéité de la pression interstitielle à l'intérieur de l'échantillon. La vitesse de chargement pour les essais non drainés est de 0,1MPa/mn.

2.3.2.5 Durée des essais

En considérant le temps nécessaire au montage de la cellule, à la saturation de l'échantillon et compte tenu des vitesses de chargement décrites ci-dessus, la durée d'un essai de compression isotrope jusqu'à 60MPa (avec 3 cycles décharge-recharge) est d'environ 3 semaines en condition drainée et 2 semaines en condition non-drainée. Pour les essais déviatoriques, la durée des essais drainés varie entre 3 et 6 semaines selon le niveau du confinement.

CHAPITRE 3. COMPORTEMENT THERMO-PORO-MECANIQUE D'UN CIMENT PETROLIER SOUS CHARGEMENT ISOTROPE

3.1 Introduction

Le comportement du ciment pétrolier présenté dans le chapitre 2 a d'abord été étudié sous chargement isotrope à température ambiante. Cette étude constitue la première partie du présent chapitre. Elle est une étape importante dans la compréhension et la caractérisation du comportement du ciment en tant qu'un matériau poreux, car c'est dans cette première étape qu'on va essayer de répondre à la question posée par Ulm *et al*. (2004): Est-ce que la pâte de ciment est un matériau poromécanique? Ou autrement dit, est-ce que le comportement du ciment peut être décrit dans le cadre de la théorie des milieux poreux? Afin de répondre à cette question, les essais classiques de poromécanique, tels que les essais de compression isotrope drainés, non-drainés et 'sans-membrane', sont réalisés sur le ciment en adaptant les procédures d'essais à la très faible perméabilité de ce matériau. L'analyse de la compatibilité et la cohérence des paramètres poromécaniques évalués à partir de ces essais nous permettront de répondre à cette question.

La section suivante de ce chapitre est consacrée à l'étude de la perméabilité du ciment et à son évolution sous chargement isotrope en fonction des variations de la porosité. Pour ce faire, une nouvelle méthode pour l'évaluation de la perméabilité en régime transitoire est développée qui conduit à une relation perméabilité-porosité pour le matériau étudié à l'aide des résultats d'un seul essai. Les paramètres poromécaniques évalués dans la première partie du chapitre sont utilisés pour l'analyse inverse des résultats des essais de l'évaluation de la perméabilité. Ceci peut être aussi considéré comme un exemple de l'application de la théorie poromécanique pour le ciment.

La dernière section de ce chapitre est dédiée à l'étude de l'effet de température sur le comportement poromécanique du ciment et sur les paramètres poromécaniques. Pour ce faire, des essais de compression isotrope drainés et 'sans-membrane' sont réalisés à 90°C.

La deuxième et la troisième partie de ce chapitre sont présentées sous la forme de deux articles rédigés en anglais. Le premier intitulé « Poromechanical behaviour of hardened cement paste under isotropic loading » est publié dans la revue 'Cement and Concrete Research'. Il présente l'étude du comportement poromécanique du ciment à température ambiante. Le second, intitulé «Evaluation of a permeability-porosity relationship in a low-permeability creeping material using a single transient test », est publié dans la revue 'International Journal of Rock Mechanics and Mining Sciences'. Il présente une étude sur l'évolution de la perméabilité du ciment sous chargement isotrope. Au début de chaque section, un résumé de l'article est présenté.

3.2 Comportement poromécanique à température ambiante

Le comportement poromécanique de la pâte de ciment durcie sous chargement isotrope est étudié en réalisant des essais de compression isotrope drainés, non-drainés et 'sans membrane' à température ambiante. Les essais drainés et non-drainés sont réalisés avec des cycles de charge-décharge et les modules de compression drainés et non-drainés et le coefficient de Skempton sont évalués dans les

cycles. Les résultats des essais ont montré le caractère fortement non-linéaire de la réponse du ciment et la présence des déformations irréversibles dans les cycles de décharge. La contrainte effective qui contrôle l'évolution du module de compression drainé est étudiée expérimentalement en réalisant les essais drainés avec différentes pressions interstitielles imposées. Le module de compression de la phase solide K_s est évalué dans l'essai 'sans membrane' égal à 21GPa et le résultat de l'essai a montré qu'il ne varie pas avec la pression appliquée. Un phénomène de dégradation des propriétés mécaniques sous la forme d'une réduction des modules élastiques drainé et non-drainé sous chargement isotrope est observé dans les résultats des essais. Les observations microscopiques des échantillons avant et après les essais ont montré que cet endommagement de ciment est provoqué par la génération de microfissures dans les échantillons y compris sous chargement isotrope. Cette microfissuration du ciment peut être expliquée par la microstructure fortement hétérogène du matériau. Les résultats des essais ont montré que le coefficient de Skempton est constant, égal à 0,4. Le module de compression K_ϕ (équation 1.10) est évalué indirectement à l'aide des résultats des essais. Les coefficients de contrainte effective correspondant aux variations de volume total (coefficient de Biot), de volume poreux, de volume solide, de porosité et le module de compression drainé sont évalués. La question de la porosité du ciment qui doit être utilisée dans les formulations poromécaniques est discutée. L'analyse des résultats obtenus montre que la porosité totale de ciment, mesurée en séchant l'échantillon à 105°C, ne doit pas être utilisée dans les formulations poromécaniques, car elle contient une partie de la porosité située dans l'espace interfoliaire de la microstructure du ciment. On a également étudié la compatibilité et la cohérence des résultats obtenus des essais de compression drainé, non-drainé et 'sans-membrane'. La bonne compatibilité des résultats montre qu'effectivement le comportement de la pâte de ciment peut être analysé dans le cadre de la théorie des milieux poreux.

Cement and Concrete Research 38 (2008) 1424–1437

Contents lists available at ScienceDirect

Cement and Concrete Research

journal homepage: http://ees.elsevier.com/CEMCON/default.asp

Poromechanical behaviour of hardened cement paste under isotropic loading

Siavash Ghabezloo [a,*], Jean Sulem [a], Sylvine Guédon [b], François Martineau [b], Jérémie Saint-Marc [c]

[a] Université Paris-Est, UR Navier, CERMES, Ecole Nationale des Ponts et Chaussées, Marne la Vallée, France
[b] Université Paris-Est, LCPC, MSRGI, Paris, France
[c] TOTAL, Management of Residual Gases Project, Pau, France

Abstract

The poromechanical behaviour of hardened cement paste under isotropic loading is studied on the basis of an experimental testing program of drained, undrained and unjacketed compression tests. The macroscopic behaviour of the material is described in the framework of the mechanics of porous media. The poroelastic parameters of the material are determined and the effect of stress and pore pressure on them is evaluated. Appropriate effective stress laws which control the evolution of total volume, pore volume, solid volume, porosity and drained bulk modulus are discussed. A phenomenon of degradation of elastic properties is observed in the test results. The microscopic observations showed that this degradation is caused by the microcracking of the material under isotropic loading. The good compatibility and the consistency of the obtained poromechanical parameters demonstrate that the behaviour of the hardened cement paste can be indeed described within the framework of the theory of porous media.

Keywords: hardened cement paste, poromechanics, effective stress, degradation, triaxial testing

1 Introduction

In oil wells, a cement sheath is placed between the rock and the casing for support and sealing purpose. The cement lining is submitted to various thermal and mechanical loadings during the life of the well from the drilling phase to the production phase and finally in the abandon phase when the well must seal the subsurface from the surface, as for instance for storage and sequestration of greenhouse gas. In due course of these solicitations, the cement can be damaged and the mechanical and transport properties can be degraded, this degradation being detrimental to its functions. The knowledge of poromechanical behaviour and permeability of this cement in oil-wells conditions, i.e. under high stress and elevated temperature, is essential for the prediction of the well performance during the exploitation and also prediction of the sealing performance of the well when CO_2 storage and sequestration is planned.

Whether the mechanical behaviour of hardened cement paste can be described within the framework of the mechanics of porous media is an open question. The main point of discussion about the possibility to actually consider the cement paste as a poromechanical material is related to the complex microstructure of the material: the porosity of this material manifests itself at different scales so that a part of the water phase can not be considered as a bulk water phase, but as structural water [1]. Recent progress of advanced micromechanical testing methods, such as nano-indentation tests, have provided direct measurements of the elastic properties of the different phases of the microstructure of the hardened cement paste [2-7] and has made it possible to estimate the poromechanical properties of this material using homogenization techniques [6,8,9]. These evaluations of the poromechanical properties are mostly supported by the experimental results obtained using non-destructive methods such as, among others, elastic resonance and ultrasonic wave velocity measurements, but have not been validated against mechanical loading tests results. Indeed very few experimental results of classical poromechanics tests, such as drained, undrained and unjacketed compression tests, can be found in the literature for the hardened cement paste. Some tests have been presented by Heukamp [10] and Heukamp *et al*. [11,12], but these studies are mostly focussed on calcium-leached cement pastes and the effect of chemical degradation on the mechanical properties of hardened cement paste. An important difficulty with the hardened cement paste is its very low permeability which makes the poromechanical tests long and expensive.

In this paper, the question whether the hardened cement paste can be considered as a poromechanical material or not is addressed on the basis of an experimental approach. The mechanical behaviour of the hardened cement paste under isotropic loading is studied through drained, undrained and unjacketed compression tests, where the classical testing procedures have been adapted for low permeability materials. In doing this, the macroscopic behaviour of the material is studied and described with the tools of the mechanics of porous media as it is done classically for saturated porous rocks. The compatibility and the consistency of the experimental results and of the obtained poromechanical parameters are discussed to state whether the behaviour of the hardened cement paste can be described within the framework of the theory of porous media.

The second part of the paper is dedicated to the theoretical aspects of modelling the elastic volumetric behaviour of a porous material which can be heterogeneous and anisotropic at the micro-scale. The general concept of effective stress is presented and discussed and the expressions of the effective stress coefficients for different physical properties of a porous material are derived. A discussion is also presented on the cement paste porosity that should be used in poromechanical

formulations. The set of parameters introduced in this section is evaluated in the experimental study. The testing program is presented in the third part of the paper and the obtained results are discussed. Observations of the microstructure of the samples have been performed before and after the mechanical loading tests using an environmental scanning electron microscope (ESEM). These microphotographs demonstrate the evolution of the microstructure during loading and the degradation phenomenon observed in the test results. These microscopic observations and the discussion of the degradation mechanisms are presented respectively in the fourth and fifth parts of the paper.

2 Poromechanical background

We present here the framework used to describe the elastic volumetric behaviour of a porous material which can be heterogeneous and anisotropic at the micro-scale. The theoretical basis of the formulation has been presented in many earlier studies. Among them, one can refer to the milestone papers and textbooks of Biot and Willis [13], Brown and Korringa [14], Rice and Cleary [15], Zimmerman [16], Berryman [17], Detournay and Cheng [18], Vardoulakis and Sulem [19], Coussy [20]. This framework is recalled here in a comprehensive manner in order to clarify the mathematical and physical significance of the different poromechanical parameters and effective stress coefficients which are evaluated in our experimental program.

2.1 Poroelastic formulation

A fluid saturated porous material can be seen as a mixture of two phases: a solid phase and a fluid phase. The solid phase may be itself made up of several constituents. The porosity ϕ is defined as the ratio of the volume of the porous space V_ϕ to the total volume V in the current (deformed) state.

$$\phi = \frac{V_\phi}{V} \tag{1}$$

For a saturated material the volume of the pore space is equal to the volume of the fluid phase. We consider a saturated sample under an isotropic state of stress σ (positive in compression). We choose two independent variables for characterizing the volumetric behaviour of a porous material: the pore pressure p_f and the differential pressure σ_d which is equivalent to Terzaghi effective stress.

$$\sigma_d = \sigma - p_f \tag{2}$$

The expression of the variations of the total volume V and of the pore volume V_ϕ introduces four parameters presented below [14]:

$$\begin{aligned} \frac{dV}{V} &= \frac{1}{V}\left(\frac{\partial V}{\partial \sigma_d}\right)_{p_f} d\sigma_d + \frac{1}{V}\left(\frac{\partial V}{\partial p_f}\right)_{\sigma_d} dp_f \\ \frac{dV_\phi}{V_\phi} &= \frac{1}{V_\phi}\left(\frac{\partial V_\phi}{\partial \sigma_d}\right)_{p_f} d\sigma_d + \frac{1}{V_\phi}\left(\frac{\partial V_\phi}{\partial p_f}\right)_{\sigma_d} dp_f \end{aligned} \tag{3}$$

$$\frac{1}{K_d} = -\frac{1}{V}\left(\frac{\partial V}{\partial \sigma_d}\right)_{p_f} \quad , \quad \frac{1}{K_p} = -\frac{1}{V_\phi}\left(\frac{\partial V_\phi}{\partial \sigma_d}\right)_{p_f} \tag{4}$$

$$\frac{1}{K_s} = -\frac{1}{V}\left(\frac{\partial V}{\partial p_f}\right)_{\sigma_d} \quad , \quad \frac{1}{K_\phi} = -\frac{1}{V_\phi}\left(\frac{\partial V_\phi}{\partial p_f}\right)_{\sigma_d} \tag{5}$$

Equation (4) corresponds to a drained isotropic compression test in which the pore pressure is controlled to remain constant in the sample. The variations of the total volume of the sample V and of the volume of the pore space V_ϕ with respect to the applied confining pressure give the drained bulk modulus K_d and the modulus K_p. Equation (5) corresponds to the so-called unjacketed compression test, in which equal increments of confining pressure and pore pressure are simultaneously applied to the sample, as if the sample was submerged, without a jacket, into a fluid under the pressure p_f. The differential pressure σ_d in this condition remains constant. The variation of the volume of the sample with respect to the applied pressure gives the unjacketed modulus K_s. The variation of the pore volume of the sample in this test, evaluated from the quantity of fluid exchanged between the sample and the pore pressure generator could in principle give the modulus K_ϕ. However experimental evaluation of this parameter is very difficult as the volume of the exchanged fluid has to be corrected for the effect of fluid compressibility, and also for the effect of the deformations of the pore pressure generator and drainage system in order to access to the variation of the pore volume of the sample. In the case of a porous material which is homogeneous and isotropic at the micro-scale, the sample would deform in an unjacketed test as if all the pores were filled with the solid component. The skeleton and the solid component experience a uniform volumetric strain with no change of the porosity [18]. For such a material $K_s = K_\phi = K_m$, where K_m is the bulk modulus of the single solid constituent of the porous material. In the case of a porous material which is composed of two or more solids and therefore is heterogeneous at the micro-scale, the unjacketed modulus K_s is some weighted average of the bulk moduli of solid constituents [17]. What this average should be is generally unknown, however, in Ghabezloo and Sulem [21] the unjacketed modulus of Rothbach sandstone was evaluated using Hill's [22] average formula and was in good accordance with the experimentally evaluated modulus. The modulus K_ϕ for such a material has a complicated dependence on the material properties. Generally it is not bounded by the elastic moduli of the solid components and can even have a negative sign if the bulk moduli of the individual solid components are greatly different one from another [23][24].

Using Betti's reciprocal theorem one obtains the following relation between the elastic moduli [14][25]:

$$\frac{1}{K_p} = \frac{1}{\phi}\left(\frac{1}{K_d} - \frac{1}{K_s}\right) \tag{6}$$

Using equation (6) the number of required moduli to characterize the volumetric behaviour of a porous material is reduced to three. Using the four moduli defined in equations (4) and (5), the variations of the total volume V and of the pore volume V_ϕ (equation (3)) can be rewritten as follows:

$$\begin{aligned} \frac{dV}{V} &= -\frac{d\sigma_d}{K_d} - \frac{dp_f}{K_s} \\ \frac{dV_\phi}{V_\phi} &= -\frac{d\sigma_d}{K_p} - \frac{dp_f}{K_\phi} \end{aligned} \tag{7}$$

The incremental volumetric strain $d\varepsilon = -dV/V$ is thus expressed as:

$$d\varepsilon = \frac{d\sigma_d}{K_d} + \frac{dp_f}{K_s} \tag{8}$$

Using the definition of the porosity presented in equation (1), the following equation is obtained for the variation of the porosity:

$$\frac{d\phi}{\phi} = \frac{dV_\phi}{V_\phi} - \frac{dV}{V} \tag{9}$$

Replacing equation (7) and then equation (6) in equation (9), the expression of the variation of porosity is found:

$$\frac{d\phi}{\phi} = -\frac{1}{\phi}\left(\frac{1-\phi}{K_d} - \frac{1}{K_s}\right)d\sigma_d + \left(\frac{1}{K_s} - \frac{1}{K_\phi}\right)dp_f \tag{10}$$

The undrained condition is defined as a condition in which the mass of the fluid phase is constant ($dm_f = 0$). Under this condition we choose two different independent variables: The total stress σ and the fluid mass m_f. The measured quantities are the total volume V and the pore pressure p_f. Writing the expression of the variation of these quantities, we can define two new parameters to describe the response of the porous material in undrained condition:

$$\frac{1}{K_u} = -\frac{1}{V}\left(\frac{\partial V}{\partial \sigma}\right)_{m_f} \quad , \quad B = \left(\frac{\partial p_f}{\partial \sigma}\right)_{m_f} \tag{11}$$

The parameter K_u is the undrained bulk modulus and B is the so-called Skempton coefficient [26]. As the fluid mass in the undrained condition is constant, the variation of the volume of the fluid is given by the fluid compression modulus K_f and the variation of the pore pressure:

$$\frac{dV_\phi}{V_\phi} = -\frac{dp_f}{K_f} \tag{12}$$

Replacing equation (12) in equation (7) and using equations (2) and (6) the expression of the Skempton coefficient B (equation (11)) is obtained:

$$B = \frac{\left(1/K_d - 1/K_s\right)}{\left(1/K_d - 1/K_s\right) + \phi\left(1/K_f - 1/K_\phi\right)} \tag{13}$$

The variation of the total volume in undrained condition is given by the undrained bulk modulus K_u as presented in equation (11). Replacing $d\varepsilon = -dV/V = d\sigma/K_u$, $d\sigma_d = d\sigma - dp_f$ and $dp_f = Bd\sigma$ in equation (8), the following expression is found for the undrained bulk modulus K_u :

$$K_u = \frac{K_d}{1 - B\left(1 - K_d/K_s\right)} \tag{14}$$

Biot modulus M can be expressed in terms of the elastic moduli defined in equations (4) and (5) [18]:

$$\frac{1}{M} = \frac{K_d}{K_s}\left(\frac{1}{K_d} - \frac{1}{K_s}\right) + \phi\left(\frac{1}{K_f} - \frac{1}{K_\phi}\right) \tag{15}$$

As mentioned earlier, the modulus K_ϕ is very difficult to measure experimentally. On the other hand, the experimental evaluation of the poroelastic parameters K_d , K_s , K_u and B is more common, so that using these moduli that can be measured independently and equations (13) and (14) one can find four different expressions for indirect evaluation of the parameter K_ϕ .

$$\frac{1}{K_\phi}=\begin{cases}\dfrac{1}{K_f}-\dfrac{\left(1/K_d-1/K_s\right)\left(1/K_u-1/K_s\right)}{\phi\left(1/K_d-1/K_u\right)} & \text{(a)}\\ \dfrac{1}{K_f}-\dfrac{\left(1-B\right)\left(1/K_d-1/K_s\right)}{\phi B} & \text{(b)}\\ \dfrac{1}{K_f}-\dfrac{1/K_u-1/K_s}{\phi B} & \text{(c)}\\ \dfrac{1}{K_f}-\dfrac{\left(1-B\right)\left(1/K_d-1/K_u\right)}{\phi B^2} & \text{(d)}\end{cases} \tag{16}$$

2.2 Effective stress concept

The concept of effective stress was first introduced by Terzaghi [27] who defined it as the difference between the total stress and the pore pressure, and attributed all measurable effects of a change in stress exclusively to changes in the effective stress.

More generally, the effective stress $\sigma'=\sigma'\left(\sigma,p_f\right)$ can be defined as a stress quantity which can be used as a single variable to express the stress dependency of a property Q of a porous material. Reducing the number of independent variables from two to one using the concept of effective stress greatly simplifies the analysis of total stress and pore pressure dependency of porous material properties.

$$Q=Q\left(\sigma,p_f\right)=Q\left(\sigma'\right) \tag{17}$$

If the total stress and the pore pressure vary in such a way that the effective stress remains constant, then no variation in the corresponding property Q is expected. Thus the expression of the effective stress can be obtained from the evaluation of the isolines of $Q(\sigma,p_f)$.

Since different material properties may depend on total stress and pore pressure in different ways, there is not a unique effective stress which would be appropriate for all properties of the material, and consequently different effective stress expressions should be defined for the different properties.

Let us now consider Q as a physical property of the porous material which is a function of the differential pressure and of the pore pressure $Q=Q\left(\sigma_d,p_f\right)$. Assuming that this function is smooth enough so that its derivatives can be defined, the incremental variation of Q can be written in the following form:

$$dQ=\frac{\partial Q}{\partial\sigma_d}d\sigma_d+\frac{\partial Q}{\partial p_f}dp_f \tag{18}$$

Introducing the definition of σ_d (equation (2)) in equation (18) we obtain:

$$dQ=\frac{\partial Q}{\partial\sigma_d}\left[d\sigma-\left(1-\frac{\partial Q/\partial p_f}{\partial Q/\partial\sigma_d}\right)dp_f\right] \tag{19}$$

The above expression shows that the variation of the property Q can be written as a function of a single incremental quantity $d\sigma'$:

$$dQ=\frac{\partial Q}{\partial\sigma_d}d\sigma' \tag{20}$$

where $d\sigma'$ is defined by

$$d\sigma'=d\sigma-n_Q dp_f \tag{21}$$

with

$$n_Q\left(\sigma_d, p_f\right) = 1 - \frac{\partial Q/\partial p_f}{\partial Q/\partial \sigma_d} \tag{22}$$

The isolines of Q are obtained by the integration of the following differential equation:

$$d\sigma' = 0 \tag{23}$$

In the close vicinity of a given state of stress $\left(\sigma_d, p_f\right)$, the isolines are generally approximated with parallel straight lines (e.g. Bernabé [28]) which is equivalent to the assumption that n_Q is a constant. Under this assumption, equation (21) can be easily integrated and a linear expression for the effective stress is obtained:

$$\sigma' = \sigma - n_Q p_f \tag{24}$$

The above expression is the most common form of the effective stress as used in the mechanics of porous media. The effective stress coefficient n_Q is equal to one in Terzaghi's definition which means that the total stress and the pore pressure have similar, but inverse, effects on the variation of the property Q. While a value of the coefficient n_Q smaller (respectively greater) than unity means that the effect of pore pressure change on the variation of the property Q is less (respectively more) important than the effect of a change in total stress. The expression of the effective stress coefficient presented in equation (22) was first presented by Todd and Simmons [29].

Zimmerman [16] and Berryman [17] have derived general effective stress rules for various physical properties of rocks and presented the expressions of the effective stress coefficients n_Q corresponding to different physical properties together with some bounds and general relations among these coefficients.

If we replace the quantity Q in equation (22) by the incremental volumetric strain $d\varepsilon = -dV/V$ and using the definitions of bulk moduli presented in equations (4) and (5), the expression of the Biot [13] effective stress coefficient α for the total volume change of a porous material is retrieved:

$$\alpha = 1 - \frac{K_d}{K_s} \tag{25}$$

Similarly, replacing Q by $-dV_\phi/V_\phi$ and using equations (4) and (5), the effective stress coefficient β corresponding to the variation of pore volume V_ϕ is found:

$$\beta = 1 - \frac{K_p}{K_\phi} = 1 - \frac{\phi}{K_\phi\left(1/K_d - 1/K_s\right)} \tag{26}$$

The effective stress coefficient χ for the variation of porosity ϕ can be obtained by re-writing equation (10) using equation (2):

$$d\phi = -\left(\frac{1-\phi}{K_d} - \frac{1}{K_s}\right)\left(d\sigma - \chi dp_f\right) \tag{27}$$

with

$$\chi = 1 - \frac{\phi\left(1/K_\phi - 1/K_s\right)}{\left(1-\phi\right)/K_d - 1/K_s} \tag{28}$$

Using equation (1) the following expression can be obtained for the variations of the volume of the solid phase $V_s = V - V_\phi$:

$$-\frac{dV_s}{V_s}=\frac{dV}{V}-\frac{d\phi}{1-\phi} \tag{29}$$

Introducing equations (8) and (10) in equation (29) and re-writing the resulted equation, the following expression is obtained for the effective stress coefficient κ for the variations of the volume of solid phase:

$$\kappa=\frac{\phi K_s}{K_\phi} \tag{30}$$

Berryman [17] has shown that the above set of effective stress coefficients for the variations of different physical properties of porous materials verifies the following inequality:

$$\kappa\le\alpha\le\beta\le\chi \tag{31}$$

Berryman underlines that the inequality $\alpha\le\chi$ is obtained by considering the empirical inequality $\phi\le\alpha$.

2.2.1 Effective stress for the drained bulk modulus

Using equation (2), equation (8) can be re-written in the following form:

$$d\varepsilon=\frac{d\sigma}{K_d}+\left(\frac{1}{K_s}-\frac{1}{K_d}\right)dp_f \tag{32}$$

For hyperelastic materials, the existence of an elastic potential guaranties that the volumetric strain ε is independent of the loading path. This condition is fulfilled when the Euler condition of integrability in equation (32) is verified:

$$\frac{\partial\left(1/K_d\right)}{\partial p_f}=\frac{\partial\left(1/K_s-1/K_d\right)}{\partial\sigma} \tag{33}$$

Considering now the drained compressibility $c_d=1/K_d$ as a function of σ and p_f, the variation of c_d can be written in the following form:

$$dc_d=\frac{\partial c_d}{\partial\sigma}d\sigma+\frac{\partial c_d}{\partial p_f}dp_f \tag{34}$$

This equation can be re-written in the following form:

$$dc_d=\frac{\partial c_d}{\partial\sigma}\left(d\sigma+\frac{\partial c_d/\partial p_f}{\partial c_d/\partial\sigma}dp_f\right) \tag{35}$$

The effective stress coefficient θ corresponding to the variations of the drained bulk modulus can be defined as:

$$\theta=-\frac{\partial c_d/\partial p_f}{\partial c_d/\partial\sigma} \tag{36}$$

Inserting equation (33) in equation (36) and replacing c_d with $1/K_d$, the following expression is found:

$$\theta = 1 - \frac{\partial\left(1/K_s\right)/\partial\sigma}{\partial\left(1/K_d\right)/\partial\sigma} \tag{37}$$

We can see that for a material with a constant unjacketed modulus K_s, the effective stress coefficient θ is equal to one and the drained bulk modulus is a function of Terzaghi effective stress $K_d = f\left(\sigma_d\right)$. Various theoretical demonstrations of this statement can be found in Zimmerman [16], Berryman [17], Coussy [20] and Gurevich [30] and from micromechanical considerations in Dormieux et al. [31]. Experimental verification is presented by Boutéca et al. [32] for two sandstones.

Coyner [33] has performed experimental measurements of the variations of the unjacketed and of the drained bulk moduli of different rocks (sandstones, limestones and granites), with a range of pressures up to 100MPa. The results showed that the maximum variation of the unjacketed modulus for the range of applied pressures is about 10%. We can evaluate the effective stress coefficients θ using the experimental data of Coyner [33] and we find numerical values very close to one, between 0.95 and 1.0. These experimental results confirm that, even for a porous material which is heterogeneous at the micro-scale and for which a small variation of the unjacketed compression modulus with applied stress is expected, this variation is insignificant regarding the effective stress coefficients θ. Thus, for most practical applications, the dependence of the bulk modulus with *Terzaghi* effective stress is an acceptable assumption.

2.3 Tangent and secant moduli

The variations of the volume of a porous material can be expressed in terms of either tangent or secant moduli. The definitions are presented in Figure (1) and equations (4) and (5). From Figure (1) we can write the following relationships between the secant and tangent moduli:

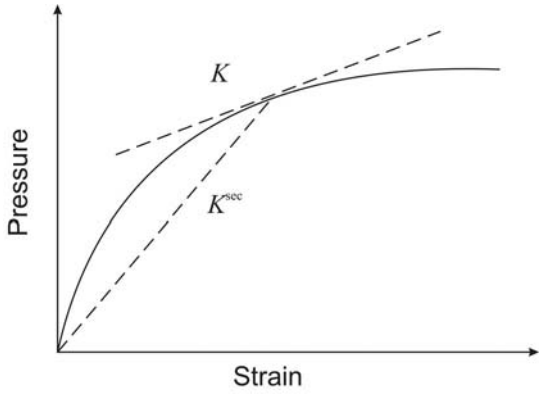

Figure 1-Definitions of the tangent and secant moduli

$$\frac{1}{K_d^{\sec}} = \frac{1}{\sigma_d}\int\frac{d\sigma_d}{K_d} \tag{38}$$

$$\frac{1}{K_s^{\sec}} = \frac{1}{p_f}\int\frac{dp_f}{K_s} \tag{39}$$

The secant modulus can be interpreted as an average value of the tangent modulus over a range of pressure. If the drained bulk modulus is a function of the Terzaghi effective stress and the unjacketed modulus is constant, which is the case for most geomaterials as mentioned in section 2.2.1, then equation (8) can be integrated and the volumetric strain can be written using the secant properties. This

assumption is similar to the one used by Zimmerman *et al*. [25] and will be justified in section 3 for the studied material.

$$\varepsilon = \frac{\sigma_d}{K_d^{\text{sec}}} + \frac{p_f}{K_s^{\text{sec}}} \tag{40}$$

We can re-write this equation, using equation (2), to find the expression of the secant Biot effective stress coefficient:

$$\varepsilon = \frac{1}{K_d^{\text{sec}}}\left(\sigma - \alpha^{\text{sec}} p_f\right) \tag{41}$$

with

$$\alpha^{\text{sec}} = 1 - \frac{K_d^{\text{sec}}}{K_s^{\text{sec}}} \tag{42}$$

The expression of Biot effective stress σ_b' is obtained from equation (41):

$$\sigma_b' = \sigma - \alpha^{\text{sec}} p_f \tag{43}$$

2.4 Cement paste porosity for poromechanical formulations

The size of pores in the microstructure of hardened cement paste covers an impressive range, from nanometre-sized gel pores, to micro-metre sized capillary pores and millimetre-sized air voids [34]. From the different microstructural models of C-S-H, it can be seen that a part of the water in the pore structure of cement paste is interlayer structural water. Feldman and Sereda [35] propose a model for multilayer structure of C-S-H that postulates the existence of interlayer spaces containing strongly adsorbed water. According to Feldman [36], the interlayer water behaves as a solid bridge between the layers and consequently the interlayer space can not be included in the porosity and the interlayer water must be regarded as a part of the solid structure of hydrated cement paste. Feldman's experiments show that the interlayer water evaporates at very low relative humidity, below 11%. This can be seen also in Jennings' [37][38] microstructural model of C-S-H, in which the amorphous colloidal structure of the C-S-H is organized in elements, called 'globules'. In Jennings' [38] model, the globule is composed of solid C-S-H sheets, intra-globule porosity and a monolayer of water on the surface. For relative humidities below 11%, a part of the water filling the intra-globule porosity is evaporated. In a porosity measurement procedure in which the sample is dried at 105°C until a constant mass is achieved, a part of the interlayer water is evaporated and is thus included in the measured porosity [34][39]. Consequently, the porosity measured by oven-drying at 105°C should not be used in poromechanical formulation, as it includes a part of the interlayer porosity. The free-water porosity is defined and measured by equilibrating the cement paste at 11% relative humidity [34][39]. Some measurements of the free-water porosity, which is obviously smaller that the total porosity measured by drying at 105°C, from Feldman [40] are presented by Jennings *et al*. [34]. From the above discussion it appears that the free-water porosity is the cement paste porosity that should be used in the poromechanical formulations. This is in accordance with the assumption made by Ulm *et al*. [1] in their multi-scale microstructural model for the evaluation of the poromechanical properties of hardened cement paste. These authors use the Jennings' [37] model and exclude the intra-globule porosity from the cement paste porosity used in the calculations. According to Ulm *et al*. [1], considering the characteristic size of the interlayer space,

which is less than ten water molecules in size, it is recognized that the water in this space can not be regarded as a bulk water phase.

Taylor [39] (in his Fig. 8.5) presents the values of total and free-water porosity derived from calculated phase compositions of mature ordinary cement paste with varying w/c ratio. The comparison of the calculated free-water porosity with the porosity measured by mercury intrusion shows that for w/c ratios smaller than 0.5, the free-water porosity can be approximated by the mercury porosity. For higher w/c ratios, the free-water porosity is somewhat higher than the mercury porosity.

3 Experimental program

In order to evaluate the parameters defined in the above section, drained and undrained isotropic compression tests as well as unjacketed tests have been performed on a hardened cement paste. The effective stress law corresponding to the variations of the drained bulk modulus is studied by performing the drained compression tests with different constant pore pressures.

3.1 Sample preparation

A class G oil well cement was used to prepare the cement paste with a water to cement ratio $w/c = 0.44$. Two additives, a dispersant and an anti-foaming agent were used in the paste. The fresh paste was conserved in 14cm cubic moulds during four days in lime saturated water at 90°C temperature. After this period, the temperature was reduced gradually to prevent the cracking of the blocs due to a sudden temperature change. Then, the blocs were cored and cut to obtain cylindrical samples with 38mm diameter and 76mm length. The two ends of the cylindrical samples were rectified to obtain horizontal surfaces. After the preparation of the samples, the geometry and the weight of the samples were measured. To insure the homogeneity and the integrity of the samples, measurements of wave velocity and dynamic elastic modulus were performed on all of them. These measurements were performed at ambient temperature.

After the sample preparation phase, the samples have been submerged in a fluid which is neutral regarding to the pore fluid of the cement paste to prevent chemical reactions during the period of curing. The samples have been cured during at least three months at 90°C in the neutral fluid for which pH=13 before performing the mechanical loading tests. Before testing, the temperature of each sample was reduced slowly to prevent any thermal cracking.

The porosity of the samples is studied by two methods: oven drying and mercury intrusion porosimetry. The total porosity is measured by drying the samples at 105°C until a constant mass is achieved, and an average value equal to $\phi = 0.35$ is obtained. As mentioned in section 2.4, this porosity includes a part of the interlayer water of the cement paste. The mercury intrusion porosimetry is performed on the samples which are dried before the tests with the freeze-drying technique using liquid nitrogen which is, according to Gallé [41], the most suitable drying procedure to investigate the pore structure of cement-based materials. With a maximum intruding pressure of 200MPa the average mercury porosity of the samples is obtained equal to $\phi = 0.26$ (Figure 2). Using the Washburn-Laplace equation ($P = -4\gamma\cos\theta/d$) and assuming a contact angle θ of 130° and a surface tension of mercury γ of 0.483N/m from Ref. [39], the maximum intruding pressure P of 200MPa corresponds to a minimum pore diameter of about 6nm. Based on the discussions of section 2.4, this value of $\phi = 0.26$ will be used as an approximation of the free-water porosity of the studied cement paste in the following poromechanical formulations.

3.2 Experimental setting

The triaxial cell used in this study can sustain a confining pressure up to 60MPa. It contains a system of hydraulic self-compensated piston. The loading piston is then equilibrated during the confining pressure build up and directly applies the deviatoric stress. The axial and radial strains are measured directly on the sample inside the cell with two axial transducers and four radial ones of LVDT type. The confining pressure is applied by a servo controlled high pressure generator. Hydraulic oil is used as confining fluid. The pore pressure is applied by another servo-controlled pressure generator with possible control of fluid volume or pore pressure. Further details on the testing system can be found in Sulem and Ouffroukh [42] and Ghabezloo and Sulem [21].

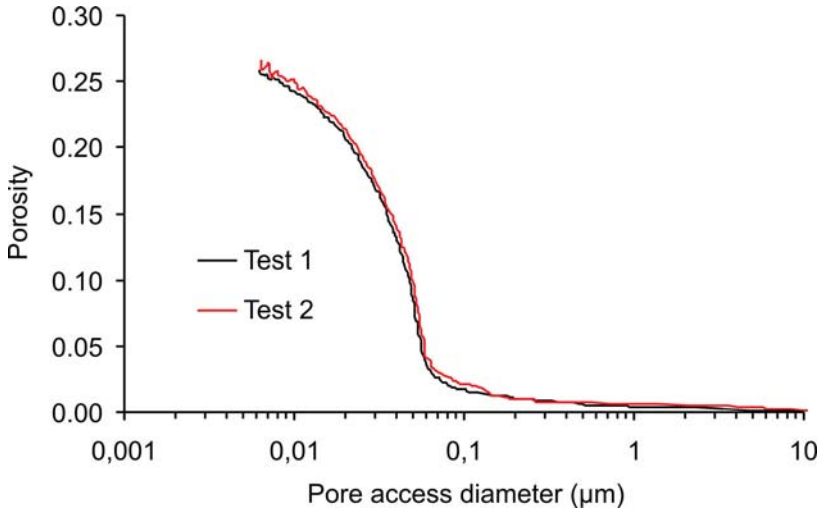

Figure 2-Results of porosity measurements by mercury intrusion

3.3 Sample saturation and loading rate

During the period of curing, the samples are stored inside the saturating fluid at 90°C for at least three months. After this period they can be considered as completely saturated. The process of installing the sample inside triaxial cell may cause a partial de-saturation of the sample. For this reason a seven days re-saturation phase is performed inside the triaxial cell. During this period, the sample is maintained under a confining pressure equal to 1.2MPa and a back fluid pressure equal to 1.0MPa is applied to the sample while the volume of the fluid injected in the sample is monitored. To prevent the chemical reactions during the test, the same neutral fluid which is used during the period of curing is used in the pore pressure generator as the saturating fluid.

For a drained test, the loading rate should be slow enough to ensure the drainage of the generated excess pore pressure in the sample. This loading rate is a function of the permeability of the tested material and of the drainage length of the sample. In order to determine the appropriate loading rate, a preliminary study was done in which the sample was in simple drainage condition. The pore pressure is maintained constant in one side of the sample. The valve situated at the other side was closed and the pore pressure was monitored using a pore pressure transducer. The confining pressure with different loading rates (0.1MPa/min, 0.075MPa/min, 0.05MPa/min, 0.02MPa/min) was applied and we observed that by using a loading rate equal to 0.02MPa/min no excess pore pressure was measured in the sample. Consequently, in order to ensure a good drainage of the sample during the tests, a loading rate equal to 0.025MPa/min is used with a double drainage system, in which the pore pressure is controlled at both sides of the sample. For undrained compression tests, a loading rate equal to 0.10MPa/min is used.

3.4 Unjacketed test

The unjacketed test is performed by applying simultaneous and equal variations of confining pressure and pore pressure. A small difference between the confining pressure and pore pressure equal to 0.5MPa is maintained inside the sample in order to avoid any leakage of the pore fluid between the sample and the membrane. A loading-unloading cycle is applied and the unjacketed modulus is calculated for the unloading part of the curve. The result is presented in the Figure (3) and shows that the unjacketed modulus does not vary with the pressure up to 50MPa and is equal to 21GPa.

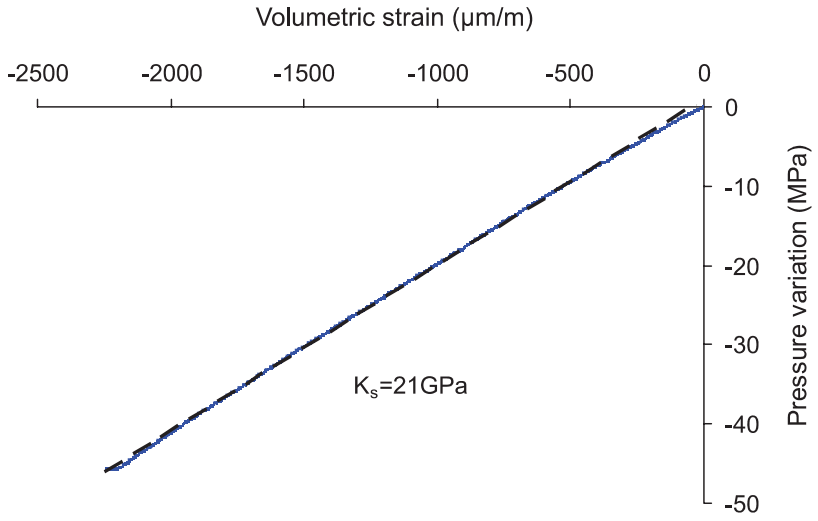

Figure 3- Unjacketed test, pressure-volumetric strain response in unloading

Considering that the unjacketed modulus does not vary with the applied pressure, using equation (37) we can conclude that the effective stress coefficient corresponding to the drained bulk modulus of the hardened cement paste is equal to one and that the bulk modulus varies with Terzaghi effective stress. This conclusion can be verified using the results of the drained compression tests and the variations of the measured modulus with confining pressure and pore pressure.

3.5 Drained compression tests

Five drained isotropic compression tests have been performed. In each test, some unloading-reloading cycles have been performed in order to evaluate the secant bulk modulus of the hardened cement paste. Three tests are performed with a constant pore pressure equal to 1.0MPa. Two other tests are performed using pore pressures equal respectively to 23.5MPa and 47.0MPa. The loading paths are presented in the Figure (4). Table (1) presents the details of the tests and of the loading cycles.

Test	Pore pressure (MPa)	Cycle n°1 (MPa)	Cycle n°2 (MPa)	Cycle n°3 (MPa)
D-1	1.0	10	20	-
D-2	1.0	25	52	-
D-3	1.0	20	40	60
D-4	23.5	36	48	60
D-5	47.0	60	-	-

Table 1- Details of the performed drained isotropic compression tests

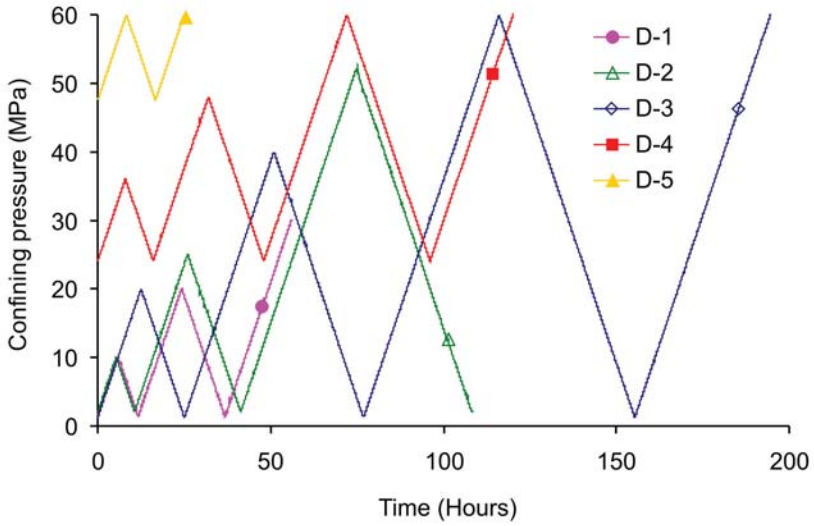

Figure 4- Loading paths of drained isotropic compression tests (D-1, D-2, D-3 with constant applied pore pressure of 1.0MPa, D-4 with constant applied pore pressure of 23.5MPa, D-5 with constant applied pore pressure of 47.0MPa)

The stress-strain curves obtained from the isotropic drained compression tests are presented in Figure (5). We can see the strongly nonlinear response of the hardened cement paste under isotropic compression and the existence of the permanent strains. Due to the slow rate of the loading, a part of the measured strains, especially at high stresses, may be due to creep. This point can easily be observed for example in the last unloading parts of D-2 and D-3 tests, where despite of the diminution of the confining pressure, the volumetric strain continues to increase. These effects are ignored in this paper and will be discussed in a future publication.

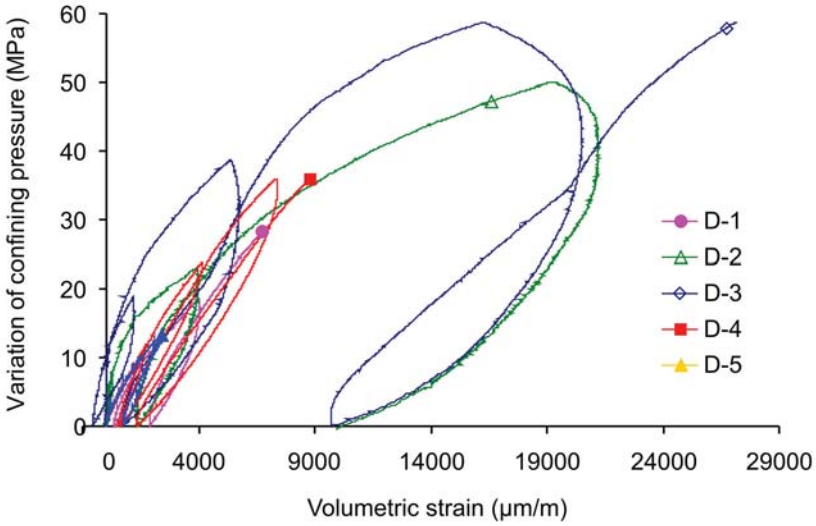

Figure 5- Drained isotropic compression tests, Pressure-volumetric strain curves

The drained bulk modulus is calculated for each unloading-reloading cycle. The method of evaluation of the modulus is presented in the Figure (6). A linear fitting of the whole unloading-reloading curve is performed and the slope of the obtained line is considered as an average secant modulus corresponding to the stress level at the beginning of the unloading phase.

Figure (7) shows the values of measured bulk modulus for different confining pressures and different pore pressures. Looking at the points corresponding to the tests performed with the pore pressure equal to 1.0MPa and 23.5MPa we observe a reduction of the bulk modulus with the confining pressure. This

behaviour and the phenomenon of degradation of the hardened cement paste and reduction of the bulk modulus under isotropic loading differs from the one commonly observed in granular porous rocks. For these rocks the bulk modulus generally increases under isotropic stress due to the closure of the pre-existing microcracks and compaction of the rock matrix. This mechanism of degradation of the bulk modulus and the highly non-linear behaviour of hardened cement paste under isotropic loading will be studied further in this paper by comparison of microphotographs of the samples before and after the compression tests.

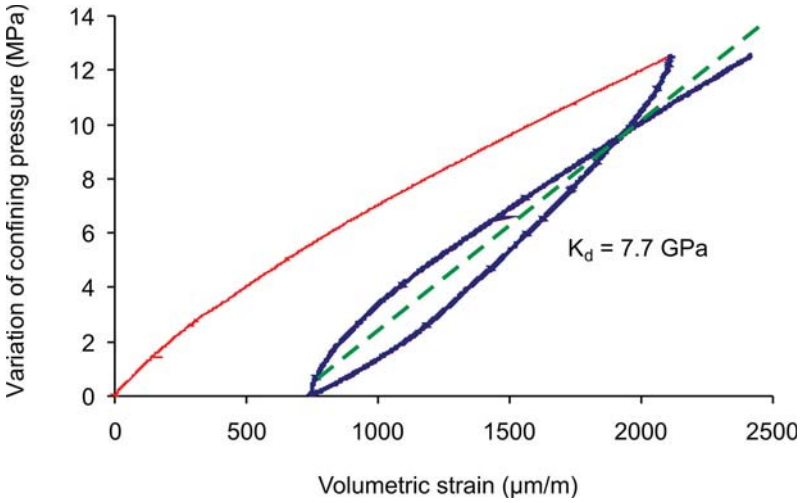

Figure 6- Evaluation of the secant bulk modulus in an unloading-reloading cycle

It can be seen in Figure (7) that at a given confining pressure, the bulk modulus increases with increase of the pore pressure. This graph shows the simultaneous effects of the confining pressure and of the pore pressure on the degradation of the hardened cement paste and on the variation of the bulk modulus, and highlights the necessity of finding a single stress variable (effective stress) to describe this phenomenon.

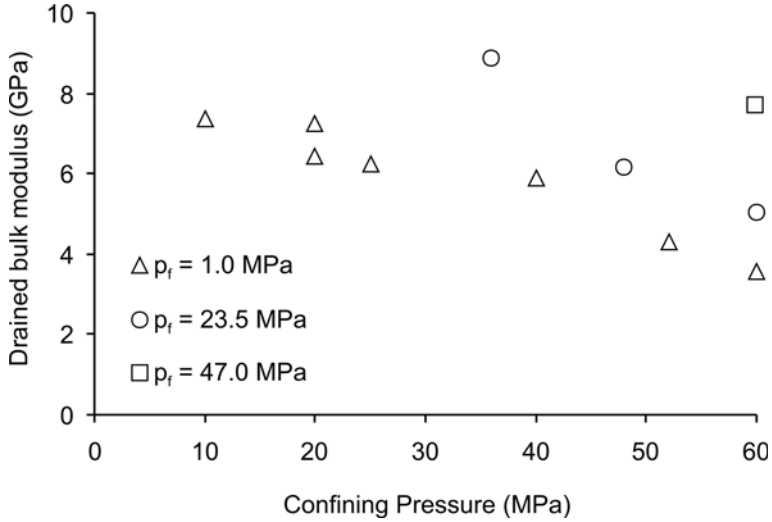

Figure 7- Variation of the drained bulk modulus with the confining pressure at various imposed pore pressures

As mentioned above, as the unjacketed modulus was found to be constant, the drained bulk modulus varies with Terzaghi effective stress. This statement can be experimentally verified here by using the results of drained compression tests. Figure (8) shows the evaluated drained bulk moduli as a function of Terzaghi effective stress calculated for each data point using the corresponding values of confining

pressure and pore pressure. We can see the good compatibility of the drained bulk moduli measured with different pore pressures when presented as a function of Terzaghi effective stress. The experimental results thus confirm the above conclusion and the following expression is obtained for the drained bulk modulus of hardened cement paste as a function of Terzaghi effective stress:

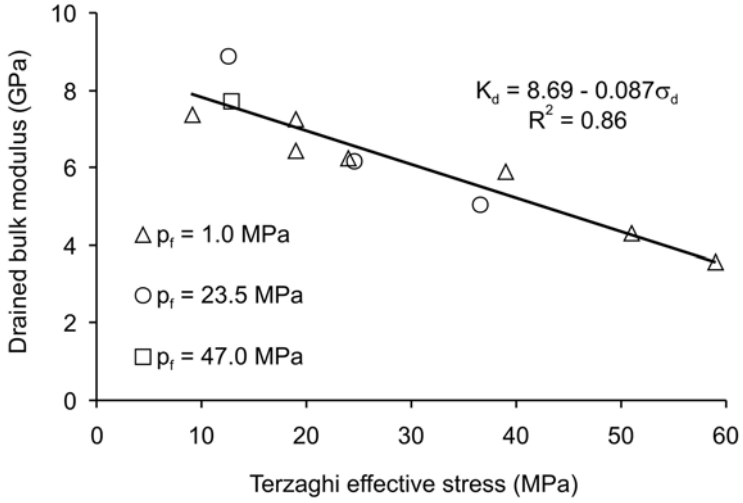

Figure 8- Variation of the drained bulk modulus with Terzaghi effective stress

$$K_d^{sec} = 8.69 - 0.087\sigma_d \qquad (K_d^{sec} \text{ in GPa and } \sigma_d \text{ in MPa}) \tag{44}$$

Equation (44) shows that the bulk modulus at zero effective stress is about 8.7GPa. On the other hand, the bulk modulus can be estimated from a simple relationship used by Heukamp *et al.* [11] from [43] between K_s, K_d and ϕ:

$$K_d = K_s\left(1-\phi\right)^3 \tag{45}$$

Replacing $K_s = 21\text{GPa}$ and $\phi = 0.26$ in equation (45), the drained bulk modulus is found equal to 8.5GPa which has a very good compatibility with the measured values.

A similar expression in the form $E = E_0\left(1-\phi\right)^3$ was used by Helmuth and Turk [44] to approximate the variations of the Young modulus of the hardened cement paste with the porosity. The parameter E_0 is the value of Young modulus at zero porosity limit and was found equal to 29GPa. The simple cubic law for the relation between the porosity and the bulk modulus (equation (45)) can be obtained from structural mechanics approaches at the micro-scale as derived for cellular solids [45]. This relation verifies the Hashin-Shtrikman [46] bounds and is very close to the modulus obtained from a self-consistent homogenisation scheme for porosities smaller that 0.45 (Figure (9)).

The expression of the drained bulk modulus presented in equation (44) and the value of the unjacketed modulus of the hardened cement paste (21GPa), enable us to determine the expression of the Biot effective stress coefficient presented in equation (42).

$$\alpha^{sec} = 0.586 + 0.004\sigma_d \qquad (\sigma_d \text{ in MPa}) \tag{46}$$

Inserting equation (45) in equation (25) the following relation is found for the Biot effective stress coefficient:

$$\alpha = 1-\left(1-\phi\right)^3 \tag{47}$$

Replacing $\phi = 0.26$ in this relation, the Biot effective stress coefficient is found equal to 0.59 which is compatible with the result presented in equation (46).

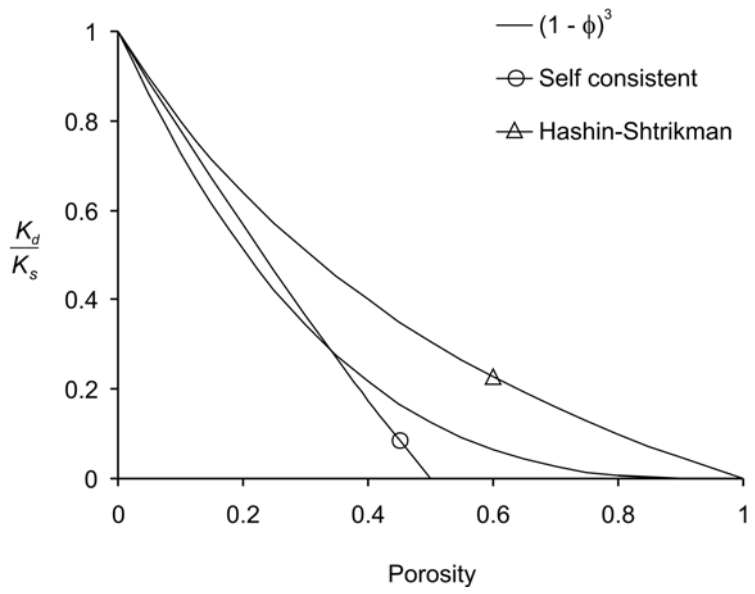

Figure 9- Comparison of equation (45) with Hashin-Shtrikman bound and self consistent homogenisation scheme

3.6 Undrained compression tests

In order to determine the undrained poroelastic parameters of hardened cement paste, (undrained bulk modulus K_u and Skempton coefficient B defined in equation (11)), two undrained isotropic compression tests were performed with three unloading-reloading cycle in each test. Table (2) presents the details of the cycles and the initial conditions of the test. The loading paths are shown in Figure (10). The measured volumetric strains during the tests are presented in Figure (11). The undrained behaviour of hardened cement paste observed in these tests shows a lower non-linearity as compared to the results of drained compression tests presented in Figure (5). We can also observe that the permanent strains measured in the unloading parts are considerably less than the strains measured in the drained tests. The undrained bulk moduli are evaluated with the same method as presented above in Figure (6) for the drained tests. It is assumed here that the undrained parameters, K_u and B, vary with Terzaghi effective stress. As it can be seen in equations (13) and (14), this assumption is verified in the case of an ideal porous material, $K_s = K_\phi = K_m$, if the solid and the fluid compression moduli, K_m and K_f, are assumed constant. As shown by Zimmerman [16], for usual values of the moduli which appear in equations (13) and (14), the undrained parameters are almost completely insensitive to deviations of K_ϕ from K_s and the results in the case of an inhomogeneous porous material differ only slightly from the one obtained for an ideal porous material. Moreover, this assumption is adopted and commonly used in different experimental studies [47][48][49][50]. The influence of this assumption on the analysis of the experimental results is studied later in this paper.

Test	Initial confining pressure (MPa)	Initial pore pressure (MPa)	Cycle n°1 (MPa)	Cycle n°2 (MPa)	Cycle n°3 (MPa)
ND-1	1.65	1.50	20	40	60
ND-2	1.85	1.65	15	30	50

Table 2- Details of the performed undrained isotropic compression tests

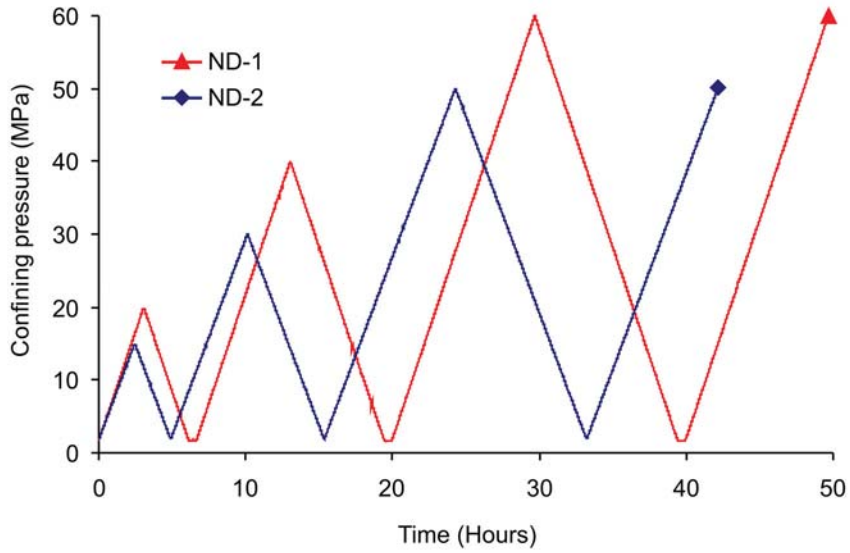

Figure 10- Loading paths of the undrained isotropic compression tests

Figure (12) presents the undrained bulk moduli evaluated in unloading-reloading cycles. The corresponding Terzaghi effective stress is calculated for each point from the imposed confining pressure and the measured pore pressure. These data are fitted with a straight line:

$$K_u^{\sec} = 11.25 - 0.099\sigma_d \qquad (K_u^{\sec} \text{ in GPa and } \sigma_d \text{ in MPa}) \tag{48}$$

As expected, for an effective stress, the undrained bulk modulus calculated by equation (48) is greater than the drained bulk modulus calculated with equation (44). The mechanism of degradation of the undrained modulus is discussed further using the results of microscopic observations of the tested samples.

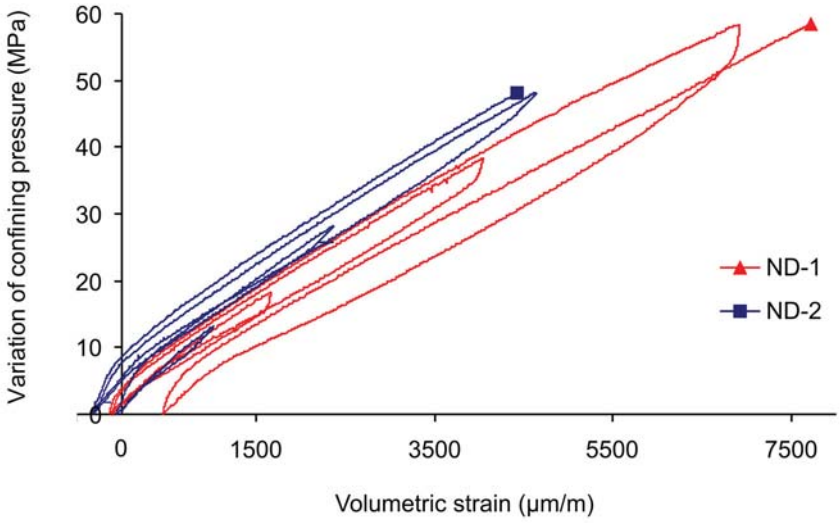

Figure 11- Undrained isotropic compression tests, pressure-volumetric strain curves

Figure (13) presents the variations of the pore pressure during the undrained loading with the confining pressure. The slope of the curve in this figure is giving the Skempton coefficient B. Notice that for a precise evaluation of the Skempton coefficient, one has to account for the effect of the deformation of the drainage and pressure measurements systems. This point is discussed in details by Ghabezloo and Sulem [21] who showed that for the testing device used here, this correction is very small. We observe the linear increase of the pore pressure in the loading and reloading parts with the confining pressure increase. In the beginning of the unloading parts, the pore pressure decrease is

retarded and the rate of change of pore pressure with the confining pressure is considerably lower than the one observed during the loading part. Below a certain stress level, about 15MPa, there is a considerable increase in the rate of decrease of the pore pressure and no excess pore pressure remains at the end of the unloading part. As it can be observed on Figure (13), the pore pressure variation in this part of the unloading curve is equal to the variation of the confining pressure. This indicates that the pore fluid has flowed between the sample and the rubber membrane and that consequently the slope of the curve in this part is not the Skempton coefficient. The same problem is observed in the beginning of the reloading parts. Because of this, the Skempton coefficients are evaluated on the central (linear) part of the reloading curves. Figure (14) presents the evaluated Skempton coefficient as a function of Terzaghi effective stress evaluated at each point and shows a very small reduction of this coefficient with the effective stress. This small variation can be neglected and the Skempton coefficient can be considered as constant, equal to the average of the measured values, $B = 0.4$.

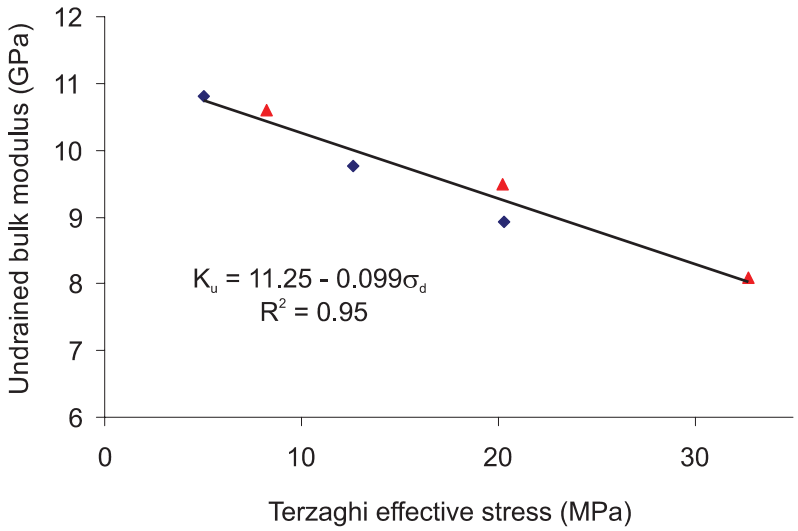

Figure 12- Variation of the undrained bulk modulus with Terzaghi effective stress

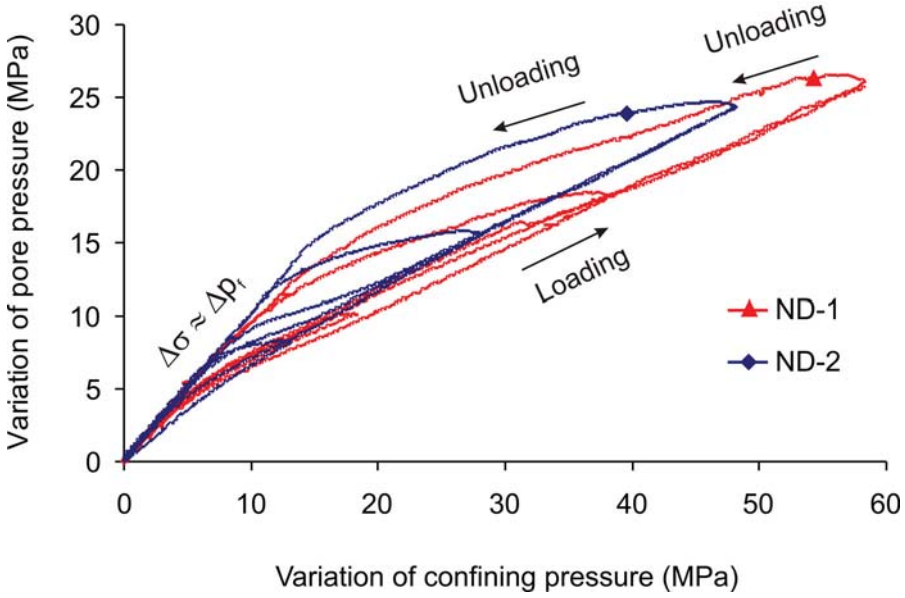

Figure 13- Undrained isotropic compression tests, pore pressure evolution

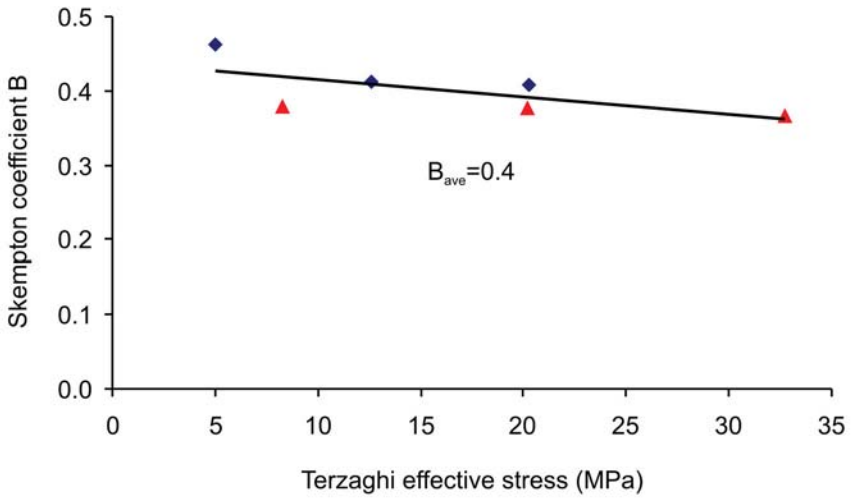

Figure 14- Variation of the Skempton coefficient B with Terzaghi effective stress

Assuming an ideal porous material for which $K_s = K_\phi$, the following relation is obtained for the Skempton coefficient by replacing equation (45) in equation (13):

$$\frac{1}{B} = 1 + \left(\frac{K_s}{K_f} - 1 \right) \frac{\phi(1-\phi)^3}{1-(1-\phi)^3} \tag{49}$$

Replacing $K_s = 21\text{GPa}$, $K_f = 2.2\text{GPa}$ and $\phi = 0.26$ in this relation, the Skempton coefficient is found equal to 0.40 which is equal to the average value obtained in the test results. Introducing equations (45) and (49) in equation (14), the undrained bulk modulus is found equal to 11.1GPa which is here again has a very good compatibility with the obtained experimental result, presented in equation (48). The good evaluation of the drained and undrained bulk moduli and also of the Skempton coefficient using simple homogenization relations (equations (45) and (49)) shows the efficiency of this method for evaluation of the poromechanical properties of heterogeneous materials, when used with proper parameters, and also the great importance of the unjacketed modulus K_s in these evaluations.

3.7 Summary of experimentally evaluated poroelastic parameters

The evaluated poroelastic parameters of hardened cement paste are summarized below:

$$\begin{aligned} &K_s = 21 \\ &K_d^{\text{sec}} = 8.69 - 0.087\sigma_d \\ &K_u^{\text{sec}} = 11.25 - 0.099\sigma_d \quad (K_{s,d,u} \text{ in GPa and } \sigma_d \text{ in MPa}) \\ &B = 0.4 \\ &\alpha^{\text{sec}} = 0.586 + 0.004\sigma_d \end{aligned} \tag{50}$$

The graphical representation of the variations of the poroelastic parameters of hardened cement paste is presented in the Figure (15). Terzaghi effective stress in this figure is limited to 40MPa which is the maximum stress level achieved in the undrained tests.

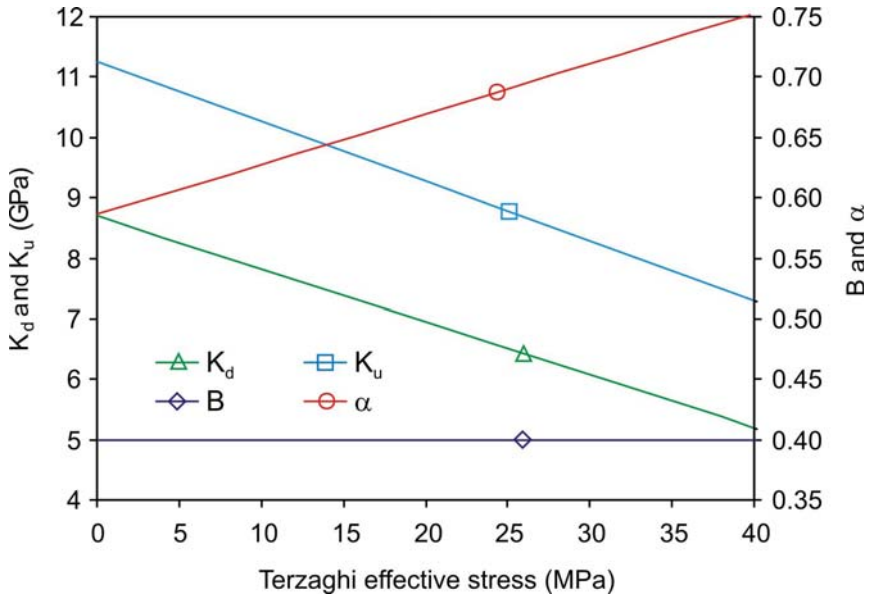

Figure 15- Variation of poroelastic parameters of the hardened cement paste with Terzaghi effective stress

4 Analysis of the overall compatibility of the experimental results

The Biot effective stress σ_b' can be calculated using equations (43) and (46). The performed undrained compression tests can be analysed using Biot effective stress to calculate the drained bulk modulus and the results can be compared with the results of the drained tests to ensure the compatibility of the drained and the undrained isotropic compression tests. Figure (16) presents the $\varepsilon - \sigma_b'$ curves of the undrained tests together with the $\varepsilon - \sigma$ curves of the drained tests. In this figure we can see the consistency of the stress-strain curves of the drained and undrained tests. The drained bulk moduli evaluated in the undrained tests as described above, are presented in Figure (17) together with the drained bulk moduli evaluated in the drained compression tests. This graph shows the good compatibility of the bulk moduli calculated in the drained and the undrained tests, and also confirms the appropriate choice of the loading rate used for the drained tests.

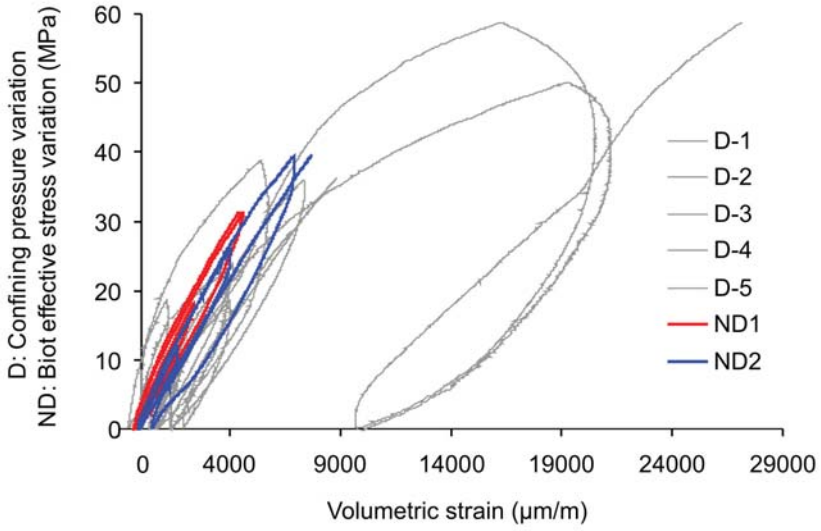

Figure 16- Evolution of the volumetric strain with the confining pressure for drained tests (D) and with Biot effective stress for undrained tests (ND)

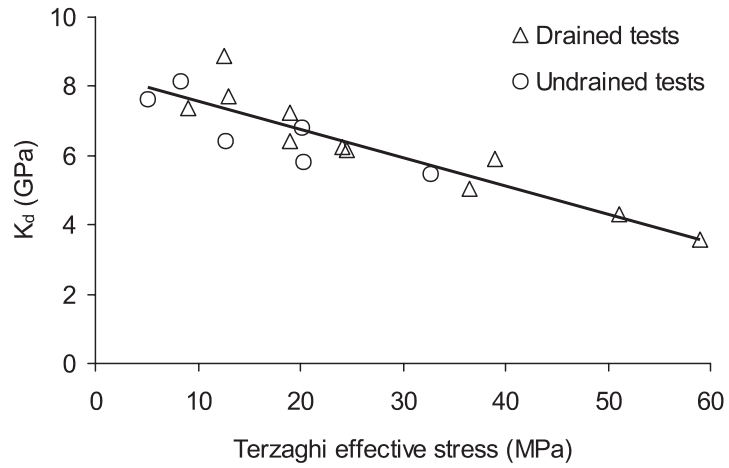

Figure 17- Drained bulk modulus evaluated in drained and undrained tests as a function of Terzaghi effective stress

In equation (46) the Biot effective stress coefficient is evaluated using the results of drained compression tests and unjacketed test. An other expression can be obtained using equations (14) and (25) to evaluate this coefficient using the results of drained and undrained compression tests:

$$\alpha = \frac{1 - K_d / K_u}{B} \tag{51}$$

By inserting equation (44) and (48), respectively for K_d and K_u, and with $B = 0.4$, the Biot coefficient can be evaluated using equation (51). Comparing the Biot coefficients evaluated using equations (46) and (51), (see Figure (18)), we can observe the good compatibility of the experimental results obtained from the drained, undrained and unjacketed compression tests.

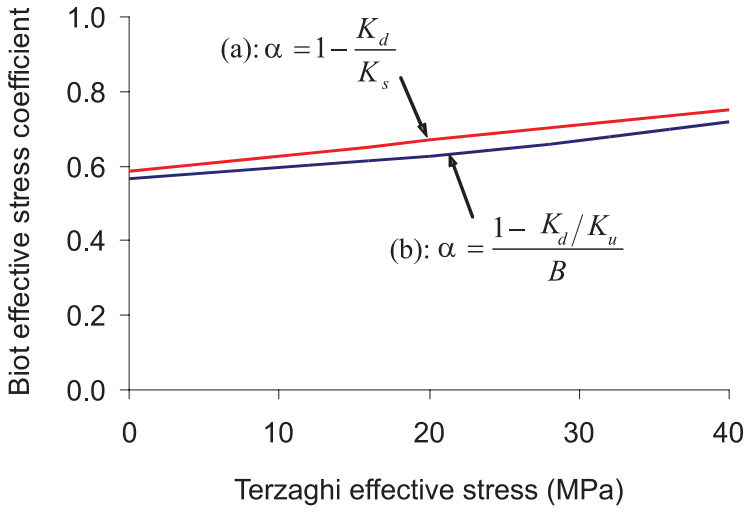

Figure 18- Comparison of Biot effective stress coefficients evaluated from (a) drained and unjacketed compression tests and (b) drained and undrained compression tests

Introducing the expression of the Biot coefficient presented in equation (25) in equation (51), the following expression is obtained for evaluation of the unjacketed modulus K_s using the results of drained and undrained tests:

$$K_s = \frac{K_d K_u B}{K_d - K_u (1 - B)} \tag{52}$$

The differential pressure during the performed unjacketed test was maintained constant equal to 0.5MPa. Using this value in equations (44) and (48), the drained and undrained bulk moduli are respectively evaluated equal to 8.65GPa and 11.20GPa. The Skempton coefficient is constant, equal to 0.4. Inserting these values in equation (52), the unjacketed modulus is evaluated equal to 20.1GPa which is compatible with the measured value equal to 21GPa and shows again the good compatibility of the obtained experimental results.

Note that the above discussion on the compatibility of the various experimental results is not affected by the cement paste porosity.

5 Analysis of the results

Using the obtained experimental results an interesting analysis can be done on the cement paste porosity that should be used in poromechanical fromulations, as discussed in section 2.4. Replacing equations (25) and (30) in inequality $\kappa \le \alpha$ of equation (31) the following inequality is obtained:

$$\frac{1}{K_\phi} \le \frac{\alpha}{\phi K_s} \tag{53}$$

Inserting inequality (53) in equation (16) the following inequalities are obtained for the cement paste porosity:

$$\phi \le \begin{cases} K_f \left(\dfrac{\alpha}{K_s} + \dfrac{\left(1/K_d - 1/K_s\right)\left(1/K_u - 1/K_s\right)}{\left(1/K_d - 1/K_u\right)} \right) & \text{(a)} \\ K_f \left(\dfrac{\alpha}{K_s} + \dfrac{\left(1-B\right)\left(1/K_d - 1/K_s\right)}{B} \right) & \text{(b)} \\ K_f \left(\dfrac{\alpha}{K_s} + \dfrac{1/K_u - 1/K_s}{B} \right) & \text{(c)} \\ K_f \left(\dfrac{\alpha}{K_s} + \dfrac{\left(1-B\right)\left(1/K_d - 1/K_u\right)}{B^2} \right) & \text{(d)} \end{cases} \tag{54}$$

Replacing the values of poroelastic parameters, $K_d = 8.69\text{GPa}$, $K_u = 11.25\text{GPa}$, $K_s = 21\text{GPa}$, $B = 0.4$, $\alpha = 0.586$ and $K_f = 2.2\text{GPa}$ in equation (54) we obtain $\phi \le 0.29$ for equations (a) and (c) and $\phi \le 0.28$ for equations (b) and (d). The obtained porosity upper limits are lower than the total porosity of the studied cement paste, evaluated by oven drying equal to 0.35. This confirms the discussion presented in section 2.4 and shows that the cement paste porosity that should be used in poromechanical formulations is smaller than the total porosity, which contains some quantity of interlayer water.

The obtained poroelastic parameters can be used in equation (16) to evaluate the modulus K_ϕ. This evaluation is done for a zero differential pressure. Inserting the above mentioned values of poroelastic parameters with $\phi = 0.26$ in equation (16), the parameter K_ϕ is evaluated equal to 21.9GPa for equation (a), 15.3GPa for equation (b), 17.3GPa for equation (c) and 13.0GPa for equation (d). We can see that despite of the good compatibility of the experimentally evaluated parameters, as shown in section 4, the indirect evaluation of the modulus K_ϕ is very difficult and the obtained values differ significantly. However, we consider the average of the obtained values for the modulus K_ϕ, equal to 16.9GPa, which is smaller than the experimentally evaluated unjacketed modulus K_s, equal to 21GPa. It should be noted that for an ideal porous material which is homogeneous and isotropic in the micro-scale, the parameters K_ϕ and K_s are equal.

Assuming that the modulus K_ϕ is constant, we can evaluate the effective stress coefficients β, χ and κ defined respectively in equations (26), (28) and (30) as functions of Terzaghi effective stress. Figure (19) presents the variations of these effective stress coefficients, and also of α and θ, with Terzaghi effective stress and we can observe on this graph that the inequality (31) is verified for the evaluated parameters.

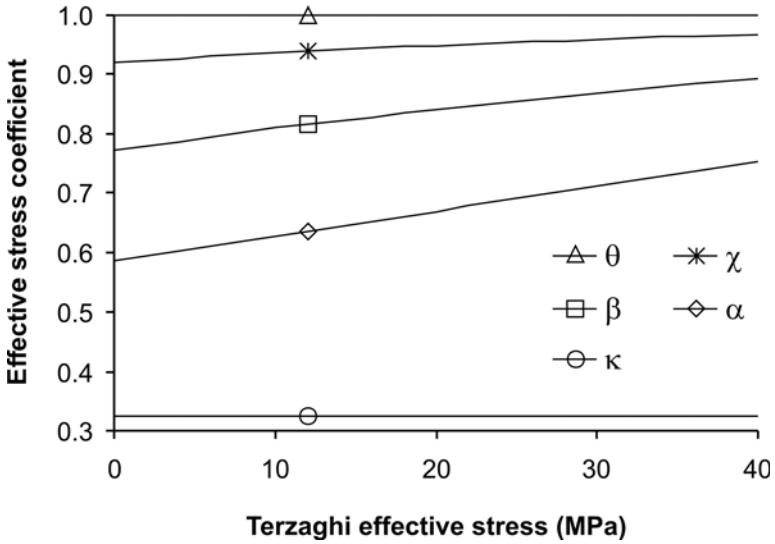

Figure 19- Effective stress coefficients corresponding to different physical properties as a function of Terzaghi effective stress (θ for drained bulk modulus, χ for porosity, β for pore volume, α for total volume and κ for solid volume)

As mentioned earlier, in this study we have assumed that the undrained parameters, K_u and B, vary with Terzaghi effective stress. Using the obtained average value of K_ϕ it is now possible to study the influence of this assumption on the above analysis. This is done by studying the effect of deviation of K_ϕ from K_s on the evaluation of Skempton coefficient. Inserting the poroelastic parameters presented above in equation (13), the Skempton coefficient is evaluated equal to 0.396 which has a very good compatibility with the measured value, equal to 0.4. Replacing K_ϕ with K_s, the evaluated value is reduced to 0.389, i.e. a change of less than 2% in the evaluated Skempton coefficient. Consequently, we can conclude that the assumption that the undrained parameters vary with Terzaghi effective stress does not influence significantly the obtained results.

6 Microscopic observations

Microscopic observations are performed on the hardened cement paste samples before and after the isotropic compression tests in order to study possible changes in the microstructure of the cement paste that could corroborate the non-linear stress-strain behaviour and degradation mechanism of the elastic moduli observed in isotropic compression tests.

6.1 Observation equipment and conditions

The observations are performed using an environmental scanning electron microscope (ESEM) which is equipped by two types of detectors: A detector of secondary electrons (SE) and a detector of backscattered electrons (BSE). The SE detector results in images which emphasize the topographical contrasts on the observed sample and have a three-dimensional appearance. In these images, steep surfaces and edges tend to be brighter than flat surfaces. The BSE detector can detect the contrast

between areas with different chemical compositions, especially when the average atomic number of the various regions is different. The brightness of the images taken by this detector tends to increase with the atomic number. In order to keep the natural contrast of the samples, the observation conditions are adapted to work in low vacuum condition.

6.2 Sample preparation

The operations of sample preparation and microscopic observation are performed shortly after each mechanical loading test in order to avoid the effects of carbonation on the sample. Working in the low vacuum condition, it is possible to observe the samples without drying them. Two types of samples were used for microscopic observations: Fractured samples and polished samples. Fractured samples are prepared by breaking the sample with a single hammer blow on a burin placed on the sample. The SE detector is used to take the images of these samples. Preparation of polished samples was performed following the normal procedure of preparation of flat-polished samples for SEM observations, including cutting, grinding and polishing steps. The details of such a procedure are presented by Stutzman and Clifton [51] and Kjellsen et al. [52]. The images of these samples are taken using the BSE detector.

6.3 Observation results

Figure (20) shows an image of the microstructure of the hardened cement paste taken on a polished intact sample with 200x magnification. As explained by Diamond [53], we can observe the unhydrated cement particles as bright entities, hydration shells surrounding the unhydrated cores and fully hydrated cement grains as smooth-textured uniformly grey areas. The hydration shells and fully hydrated grains, formed in originally grain-filled space, are called 'inner products' and appear non-porous at this magnification. These inner products are separated from each other by a groundmass or 'outer product' deposited in the originally water-filled space which is irregularly textured and has a much less homogeneous appearance. This image clearly shows the very heterogeneous microstructure of the hardened cement paste.

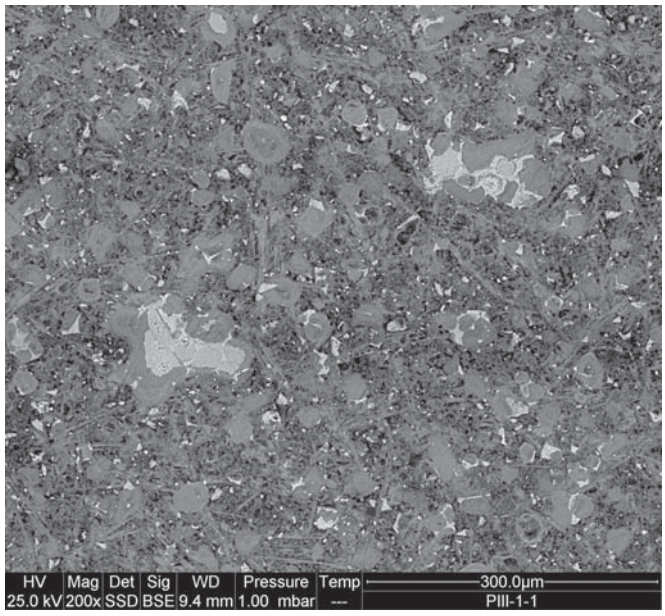

Figure 20- Microphotograph of the heterogeneous microstructure of the hardened cement paste, image taken on an intact, polished sample

Figure (21) shows an image taken after a drained isotropic compression test on a fractured sample with 400x magnification and we can see clearly the formation of a microcrack in the cement paste. Several images taken on different samples after the drained compression tests did not show any preferential direction for the microcracks. The length of the observed microcracks is generally between 100 and 200 µm. To ensure that these microcracks are not produced during the preparation of the sample, the same preparation method by fracturing is applied on two intact samples. The microscopic observation of these samples did not show any microcracks. Figure (22) shows another image taken after a drained compression test on a polished sample with 50x magnification. We can see on this image, an other type of inhomogeneity of the hardened cement paste in the form of areas with different grain densities and porosities, exhibited at a greater scale as compared to the microstructural inhomogeneity observed in Figure (20). This type of inhomogeneity has been also observed by Diamond [53]. On this image we can also observe the rupture of an air void situated in the more porous area. The traces of the polishing operation performed during the sample preparation can be observed as straight lines in the left part of the image presented in Figure (22). These traces are parallel and cannot be confounded with eventual microcracks generated during the mechanical loading test. Another example of the rupture of an air void is presented in Figure (23), taken on a polished sample after a drained compression test. Microscopic observation of the samples after the undrained compression tests shows the same type of microcracking of the samples under isotropic loading. An example, taken on a fractured surface with 1200x magnification, is presented in Figure (24) and shows a microcrack with an opening of a few microns. It should be mentioned that this opening is observed after the test on the unloaded sample.

These images show that the two different observation methods used in this study, backscattered electron SEM imaging on the polished samples and secondary electron SEM imaging on the fractured samples, are two complementary methods for the observation of the microcracked samples. The images taken on the polished samples show clearly the heterogeneity of the microstructure of the hardened cement paste and the details of the rupture of the microstructure near the air voids. But the observation and detection of the microcracks on these images is more difficult than on the images taken on the fractured samples. These latter provide a three-dimensional and very clear view of the existing microcracks.

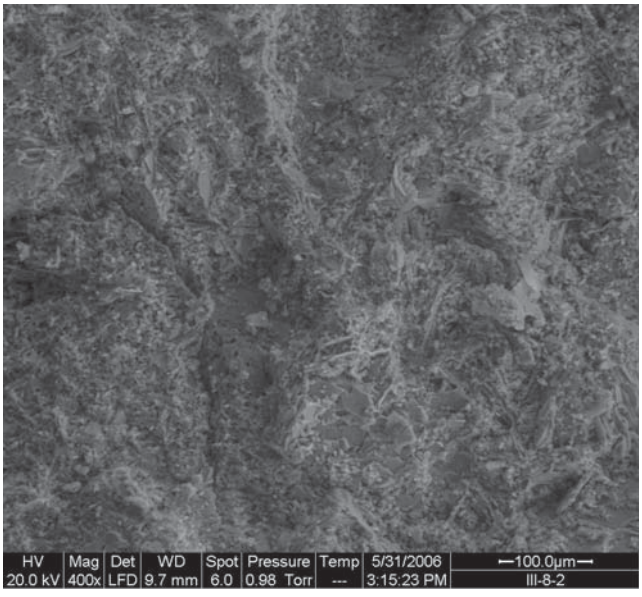

Figure 21- Microcracking of the sample, image taken on a fractured sample after a drained isotropic compression test

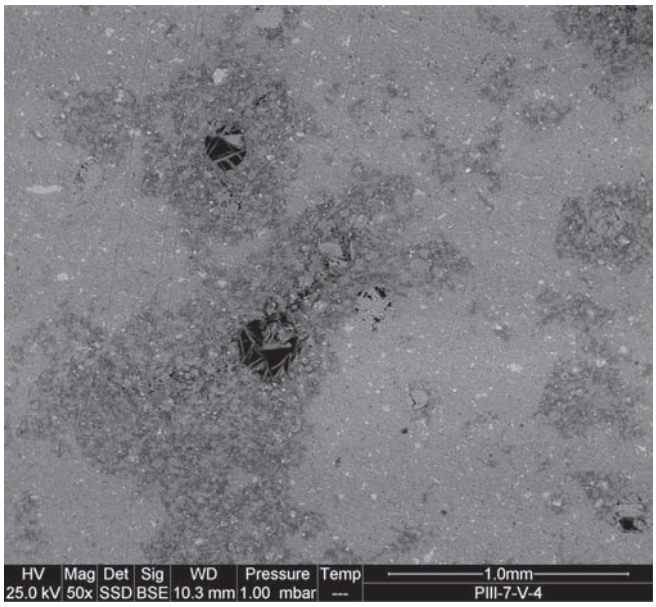

Figure 22- Microphotograph of the heterogeneous microstructure of the hardened cement paste and the rupture of the air voids, image taken on a polished sample after a drained isotropic compression test

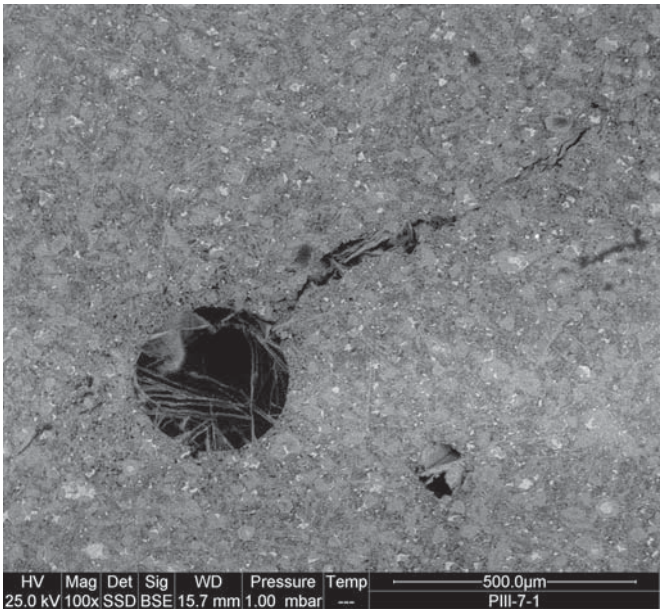

Figure 23- Rupture of an air void, image taken on a polished sample after a drained isotropic compression test

7 Mechanism of degradation under isotropic loading

The microscopic observations presented in the preceding section showed the presence of two types of heterogeneities in the microstructure of the hardened cement paste. The first type of inhomogeneity (Figure (20)), exhibited at a smaller scale, is due to the presence of different phases, including unhydrated grains, low density and high density C-S-H, CH crystals and the macro-porosity in the microstructure of the cement paste. These phases have different mechanical properties which are evaluated by different experimental methods, as in particular the nanoindentation method, by Monterio and Chang [2], Acker [3], Le Bellego [4], Velez et al. [5], Constantinides and Ulm [6]. Ulm et al. [1] have presented a table which summarizes the results obtained in these studies which can be used to evaluate the bulk modulus of the different phases of the microstructure of the hardened cement paste. The bulk modulus is evaluated equal to 14GPa and 19GPa respectively for low density and high density

C-S-H, 32GPa for CH crystals and between 104GPa and 121GPa for unhydrated grains. The unjacketed modulus of the hardened cement paste, evaluated equal to 21GPa in our experiments, is some weighted average of the bulk moduli of different phases of the microstructure. The presence in the microstructure of the hardened cement paste of various materials with bulk moduli which differ by one order of magnitude may lead to incompatible deformations at the interface between the various materials which can induce microcracking and degradation of the mechanical properties even under isotropic loading.

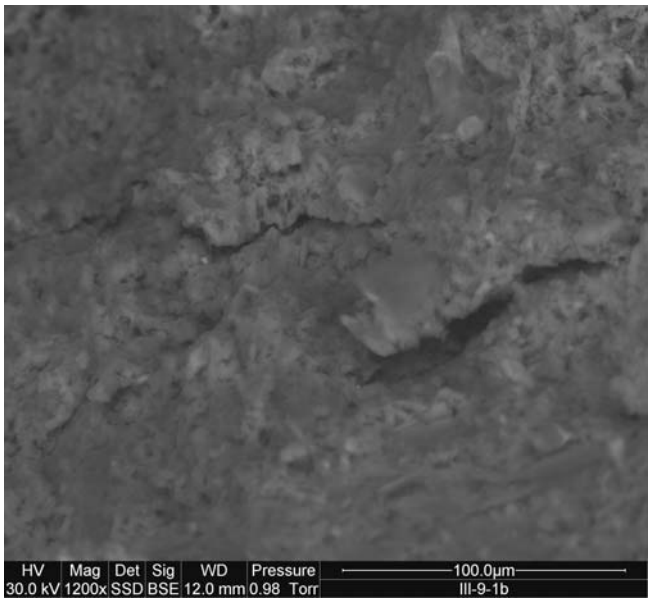

Figure 24- Microcracking of the sample, image taken on a fractured sample after an undrained isotropic compression test

The second type of inhomogeneity (Figure (22)) is presented at a greater scale as compared to the first type in the form of areas with different porosities and therefore with different average mechanical properties. The difference between the average elastic moduli of two adjacent areas in the microstructure can also cause microcracking and degradation of the material under isotropic loading. This can be seen in the images showing the rupture of the air voids presented in the Figure (22).

8 Conclusions

The poromechanical behaviour of hardened cement paste under isotropic loading is studied on the basis of an experimental testing program of drained, undrained and unjacketed compression tests. The macroscopic behaviour of the material is described in the framework of the mechanics of porous media. The poroelastic parameters of the material are determined and the effect of stress and pore pressure on them is evaluated. The unjacketed modulus of hardened cement paste is evaluated equal to 21GPa and the tests results show that it does not vary with the applied pressures. Secant drained and undrained bulk moduli and the Skempton coefficient of the material are evaluated in unloading-reloading cycles at different stress levels during the isotropic drained and undrained compression tests. Drained compression tests are performed with different pore pressures and show that the drained bulk modulus is a function of Terzaghi effective stress. Test results show the reduction of drained and undrained bulk moduli with Terzaghi effective stress increase. The microscopic observation of the samples showed that this degradation phenomenon is caused by the microcracking of the material under isotropic loading. The microcracking can be caused by the heterogeneity of the microstructure of the hardened cement paste which manifests itself at different scales. The Skempton coefficient is found to be constant, equal

to 0.4. Appropriate effective stress laws which control the evolution of total volume, pore volume, solid volume and porosity of the material are discussed. The Biot effective stress coefficient increases linearly with Terzaghi effective stress. Analysis of the experimental results showed that the cement paste total porosity, measured by oven-drying at 105°C, can not be used in poromechanical formulations. The drained and undrained bulk moduli, the Skempton coefficient and the Biot effective stress coefficient are well reproduced with simple homogenization equations using the evaluated unjacketed modulus and the porosity. Finally, the good compatibility and consistency of the obtained poromechanical parameters demonstrates that the behaviour of the hardened cement paste can be indeed described within the framework of the theory of porous media.

9 Acknowledgments

The authors gratefully acknowledge TOTAL for supporting this research. They wish also to thank Xavier Boulay for performing mercury porosimetry experiments.

10 References

[1] F.-J. Ulm, G. Constantinides, F.H. Heukamp, Is concrete a poromechanics material? - A multiscale investigation of poroelastic properties, Materials and Structures 37 (265) (2004) 43-58.

[2] P.J.M. Monteiro, C.T. Chang, The elastic moduli of calcium hydroxide, Cement and Concrete Research 25(8) (1995) 1605-1609.

[3] P. Acker, Micromechanical analysis of creep and shrinkage mechanisms, in F.-J. Ulm, Z.P. Bažant and F.H. Wittmann, editors, Creep, Shrinkage and Durability Mechanics of Concrete and other quasi-brittle Materials, Cambridge, MA, August 2001 (Elsevier, Oxford UK, 2001) 15-25.

[4] C. Le Bellego, Couplage chimie-mécanique dans les structures en béton attaquées par l'eau: étude expérimentale et analyse numérique, PhD. Dissertation, ENS de Cachan, France, 2001.

[5] K. Velez, S. Maximilien, D. Damidot, G. Fantozzi, F. Sorrentino, Determination by nanoindentation of elastic modulus and hardness of pure constituents of Portland cement clinker, Cement and Concrete Research 31(4) (2001) 555-561.

[6] G. Constantinides, F.-J. Ulm, The effect of two types of C-S-H on the elasticity of cement-based materials: Results from nanoindentation and micromechanical modelling, Cement and Concrete Research 34 (2004) 67-80.

[7] G. Constantinides, F.-J. Ulm, The nanogranular nature of C–S–H. Journal of the Mechanics and Physics of Solids 55 (2007), 64-90.

[8] C.-J. Haecker, E.J. Garboczi, J.W. Bullard, R.B. Bohn, Z. Sun, S.P. Shah, T. Voigt, Modeling the linear elastic properties of Portland cement paste, Cement and Concrete Research 35 (2005) 1948-1960.

[9] J. Sanahuja, L. Dormieux, G. Chanvillard, Modelling elasticity of a hydrating cement paste, Cement and Concrete Research 37 (2007) 1427-1439.

[10] F.H. Heukamp, Chemomechanics of calcium leaching of cement-based materials at different scales: The role of CH-dissolution and C-S-H degradation on strength and durability performance of materials and structures, PhD Dissertation, Massachusetts Institute of Technology, (2003).

[11] F.H. Heukamp, F.-J. Ulm, J.T. Germaine, Mechanical properties of calcium-leached cement pastes ,Triaxial stress states and the influence of the pore pressure, Cement and Concrete Research 31 (2001) 767-774.

[12] F.H. Heukamp, F.-J. Ulm, J.T. Germaine, Poroplastic properties of calcium-leached cement-based materials, Cement and Concrete Research 33 (2003) 1155–1173.

[13] M.A. Biot, D.G. Willis, The elastic coefficients of the theory of consolidation, Journal of Applied Mechanics 24 (1957) 594-601.

[14] R.J.S. Brown, J. Korringa, On the dependence of the elastic properties of a porous rock on the compressibility of the pore fluid, Geophysics 40 (1975) 608-616.

[15] J.R. Rice, M.P. Cleary, Some basic stress diffusion solutions for fluid-saturated elastic porous media with compressible constituents, Review of geophysics and space physics 14 (2) (1976) 227-240.

[16] R.W. Zimmerman, Compressibility of sandstones, Elsevier Sci., Amsterdam, 1991.

[17] J.G. Berryman, Effective stress for transport properties of inhomogeneous porous rock, Journal of Geophysical Research 97 (1992) 17409-17424.

[18] E. Detournay, A.H.-D. Cheng, Fundamentals of Poroelasticity, Chap. 5 in Comprehensive Rock Engineering: Principles, Practice and Projects, Vol. II, Analysis and Design Method, ed. C. Fairhurst, Pergamon, (1993) 113-171.

[19] I. Vardoulakis, J. Sulem, Bifurcation Analysis in Geomechanics. Blackie Academic and Professional, 1995.

[20] O. Coussy, Poromechanics, John Wiley and Sons, 2004.

[21] S. Ghabezloo, J. Sulem, Stress dependent thermal pressurization of a fluid-saturated rock, Rock Mechanics and Rock Engineering 42(1) (2009) 1-24.

[22] R. Hill, The elastic behavior of crystalline aggregate, Proc. Physical Soc., London, A65 (1952) 349-354.

[23] P.A. Berge, J. G. Berryman, Realizability of Negative Pore Compressibility in Poroelastic Composites, Journal of Applied Mechanics 62(4) (1995) 1053-1062.

[24] P.A. Berge, Pore Compressiblity in Rocks, Biot Conference on Poromechanics, Louvain-la-Neuve, Belgium, September 14-16, 1998.

[25] R.W. Zimmerman, W.H. Somerton, M.S. King, Compressibility of porous rocks, Journal of Geophysical Research 91(B12) (1986) 12765-12777.

[26] A.W. Skempton, The Pore Pressure Coefficients A and B, Géotechnique 4 (1954) 143-147.

[27] K. Terzaghi, The shearing resistance of saturated soils and the angle between the planes of shear, First Int. Conf. Soil Mech., Vol. 1, Harvard Univ., Cambridge, Mass. (1936) 54-56.

[28] Y. Bernabé, The effective pressure law for permeability in Chelmsford granite and Barre granite, Int J Rock Mech Min Sci & Geomech Abstr 23-3 (1986) 267-275.

[29] T. Todd, G. Simmons, Effect of pore pressure on the velocity of compressional waves in low porosity rocks, Journal of Geophysical Research, 77 (1972) 3731-3743.

[30] B. Gurevich, A simple derivation of the effective stress coefficient for seismic velocities in porous rocks, Geophysics, 69 (2) (2004) 393-397.

[31] L. Dormieux, A. Molinari, D. Kondo, Micromechanical approach to the behavior of poroelastic materials, Journal of the Mechanics and Physics of Solids, 50 (2002) 2203-2231.

[32] M.J. Boutéca, D. Bary, J.M. Piau, N. Kessler, M. Boisson, D. Fourmaintraux, Contribution of Poroelasticity to Reservoir Engineering: Lab Experiments, Application to Core Decompression and Implication in HP-HT Reservoirs Depletion, Paper SPE/ISRM 28093 (1994).

[33] K.B. Coyner, Effects of stress, pore pressure, and pore fluids on bulk strain, velocity, and permeability in rocks. PhD thesis, Massachusetts Institute of Technology, Dept. of Earth, Atmospheric and Planetary Sciences, 1984.

[34] H.M. Jennings, J.J. Thomas, J.J. Chen, D. Rothstein, Cement as a Porous Materials, Chapter 6.11 in Handbook of Porous Solids, ed. F. Schuth, K. Sing, J. Weitkamp. Wiley-VCH, 5, 2971-3028, 2002.

[35] R.F. Feldman, P.J. Sereda, A model for hydrated Portland cement paste as deduced from sorption-length change and mechanical properties, Materials and Structures 1(6) (1968) 509-520.

[36] R.F. Feldman, Factors affecting young's modulus - porosity relation of hydrated portland cement compacts, Cement and Concrete Research 2 (4) (1972) 375-386.

[37] H.M. Jennings, A model for the microstructure of calcium silicate hydrate in cement paste, Cement and Concrete Research 30 (1) (2000) 101-116.

[38] H.M. Jennings, Refinements to colloid model of C-S-H in cement: CM-II, Cement and Concrete Research 38 (3) (2008) 275-289.

[39] H.F.W. Taylor, Cement chemistry, Thomas Telford, London, 1997.

[40] R.F. Feldman, Helium flow and density measurement of the hydrated tricalcium silicate-water system, Cement and Concrete Research 2 (1) (1972) 123-136.

[41] C. Gallé, Effect of drying on cement-based materials pore structure as identified by mercury intrusion porosimetry: A comparative study between oven-, vacuum-, and freeze-drying, Cement and Concrete Research 31 (10) (2001) 1467-1477.

[42] J. Sulem, H. Ouffroukh, Hydromechanical Behaviour of Fontainebleau Sandstone, Rock Mechanics and Rock Engineering 39 (3) (2006) 185-213.

[43] K. Kendall, A.J. Howard, J.D. Birchall, P.L. Pratt, B.A. Proctor, S.A. Jefferis, The Relation between Porosity, Microstructure and Strength, and the Approach to Advanced Cement-Based Materials, Philosophical Transactions of the Royal Society of London. Series A, Mathematical and Physical Sciences 310 (1511) (1983), 139-153.

[44] R.A. Helmuth and D.H. Turk, Elastic moduli of hardened Portland cement and tricalcium silicate pastes: effect of porosity, Symposium on Structure of Portland Cement Paste and Concrete (Special Report 90), Highway Research Board, Washington, D.C. (1966), pp. 135–144.

[45] L.J. Gibson, M.F. Ashby, Cellular Solids, Structure and Properties, Pergamon Press, 1988.

[46] Z. Hashin, S. Shtrikman, Note on a variational approach to the theory of elastic composite materials, J. Franklin Inst. 271 (1961) 336-341.

[47] G. Mesri, K. Adachi, C.R. Ulrich, Pore-pressure response in rock to undrained change in all-around stress. Géotechnique 26 (2) (1976), 317-330.

[48] D.H. Green, H.F. Wang, Fluid pressure response to undrained compression in saturated sedimentary rock, Geophysics 51 (4) (1986), 948-956.

[49] J.T. Fredrich, J.W. Martin, R.B. Clayton, Induced pore pressure response during undrained deformation of tuff and sandstone, Mechanics of Materials 20 (1995), 95-104.

[50] D.A. Lockner, S.A. Stanchits, Undrained poroelastic response of sandstones to deviatoric stress change. Journal of Geophysical Research 107 (B12) (2002), 2353.

[51] P.E. Stutzman, J.R. Clifton, Specimen preparation for scanning electron microscopy. In: Proceedings of the 21st International Conference on Cement Microscopy, Las Vegas (1999), 10-22.

[52] K.O. Kjellsen, A. Monsøy, K. Isachsen, R.J. Detwiler, Preparation of flat-polished specimens for SEM-backscattered electron imaging and X-ray microanalysis - importance of epoxy impregnation, Cement and Concrete Research 33 (2003) 611-616.

[53] S. Diamond, The microstructure of cement paste and concrete - a visual primer, Cement & Concrete Composites 26 (2004) 919–933.

3.3 Evolution de la perméabilité sous chargement isotrope

La perméabilité du ciment est une fonction du rapport w/c, du degré ou de la durée d'hydratation, de la température d'hydratation et du type du ciment. Breysse et Gérard (1997) ont fait des analyses statistiques sur les résultats de plusieurs essais de perméabilité publiés dans la littérature et ils ont proposé les relations suivantes pour la perméabilité des pâtes de ciment en fonction du rapport w/c et de la porosité ϕ:

$$\log k\left(\mathrm{m}^2\right) = 6{,}397\frac{w}{c} - 22{,}341 \tag{3-1}$$

$$\log k\left(\mathrm{m}^2\right) = 5{,}95\phi - 15{,}874 \tag{3-2}$$

Pour un rapport w/c égal à 0,44, l'ordre de grandeur de la perméabilité du ciment est estimé entre 10^{-19} et 10^{-20} m^2. Pour cette gamme de perméabilité, le temps nécessaire pour faire des mesures en régime permanent est très long. C'est pourquoi, on choisit d'évaluer la perméabilité en régime transitoire.

La perméabilité du ciment est influencée par deux phénomènes : D'une part le développement d'une microfissuration que nous avons observée dans les échantillons chargés sous contraintes isotropes et d'autre part la diminution de porosité résultant de la compaction de l'échantillon. La présence de microfissures telle que l'ont montrée les observations microscopiques peut conduire à une augmentation de la perméabilité. La compaction de l'échantillon sous la pression de confinement conduit au contraire à une diminution de la perméabilité. Ces différents phénomènes nécessitent le développement d'une méthode adaptée de mesure de la perméabilité du ciment. Cette méthode doit être réalisable pour toute la gamme de pressions de confinement utilisées dans les essais de compression isotropes, capable de prendre en compte le comportement poro-mécanique du ciment et la dépendance des modules en fonction de la contrainte effective, capable d'étudier l'effet des contraintes, des déformations, de l'endommagement et de la contraction de l'espace poreux, sur la perméabilité du ciment. De plus cette méthode doit pouvoir être mise en oeuvre sur une durée relativement courte.

C'est pourquoi, nous avons développé une méthode d'évaluation de la perméabilité en régime transitoire dans laquelle la surpression interstitielle générée dans un échantillon dans les essais non-drainés est utilisée. A la fin d'un essai non-drainé, la pression interstitielle initialement homogène à l'intérieur de l'échantillon est libérée à une extrémité de l'échantillon. Ceci impose un fort gradient de pression dans l'échantillon, ce qui provoque le drainage du fluide interstitiel vers l'extérieur de l'éprouvette. La pression interstitielle est mesurée à l'autre extrémité de l'échantillon et cette mesure est utilisée dans une analyse inverse permettant d'évaluer la perméabilité du ciment. Cette analyse est réalisée en prenant en compte les déformations élastiques de l'échantillon dues aux variations de la contrainte effective au cours de l'essai, et également les déformations différées de l'échantillon au cours de l'essai sous chargement isotrope. A cause de la variation de la perméabilité due aux déformations différées de l'échantillon au cours de l'essai, les résultats ne peuvent pas être analysés uniquement en terme des contraintes. Par conséquent les résultats sont analysés en terme de la variation de la porosité et permettent d'établir une relation perméabilité-porosité pour l'évolution de la perméabilité du ciment sous chargement isotrope. Cette relation perméabilité-porosité est présentée dans la forme d'une loi de puissance avec une puissance égale à 11, qui ne varie pas de façon significative avec les variations de

l'état des contraintes ou les déformations de fluage, et montre la diminution de la perméabilité de l'échantillon au cours de l'essai. Cette diminution de la perméabilité, malgré la génération des microfissures sous l'effet de chargement isotrope montre que la compaction de la matrice poreuse du ciment sous chargement isotrope a un effet sur la perméabilité plus important que la microfissuration, étant donné que les fissures peuvent rester fermées sous l'effet du chargement.

International Journal of Rock Mechanics & Mining Sciences 46 (2009) 761–768

Contents lists available at ScienceDirect

International Journal of Rock Mechanics & Mining Sciences

journal homepage: www.elsevier.com/locate/ijrmms

Evaluation of a permeability–porosity relationship in a low-permeability creeping material using a single transient test

Siavash Ghabezloo [a,*], Jean Sulem [a], Jérémie Saint-Marc [b]

[a] Université Paris-Est, UR Navier, CERMES, Ecole Nationale des Ponts et Chaussées, 6-8 avenue Blaise Pascal, Cité Descartes, 77455 Champs-sur-Marne, Marne la Vallée cedex 2, France

[b] TOTAL, Management of Residual Gases Project, Pau, France

Abstract

A method is presented for the evaluation of the permeability-porosity relationship in a low-permeability porous material using the results of a single transient test. This method accounts for both elastic and non-elastic deformations of the sample during the test and is applied to a hardened class G oil well cement paste. An initial hydrostatic undrained loading is applied to the sample. The generated excess pore pressure is then released at one end of the sample while monitoring the pore pressure at the other end and the radial strain in the middle of the sample during the dissipation of the pore pressure. These measurements are back analysed to evaluate the permeability and its evolution with porosity change. The effect of creep of the sample during the test on the measured pore pressure and volume change is taken into account in the analysis. This approach permits to calibrate a power law permeability-porosity relationship for the tested hardened cement paste. The porosity sensitivity exponent of the power-law is evaluated equal to 11 and is shown to be mostly independent of the stress level and of the creep strains.

Keywords: permeability, porosity, transient method, creep, hardened cement paste

1 Introduction

The evaluation of the permeability in the laboratory is basically an inverse problem. The two most widely used methods for evaluation of the permeability of geomaterials are the steady state method and the transient pulse method. The steady state method consists in applying a constant pressure gradient to the sample and measuring the resulted flow rate. The permeability of the sample is then calculated using Darcy's law. This method is particularly appropriate for high permeability materials. The transient pulse method is based on the evaluation of the decay of a small step change of pressure imposed in one end of a sample. This method, which was pioneered by Brace *et al*. [1], is appropriate for low permeability materials and is used extensively to evaluate the permeability of different geomaterials (e.g. Bernabé [2][3] on granite, Escoffier *et al*. [4] on mudstone). In the original setting of Brace *et al*. [1], a cylindrical sample is connected to two fluid reservoirs with equal pressures. A sudden increase of the fluid pressure in the upstream reservoir unbalances the system and causes a fluid flow from this reservoir, through the sample to the downstream reservoir in order to equilibrate the pressures in the sample and in the reservoirs. The permeability of the sample is then back analysed from the kinetics of the decay of the pressure in the upstream reservoir. Some alternative methods to evaluate the permeability of low permeability materials have been recently developed by monitoring the response of a saturated body to mechanical and thermal strains. Among them, the beam bending method [5][6][7] is based on the fact that bending of a saturated porous beam creates a pressure gradient in the pores, as the top half is in compression and the half bottom is in tension. This pressure gradient causes the fluid flow to equilibrate the pressure and consequently the force required to sustain a fixed deflection decreases. The permeability and also the elastic modulus of the body are evaluated by analysing the kinetics of force relaxation. Thermopermeametry is another method that is based on the analysis of thermal expansion kinetics [6][7][8]. The thermal expansion of water is higher than the one of solids, so a rapid temperature increase and then isothermal hold of a saturated porous body causes an initial dilation and pore fluid pressurization due to the greater expansion of the pore fluid. This initial dilation is then followed by a contraction of the body caused by the dissipation of the excess pore pressure and the fluid outflow. Analysis of the kinetics of thermal dilation yields the permeability of the body. Beam bending and thermopermeametry methods were originally developed for gels and later extended to more rigid materials like cement paste and mortar. Dynamic pressurization [9][10] is another permeability evaluation method which is performed on a sample that is enclosed in a vessel full of fluid under a constant pressure. In the initial state, the pressure in the vessel and the sample pore pressure are in equilibrium. A sudden increase of the pressure in the vessel causes an initial contraction of the sample. This contraction, when the pressure is kept constant, is followed by a time dependent dilation due to the progressive increase of the sample pore pressure to reach equilibrium with the pressure inside the vessel. The permeability is then evaluated by analysing the kinetics of the dilation of the sample.

One can see that these methods used for evaluation of transport properties of low permeability materials are based on the analysis of the kinetics of diffusion of pore pressure or the strains induced by pore pressure diffusion. The same principle is used in this work for the evaluation of the permeability of a hardened cement paste. The test method used here is similar to the one presented by Hart and Wang [11] as a single test method for evaluation of poroelastic constants and flow parameters of low permeability rocks. These authors used the excess pore pressure generated in a sample due to an undrained loading for the evaluation of the permeability. The pressure at one side of the sample is

connected to a reservoir with a constant volume and the kinetics of the pore pressure variations at the other end of the sample and in the reservoir is analysed for evaluation of the permeability.

Our experimental study for the evaluation of the permeability of a hardened cement paste is a part of a larger study on the thermo-poro-mechanical behaviour of this material for petroleum applications. Indeed, in oil wells, a cement sheath is placed between the rock and the casing for support and sealing purpose. The cement lining is submitted to various thermal and mechanical loadings during the life of the well from the drilling phase to the production phase and finally in the abandonment phase when the well must seal the subsurface from the surface, as for instance for storage and sequestration of greenhouse gas. In due course of these actions, the cement can be damaged and the mechanical and transport properties can be degraded, this degradation being detrimental to its functions. Moreover, the determination of the permeability of this cement over time is essential for the prediction of the sealing performance of the well when CO_2 storage and sequestration is planned. The results of our previous experimental study including drained and undrained hydrostatic compression tests, unjacketed tests and drained and undrained heating tests have been presented in Ghabezloo *et al*. [12][13].

By applying an undrained hydrostatic loading, an excess pore pressure is generated inside the sample, related to the applied hydrostatic stress by the Skempton coefficient of the material. At the end of the hydrostatic loading phase, a constant pore pressure much lower than the existing pore pressure inside the sample is applied at one end of the sample. Under this pressure boundary condition, the pore fluid flows out of the sample and the pore pressure decreases. The pore pressure change at the other end of the sample and the radial strain in the middle of the sample are both measured as functions of time and back analysed to evaluate the permeability. During the test, the pore pressure in the sample varies greatly from one end to another. This variable pore pressure keeping the confining pressure constant, induces a variable effective stress in the sample and results in a heterogeneous strain field. The stress-dependent character of the poroelastic parameters of the hardened cement paste (Ghabezloo *et al*. [12]) and also the creep of the material during the test add some particular aspects to the back-analysis, which makes this problem different from the classical solutions of transient permeability evaluation tests. The porosity changes due to the increase of the effective stress and also the presence of additional creep deformations induce a decrease of the permeability during the test. The coupled measurement of pore pressure and deformations during the test is back analysed to evaluate the permeability-porosity relationship using the results of a single transient test.

It is well-known that there is no unique permeability-porosity relationship that can be applied to all porous materials. As mentioned by Bernabé *et al*. [14], one reason is that the porosity is a scale invariant material property; if the material and its pore space could be uniformly expanded or contracted everywhere, there would be no change in the porosity, but the permeability would change in this case. Moreover, different pores in a given material have different contributions to the permeability of the material according to their size and shape. The porosity takes into account only the relative volume of the pores to the total volume, and not the shape and the distribution of the size of the pores. Thus two porous materials with the same porosity, but different pore shape and pore-size distributions, must have different permeabilities. For a given evolution process that changes both permeability and porosity of a porous material, for example elastic or plastic compaction, microcracking or chemical alteration, it is usually assumed that there is a power-law relationship $k \propto \phi^{\alpha}$ between these parameters (Bernabé *et al*. [14]). The exponent of this relation may be integer or non-integer, constant or variable, according to the properties of the material and of the evolution process. Based on the experimental data of Bernabé *et al* [15], Walder and Nur [16] postulated a slightly different power-law in which the permeability vanishes

at a critical non-zero porosity. David *et al*. [17] presented a compilation of published data on the permeability-porosity relationships for different geomaterials. One can see that the reported values of exponent α vary between 1.1 and 25.4 for different materials and the higher values correspond in general to rocks with a high porosity. However, no clear correlation between α and the petrophysical properties could be found. Experimental study of Zhu and Wong [18] on Berea and Boise sandstones resulted in a variable α which increases when pressure increases. Meziani [19] performed an experimental study on the gas permeability of mortar under hydrostatic loading and found a strongly non-linear permeability-porosity relationship. The exponent α is found to be a decreasing function of the loading level, decreasing from 36 to 26 when the confining pressure is increased up to 57 MPa. Based on an idea presented by Bernabé *et al*. [14], the total porosity of the rock can be separated into two categories of effective and non-effective porosity according to the contribution of the pores in the fluid transport. These two quantities are not purely geometrical and depend on the fluid velocity field. These authors propose that the exponent α is related to the ratio of the effective to non-effective porosity and its variation during an evolution process so that α is dependent upon the particular physical process of porosity evolution and the pore geometry of the material. Consequently as emphasized by Bernabé *et al*. [14], searching a permeability-porosity relationship is meaningful either for a given rock sample during a porosity evolution process, for example elastic compaction, or for different rock samples only if these samples correspond to different stages of the same evolution process.

2 Poromechanical background

We present here the framework used to describe the response of the sample during the performed test. The equations are written for a porous material which is not necessarily homogeneous and isotropic at the micro-scale. The theoretical basis of the formulation has been presented in many earlier studies. Among them, one can refer to the milestone papers and textbooks of Biot and Willis [22], Brown and Korringa [23], Rice and Cleary [24], Zimmerman [25], Detournay and Cheng [26], Vardoulakis and Sulem [27], Wang [28], Coussy [29]. This framework is recalled here in a comprehensive manner in order to clarify the mathematical and physical significance of the different parameters used in the analysis and also to take into account the effect of non-elastic strains in the evaluation of the permeability.

2.1 Poroelastic formulation

The porosity ϕ of a porous material is defined as the ratio of the volume of the porous space V_ϕ to total volume V in the actual (deformed) state:

$$\phi = \frac{V_\phi}{V} \tag{1}$$

We consider a saturated sample under an isotropic state of stress σ (positive in compression) and we define the differential pressure σ_d (i.e. Terzaghi effective stress) as the difference between the confining pressure σ and the pore pressure p_f.

$$\sigma_d = \sigma - p_f \tag{2}$$

The variations of the total volume V and of the pore volume V_ϕ are given in the following expressions as a function of variations of two independent variables, σ_d and p_f:

$$\frac{dV}{V} = -\frac{d\sigma_d}{K_d} - \frac{dp_f}{K_s}$$
$$\frac{dV_\phi}{V_\phi} = -\frac{d\sigma_d}{K_p} - \frac{dp_f}{K_\phi} \quad (3)$$

Where K_d, K_s, K_p and K_ϕ are four elastic moduli defined below:

$$\frac{1}{K_d} = -\frac{1}{V}\left(\frac{\partial V}{\partial \sigma_d}\right)_{p_f} \quad , \quad \frac{1}{K_p} = -\frac{1}{V_\phi}\left(\frac{\partial V_\phi}{\partial \sigma_d}\right)_{p_f} \quad (4)$$

$$\frac{1}{K_s} = -\frac{1}{V}\left(\frac{\partial V}{\partial p_f}\right)_{\sigma_d} \quad , \quad \frac{1}{K_\phi} = -\frac{1}{V_\phi}\left(\frac{\partial V_\phi}{\partial p_f}\right)_{\sigma_d} \quad (5)$$

Equation (4) corresponds to an isotropic drained compression test in which the pore pressure is kept constant inside the sample. The variations of the total volume of the sample V and of the volume of the pore space V_ϕ with the applied confining pressure give respectively the drained bulk modulus K_d and the modulus K_p. Equation (5) corresponds to the unjacketed compression test, in which equal increments of confining pressure and pore pressure are simultaneously applied to the sample. The differential pressure σ_d in this condition remains constant. The variation of the volume of the sample with respect to the applied pressure gives the unjacketed modulus K_s. The variation of the pore volume of the sample in this test could in principle be used to evaluate the modulus K_ϕ. However experimental evaluation of this parameter is very difficult as the volume of the fluid exchanged between the sample and the pore pressure generator has to be corrected for the effect of fluid compressibility, and also for the effect of the deformations of the pore pressure generator and of the drainage system in order to access to the true variation of the pore volume of the sample. In the case of a porous material which is homogeneous and isotropic at the micro-scale $K_s = K_\phi = K_m$, where K_m is the bulk modulus of the single solid constituent of the porous material. In the case of a porous material which is composed of two or more solids and therefore is heterogeneous at the micro-scale, the unjacketed modulus K_s is some weighted average of the bulk moduli of solid constituents [30]. The modulus K_ϕ for such a material has a complicated dependence on the material properties. Generally it is not bounded by the elastic moduli of the solid components and can even have a negative sign if the bulk moduli of the individual solid components are greatly different one from another [31][32]. From Betti's reciprocal theorem, the following relation holds between the elastic moduli [23][33]:

$$\frac{1}{K_p} = \frac{1}{\phi}\left(\frac{1}{K_d} - \frac{1}{K_s}\right) \quad (6)$$

Using equation (6), the number of the required parameters to characterize the volumetric poro-elastic behaviour of a porous material is reduced to three, and among them, the experimental evaluation of the modulus K_ϕ is very difficult. Using the definition of the porosity presented in equation (1), the following equation is obtained for the variation of the porosity:

$$\frac{d\phi}{\phi} = \frac{dV_\phi}{V_\phi} - \frac{dV}{V} \quad (7)$$

Replacing equation (3) and then equation (6) in equation (7), the expression of the variation of porosity is found:

$$\frac{d\phi}{\phi} = -\frac{1}{\phi}\left(\frac{1-\phi}{K_d} - \frac{1}{K_s}\right)d\sigma_d + \left(\frac{1}{K_s} - \frac{1}{K_\phi}\right)dp_f \tag{8}$$

As shown by Hart and Wang [34], for the case of the axisymmetric triaxial test, the transient pore pressure can be approximated by the solution obtained for the one-dimensional diffusive flow except at early times for which the fully coupled poroelastic response includes also radial flow. Thus, for the analysis of the test results, the one-dimensional solution is used in the following.

Consider now an elementary volume with the z axis parallel to flow direction, q the fluid mass flux per surface area S (orthogonal to z) and M_f the total fluid mass inside the volume. Fluid mass conservation implies that:

$$\frac{1}{V}\frac{dM_f}{dt} + \frac{\partial q}{\partial z} = 0 \tag{9}$$

Let's define m_f as the fluid mass per unit volume of the porous material, $m_f = M_f / V = \rho_f \phi$. The variations of m_f is written as:

$$\frac{dm_f}{dt} = \frac{1}{V}\frac{dM_f}{dt} - \frac{M_f}{V}\frac{dV/V}{dt} \tag{10}$$

Replacing equation (10) in equation (9) we obtain:

$$\frac{dm_f}{dt} + m_f\frac{dV/V}{dt} + \frac{\partial q}{\partial z} = 0 \tag{11}$$

Knowing that $m_f = \rho_f \phi$ we can write $dm_f = \phi d\rho_f + \rho_f d\phi$. Replacing $d\rho_f = \rho_f dp_f / K_f$ and equation (7) in this relation we obtain:

$$dm_f = \phi\rho_f\frac{dp_f}{K_f} + \phi\rho_f\left(\frac{dV_\phi}{V_\phi} - \frac{dV}{V}\right) \tag{12}$$

Inserting equation (12) and $m_f = \rho_f \phi$ in equation (11) the following expression is obtained:

$$\phi\rho_f\left(\frac{1}{K_f}\frac{dp_f}{dt} + \frac{dV_\phi/V_\phi}{dt}\right) + \frac{\partial q}{\partial z} = 0 \tag{13}$$

Replacing equation (3) and then equation (6) in equation (13) the following relation is found for the case of $d\sigma = 0$:

$$\rho_f\left[\phi\left(\frac{1}{K_f} - \frac{1}{K_\phi}\right) + \left(\frac{1}{K_d} - \frac{1}{K_s}\right)\right]\frac{dp_f}{dt} + \frac{\partial q}{\partial z} = 0 \tag{14}$$

The fluid mass flux q in equation (14) is given by Darcy's law:

$$q = -k\frac{\rho_f}{\mu_f}\frac{\partial p_f}{\partial z} \tag{15}$$

where k is the permeability and μ_f is the fluid viscosity. Replacing equation (15) in equation (14) the following expression is obtained:

$$\frac{dp_f}{dt} = \frac{\beta_u}{\rho_f}\frac{\partial}{\partial z}\left(k\frac{\rho_f}{\mu_f}\frac{\partial p_f}{\partial z}\right) \tag{16}$$

where:

$$\beta_u = \frac{1}{\phi\left(1/K_f - 1/K_\phi\right) + \left(1/K_d - 1/K_s\right)} \tag{17}$$

2.2 Effect of non-elastic strains

The above framework can be extended to account for the effect of non-elastic strains which can be produced during the test. These strains can be plastic, viscoelastic or viscoplastic and induce non-elastic porosity changes. The non-elastic changes of the total volume, pore volume and solid volume are defined by:

$$dV^{ne} = dV - dV^e \; ; dV_\phi^{ne} = dV_\phi - dV_\phi^e \; ; dV_s^{ne} = dV_s - dV_s^e \tag{18}$$

The non-elastic increment of pore volume dV_ϕ^{ne} can be calculated from the definition of the porosity (equation (1)) and knowing that $V_\phi = V - V_s$.

$$dV_\phi^{ne} = dV_\phi - dV_\phi^e = V\left[-d\varepsilon^{ne} + (1-\phi)d\varepsilon_s^{ne}\right] \tag{19}$$

From (19) we obtain:

$$\frac{dV_\phi^{ne}}{V_\phi} = \frac{-1}{\phi}\left[d\varepsilon^{ne} - (1-\phi)d\varepsilon_s^{ne}\right] \tag{20}$$

Using equation (20), equation (3) is re-written with the additional contribution of the non-elastic volume changes:

$$\begin{aligned} -\frac{dV}{V} &= \frac{d\sigma_d}{K_d} + \frac{dp_f}{K_s} + d\varepsilon^{ne} \\ -\frac{dV_\phi}{V_\phi} &= \frac{d\sigma_d}{K_p} + \frac{dp_f}{K_\phi} + \frac{d\varepsilon^{ne}}{\phi} - \frac{1-\phi}{\phi}d\varepsilon_s^{ne} \end{aligned} \tag{21}$$

Using equations (7) and (21) the following relation is obtained for the variations of the porosity:

$$\frac{d\phi}{\phi} = -\frac{1}{\phi}\left(\frac{1-\phi}{K_d} - \frac{1}{K_s}\right)d\sigma_d + \left(\frac{1}{K_s} - \frac{1}{K_\phi}\right)dp_f - \frac{1-\phi}{\phi}\left(d\varepsilon^{ne} - d\varepsilon_s^{ne}\right) \tag{22}$$

Replacing equation (21) and then equation (6) in equation (13) the following relation is found for the case of $d\sigma = 0$:

$$\rho_f\frac{dp_f}{dt}\left[\phi\left(\frac{1}{K_f} - \frac{1}{K_\phi}\right) + \left(\frac{1}{K_d} - \frac{1}{K_s}\right)\right] - \rho_f\frac{d\varepsilon^{ne} - (1-\phi)d\varepsilon_s^{ne}}{dt} + \frac{\partial q}{\partial z} = 0 \tag{23}$$

Replacing equations (15) and (17) in equation (23) the following expression is found:

$$\frac{dp_f}{dt} - \beta_u\frac{d\varepsilon^{ne} - (1-\phi)d\varepsilon_s^{ne}}{dt} = \frac{\beta_u}{\rho_f}\frac{\partial}{\partial z}\left(k\frac{\rho_f}{\mu_f}\frac{\partial p_f}{\partial z}\right) \tag{24}$$

If the non-elastic strains of the solid phase are neglected with respect to the total non-elastic strains, which is a common assumption for most geomaterials, equation (24) can be simplified in the following form:

$$\frac{dp_f}{dt} - \beta_u \frac{d\varepsilon^{ne}}{dt} = \frac{\beta_u}{\rho_f} \frac{\partial}{\partial z}\left(k \frac{\rho_f}{\mu_f} \frac{\partial p_f}{\partial z} \right) \tag{25}$$

3 Experimental program

A class G oil well cement is used to prepare the cement paste with a water to cement ratio $w/c = 0.44$. The fresh paste is conserved in 14cm cubic moulds for four days in lime saturated water at 90°C temperature. This temperature is chosen in order to reproduce the curing conditions of a cement lining installed in a deep oil well. After four days the temperature is gradually reduced in order to prevent any cracking of the blocs due to a sudden temperature change. Then, the blocs are cored and cut to obtain cylindrical samples with 38 mm diameter and 76 mm length. The two ends of the cylindrical samples are rectified to obtain planar surfaces perpendicular to the axis. After the sample preparation phase, the samples are cured for at least three months in a bath containing a chemically neutral solution towards the cement paste under a controlled temperature of 90°C. Before performing a test, the temperature of the sample is reduced slowly to prevent any thermal cracking. The porosity of the studied cement paste was evaluated by mercury intrusion porosimetry to be equal to $\phi = 0.26$. More details about the preparation of the samples can be found in Ghabezloo *et al*. [12].

The triaxial cell used in this study can sustain a confining pressure up to 60 MPa. It contains a system of hydraulic self-compensated piston. The loading piston is then equilibrated during the confining pressure build up and directly applies the deviatoric stress. The axial and radial strains are measured directly on the sample inside the cell with two axial transducers and four radial ones of LVDT type. The confining pressure is applied by a servo controlled high pressure generator. Hydraulic oil is used as confining fluid. The pore pressure is applied by another servo-controlled pressure generator with possible control of pore volume or pore pressure. More details on this triaxial equipment are found in Sulem and Ouffroukh [20] and in Ghabezloo and Sulem [21].

After the curing period the samples which are stored in a fluid at 90°C can be considered as completely saturated. The process of installing the sample inside triaxial cell may cause a partial de-saturation of the sample. For this reason a seven days re-saturation phase is performed inside the triaxial cell. During this period, the sample is maintained under a confining pressure equal to 1.2MPa and a back fluid pressure equal to 1.0MPa is applied to the sample while the volume of the fluid injected in the sample is monitored.

As explained earlier, the present permeability test is performed after an undrained hydrostatic compression test and uses the induced excess pore pressure inside the sample for the evaluation of the permeability. One can see several advantages in this method. First it gives access to the permeability of the sample under different states of stress (including high levels of stress and pore pressure) with a single test and gives thus an estimate of the porosity permeability relationship. Moreover, in creeping materials with low permeability, the standard tests cannot give accurate information on the short-term behaviour but only allows an estimation of the long-term permeability. An other marginal advantage is that one high capacity pressure generator for the application of the confining pressure and a low capacity one for the saturation process and the application of the pore pressure at one end of the sample are needed, while, in a conventional permeability test two additional high capacity pressure generators are

needed for application and control of the pore pressure at the ends of the sample. The undrained loading is performed using a loading rate equal to 0.1MPa/min. This loading rate is slow enough to ensure the homogeneity of the generated pore pressure inside the sample. After the undrained loading phase, the pore pressure at one end of the sample is reduced instantaneously to a low value (1.0MPa) which causes a fluid flow out of the sample. The other end the drainage system is closed and the pore pressure is monitored using a pore pressure transducer. The volume of the drainage and pressure measurement system at the closed side of the sample influences the measurement of the pore pressure. In our triaxial cell the total volume of the drainage system for an undrained loading is equal to 2300mm^3 which is a relatively small volume. 400mm^3 of this volume is connected to the lower side of the sample and the remaining 1900mm^3 is connected to the upper side. In order to minimize the effect of the dead volume of the drainage system, the fluid flow is established at the upper side which has a greater dead volume and the pressure measurement is performed at the lower side which has a smaller dead volume. Comparing this small dead volume (400mm^3) to the volume of the pore space of the sample (22410mm^3), one can see that the correction of the pore pressure measurement as derived in Ghabezloo and Sulem [21] can be neglected.

The instantaneous reduction of the pore pressure at the upper end of the sample causes a high pressure gradient and a flow of the pore fluid out of the sample. The gradual decrease of the pore pressure inside the sample, while the confining pressure is kept constant, increases the effective stress in a non-uniform manner along the height of the sample which results in non-uniform deformations. Depending on the nature of the tested material and on the magnitude of effective stress change, these deformations may include a non-elastic part. Non-elastic strains have a significant effect on the response of the sample and should be taken into account in the analysis of the test results. During the test, the radial deformations are measured using four LVDT transducers in the middle of the sample. These measured deformations along with the pore pressure measurements are used in the back analysis of the permeability as shown in the next section.

Three permeability tests (A, B and C) were performed. The test results are presented on Figure (1) where the pore pressure measured at the lower end of the sample and the radial strain measured in the middle of the sample are plotted as functions of time. The three tests correspond to different confining pressures and different initial pore pressure inside the sample. Tests B and C have been performed on the same sample. At the end of the test B the sample is unloaded in drained condition and then reloaded in undrained condition up to 50MPa, then test C is performed. One can see in Figure (1) that for all the tests the rate of pore pressure decrease reduces significantly after about 7 hours. One can also observe that despite the small change of effective stress after 7 hours, the measured strains continue to increase significantly. This phenomenon may be attributed to the creep of the hardened cement paste under the applied effective stress.

4 Analysis of the results

The results obtained in the performed test are back analysed to evaluate the permeability of the sample and its changes during the test. The analysis is performed using equation (25) which takes into account the effect of non-elastic strains produced during the test. As one can see in this equation, the poroelastic properties of the tested material must be known to evaluate the β_u parameter (equation (17)). The results of a previous experimental study on the poromechanical behaviour of the considered hardened cement paste are presented in Ghabezloo *et al*. [12]. The unjacketed modulus K_s was evaluated equal to 21GPa. Several drained hydrostatic compression tests revealed the stress dependency

of the drained bulk modulus K_d of the hardened cement paste. The test results showed the degradation of the elastic bulk modulus with the effective stress increase:

$$K_d = 8.69 - 0.087\sigma_d \qquad \left(K_d : \text{GPa}, \sigma_d : \text{MPa}\right) \tag{26}$$

The microscopic observation of the samples after the drained tests showed that this damage phenomenon is caused by the micro-cracking of the hardened cement paste, even under hydrostatic loading, which can be attributed to the heterogeneity of the microstructure of this material. The parameter K_ϕ, as explained above, is very difficult to evaluate and is commonly taken equal to the unjacketed modulus K_s. It can be shown that the deviation of this parameter from the unjacketed modulus K_s does not have a great influence on the poromechanical formulations (Zimmerman *et al.*, [33]). The physical parameters of pore fluid, ρ_f, μ_f and K_f are taken equal to the ones of pure water and their variations with pore pressure are taken into account (Spang [35]).

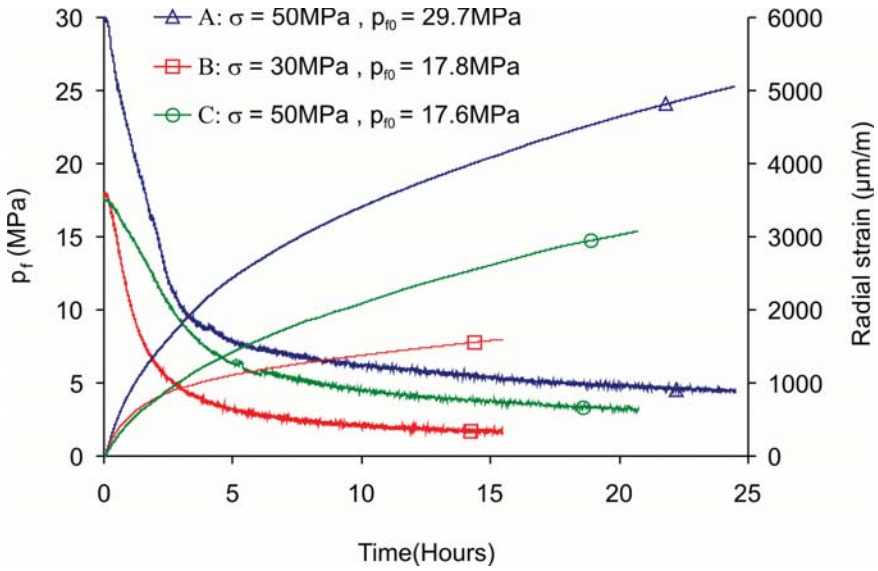

Figure 1- Results of the permeability tests: Evolution of the pore pressure measured at the lower end of the sample and of the radial strain measured at the middle of the sample during the test.

The elastic strains due to the variations of the pore pressure can be calculated easily using equation (3). The LVDTs measurements give the radial deformations in the middle of the sample. The measured radial strains are decomposed into an elastic and a non-elastic part. Due to the non-uniformity of the pore pressure, different points of the sample undergo different deformation. In order to estimate these strains in all points of the sample a constitutive law must be assumed for the non-elastic part of the strains. The parameters of this model are calibrated from the strains measured in the middle of the sample. Here we assume that the non-elastic part of the strains is of viscoelastic type and we choose a simple model, composed of a system of parallel spring and dashpot. We also assume that the creep rate is controlled by Terzaghi effective stress (i.e. differential pressure σ_d).

$$\frac{d\varepsilon^{ne}}{dt} = a\left(b\sigma_d - \varepsilon^{ne}\right) \tag{27}$$

In equation (27), a and b are two model parameters; $(ab)^{-1}$ is the viscosity and b is the compressibility of the underlying dashpot and spring model. It should be noted at this point that, as the tested samples have experienced different loading paths before the permeability tests, their creep behaviour may be different so that a and b should be calibrated for each test.

The variations of the stress state and also the deformations of the sample during the test can modify its permeability. In order to evaluate and take into account the variation of the permeability during the test, we can assume that the permeability varies either with the stress state or with the porosity changes. Assuming that the permeability is controlled by the stress state is appropriate if the deformation process is elastic. In that case, an appropriate effective stress law for the variation of the permeability has to be established, as explained in Ghabezloo *et al*. [36]. On the other hand, for a material which exhibits time-dependent deformation, such an assumption is not appropriate as for example, the permeability changes during a creep test due to the deformation process whereas the stress state remains constant. Thus, for complex deformation process, empirical permeability-porosity laws are commonly used. We choose here a power law $k/k_0 = \left(\phi/\phi_0\right)^{\alpha}$, so that we can write:

$$\frac{dk}{k} = \alpha \frac{d\phi}{\phi} \tag{28}$$

As mentioned before, the coefficient α may be constant or variable, integer or non-integer, according to the properties of the material and of the evolution process. For the sake of simplicity, in the back analysis of the results a constant integer coefficient is assumed. The exponent α and the initial permeability k_0 are evaluated in the back analysis of the experimental results. Before the beginning of the permeability evaluation test, the permeability of the sample is first modified by the applied undrained loading. The undrained test performed on this sample with three unloading-reloading cycles at different levels of confining pressure, as presented in Ghabezloo *et al*. [12], does not show any irreversible strains in unloading. Consequently the variations of the sample porosity caused by the applied undrained loading can be easily evaluated using equation (8) by knowing the final values of confining pressure and pore pressure. The initial porosity is equal to $\phi_0 = 0.26$ and the drained bulk modulus K_d is calculated using equation (26) for the average effective stress during the undrained loading. Using these parameters, the porosity change and the resulting permeability change caused by the initial undrained loading can be evaluated (equation (28)).

The back analysis of the test results using equation (25) is performed using a finite difference numerical scheme. The first analysis is performed on test A. The parameters a and b, the exponent α and the initial permeability k_0 are evaluated using the least square method. The error between the computed results and the measured data is calculated as the sum of errors corresponding to the pore pressure and the radial strain. For each iteration, the parameters are changed manually and the sum of square of the difference between the measured and the calculated values is calculated on a set of points. The best fitting parameters are then evaluated by minimizing the calculated error. For the test A the following parameters are found: $a = 2\times10^{-5}\,\mathrm{s}^{-1}$, $b = 3.2\times10^{-4}\,\mathrm{MPa}^{-1}$, $\alpha = 11$ and $k_0 = 1.07\times10^{-19}\,\mathrm{m}^2$. The results of the numerical simulation together with the experimental data are presented in Figure (2). One can see that the measured radial strains are well reproduced in the simulation using the assumed viscoelastic model and the calibrated parameters. The measured pore pressure at the lower end of the sample is also well reproduced by the model.

The variation of calculated permeability at the centre of the sample during the test is presented in Figure (3). One can see an initial permeability reduction from $1.07\times10^{-19}\,\mathrm{m}^2$ to $1.03\times10^{-19}\,\mathrm{m}^2$ under the effect of the initial undrained loading followed by a progressive reduction to $6.34\times10^{-20}\,\mathrm{m}^2$ at the end of the test. We observe that the undrained loading phase does not modify much the permeability of the sample. By doing this analysis we obtain a permeability porosity relationship for the tested sample using the results of a single transient test under the following form:

$$k = 1.07 \times 10^{-19} \left(\frac{\phi}{0.26} \right)^{11} \tag{29}$$

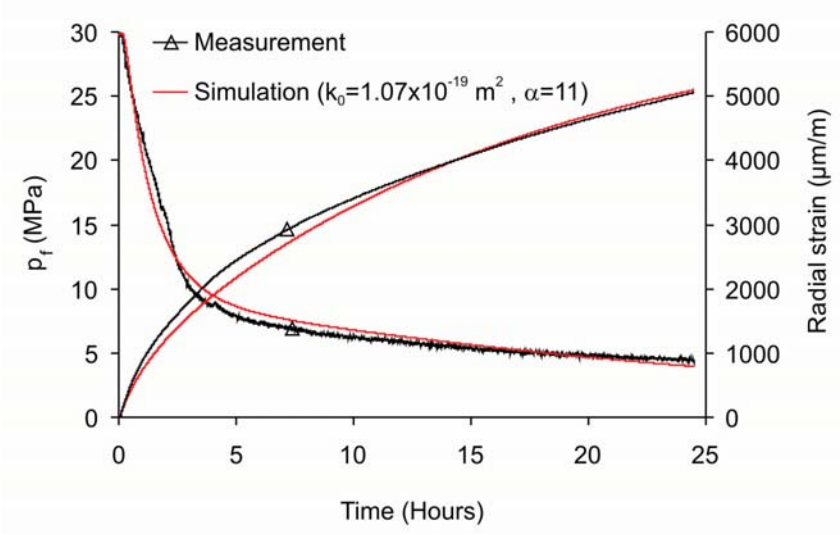

Figure 2- Test A: Test results and numerical simulation.

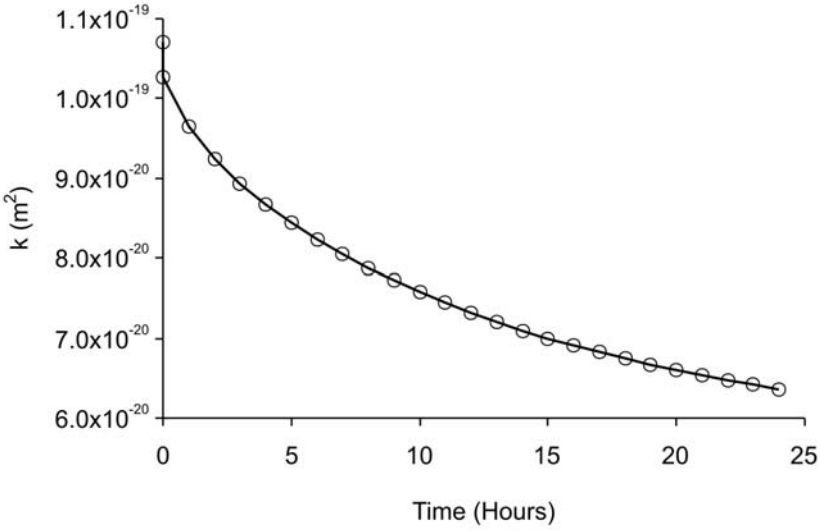

Figure 3- Test A: Evolution of the calculated permeability at the centre of the sample.

The above computation takes into account both the effect of non-elastic deformation and the effect of permeability change with porosity. In order to investigate separately these two effects, two additional simulations are performed. In the first one, the analysis is performed by neglecting the effect of non-elastic strains during the test and by considering a constant permeability (case 1). In the second one, the effect of non-elastic strains is taken into account, keeping a constant permeability (case 2). For each case the required parameters are evaluated using the least square algorithm. The results are presented on the Figure (4) and compared with the results of the complete model (case 3). For case 1, significant differences between the experimental results and the computed ones are observed. Especially the important difference between the measured and the calculated radial strain shows that it is essential to take into account the effect of non-elastic strains in the analysis of the test results. The results of case 2 show that an acceptable response can be obtained by considering the effect of non-elastic strains even with a constant permeability. Case 3 is identical to the analysis presented on Figure (2) and results in an even better compatibility with the experimental results in particular for the permeability curve in the last part of the test. For case 2, a constant permeability is evaluated equal to $8.30 \times 10^{-20}\,\mathrm{m}^2$ and can be seen

as an average permeability of the deforming sample during the test. The relatively small difference between the results of case 2 and case 3 is due to the small reduction of the porosity and consequently of the permeability of the sample during the test (Figure (3)).

Two main physical mechanisms occur in the course of the loading process, micro-cracking as mentioned above and compaction. The reduction of the permeability during the test shows that the compaction process is dominant and that the net result of these two mechanisms is a reduction of the permeability. Moreover, one can infer that the induced micro-cracks remain closed under stress and do not influence the permeability significantly.

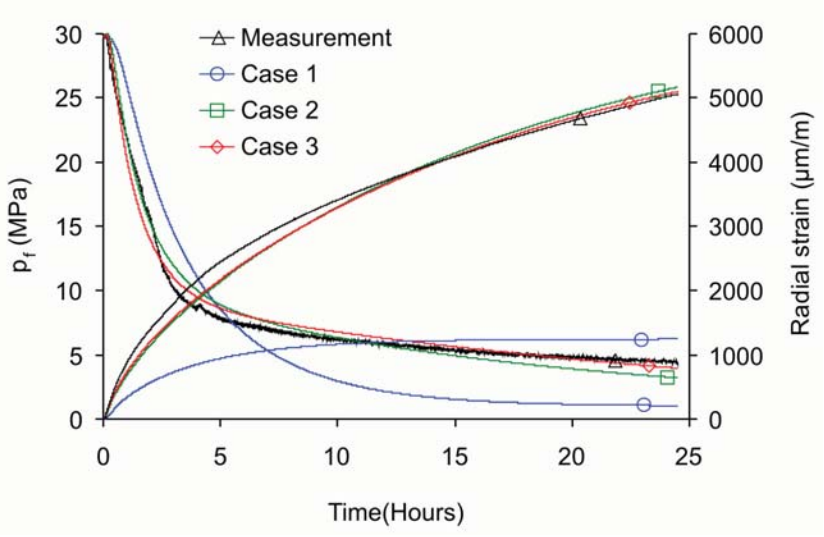

Figure 4- Test A: Effect of non-elastic strains and porosity dependent permeability: Case 1: Elastic solution, constant permeability; Case 2: Non-elastic solution, constant permeability; Case 3: Non-elastic solution, porosity dependent permeability.

For the analysis of the results of the tests B and C we assume that the coefficient α is only a function of the compaction process and consequently is the same for all tests, equal to 11. For each of the tests B and C, the coefficients a and b of equation (27) and the initial permeability k_0 are evaluated to find the best accordance between the simulation and the test results. For test B the following parameters are found: $a = 4.1\times10^{-5}\,\mathrm{s}^{-1}$, $b = 1.3\times10^{-4}\,\mathrm{MPa}^{-1}$ and $k_0 = 1.20\times10^{-19}\,\mathrm{m}^2$. For this sample we thus obtain the following permeability law:

$$k = 1.20\times10^{-19}\left(\frac{\phi}{0.26}\right)^{11} \tag{30}$$

At the end of this test, the permeability of the node at the centre of the sample is $1.02\times10^{-19}\,\mathrm{m}^2$. As mentioned above, this sample is then unloaded in drained condition and test C is performed on the same specimen. For test C the evaluated parameters are: $a = 2.4\times10^{-5}\,\mathrm{s}^{-1}$, $b = 1.8\times10^{-4}\,\mathrm{MPa}^{-1}$ and $k_0 = 9.40\times10^{-20}\,\mathrm{m}^2$. As expected, the initial permeability of the sample calculated for test C is very close to the final permeability of the sample in test B which gives confidence in the approach. The results are presented in Figures (5) and (6) where a good compatibility between the simulation and the test results can be observed. In Figure (6) a small pore pressure increase can be observed in the beginning of the test C in the results of the numerical simulation. Due to the high value of the initial effective stress in this test (32.4MPa) and also the low permeability of the sample, in the beginning of the test the effect of the creep deformations is more important than the effect of the pore pressure diffusion. This explains the small initial pore pressure increase obtained in the simulation.

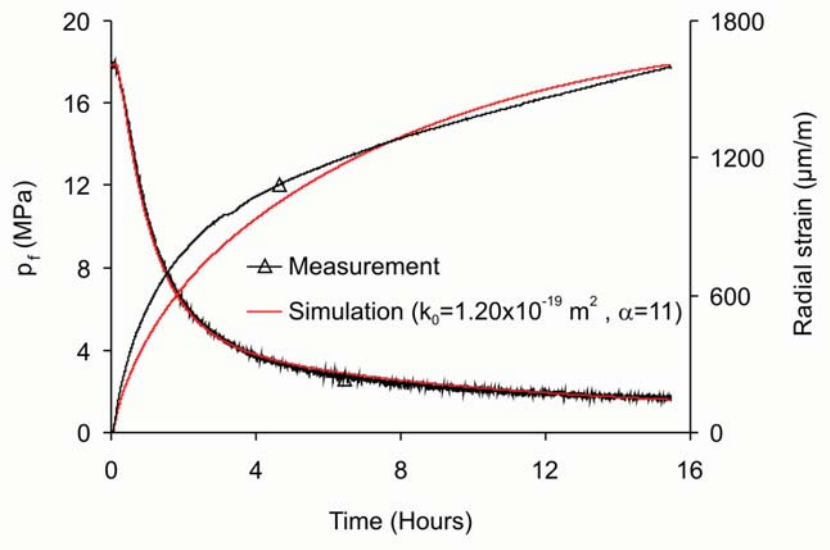

Figure 5- Test B: Test results and numerical simulation.

The evaluated value of the porosity sensitivity exponent α, equal to 11, is a relatively high value comparing with the range of variations of α for other geomaterials. Such a high value of α is usually attributed to a pore structure containing relatively large, pressure-insensitive nodal pores connected to each other by narrow pressure-sensitive throats (Bernabé *et al*. [14]) or to a pore structure in which pocket-like pores contribute much to the porosity and little to the permeability (David *et al*. [17]). This latter description seems to be mostly appropriate for the case of a permeability-porosity relationship which is established for different samples of a porous material with different porosities. Based on the idea of Bernabé *et al*. [14], a high value of α means that as a result of the compaction process, the reduction of the effective porosity is more important than the reduction of the non-effective porosity, or that some part of the effective porosity is transformed into non-effective porosity. We have shown that for two samples of a given material, the permeability evolves with the porosity with the same value of α, mostly independently of the level of effective stress or creep deformations in the three performed tests. This shows that in the absence of a difference between the pore shape and geometry of the samples, the permeability variation is controlled by the process of porosity evolution, which is the same in the different tests. This result is in accordance with the idea of Bernabé *et al*. [14], as explained here above.

The obtained permeability-porosity relationship with an exponent α equal to 11 should not be seen as a general permeability-porosity law for cement paste but specific to the cement used in this study and to the specific hydrostatic compaction process. This relation could in principle be combined with other empirical relationships found in the literature which describe the evolution of the permeability of the cement paste with other parameters such as w/c (water to cement ratio), the pore size distribution etc… For example Breysse and Gérard [37] performed a statistical analysis on the values of permeability of different cement pastes prepared with different w/c ratios as reported in the literature and found a power law for the relationship between the permeability and w/c. Higher values of w/c result in a cement paste with a higher initial porosity and thus a higher initial permeability. Breysse and Gerard relationship can be used to evaluate the initial permeability to be put in our permeability evolution law. On the other hand empirical relationships can be found in the literature to estimate the initial porosity as a function of w/c (Taylor [38]).

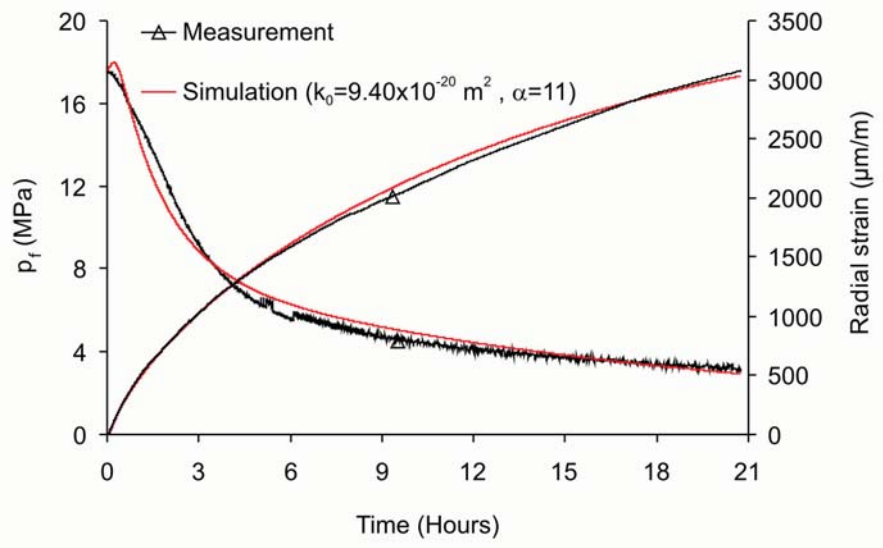

Figure 6- Test C: Test results and numerical simulation.

5 Conclusions

The permeability-porosity relationship for a hardened class G oil well cement paste is evaluated experimentally using a single transient test. The excess pore pressure generated in the sample after an undrained hydrostatic compression test is used for the evaluation of the permeability. This pressure is released at one end of the sample and the variations of the pore pressure at the other end and also the radial deformations in the middle of the sample are measured during the dissipation of the pore pressure. The major advantage of the proposed method as compared to the classical steady state or transient permeability measurement methods, which are performed at a given level of stress, is that one can directly access to the permeability-porosity relationship in a single test. The test results are back analysed to evaluate a power-law permeability-porosity relationship. The creep of the sample during the test and its effect on the measured pore pressure and deformations are introduced in the formulation and are taken into account in the back analysis of the results. For a non creeping material, the same type of analysis can be used to assess a permeability-effective stress relationship. The exponent of the power-law is evaluated equal to 11 in one of the tests and is shown to be the same for the other tests with different initial stress and pore pressure levels. Consequently we can conclude that this coefficient is mostly dependent upon the compaction process which modifies the porosity of the material in accordance with the idea presented by Bernabé *et al*. [14].

It should be emphasized that the obtained power-law relationship describes the variations of the permeability of a given hardened cement paste with a given initial porosity submitted to a hydrostatic loading. In order to extrapolate this law to other cement pastes, prepared with different w/c ratio, one can use empirical relationships existing in the literature which relate the initial permeability and the initial porosity to this parameter.

6 Acknowledgments

The authors gratefully acknowledge TOTAL for supporting this research. They wish also to thank Yves Bernabé and Ahmad Pouya for fruitful comments and discussions and François Martineau for his assistance in the experimental work.

7 References

[1] Brace W, Walsh J, Frangos W. Permeability of Granite under High Pressure. Journal of Geophysical Research 1968;73(6):2225-2236.

[2] Bernabé Y. The effective pressure law for permeability in Chelmsford granite and Barre granite. Int J Rock Mech Min Sci & Geomech Abstr 1986;23(3):267-275.

[3] Bernabé Y. The effective pressure law for permeability during pore pressure and confining pressure cycling of several crystalline rocks, Journal of Geophysical Research 1987;92(B1):649-657.

[4] Escoffier S, Homand F, Giraud A, Hoteit N, Kun Su. Under stress permeability determination of the Meuse/Haute-Marne mudstone. Engineering Geology 2005;81(3):329-340.

[5] Scherer, GW. Bending of gel beams: method of characterizing mechanical properties and permeability, J. Non-Cryst. Solids 1992;142(1-2):18-35.

[6] Scherer GW. Characterization of saturated porous bodies. Concr Sci Eng 2004;37(265):21-30.

[7] Scherer GW, Valenza II JJ, Simmons G, New methods to measure liquid permeability in porous materials. Cement and concrete research 2006;37:386-397.

[8] Ai H, Young JF, Scherer GW. Thermal expansion kinetics: method to measure permeability of cementitious materials: II, application to hardened cement paste. J Am Ceram Soc 2004;84(2):385–391, Erratum, J. Am. Ceram. Soc. 87(8):1611.

[9] Scherer GW. Dynamic pressurization method for measuring permeability and modulus: I. Theory. Materials & Structures 2006;39:1041-1057.

[10] Grasley ZC, Valenza II JJ, Scherer GW, Lange DA, Dynamic pressurization method for measuring permeability and modulus: II. cementitious materials. Materials & Structures 2007;40:711-721.

[11] Hart DJ, Wang HF. A single test method for determination of poroelastic constants and flow parameters in rocks with low hydraulic conductivities, Int J Rock Mech Min Sci 2001;38:577-583.

[12] Ghabezloo S, Sulem J, Guedon S, Martineau F, Saint-Marc J. Poromechanical behaviour of hardened cement paste under isotropic loading. Cement and Concrete Research 2008;38(12): 1424-1437.

[13] Ghabezloo S, Sulem J, Saint-Marc J. The effect of undrained heating on a hardened cement paste. Cement and Concrete Research 2009;39(1):54-64.

[14] Bernabé Y, Mok U, Evans B. Permeability-porosity Relationships in Rocks Subjected to Various Evolution Processes. Pure and Applied Geophysics 2003;160:937-960.

[15] Bernabé Y, Brace WF, Evans B. Permeability, porosity and pore geometry of hot-pressed calcite. Mechanics of Materials 1982;1:173-183.

[16] Walder J, Nur A. Porosity reduction and crustal pore pressure development. Journal of Geophysical Research 1984;89:11539-11548.

[17] David C, Wong T-F, Zhu W, Zhang J. Laboratory measurement of compaction-induced permeability change in porous rocks: Implications for the generation and maintenance of pore pressure excess in the crust. Pure and Applied Geophysics 1994;143(1-3):425-456.

[18] Zhu W, Wong T-f. The transition from brittle faulting to cataclastic flow: Permeability evolution, Journal of Geophysical Research 1997;102(B2): 3027-3041.

[19] Meziani H. Gas permeability measurements of cement-based materials under hydrostatic test conditions using a low-transient method. Magazine of Concrete Research 2006;58(8):489-503.

[20] Sulem J, Ouffroukh H. Hydromechanical Behaviour of Fontainebleau Sandstone. Rock Mechanics and Rock Engineering 2006;39(3):185-213.

[21] Ghabezloo S, Sulem J. Stress dependent thermal pressurization of a fluid-saturated rock. Rock Mechanics and Rock Engineering 2009;42(1):1-24.

[22] Biot MA, Willis DG. The elastic coefficients of the theory of consolidation. Journal of Applied Mechanics 1957;24:594-601.

[23] Brown RJS, Korringa J. On the dependence of the elastic properties of a porous rock on the compressibility of the pore fluid. Geophysics 1975;40:608-616.

[24] Rice JR, Cleary MP. Some basic stress diffusion solutions for fluid-saturated elastic porous media with compressible constituents. Review of geophysics and space physics 1976;14(2):227-240.

[25] Zimmerman RW. Compressibility of sandstones. Amsterdam: Elsevier, 1991.

[26] Detournay E, Cheng AH-D. Fundamentals of Poroelasticity, In: Comprehensive Rock Engineering: Principles, Practice and Projects, Vol. II, Analysis and Design Method, C. Fairhurst ed.: Pergamon, 1993, pp 113-171.

[27] Vardoulakis I, Sulem J. Bifurcation Analysis in Geomechanics. Blackie Academic and Professional, 1995.

[28] Wang HF. Theory of Linear Poroelasticity with Applications to Geomechanics and Hydrogeology, Princeton University Press, 2000.

[29] Coussy O. Poromechanics. John Wiley and Sons, 2004.

[30] J.G. Berryman, Effective stress for transport properties of inhomogeneous porous rock, Journal of Geophysical Research 1992;97:17409-17424.

[31] P.A. Berge, J. G. Berryman, Realizability of Negative Pore Compressibility in Poroelastic Composites, Journal of Applied Mechanics 1995;62(4):1053-1062.

[32] P.A. Berge, Pore Compressiblity in Rocks, Biot Conference on Poromechanics, Louvain-la-Neuve, Belgium, September 14-16, 1998.

[33] Zimmerman RW, Somerton WH, King MS. Compressibility of porous rocks. Journal of Geophysical Research 1986;91(B12):12765-12777.

[34] Hart DJ, Wang HF. Poroelastic effects during a laboratory transient pore pressure test, In: Poromechanics, Thimus JF, Abousleiman Y, Cheng AHD, Coussy O, and Detournay E. ed.:, Balkema, Rotterdam, 1998, pp 579-582.

[35] Spang B. Excel Add-In for Properties of Water and Steam in SI-Units. http://www.cheresources.com/iapwsif97.shtml, 2002.

[36] Ghabezloo S, Sulem J, Guedon S, Martineau F. Effective stress law for the permeability of a limestone. Int J Rock Mech Min Sci 2009;46(2):297-306.

[37] Breysse D, Gérard B. Modelling of permeability in cement-based materials: Part 1-Uncracked medium. Cement and Concrete Research 1997;27(5):761-775.

[38] Taylor HFW. Cement chemistry, London: Thomas Telford, 1997

3.4 Effet de température sur le comportement poromécanique

L'effet de température sur le comportement poromécanique du ciment est étudié en réalisant un essai 'sans-membrane' et deux essais de compression isotrope drainés à 90°C. On présente également dans cette section quelques résultats sur l'effet de la température sur le fluage du ciment.

3.4.1 Essai de compression isotrope 'sans membrane' à 90°C

Un essai de la compression 'sans membrane' a été réalisé à 90°C. Un cycle de charge-décharge atteignant une pression de confinement de 50MPa a été appliqué et le module de compression de la phase solide est évalué dans la phase de décharge. Le module de compression de la matrice solide du ciment évalué à 90°C (17,5GPa) est légèrement inférieur au module mesuré à température ambiante (21GPa) (Figure 3-1).

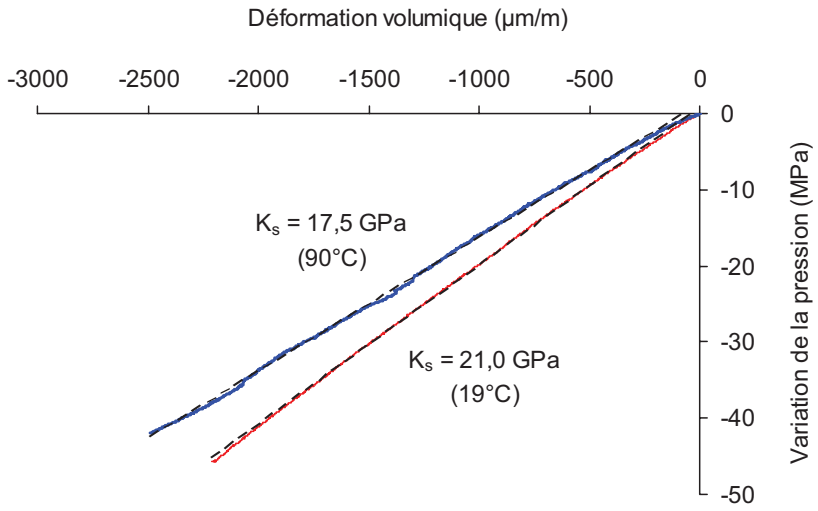

Figure 3-1- Essai de compression isotrope 'sans membrane' réalisé à 90°C, comparaison avec l'essai réalisé à température ambiante

3.4.2 Essais de compression isotrope drainés à 90°C

Deux essais de compression isotrope drainés avec trois cycles de décharge-recharge ont été réalisés à 90°C. Les détails des essais avec les pressions de confinement maximales atteintes pour chaque cycle sont présentés sur le Tableau 3-1.

Essai	Pression interstitielle (MPa)	Cycle N°1 (MPa)	Cycle N°2 (MPa)	Cycle N°3 (MPa)
DT-1	1,6	20	35	50
DT-2	1,0	15	25	40

Tableau 3-1 Essais de compression isotrope drainés réalisés à 90°C

Les chemins de chargement sont présentés sur la Figure 3-2. La Figure 3-3 présente les déformations volumiques mesurées en fonction de la pression de confinement. La comparaison avec les essais réalisés à température ambiante montre que les déformations mesurées à 90°C sont considérablement supérieures à celles mesurées à température ambiante. Les modules de compression drainés sont évalués

de la même façon que pour les essais précédents. L'évolution du module de compression drainé avec la contrainte effective de Terzaghi à 90°C est approximée par la relation suivante (Figure 3-4):

$$K_d = 5,26 - 0,034\sigma_d \tag{3-3}$$

Les modules de compression drainés mesurés à température ambiante sont aussi présentés sur la Figure 3-4. La comparaison des résultats montre que les modules mesurés à 90°C sont plus faibles que ceux mesurés à température ambiante.

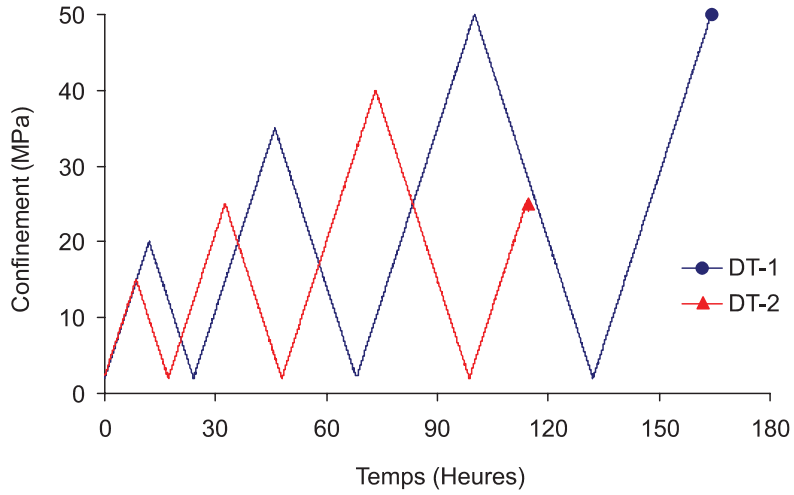

Figure 3-2- Essais de compression isotrope drainés à 90°C : Chemins de chargements

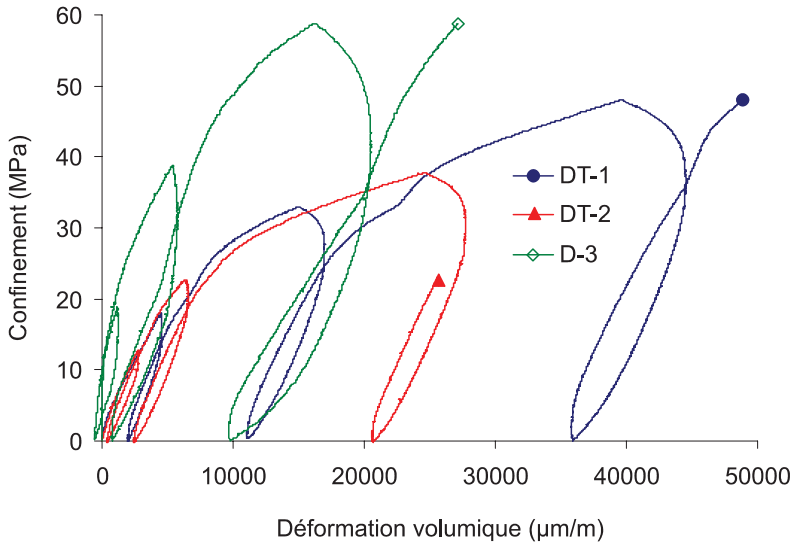

Figure 3-3- Essais de compression isotrope drainés à 90°C (DT-1, DT-2) et à température ambiante (D-3): Déformation volumique - Pression de confinement

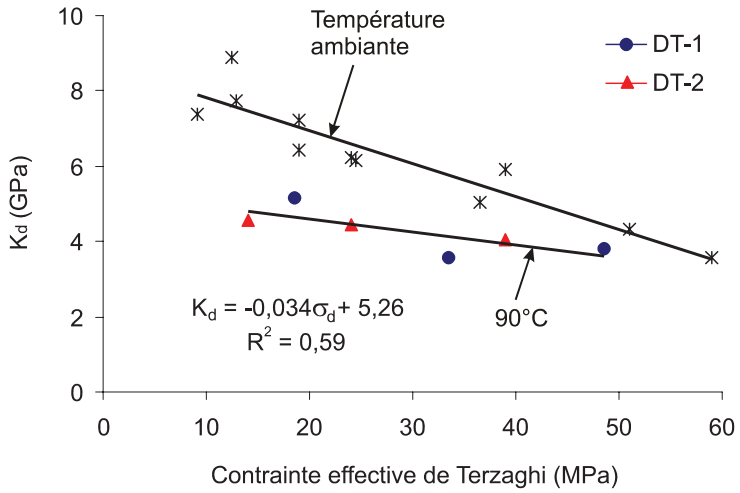

Figure 3-4- Modules de compression drainé mesurés à 90°C et à température ambiante en fonction de la contrainte effective de Terzaghi

En utilisant la relation suivante, présentée dans la section 3.2, on peut évaluer le module de compression drainé en fonction de la porosité et du module K_s :

$$K_d = K_s\left(1-\phi\right)^3 \tag{3-4}$$

En utilisant $\phi = 0,26$ et $K_s = 17.5\text{GPa}$ dans cette relation, le module de compression drainé K_d est évalué égal à 7,1GPa. Cette valeur est supérieure au module évalué expérimentalement pour une contrainte effective nulle, égal à 5,26GPa (équation (3-3)).

A partir de la valeur du module de compression K_s (17,5GPa) et de l'expression du module de compression drainé K_d (équation (3-3)), on peut calculer l'expression du coefficient de Biot à 90°C en fonction de la contrainte de Terzaghi:

$$\alpha^{\text{sec}} = 0,7 + 0,002\sigma_d \tag{3-5}$$

La Figure 3-5 présente la comparaison des coefficients de Biot à température ambiante et à 90°C. On observe que le coefficient de Biot à 90°C est supérieur à celui à température ambiante.

Le coefficient B de Skempton peut être évalué à l'aide de l'équation (2.27). En remplaçant $K_d = 5,26\text{GPa}$, $K_s = K_\phi = 17,5\text{GPa}$, $K_f = 2,1\text{GPa}$ et $\phi = 0,26$ dans cette équation on obtient $B = 0,55$ qui est plus grand que le coefficient de Skempton mesuré à température ambiante, égal à 0,4. En utilisant l'équation (2.30) on peut aussi évaluer le module de compression non-drainé à 90°C, égal à 8,54GPa, qui est inférieur à celui mesuré à température ambiante, égal à 11,25GPa.

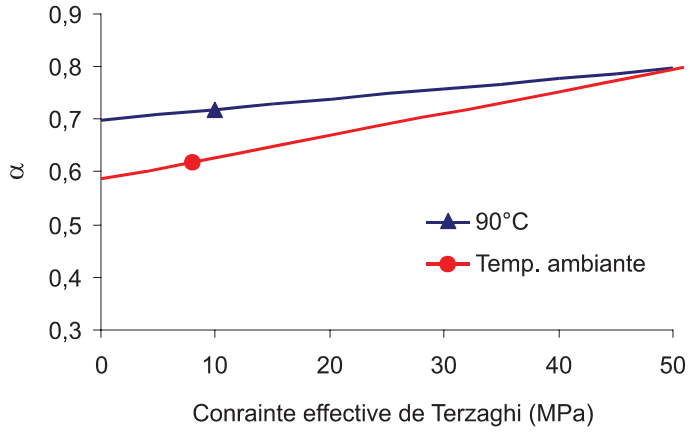

Figure 3-5- Comparaison des coefficients de Biot à température ambiante et à 90°C

3.4.3 Fluage sous contraintes isotropes

A la fin de l'essai de compression isotrope drainé réalisé sur l'échantillon de l'essai DT-1, le chargement isotrope est maintenu constant à 50MPa pendant environ 100 heures. La Figure 3-6 présente les déformations volumiques mesurées pendant cette phase de fluage. On observe une déformation de fluage supérieure à 2,5% que nous pouvons comparer avec la déformation mesurée durant le chargement isotrope d'environ 5% (Figure 3-3). Sur la Figure 3-7, nous présentons une comparaison de la première partie de cet essai de fluage (à 50MPa, à 90°C) avec deux phases de fluage réalisées à température ambiante sous 46MPa et 20MPa. La déformation de fluage est, comme attendu, beaucoup plus importante à 90°C qu'à température ambiante. On peut aussi observer qu'à température ambiante, les déformations mesurées sous 46MPa de pression de confinement sont considérablement plus importantes que celle mesurées sous 20MPa.

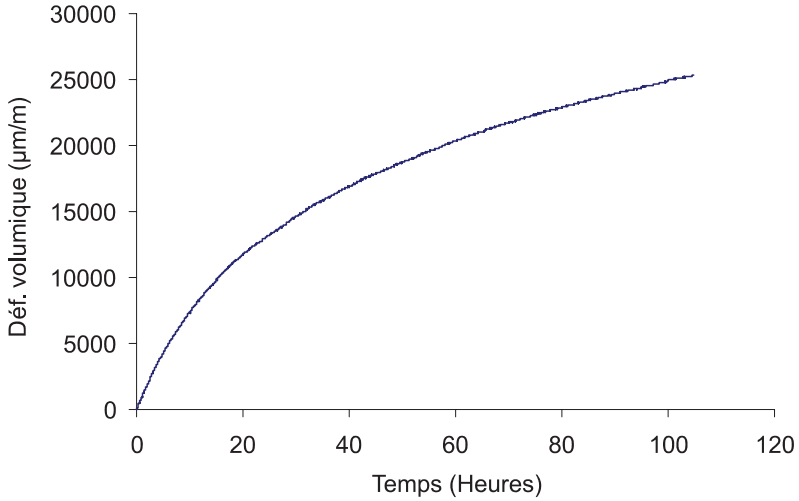

Figure 3-6- Fluage sous contrainte isotrope (90°C-50 MPa)

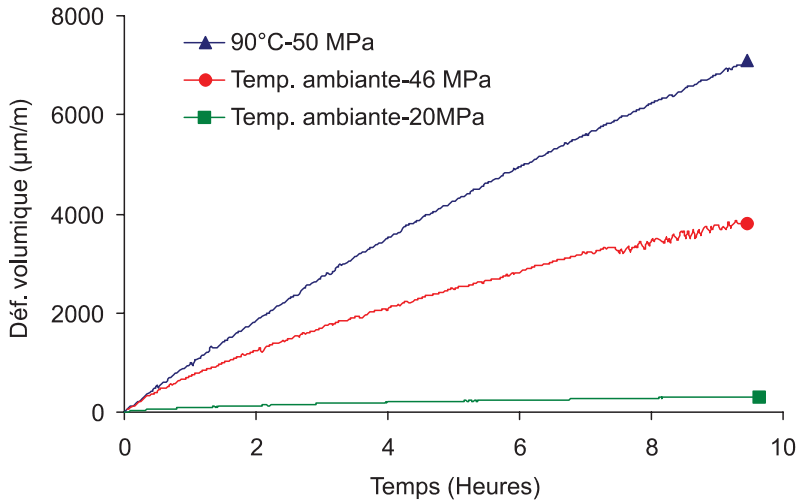

Figure 3-7- Effet de température et la pression de confinement sur le fluage sous contraintes isotropes

3.5 Conclusions

En résumé, à partir des essais isotropes sur la pâte de ciment durcie et de l'analyse des résultats, nous pouvons tirer les conclusions suivantes :

1- **La pâte de ciment durcie est un matériau poromécanique**. Le comportement de ce matériau peut être effectivement décrit par la théorie des milieux poreux.
2- Les paramètres poroélastiques de la pâte de ciment étudiée (w/c=0,44) à température ambiante sont les suivants:

$$\begin{aligned} &K_s = 21 \\ &K_d^{\sec} = 8,69 - 0,087\sigma_d \\ &K_u^{\sec} = 11,25 - 0,099\sigma_d \\ &B = 0,4 \\ &\alpha^{\sec} = 0,586 + 0,004\sigma_d \\ &K_\phi = 16,9 \end{aligned} \qquad (K_{s,d,u,\phi}\text{: GPa},\ \sigma_d\text{: MPa}) \qquad (3\text{-}6)$$

3- Les résultats expérimentaux confirment que le module de compression drainé K_d du ciment varie avec la contrainte effective de *Terzaghi*. Ceci est compatible avec la mesure d'un module K_s constant pour le ciment étudié.
4- Un phénomène de dégradation des modules élastiques est observé dans les résultats des essais. Les observations microscopiques des échantillons avant et après les essais montrent que ce phénomène est dû à la microfissuration du ciment sous chargement isotrope. Cette microfissuration peut être expliquée par la microstructure fortement hétérogène du matériau.
5- L'analyse des résultats expérimentaux montre que la porosité de ciment qui doit être utilisée dans les formulations poromécanique est inférieure à la porosité totale du ciment, mesurée en séchant l'échantillon à 105°C. La porosité qui doit être utilisée, est vraisemblablement la porosité de l'eau libre qui peut être mesurée en mettant le ciment en équilibre à 11% d'humidité relative. Cette porosité pour les pâtes du ciment avec w/c<0,5 peut être approximée par la porosité mesurée au porosimètre à mercure.
6- La perméabilité du ciment diminue sous chargement isotrope. Ceci montre que la compaction de la matrice poreuse de ciment a un effet plus important sur la perméabilité que la microfissuration, étant donné que les fissures peuvent rester fermées sous l'effet du chargement.
7- Sous chargement isotrope, la perméabilité du ciment diminue avec la variation de la porosité selon une loi puissance présentée ci-dessous. La puissance égale à 11 est une caractéristique du processus de compaction de ciment sous chargement isotrope et ne peut pas être utilisée pour la variation de la porosité dans un autre processus d'évolution de la porosité.

$$k\left(\mathrm{m}^2\right) = 1,14\times10^{-19}\left(\frac{\phi}{0,26}\right)^{11} \qquad (3\text{-}7)$$

8- Les paramètres poroélastiques de la pâte de ciment étudié (w/c=0,44) à 90°C sont les suivants:

$$
\begin{aligned}
&K_s = 17,5 \\
&K_d^{\sec} = 5,26 - 0,034\sigma_d \\
&\alpha^{\sec} = 0,7 + 0,002\sigma_d \qquad (K_{s,d,u}\text{ : GPa },\ \sigma_d\text{ : MPa}) \qquad (3\text{-}8) \\
&\left.\begin{aligned} K_u^{\sec} &= 8,5 \\ B &= 0,55 \end{aligned}\right\} \text{évalués pour } \sigma_d = 0
\end{aligned}
$$

9- Les résultats expérimentaux montrent la dégradation des propriétés poroélastiques du ciment due à l'augmentation de la température. Cette dégradation se manifeste dans la diminution des modules élastiques et l'augmentation des coefficients de Biot et de Skempton.

10- Le fluage du ciment sous chargement isotrope augmente sensiblement avec l'augmentation de la température.

3.6 Perspectives

A court terme, l'étude du comportement thermo-poro-mécanique du ciment pétrolier sous chargement isotrope présentée dans ce chapitre peut être complétée en réalisant des études suivantes :

1- Il est important d'explorer de façon plus approfondie l'effet de fluage du ciment sur le comportement poromécanique sous chargement isotrope. Ceci peut se faire d'une part en réalisant des essais de fluage sous chargement isotrope et aussi en utilisant les résultats des essais de compression isotrope réalisés à température ambiante pour le développement d'un modèle de comportement qui, en plus des aspects de l'élasticité non-linéaire, prend en compte le comportement différé du ciment sous chargement isotrope.

2- L'effet des déformations du fluage sur les paramètres poroélastiques du ciment peut être étudié dans des essais spécialement programmés alternant des phases de chargement et des phases de fluage. Dans le modèle présenté pour le comportement poroélastique non-linéaire du ciment, les paramètres dépendent de la contrainte effective. Sous une contrainte effective constante, les déformations de fluage peuvent avoir deux effets opposés : (a) la compaction de la matrice poreuse et la diminution de la porosité conduit à une augmentation des modules élastiques, (b) les déformations de fluage peuvent également provoquer la génération de nouvelles microfissures, ce qui conduit à une diminution des modules élastiques.

3- La caractérisation du comportement poromécanique du ciment à 90°C peut être complété en réalisant quelques essais supplémentaires. Réaliser deux essais de compression isotrope non-drainés semble être indispensable. Ceci va permettre de réaliser une analyse de compatibilité des données, similaire à celle présentée pour les essais réalisés à température ambiante. Les résultats des essais non-drainés vont également permettre d'évaluer le module K_ϕ et par conséquent les différents coefficients de la contrainte effective à 90°C, tels qu'on les a définis à température ambiante.

4- Afin d'étudier la relation perméabilité-porosité du ciment à 90°C, des essais d'évaluation de la perméabilité, similaires à ceux réalisés à température ambiante, peuvent être réalisés après les essais de compression isotrope non-drainés, mentionnés ci-dessus.

5- Enfin, il serait intéressant de réaliser une étude expérimentale semblable à celle présentée dans ce chapitre, à une température intermédiaire, par exemple 50°C, afin d'avoir une image plus claire de l'évolution des paramètres poromécaniques du ciment avec la température.

CHAPITRE 4. **PRESSURISATION THERMIQUE D'UN CIMENT PETROLIER**

4.1 Introduction

Dans le chapitre précédent le comportement poromécanique à température constante et la variation de la perméabilité du ciment sous chargement isotrope ont été étudiés et présentés. Ce chapitre est dédié à l'étude de comportement du ciment lorsqu'il est soumis à des variations de température. Ceci est important pour l'analyse et la compréhension de la réponse des puits pétroliers soumis à des chargements thermiques. Lorsqu'un puits pétrolier est soumis à de rapides variations de température, les déformations et la surpression interstitielle qui en résultent peuvent porter atteinte à l'intégrité du puits. Ce phénomène de pressurisation thermique induit lors d'un chauffage en conditions non-drainées est dû à la différence entre le coefficient d'expansion thermique du fluide interstitiel et celui de la matrice solide d'environ un ordre de grandeur. Une étude préliminaire, théorique et expérimentale a été menée sur un grès. Les effets des déformations mécaniques et thermiques du système de drainage lors d'un essai de chauffage non-drainé ont été analysés et une méthode simple a été développée pour apporter une correction aux valeurs de la pression interstitielle mesurée. Le comportement thermique du ciment a été étudié expérimentalement dans les essais de chauffage drainés et non-drainés et le coefficient de pressurisation thermique ainsi que les coefficients d'expansion thermique drainée et non-drainée du ciment ont été évalués. L'anomalie du comportement thermique du fluide interstitiel du ciment due à son confinement dans des pores de très petite taille a été étudiée à partir des résultats expérimentaux de pressurisation thermique.

Ce chapitre est présenté sous la forme de deux articles, rédigés an anglais. Le premier, intitulé « Stress-dependent thermal pressurization of a fluid-saturated rock » est publié dans la revue «Rock Mechanics and Rock Engineering ». Il présente les fondements théoriques de l'analyse du phénomène de pressurisation thermique dans les matériaux poreux saturés, le protocole expérimental pour l'étude en laboratoire du phénomène et les résultats de l'étude préliminaire réalisés sur un grès. Le deuxième article, intitulé « The effect of undrained heating on a fluid saturated hardened cement paste » est publié dans la revue « Cement and Concrete Research ». Il présente une étude théorique et expérimentale de la pressurisation thermique pour le ciment.

4.2 Etude préliminaire: pressurisation thermique d'une roche saturée

L'augmentation de la température dans les milieux poreux saturés en conditions non-drainées conduit à un phénomène de pressurisation thermique du fluide interstitiel due à la différence des coefficients d'expansion thermique du fluide et de la matrice solide. Cette augmentation de la pression interstitielle induit une diminution de la contrainte moyenne effective et peut conduire à la rupture en cisaillement du matériau. Ce phénomène de pressurisation thermique est étudié théoriquement et expérimentalement pour une roche granulaire saturée à partir d'essais de chauffage drainé et non-drainé sous un état de contrainte isotrope maintenu constant. La formulation poromécanique utilisée dans cet article, au contraire du reste de la thèse, est développée pour un matériau poreux idéal qui satisfait les conditions de

micro-isotropie et micro-homogénéité. Une méthode simple est présentée pour la correction de l'effet des déformations thermiques et mécaniques du système de drainage de la cellule triaxiale sur la pression interstitielle mesurée lors d'un essai de chauffage non-drainé. Les résultats de l'essai de chauffage non-drainé réalisé sur le grès mettent en évidence la forte non-linéarité du phénomène de la pressurisation thermique dans cette roche. Le résultat d'un essai de compression isotrope drainé montre la non-linéarité du comportement mécanique de la roche et l'augmentation du module de compression drainé avec la contrainte effective de Terzaghi. Une simulation analytique de l'essai de chauffage non-drainé réalisé à l'aide des résultats des essais de compression isotrope « sans membrane », des essais de compression drainés et de l'essai de chauffage drainé montre clairement que ce coefficient de pressurisation thermique dépend à la fois de la température et la contrainte effective. La dépendance de ce coefficient en température est due aux variations des propriétés physiques de l'eau (coefficient d'expansion thermique et compressibilité) avec la température. La dépendance de ce coefficient en contrainte effective est due à la variation du module de compression drainé du matériau avec contrainte effective de Terzaghi. Les résultats de la simulation analytique ont montré une bonne compatibilité avec les données expérimentales de l'essai. Ces résultats permettent de calculer le coefficient de pressurisation thermique de la roche étudiée en fonction de la température et l'état de contraintes.

Rock Mech Rock Engng (2009) 42: 1–24
DOI 10.1007/s00603-008-0165-z
Printed in The Netherlands

Rock Mechanics
and Rock Engineering

Stress dependent thermal pressurization of a fluid-saturated rock

By

S. Ghabezloo, J. Sulem

Université Paris-Est, Ecole Nationale des Ponts et Chaussées,
CERMES-UR Navier, Marne la Vallée, France

Received June 4 2007; Accepted December 19 2007; Published online May 5 2008

Abstract

Temperature increase in saturated porous materials under undrained conditions leads to thermal pressurization of the pore fluid due to the discrepancy between the thermal expansion coefficients of the pore fluid and of the solid matrix. This increase in the pore fluid pressure induces a reduction of the effective mean stress and can lead to shear failure or hydraulic fracturing. The equations governing the phenomenon of thermal pressurization are presented and this phenomenon is studied experimentally for a saturated granular rock in an undrained heating test under constant isotropic stress. Careful analysis of the effect of mechanical and thermal deformation of the drainage and pressure measurement system is performed and a correction of the measured pore pressure is introduced. The test results are modelled using a non-linear thermo-poro-elastic constitutive model of the granular rock with emphasis on the stress-dependent character of the rock compressibility. The effects of stress and temperature on thermal pressurization observed in the tests are correctly reproduced by the model.

Key words: granular rock, thermal pressurization, pore pressure, thermo-poro-elasticity

1 Introduction

Temperature increase in saturated porous materials leads to thermal pressurization of the pore fluid due to the discrepancy between the thermal expansion coefficients of the pore fluid and of the solid phase. This increase in the pore fluid pressure induces a reduction of the effective mean stress, and can lead to shear failure or hydraulic fracturing. This phenomenon is important in petroleum engineering where the reservoir rock or the well cement lining undergoes sudden temperature changes as well as in environmental engineering for radioactive waste disposal in deep clay geological formations. It is also important in geophysics in the studies of rapid fault slip events when shear heating tends to increase the pore pressure and to decrease the effective compressive stress and the shearing resistance of the fault material (Rempel and Rice 2006, Sulem et al. 2007). Important theoretical advances have been proposed in the study of thermal weakening of fault during coseismic slip and one can find an extensive literature review on the subject in the comprehensive paper of Rice (2006). In this paper, Rice emphasises the need of laboratory data to constrain theoretical modelling of these mechanisms. In particular thermal pressurization of rocks during seismic slip is highly influenced by damage and inelastic deformation inside the fault zones. The presence of clay material in fault zones also affects thermal pressurization as possible collapse of the clay under thermal loading may activate fluid pressurization (Sulem et al. 2007).

The values of the undrained thermal pressurization coefficient, defined as the pore pressure increase due to a unit temperature increase in undrained condition, is thus largely dependent upon the nature of the material, the state of stress, the range of temperature change, the induced damage. In the literature we can find values that differ from two orders of magnitude: In Campanella and Mitchell (1968) different values are found from 0.01 MPa/°C for clay to 0.05 MPa/°C for sandstone. Palciauskas and Domenica (1982) estimate a value of 0.59MPa/°C for Kayenta sandstone. On the basis of Sultan (1997) experimental data on Boom clay, Vardoulakis (2002) estimates this coefficient as 0.06 MPa/°C. For a clayey fault gouge extracted at a depth of 760m in Aigion fault in the Gulf of Corinth (Greece), the value obtained by Sulem et al. (2004) is 0.1 MPa/°C and for intact rock at great depth, the value given by Lachenbruch (1980) is 1.5 MPa/°C. For a mature fault at 7km depth at normal stress of 196 MPa, ambient pore pressure of 70 MPa, and ambient temperature of 210°C, Rice (2006) estimates this coefficient as 0.92MPa/°C in case of intact fault walls and 0.31MPa/°C in case of damage fault wall.

The large variability of the thermal pressurization coefficient highlights the necessity of laboratory studies. The aim of this paper is to study the phenomenon of thermal pressurization, theoretically and experimentally for a saturated granular rock. The stress dependency of the compression modulus of granular rocks has important consequences on the thermal response in undrained condition and this phenomenon is addressed here. In the treatment of the test results, the effect of mechanical and thermal deformation of the drainage system is carefully analysed and taken into account.

2 Thermo-poro-mechanical background

The equations governing the phenomenon of the thermo-mechanical pressurization of porous materials are presented here for an ideal porous material characterized by a fully connected pore space and by a microscopically homogeneous (i.e., composed of only one solid material) and isotropic solid phase. These equations can be derived using the approach of Bishop and Eldin (1950). In this approach, schematized on Figure (1), the problem of thermo-mechanical loading is broken up into three

independent sub-problems. Assuming isotropic elasticity, the volumetric changes of the porous material element and its components, are written separately, as presented on table (1). In this table,

- V is the total volume
- n is the Lagrangian porosity,
- $\Delta\sigma$, ΔT and Δu are the variations of the mean stress (positive in compression), the temperature and the pore pressure respectively,
- c_f and c_s are respectively the compressibility of pore fluid and of the solid phase,
- c_d is the drained compressibility of the porous material,
- α_f and α_s are respectively the volumetric thermal expansion coefficient of pore fluid and solid phase.

The index 0 denotes the reference state.

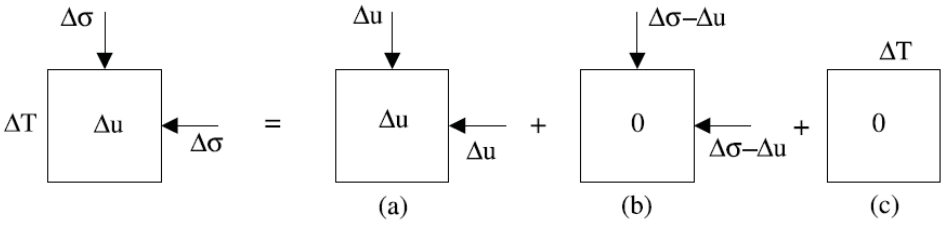

Figure 1: Decomposition of the problem of a thermo-mechanical loading into three independent problems

Problem	Variation of volume of constituents		Variation of volume of element
	Pore fluid	Solid phase	
(a)	$-n_0 V_0 c_f \Delta u$	$-(1-n_0) V_0 c_s \Delta u$	$-V_0 c_s \Delta u$
(b)	-	$-V_0 c_s (\Delta\sigma - \Delta u)$	$-V_0 c_d (\Delta\sigma - \Delta u)$
(c)	$n_0 V_0 \alpha_f \Delta T$	$(1-n_0) V_0 \alpha_s \Delta T$	$V_0 \alpha_s \Delta T$

Table 1: Variation of volume of the porous material and its constituents for the three independent problems presented in Figure (1)

A clear distinction must be made between the Lagrangian and the Eulerian porosity (Rice and Cleary 1976, Coussy 2004). The Lagrangian porosity n is defined as the pore volume per unit volume of porous material in the reference state (also called pore volume fraction), while the Eulerian porosity ϕ is defined as the pore volume per unit volume of porous material in actual state. Both quantities are identical in the reference state ($n_0 = \phi_0$) but differ in the actual (deformed) state. The following relations hold for the Lagrangian and Eulerian porosity change:

$$n - n_0 = \frac{V_n - V_{n0}}{V_0} \tag{1}$$

$$\phi - \phi_0 = \frac{V_n}{V} - \frac{V_{n0}}{V_0} \tag{2}$$

$$n - n_0 = \phi - \phi_0 + \phi\left(\frac{V}{V_0} - 1\right) \tag{3}$$

where $V_n = nV_0$ is the volume of the pore space in actual state and $V_{n0} = n_0 V_0$ is the volume of the pore space in reference state.

The problem (a) in the Figure (1) corresponds to a particular loading case, called 'unjacketed' loading case, where an isotropic stress and a pore pressure of equal magnitudes are simultaneously

applied to a volume element. This loading is as if the sample is submerged, without a jacket, in a fluid under pressure and results in a uniform pressure distribution in the solid phase. In the case of an ideal porous material, the material would deform as if all the pores were filled with the solid component. The skeleton and the solid component experience a uniform volumetric strain with no change of the Eulerian porosity ϕ (Detournay and Cheng 1993).

$$\frac{\Delta V_s}{V_s} = \frac{\Delta V_n}{V_n} = \frac{\Delta V}{V} \tag{4}$$

The problem (b) in the Figure (1) corresponds to Terzaghi effective stress loading. In this case the isotropic stress acting on the solid phase is $\left(\Delta\sigma - \Delta u\right)/\left(1-n_0\right)$ and the corresponding variation of volume is given by:

$$\Delta V_s = -(1-n_0)V_0 c_s \frac{\Delta\sigma - \Delta u}{1-n_0} = -V_0 c_s \left(\Delta\sigma - \Delta u\right) \tag{5}$$

The problem (c) in the Figure (1) is a drained thermal loading under constant total stress. For an ideal porous material, the variation of volume of the porous element is characterized by the thermal expansion coefficient of the solid phase α_s. In this case no change in Eulerian porosity ϕ is expected because an isotropic thermal expansion would cause a proportional change in every linear dimension of the body (McTigue 1986).

Assuming incremental linear thermo-elasticity, the total variation of volume of the porous material is obtained as the sum of the volume change of each sub-problem.

The variation of the Lagrangian porosity n (equation (1)), can be written as the difference between the volume change of the element and the volume change of the solid phase:

$$\begin{aligned}\Delta n = \frac{\Delta V - \Delta V_s}{V_0} = \left[-c_s \Delta u - c_d\left(\Delta\sigma - \Delta u\right) + \alpha_s \Delta T\right] \\ -\left[-\left(1-n_0\right)c_s \Delta u - c_s\left(\Delta\sigma - \Delta u\right) + \left(1-n_0\right)\alpha_s \Delta T\right]\end{aligned} \tag{6}$$

Equation (6) can be simplified to obtain the following expression for the elastic change of porosity in drained condition:

$$\Delta n = -\left(c_d - c_s\right)\Delta\sigma + n_0 c_n \Delta u + n_0 \alpha_n \Delta T \tag{7}$$

where c_n and α_n are respectively the compressibility and the volumetric thermal expansion coefficient of pore-volume defined by the following expressions:

$$c_n = \frac{1}{n_0}\left[c_d - \left(1+n_0\right)c_s\right] \tag{8}$$

$$\alpha_n = \alpha_s \tag{9}$$

Replacing $\phi = \phi_0 + \Delta\phi$ in the equation (3) and considering only the first order terms the variation of the Eulerian porosity can be written in the following form:

$$\Delta\phi = \Delta n - \phi_0 \frac{\Delta V}{V_0} \tag{10}$$

In equation (10) Δn is given by equation (7) and $\Delta V/V_0$ is the sum of the variations of volume of the three sub-problems presented in the Figure (1). With $\phi_0 = n_0$ and using equations (8) and (9) the

following expression is found for the variation of the Eulerian porosity, which is equivalent to the expression given by McTigue (1986) for an ideal porous material:

$$\Delta\phi = -\left[c_d\left(1-\phi_0\right)-c_s\right]\left(\Delta\sigma-\Delta u\right) \tag{11}$$

This equation clearly highlights that, as mentioned above, a drained temperature change does not affect the Eulerian porosity in case of an ideal porous material.

For undrained thermo-mechanical loading (no change in the pore fluid mass), the volume change of the element is equal to the sum of the variations of volume of its constituents:

$$\begin{aligned} &-c_s\Delta u - c_d\left(\Delta\sigma-\Delta u\right)+\alpha_s\Delta T = \\ &-\left(1-n_0\right)c_s\Delta u - c_s\left(\Delta\sigma-\Delta u\right)+\left(1-n_0\right)\alpha_s\Delta T - n_0 c_f\Delta u + n_0\alpha_f\Delta T \end{aligned} \tag{12}$$

Equation (12) can be simplified to obtain the following expression for the pore pressure change due to a thermo-mechanical loading.

$$\Delta u = B\,\Delta\sigma + \Lambda\,\Delta T \tag{13}$$

where B is the Skempton's (1954) coefficient

$$B = \frac{\left(c_d - c_s\right)}{n_0\left(c_f - c_s\right)+\left(c_d - c_s\right)} \tag{14}$$

and Λ is the coefficient of thermal pressurization

$$\Lambda = \frac{n_0\left(\alpha_f - \alpha_s\right)}{n_0\left(c_f - c_s\right)+\left(c_d - c_s\right)} \tag{15}$$

Using the equations (8) and (9), the thermal pressurization coefficient Λ (equation (15)) can be expressed in terms of the thermal expansion coefficient and the compressibility of the pore-volume, α_n and c_n respectively, and the expression given by Rice (2006) is retrieved:

$$\Lambda = \frac{\alpha_f - \alpha_n}{c_f + c_n} \tag{16}$$

Equation (16) clearly highlights that the discrepancy between the thermal expansion of the pore fluid and that of the pore volume is the factor causing the thermal pressurization of porous materials.

Similarly, the volumetric strain of the element ε_v (positive in contraction) is obtained as the sum of the variations of volume in the three sub-problems per unit total volume (in reference state):

$$\varepsilon_v = -\frac{\Delta V}{V_0} = c_s\Delta u + c_d\left(\Delta\sigma-\Delta u\right)-\alpha_s\Delta T \tag{17}$$

By replacing Δu with the expression given in equation (13), one finds the following expression for the volumetric deformation of a porous material subjected to a thermo-mechanical loading:

$$\varepsilon_v = c_u\,\Delta\sigma - \alpha_u\,\Delta T \tag{18}$$

where c_u and α_u are respectively the undrained compressibility and the undrained volumetric thermal expansion coefficient of porous material expressed by the following equations:

$$c_u = c_d - B\left(c_d - c_s\right) \tag{19}$$

$$\alpha_u = \alpha_s + \Lambda\left(c_d - c_s\right) \tag{20}$$

Using the equations (14) and (15) the expression of the undrained thermal expansion coefficient of a thermo-elastic porous material given by McTigue (1986) is retrieved.

$$\alpha_u = \alpha_s + Bn_0\left(\alpha_f - \alpha_s\right) \tag{21}$$

3 Thermal pressurization of granular rocks

The phenomenon of thermal pressurization has been studied experimentally on Rothbach sandstone. The Rothbach sandstone has a porosity of 16%. Its composition is 85% quartz, 12% feldspars and 3% clay.

3.1 Experimental setting

A schematic of the triaxial cell used in this study is shown in Figure (2). This cell can sustain a confining pressure up to 60 MPa. It contains a system of hydraulic self-compensated piston. The loading piston is then equilibrated during the confining pressure build up and directly applies the deviatoric stress. The axial and radial strains are measured directly on the sample inside the cell with two axial transducers and four radial ones of LVDT type (see section AA on Figure (2)). These internal devices allow to avoid the main errors of strain measurements of devices external to the cell such as the compliance of the loading device, the tilting of the specimen and the bedding errors at the ends of the specimen. The confining pressure is applied by a servo controlled high pressure generator. Hydraulic oil is used as confining fluid. The pore pressure is applied by another servo-controlled pressure generator with possible control of pore volume or pore pressure.

The heating system consists of a heating belt around the cell which can apply a temperature change with a given rate and regulate the temperature, and a thermocouple which measures the temperature of the heater. In order to limit the temperature loss, an insulation layer is inserted between the heater element and the external wall of the cell. A second insulation element is also installed beneath the cell. The heating system heats the confining oil and the sample is heated consequently. Therefore there is a discrepancy between the temperature of the heating element in the exterior part of the cell and that of the sample. In order to control the temperature in the centre of the cell, a second thermocouple is placed at the vicinity of sample. The temperature given by this transducer is considered as the sample temperature in the analysis of the test results.

3.2 Effect of mechanical and thermal deformation of the drainage system

The undrained condition is defined as a condition in which there is no change in the fluid mass of the porous material. Achieving this condition in a conventional triaxial system is very difficult. In these systems an undrained test is usually performed by closing the valves of the drainage system. As the drainage system has a non-zero volume, it experiences volume changes due to its compressibility and its thermal expansivity. A variation of the volume in the drainage system induces a fluid flow into or out of the sample to achieve pressure equilibrium between the sample and the drainage system. This fluid mass exchange between the sample and the drainage system and more generally the mechanical and thermal deformations of the drainage system modify the measured pore pressure during the test.

Wissa (1969) was the first who studied this problem for a mechanical undrained loading. He presented an expression for the measured pore pressure increase as a function of the compressibilities of water, soil skeleton, pore-water lines and pressure measurement system, but the compressibility of the

solid phase was not considered in this work. Bishop (1976) completed the formulation of Bishop (1973) and presented an extension of the work of Wissa (1969) taking into account the compressibility of the solid grains. The proposed expression was first used by Mesri et al. (1976) to correct the measured pore pressure in undrained isotropic compression tests.

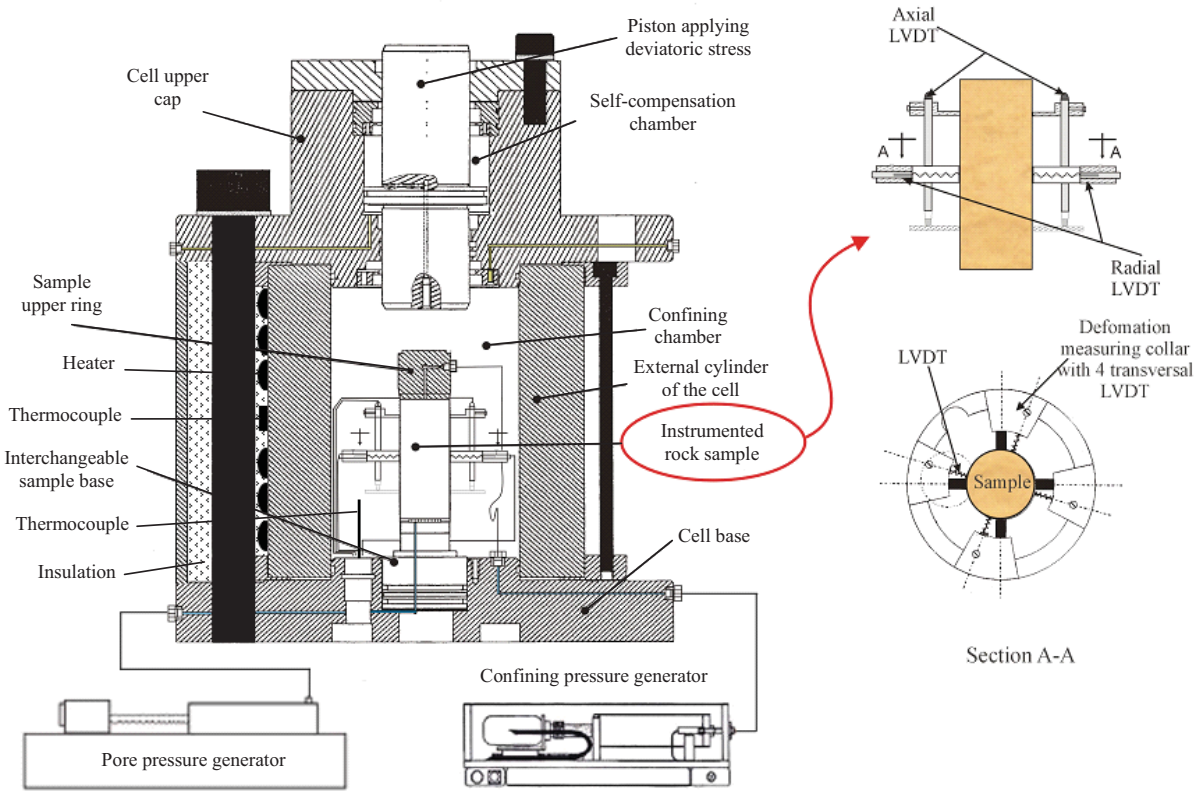

Figure 2: Triaxial cell

3.2.1 Analysis of the correction terms

We here present an extension of the work of Bishop (1976) to take into account the mechanical compressibility and the thermal expansivity of the drainage and pressure measurement system on the measured pore pressure increase during an undrained thermo-mechanical loading. The same approach as the one used in section (2) for the derivation of the governing equations can be used here by taking into account the drainage system. The problem is schematized in Figure (3) and the volume changes for the porous material element, its constituents and the drainage system are presented in table (2).

Four additional parameters are introduced in the problem to take into account the influence of the drainage system. V_L is the volume of fluid in the drainage system. c_L and α_L are the compressibility and the thermal expansion coefficient of the drainage system respectively defined as the variation of the volume of drainage system due to a unit variation in pore pressure and temperature. The parameter c_L is equivalent to $C_L + C_M$ in Wissa (1969) and Bishop (1976) who give some typical values of this parameter which varies between 0.08 and 0.3 mm^3/MPa.

In most triaxial devices, the drainage system can be separated into two parts, one situated inside the triaxial cell and the other one situated outside the cell. In the part inside the cell, one can assume that the temperature change ΔT is the same as the one of the sample; in the other part situated outside the cell, the temperature change is smaller than ΔT and varies along the drainage lines. Let us define an

equivalent temperature change ΔT_L such that the volume change of the entire drainage system caused by ΔT_L is equal to the volume change induced by the real non homogeneous temperature field. The temperature ratio $\beta = \Delta T_L / \Delta T$ is an additional parameter which is evaluated on a calibration test as explained further (see section 3.2.2). As the thermal expansion coefficient and the compressibility of water both vary with temperature, the parameters used for the water in the drainage system, α_{fL} and c_{fL}, are different from the parameters used for the pore fluid of the rock.

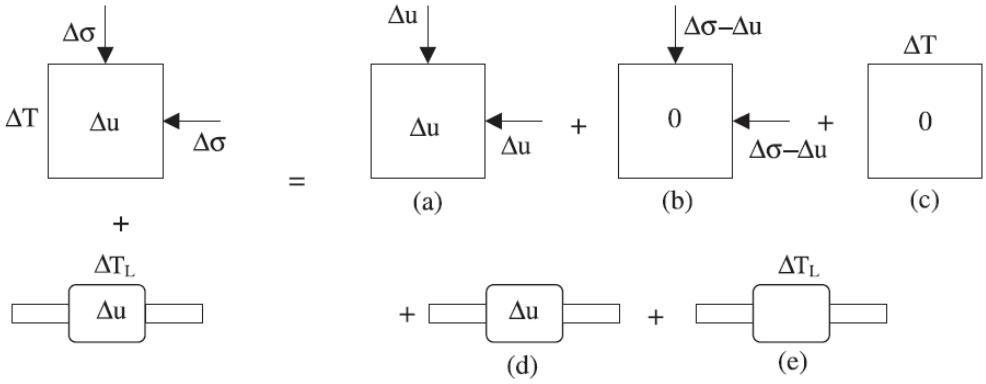

Figure 3: Decomposition of the problem of a thermo-mechanical loading with taking into account the drainage and pressure measurement system

Problem	Variation of volume of constituents		Variation of volume of element
	Pore fluid	Solid phase	
(a)	$-n_0 V_0 c_f \Delta u$	$-(1-n_0) V_0 c_s \Delta u$	$-V_0 c_s \Delta u$
(b)	-	$-V_0 c_s (\Delta\sigma - \Delta u)$	$-V_0 c_d (\Delta\sigma - \Delta u)$
(c)	$n_0 V_0 \alpha_f \Delta T$	$(1-n_0) V_0 \alpha_s \Delta T$	$V_0 \alpha_s \Delta T$
	Fluid in drainage system	Drainage system	
(d)	$-V_L c_{fL} \Delta u$	$c_L \Delta u$	-
(e)	$V_L \alpha_{fL} \beta \Delta T$	$\alpha_L \beta \Delta T$	-

Table 2: Variations of volume of the porous material, its constituents and the drainage and pressure measurement system for the independent problems presented in Figure (3)

For undrained condition, as mentioned before, the overall volume change of an element is the sum of the volume changes of its constituents. The volume change of the pore fluid must be decreased by a correction term corresponding to volume change of the drainage system. This correction term can be evaluated as the change of volume of the drainage system minus the change of volume of water in the drainage system, and is expressed as $V_L c_{fL} \Delta u - V_L \alpha_{fl} \beta \Delta T + c_L \Delta u + \alpha_L \beta \Delta T$. Consequently, the following expression is obtained for the measured pore pressure due to a thermo-mechanical loading:

$$\Delta u = B_{mes}\, \Delta\sigma + \Lambda_{mes}\, \Delta T \tag{22}$$

B_{mes} and Λ_{mes} are the measured Skemptons's coefficient and thermal pressurization coefficient respectively.

$$B_{mes} = \frac{(c_d - c_s)}{n_0 (c_f - c_s) + (c_d - c_s) + \dfrac{V_L c_{fL} + c_L}{V_0}} \tag{23}$$

$$\Lambda_{mes} = \frac{n_0\left(\alpha_f - \alpha_s\right) + \dfrac{\beta\left(V_L\alpha_{fL} - \alpha_L\right)}{V_0}}{n_0\left(c_f - c_s\right) + \left(c_d - c_s\right) + \dfrac{V_L c_{fL} + c_L}{V_0}} \tag{24}$$

Using the equations (8) and (9) the measured thermal pressurization coefficient can be expressed in terms of the compressibility and the thermal expansion coefficient of the pore volume:

$$\Lambda_{mes} = \frac{\alpha_f - \alpha_n + \dfrac{\beta\left(V_L\alpha_{fL} - \alpha_L\right)}{n_0 V_0}}{c_f + c_n + \dfrac{V_L c_{fL} + c_L}{n_0 V_0}} \tag{25}$$

The (corrected) Skempton's and thermal pressurization coefficients (equations (14) and (16)) can thus be expressed from the measured ones as:

$$B_{cor} = \frac{1}{\dfrac{1}{B_{mes}} - \dfrac{V_L c_{fL} + c_L}{V_0\left(c_d - c_s\right)}} \tag{26}$$

$$\Lambda_{cor} = \frac{\Lambda_{mes}}{1 + \dfrac{\beta\left(V_L\alpha_{fL} - \alpha_L\right)}{n_0 V_0\left(\alpha_f - \alpha_n\right)} - \Lambda_{mes}\dfrac{V_L c_{fL} + c_L}{n_0 V_0\left(\alpha_f - \alpha_n\right)}} \tag{27}$$

Equation (26) is the same as the one given by Bishop (1976) for the correction of the measured pore pressure during a mechanical loading.

The correction method proposed here is quite simple. It is applied directly on the results of the test and only requires two simple calibration tests (see next section), but it is restricted to elastic response of the sample and of the drainage system. It differs from the method proposed by Lockner and Stanchits (2002) who have modified the procedure of the test itself by imposing a computer-generated virtual 'no-flow boundary condition' at the sample-endplug interface to insure that no volume change occurs in the drainage system.

3.2.2 Calibration of the correction parameters

The volume of fluid in the drainage system, V_L, can be measured directly or estimated by using the geometrical dimensions of the drainage system. For the triaxial cell used in the present study, $V_L = 2300\,mm^3$. The compressibility of the drainage and pressure measurement systems c_L is evaluated by applying a fluid pressure and by measuring the corresponding volume change in the pore pressure generator. A metallic sample is installed inside the cell to prevent the fluid to go out from the drainage system. Fluid mass conservation is written in the following equation which is used to calculate the compressibility c_L of the drainage system:

$$\Delta V_L = \left(c_L + V_L c_f\right)\Delta u \tag{28}$$

Δu and ΔV_L are respectively the pore pressure and the volume change measured by the pressure generator. For a single measurement, the volume change ΔV_L accounts also for the compressibility of the pressure generator and of the lines used to connect the generator to the main drainage system. To exclude the compressibility of these parts, a second measurement is done only on the pressure generator

and the connecting lines. The volume change ΔV_L used in equation (28) is the difference between these two measurements. The compressibility of the drainage system, c_L, is evaluated equal to 0.27 mm^3/MPa.

The parameter β and the thermal expansivity of the drainage system α_L are evaluated using an undrained heating test which is performed using a metallic sample with the measurement of the fluid pressure change in the drainage system. For the metallic sample $n_0 = 0$ and $c_d = c_s$ so that equation (24) is reduced to the following expression:

$$\Lambda_{mes} = \frac{\beta\left(V_L \alpha_{fL} - \alpha_L\right)}{V_L c_{fL} + c_L} \tag{29}$$

The thermal expansion coefficient α_{fL} and the compressibility c_{fL} of water are known as functions of temperature and pressure (Spang 2002). As these variations are highly non-linear, the parameters β and α_L cannot be evaluated directly but are back analysed from the calibration test results: the undrained heating test of the metallic sample is simulated analytically using equation (29) with a step by step increase of the temperature. For each step the corresponding water thermal expansion and compressibility are used. The parameters β and α_L are back-calculated by minimizing the error between the measurement and the simulation results using a least-square algorithm. The test result and the back analysis are presented in Figure (4). The parameter β is found equal to 0.46 and the thermal expansivity of the drainage system α_L for this test is found equal to 0.31 mm^3/°C.

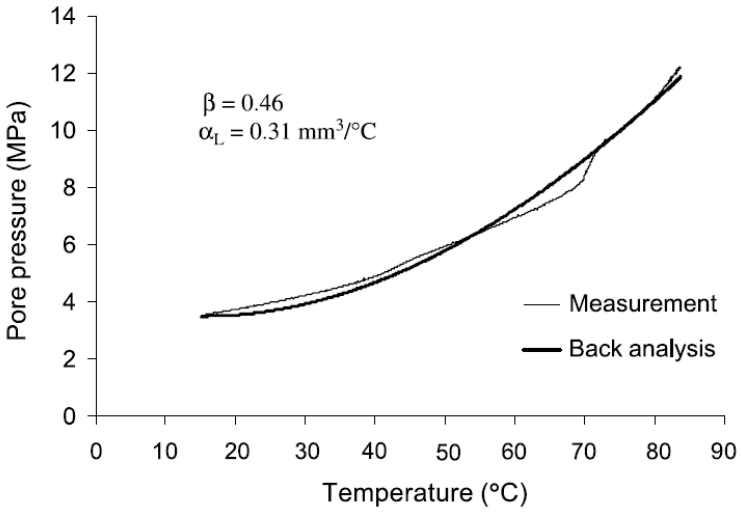

Figure 4: Calibration test for evaluation of the temperature ration β and the thermal expansion α_L of the drainage system-comparison with back analysis of the test

3.3 Mechanical behaviour of Rothbach sandstone

Equation (15) shows that to evaluate the thermal pressurization coefficient of a porous material, its drained compressibility and the compressibility of the solid phase, c_d and c_s respectively, must be known. In order to measure the compressibility of the solid phase, an isotropic compression test, called 'unjacketed test', was carried out in which equal increments of the confining pressure and the pore pressure were applied simultaneously, (see sub-problem (a) in Figure (1)). The compression modulus measured in this test, called the unjacketed modulus, is equal to the compression modulus of the solid grains for an ideal porous material. In the case of in inhomogeneous porous material (i.e., composed of

two or more solids) the unjacketed modulus is some average of the bulk modulus of the constituents (Berryman 1992). As explained by Berryman, what this average should be is generally not known, but can be estimated in some simple cases using homogenisation techniques. The stress-strain response of the performed test is presented in Figure (5). The unjacketed modulus of the Rothbach sandstone, $K_s = 1/c_s$, is obtained as the slope of this curve equal to 41.6 GPa. This value is identified to the compression modulus K_s of the solid phase which appears in the above poromechanical formulation (see Table 1).

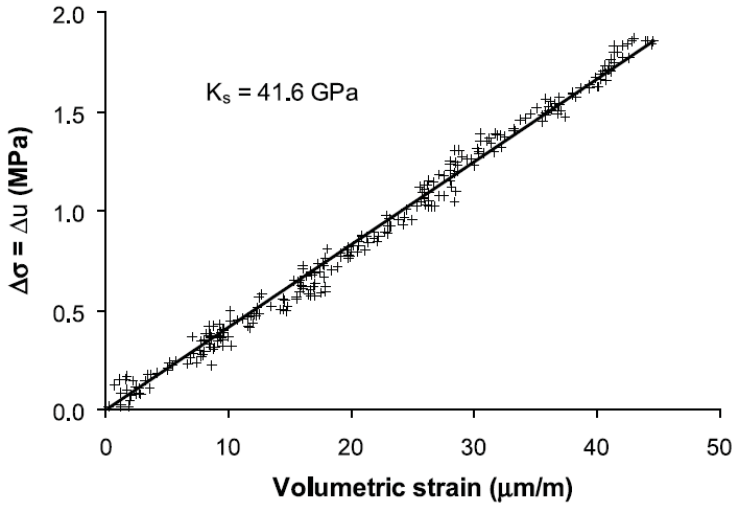

Figure 5: Unjacketed test on Rothbach sandstone: evaluation of the compressibility of solid phase

The unjacketed compressibility can also be estimated by knowing the mineralogy of the rock and the compressibility of each constituent. As mentioned above, the Rothbach sandstone contains 85% quartz, 12% feldspars and 3% clay. The values of elastic properties of different minerals can be found in Bass (1995). The compression modulus of quartz and the average compression modulus of feldspars are equal to 37.8 and 69.1 GPa respectively. The compression modulus of the clay solid grains is equal to 50 GPa (Skempton 1960, McTigue 1986). The homogenized unjacketed modulus can be evaluated using Hill's (1952) average formula:

$$K_s^{\hom} = \frac{1}{2}\left[\sum f_i K_s^{(i)} + \left(\sum \frac{f_i}{K_s^{(i)}}\right)^{-1}\right] \tag{30}$$

where f_i and $K_s^{(i)}$ are the volume fraction and the compression modulus of the ith constituent respectively. Using equation (30) the homogenized unjacketed modulus of Rothbach sandstone is evaluated equal to 41.1 GPa which confirms the measured value (41.6 GPa).

To measure the drained compressibility of the rock, an isotropic drained compression test with a loading and unloading cycle has been carried out. In this test, a fluid back pressure of 1MPa was maintained constant inside the sample. In the Figure (6) the volumetric strain response is shown versus the applied total stress. The observed non-linear response reflects the stress-dependent character of the rock compressibility (Zimmerman 1991, Sulem et al. 1999, 2006). Moreover this curve exhibits a different response in loading and unloading and irreversible deformation. Therefore the elastic tangent drained compression modulus, $K_d = 1/c_d$ is evaluated on the unloading curve.

For a porous material with a constant unjacketed modulus K_s it can be shown theoretically that the stress-dependent drained bulk modulus K_d depends on Terzaghi effective stress $\sigma'_{Terzaghi} = \sigma - u$.

Various theoretical demonstrations of this statement can be found in Zimmerman (1991), Berryman (1992) Coussy (2004) and Gurevich (2004) and from micromechanical considerations in Dormieux et al. (2002). Experimental verification is presented by Boutéca et al. (1994) for two sandstones. In the following, the results are analysed and presented in terms of Terzaghi effective stress.

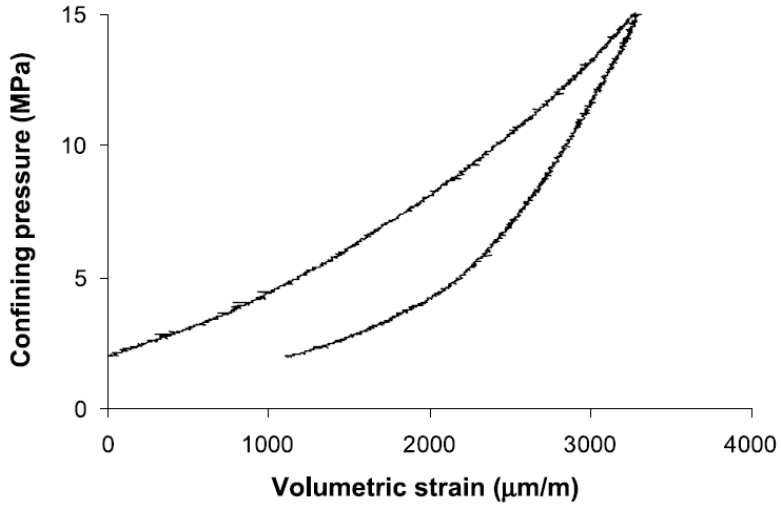

Figure 6: Drained hydrostatic compression test on Rothbach sandstone

The slope of the unloading curve is directly evaluated on the experimental data presented on Figure (6). For this test, the data were recorded every 2 seconds which corresponds approximately to 15 kPa of stress increment. In order to minimise the effect of small fluctuations of the recorded data on the resulting derivative, one can either fit the data with a mathematical function and calculate the derivative or evaluate the slope by a difference quotient calculated on a discrete set of *N* points centred on the corresponding point. The choice of N depends on the quality of the experimental data and on the amplitude of the fluctuations. The first method is commonly used and gives generally satisfactory results. However the mathematical form of the assumed fitting function obviously determines the derivative. Different mathematical functions can give equally good results for the fitting of given data, and result in different evaluations of the derivative. The second method based on discrete derivative calculus is used here. The slope S of a $x-y$ curve is given by:

$$S = \frac{\sum x^{(i)} \sum y^{(i)} - N \sum x^{(i)} y^{(i)}}{\left(\sum x^{(i)}\right)^2 - N \sum \left(x^{(i)}\right)^2} \tag{31}$$

where $x^{(i)}$ and $y^{(i)}$ are the coordinates of the ith point. To calculate the drained compression modulus K_d the $x^{(i)}$ and $y^{(i)}$ are respectively $\varepsilon_v^{(i)}$ and $\sigma'^{(i)}$, the volumetric strain and effective stress data at the ith point. With $N = 61$ the resulted compression modulus plotted as a function of the effective stress curve is presented in Figure (7). Based on these results, the tangent compression modulus K_d can be approximated with a bi-linear equation.

$$\begin{aligned} K_d &= 0.96\sigma' + 0.70 \qquad \sigma' \le 9\,MPa \\ K_d &= 0.07\sigma' + 8.72 \qquad \sigma' > 9\,MPa \end{aligned} \quad \text{with } K_d \text{ in GPa and } \sigma' \text{ in MPa} \tag{32}$$

Equation (32) expresses that the compression modulus increases significantly at relatively low effective stress (up to 9 MPa) and does not evolve much above this value. However, at higher stresses it is expected that pore collapse and grain crushing phenomena will induce a reduction of the compression modulus (Fortin et al. 2005).

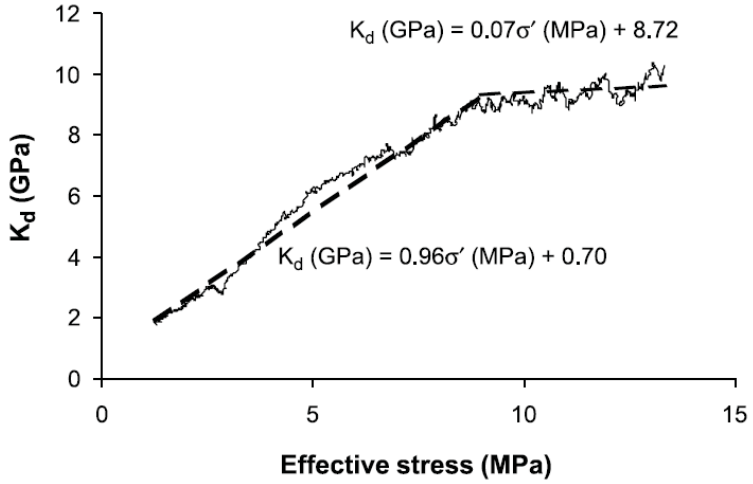

Figure 7: Drained compression modulus of Rothbach sandstone as a function of the effective stress

3.4 Thermal behaviour of Rothbach sandstone

In order to measure the thermal expansion coefficient of the rock, a drained heating test (see sub-problem (c) in Figure (1)) was carried out under a constant confining pressure. In the case of an inhomogeneous porous material (i.e., composed of two or more solids), the variation of volume of the sample in this test is characterized by the drained thermal expansion coefficient α_d. This coefficient can be expressed in terms of average over the porous medium volume (Palciauskas and Domenico 1982).

$$\alpha_d = \left(1 - n_0\right)\alpha_s + n_0\,\alpha_n \tag{33}$$

The difference between the expansion coefficients α_d and α_s reflects the difference between the thermal response of the bulk porous medium and that of the solid phase alone (McTigue 1986). In practice, the coefficient α_d also takes into account the non-reversible thermal deformations which can be produced by the microfracture generation due to the discrepancy between the thermal expansions of different minerals within the rock (Palciauskas and Domenico 1982). According to the experimental study of Walsh (1973), microfracture generation is only initiated at elevated temperatures. The test results also show that the reversible component of the drained expansivity α_d is approximately equal to that of the solid phase α_s. However, in practice, the expansion coefficient α_d is commonly used in the literature as a thermo-elastic coefficient (equivalent to α_b in Palciauskas and Domenico (1982) and α_s' in McTigue (1986)).

Using equation (9) in the equation (33) in the case of an ideal porous material, one finds $\alpha_d = \alpha_s$.

The initial temperature of the performed drained heating test was 21°C. The confining pressure and the pore water pressure during the test were maintained constant at 2.5 MPa and 1.0 MPa respectively. The drained thermal expansion coefficient is the slope of the temperature-volumetric strain response and is evaluated as $28\times10^{-6}\left(°C\right)^{-1}$ (Figure 8).

The coefficient of thermal expansion of the solid phase α_s can also be evaluated using homogenisation theory, knowing the mineralogy of the rock and the thermal expansion coefficients of its constituents. The following equation can be used to calculate the average thermal expansion coefficient of a two phase linear thermo-elastic composite material (Berryman 1995, Zaoui 2000):

$$\alpha_s^{\hom} = \left(f_1\alpha_s^{(1)} + f_2\alpha_s^{(2)}\right) + \frac{\dfrac{1}{K_s^{\hom}} - \left(\dfrac{f_1}{K_s^{(1)}} + \dfrac{f_2}{K_s^{(2)}}\right)}{\dfrac{1}{K_s^{(2)}} - \dfrac{1}{K_s^{(1)}}}\left(\alpha_s^{(2)} - \alpha_s^{(1)}\right) \tag{34}$$

where $\alpha_s^{(i)}$ is the thermal expansion coefficient of the ith constituent. The other parameters are introduced before in equation (30). Note that equation (34) reflects the thermo-mechanical coupling as the compressibility of the constituents and of the composite material affects its thermal expansion.

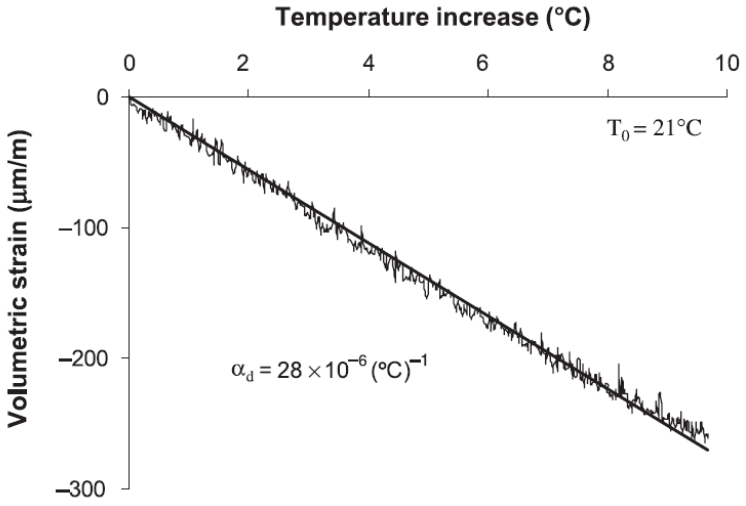

Figure 8: Drained heating test on Rothbach sandstone

The thermal expansion coefficient of quartz is equal to $33.4\times10^{-6}\left(°C\right)^{-1}$ (Palciauskas and Domenico 1982). The average thermal expansion coefficient of feldspars can be taken equal to $11.1\times10^{-6}\left(°C\right)^{-1}$ (Fei 1995). For the clay solid grains this coefficient is equal to $34\times10^{-6}\left(°C\right)^{-1}$ (McTigue 1986). Considering the small volume fraction of clay in Rothbach sandstone, the equation (34) can be used to calculate the homogenized thermal expansion coefficient of solid grains by neglecting this part and taking into account only quartz and feldspar minerals. Using the given parameters and the $K_s^{\hom}$ calculated with equation (30), the thermal expansion coefficient of Rothbach sandstone is found equal to $29.7\times10^{-6}\left(°C\right)^{-1}$. This value is in very good accordance with the measured thermal expansion coefficient equal to $28\times10^{-6}\left(°C\right)^{-1}$.

The phenomenon of thermal pressurization was studied in an undrained heating test under constant isotropic stress equal to 10 MPa. The initial temperature of the sample was 20°C. The results are shown on Figures (9) and (10) where the measured pore pressure increase and the volumetric strain are plotted versus the temperature increase. The non-linearity of the observed thermal pressurization is due to the (effective) stress-dependent compressibility of the sandstone and also to the temperature and pressure dependent compressibility and thermal expansion of pore water.

For a pore pressure close to the confining pressure, the pressurization curve becomes almost horizontal and no more fluid pressurization is observed. This phenomenon is probably due to the presence of water between the sample and the rubber membrane when the difference between the confining pressure and the pore pressure is too small. At the beginning of the test the volumetric strain could not be recorded due to a failure of the displacement sensors inside the triaxial cell. Therefore the volumetric strain-temperature curve only starts from 40°C.

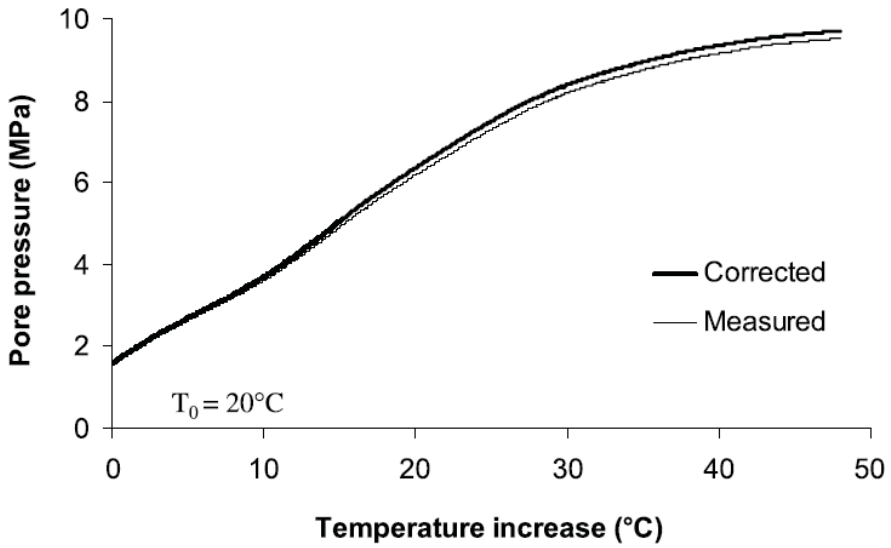

Figure 9: Undrained heating test on Rothbach sandstone: pore pressure change versus temperature increase – measured and corrected values

The coefficient of thermal pressurization is calculated for the measured temperature and pore pressure increase. Here again because of the small fluctuations of the experimental data, the derivative was calculated using equation (31). To calculate the thermal pressurization coefficient Λ the $x^{(i)}$ and $y^{(i)}$ are respectively $T^{(i)}$ and $p^{(i)}$, the temperature and pore pressure increase data at the ith point. The calculated thermal pressurization for $N = 61$ is presented on the Figure (11) as a function of the temperature. We can see that the thermal pressurization coefficient Λ increases up to about 0.25 MPa/°C and then decreases to 0.025 MPa/°C at the end of the test.

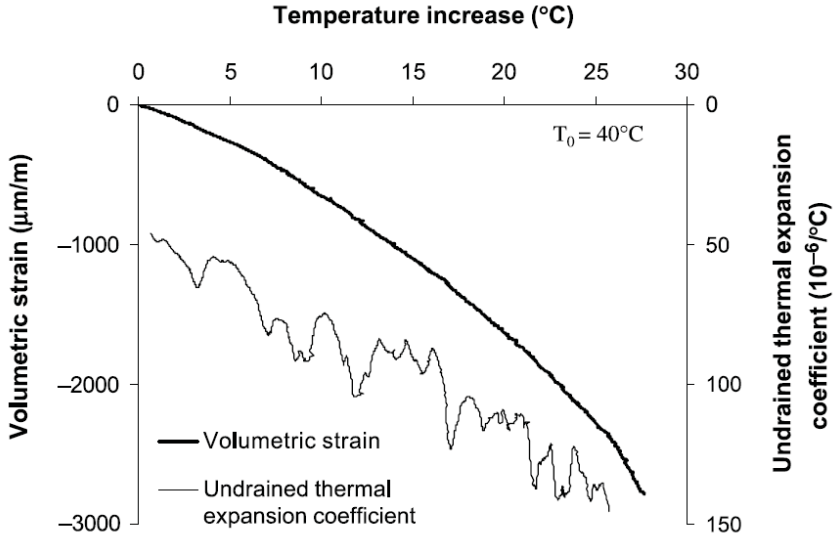

Figure 10: Undrained heating test on Rothbach sandstone: volumetric strain and undrained thermal expansion coefficient versus temperature increase

The undrained thermal expansion coefficient α_u is calculated using equation (31) replacing $x^{(i)}$ and $y^{(i)}$ respectively by $T^{(i)}$ and $\varepsilon_v^{(i)}$, the temperature and the volumetric strain data at the ith point. The result is presented in the Figure (10) and shows the increase of the undrained thermal expansion coefficient with the temperature. This important increase is mainly attributed to the increase of the thermal expansion coefficient of pore water with the temperature, shown in Figure (12).

3.5 Correction of measured pressurization

The observed pore pressure increase during the undrained heating test is corrected for the effect of drainage and pressure measurement system using equation (27). Because of the small fluctuations of the recorded data, this correction cannot be done directly on the coefficients calculated using equation (31). The measured temperature and pore pressure are first fitted with sixth degree polynomials as a function of data acquisition time and then the derivative of the pore pressure with respect to temperature (equal to the thermal pressurization coefficient Λ), is calculated (Figure 11). The comparison with the curve calculated using the equation (31) shows a good compatibility between the results. The corrected pressurization curve is then calculated and presented in the Figure (9). The corrected pore pressure is slightly greater than the measured one. However, due to the small volume of the drainage system, this difference is very limited. The corrected values of the thermal pressurization coefficient are also presented in Figure (11).

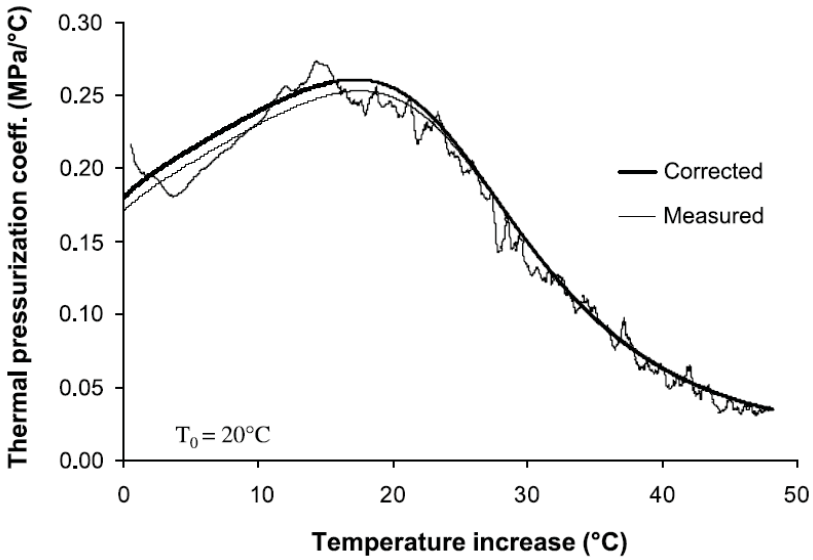

Figure 11: Undrained heating test on Rothbach sandstone: thermal pressurization coefficient versus temperature increase – measured and corrected values

4 Analytical simulation of the undrained heating test

The above analysis is validated through the simulation of the undrained heating test and comparison with the experimental results.

The formulation presented for the undrained thermo-elastic behaviour of porous materials along with the non-linear elastic constitutive model developed for the Rothbach sandstone enable us to simulate analytically the undrained heating test. As the test was performed under a constant confining pressure, the term $\Delta\sigma$ in the equations (13) and (18) is null. The pore pressure increase, while the confining pressure is maintained constant, induces a decrease of the effective stress (elastic unloading) and thus the expression of the compression modulus in unloading (equation (32)), must be used to calculate c_n in equation (16). It is assumed that the rock compressibility is not affected by temperature changes. The volumetric strains were calculated using equation (18). The thermal expansion coefficient and the compressibility of water depend upon the pore pressure and the temperature and this dependency is taken into account (Spang 2002). Figures (12) and (13) present respectively the variations of thermal expansion coefficient and compressibility of water with temperature for different pressures.

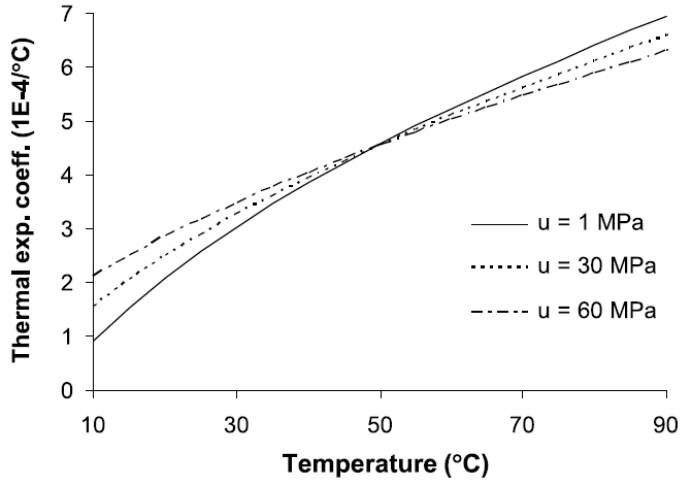

Figure 12: Variation of the thermal expansion coefficient of water with temperature and pressure

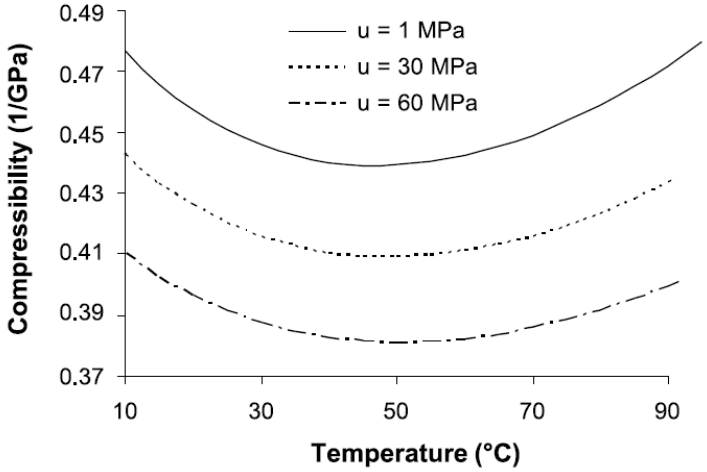

Figure 13: Variation of the compressibility of water with temperature and pressure

The results of simulation presented on Figures (14), (15), (16) and (17) show a good agreement with the results of undrained heating test. The phenomenon of thermal pressurization and also the undrained thermal expansion of the rock are well reproduced using the results of the drained isotropic compression and drained heating tests. This analytical simulation of the undrained heating test clearly shows the non-linear and (effective) stress-dependent character of thermal pressurization. Among the four parameters of equation (16), α_n is equal to $28\times10^{-6}\left(°C\right)^{-1}$ and remains constant during the simulation. c_f varies slightly between 0.45 GPa^{-1} and 0.43 GPa^{-1}. Therefore the variation of the thermal pressurization coefficient Λ is mainly controlled by the variations of α_f and c_n. The thermal expansion of water α_f varies with temperature and pressure and increases from $2.09\times10^{-4}\left(°C\right)^{-1}$ to $5.64\times10^{-4}\left(°C\right)^{-1}$ during the simulation. The compressibility of pore-volume c_n is calculated using equation (8). The compressibility of solid phase c_s is considered constant and the drained compressibility of rock c_d increases when the effective stress decreases (equation (32)). During the test, the pore pressure increase while the confining pressure is maintained constant, induces a decrease of the effective stress. Consequently the compressibility of pore-volume c_n increases during the simulation from 0.47 GPa^{-1} in the beginning of the simulation to 8.52 GPa^{-1} at the end for a zero effective stress. In the beginning of the test the increase of α_f with the temperature dominates and the thermal pressurization coefficient Λ

increases up to about 0.24 MPa/°C. Then the important increase of c_n decreases Λ to 0.06 MPa/°C at the end of the test.

As mentioned above, during the undrained heating test, the observed pore pressure cannot reach the confining pressure. However analytical simulation makes it possible to predict the critical temperature for which the pore pressure reaches the confining pressure: 68°C for this test.

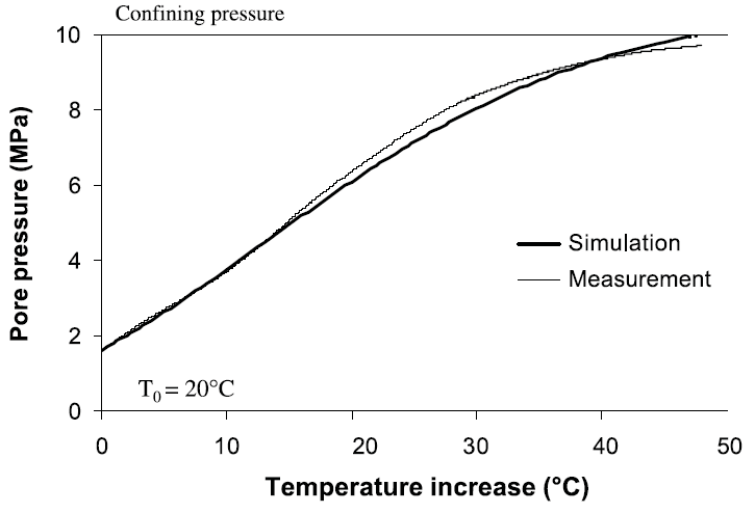

Figure 14: Analytical simulation of the undrained heating test on Rothbach sandstone, comparison with the measured pore pressure

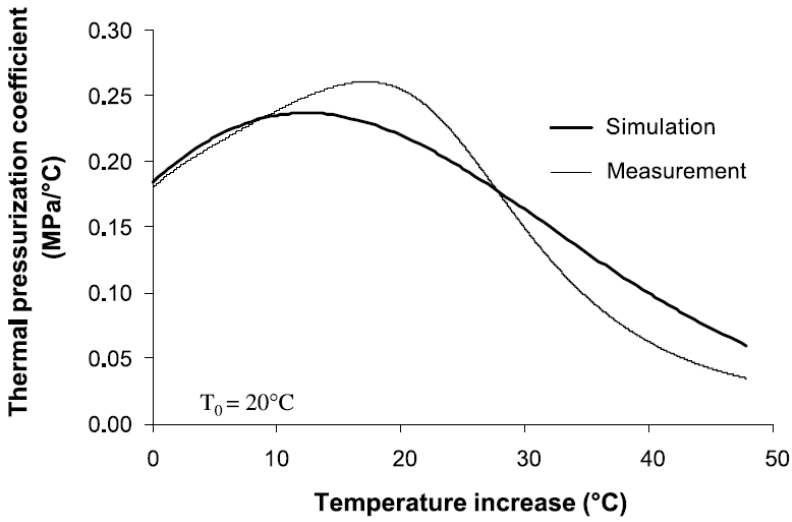

Figure 15: Analytical simulation of the results of the undrained heating test on Rothbach sandstone, comparison with the measured thermal expansion coefficient

5 Stress and temperature dependency of the thermal pressurization coefficient

In the previous sections the temperature and stress-dependent character of the thermal pressurization coefficient is clearly shown by the experimental results of the undrained heating test and the analytical simulation of this test. On one hand the temperature dependency of this coefficient is mainly due to the increase of the thermal expansion coefficient and in a lesser extent to the change of water compressibility with temperature. In some geomaterials the parameters c_d and c_s and consequently the pore-volume compressibility c_n (equation (8)) are also temperature sensitive which will also influence

the coefficient Λ. On the other hand the stress-dependency of the thermal pressurization coefficient is also due to the stress-dependent character of the drained compressibility c_d and consequently of the pore-volume compressibility c_n of the porous material, as presented above for the Rothbach sandstone.

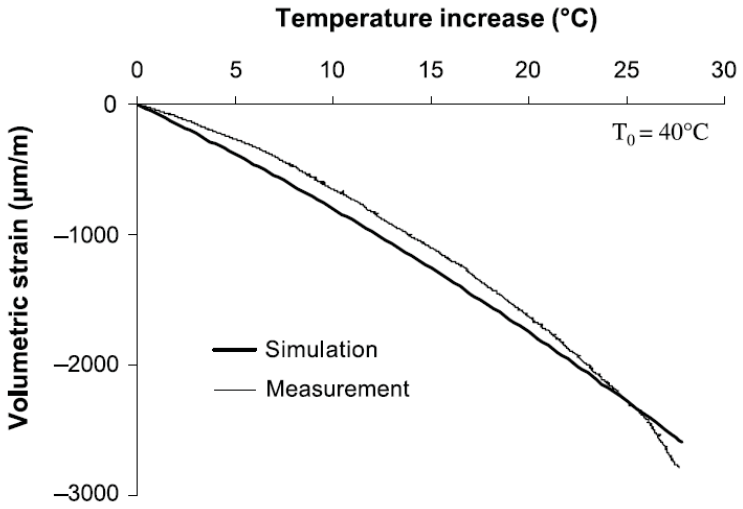

Figure 16: Analytical simulation of the results of the undrained heating test on Rothbach sandstone, comparison with the measured volumetric strain

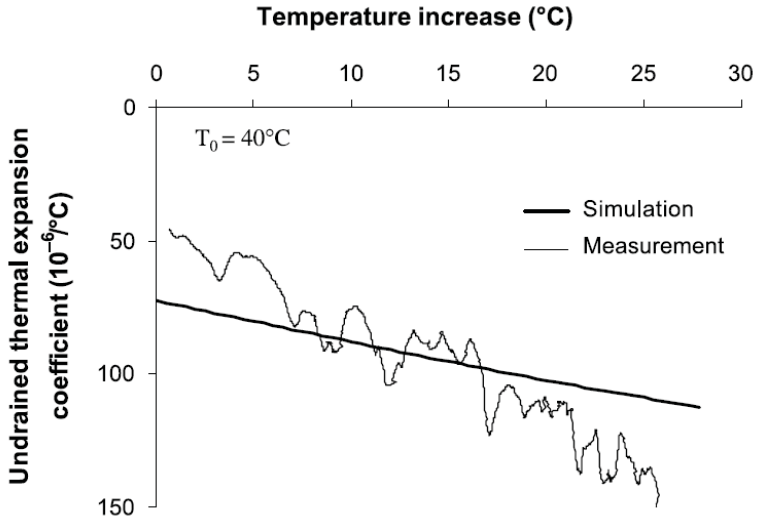

Figure 17: Analytical simulation of the results of the undrained heating test on Rothbach sandstone, comparison with the measured undrained thermal expansion coefficient

The first measurement of the thermal pressurization coefficient for sandstone is probably due to Campanella and Mitchell (1968) who also observed the stress-dependency of this coefficient. Applying a temperature increase from 5°C to 15°C, the measured Λ coefficient for 0.25 MPa and 0.58 MPa effective stresses was found respectively equal to 0.02 MPa/°C and 0.05 MPa/°C.

It is common in the literature to use a single average value for the thermal pressurization coefficient. This average value is calculated using the average values of α_f and c_f for a considered temperature range, and constant α_n and c_n coefficients. For example, Palciauskas and Domenico (1982) used the data provided by Dropek et al (1978) to estimate the coefficient of thermal pressurization of Kayenta sandstone. With $n = 0.2$, $K_d = 9.52 GPa$, $K_s = 39.1 GPa$ and the average water properties between 10°C to 90°C, the coefficient Λ was estimated equal to 0.59 MPa/°C.

Using the non-linear elastic model presented in equation (32), the measured values of α_s and c_s and knowing the compressibility and thermal expansion coefficient of water as functions of temperature and pore pressure, we can evaluate the thermal pressurization coefficient Λ of Rothbach sandstone as a function of temperature and effective stress (equation (16)) and obtain a good accordance with the undrained heating test as shown above. The calculated coefficient Λ is presented on Figure (18) as a function of the effective stress up to 15 MPa and for different temperatures from 20°C to 90°C. The results show clearly the (effective) stress and temperature dependent character of the thermal pressurization coefficient. The stress-dependency is significant in the range of stress-dependency of the rock compressibility (up to 9 MPa). The values of the coefficient Λ vary from 0.02 to 0.72 MPa/°C depending on the effective stress and the temperature.

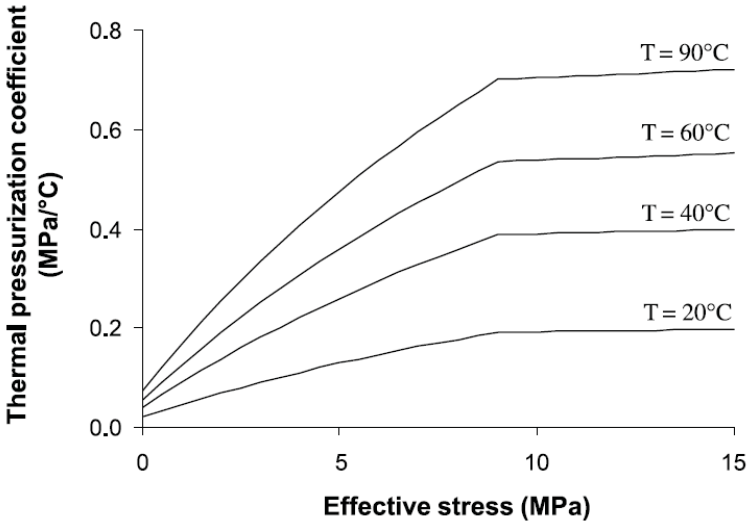

Figure 18: Variation of thermal pressurization coefficient of Rothbach sandstone with effective stress and temperature

6 Conclusion

The phenomenon of thermal pressurization is studied theoretically and experimentally for a saturated granular rock, the Rothbach sandstone. It has been demonstrated that this phenomenon is controlled, on one hand by the discrepancy between the thermal behaviour of the pore fluid and of the solid phase, and on the other hand by the compressibility of the pore volume. The strong influence of stress and temperature on thermal pressurization of rocks is explained by the stress-dependent character of the compressibility of porous rocks and by the effect of temperature and pressure on the thermal and mechanical properties of water.

The experimental study has consisted first in the characterisation of the mechanical and thermal response of the solid phase of the rock. A stress-dependent elastic model has been calibrated on a drained compression test. The experimental results of an undrained heating test showed clearly the stress and temperature dependent character of the thermal pressurization coefficient. In the analysis of the tests data, the effect of mechanical and thermal deformation of the drainage system has been accounted for. The results of the undrained heating test have been theoretically simulated and a good agreement with the experimental results has been obtained. This approach gives confidence in the evaluation of the thermal pressurization coefficient for various conditions of temperature and stress level.

7 Acknowledgments

The authors wish to thank Sylvine Guédon and Ahmad Pouya for fruitful discussions. They wish also to thank François Martineau for his assistance in the experimental work.

8 References

Bass, J.D. (1995): Elasticity of Minerals, Glasses, and Melts, in Mineral Physics and Crystallography: A Handbook of Physical Constants, American Geophysical Union Online Reference Shelf 2, Thomas J. Ahrens, Editor, 45-63

Berryman, J. G., (1992): Effective stress for transport properties of inhomogeneous porous rock, Journal of Geophysical Research, 97, 17409-17424

Berryman, J. (1995): Mixture Theories for Rock Properties, in Rock physics & phase relations: A Handbook of Physical Constants, American Geophysical Union Online Reference Shelf 3, Thomas J. Ahrens, Editor, 205-228

Bishop, A.W. and Eldin, A.K.G. (1950): Undrained triaxial tests on saturated sands and their significance in the general theory of shear strength, Géotechnique 2, No. 1, 13-32

Bishop, A.W. (1973): The influence of an undrained change in stress on the pore pressure in porous media of low compressibility, Géotechnique 23(3).

Bishop, A.W. (1976): The influence of system compressibility on the observed pore pressure response to an undrained change in stress in saturated rock, Géotechnique 26, No 2, 371-375

Boutéca M.J., Bary D., Piau, J.M., Kessler, N., Boisson, M., Fourmaintraux, D. (1994): Contribution of Poroelasticity to Reservoir Engineering: Lab Experiments, Application to Core Decompression and Implication in HP-HT Reservoirs Depletion, Proceedings of the Eurock'94, Delft, Balkema, Rotterdam, Paper SPE/ISRM 28093

Campanella, R.G. and Mitchell, J.K. (1968): Influence of temperature variations on soil behaviour, Jnl Soil Mech. Fdn Div., Am. Soc. Civ. Engrs, 94, SM3, 709-734

Coussy, O. (2004): Poromechanics, John Wiley & Sons

Detournay, E. and Cheng, A.H.-D. (1993): Fundamentals of Poroelasticity, Chap. 5 in Comprehensive Rock Engineering: Principles, Practice and Projects, Vol. II, Analysis and Design Method, ed. C. Fairhurst, Pergamon, 113-171

Dormieux, L., Molinari, A. and Kondo, D. (2002): Micromechanical approach to the behavior of poroelastic materials, Journal of the Mechanics and Physics of Solids, 50, 2203-2231

Dropek, R.K., Johnson, J.N., Walsh, J.B. (1978): The influence of pore pressure on the mechanical properties of Kayenta sandstone, Journal of Geophysical Research, Vol. 83, No. B6, 2817-2824

Fei, Y. (1995): Thermal Expansion, in Mineral Physics and Crystallography: A Handbook of Physical Constants, American Geophysical Union Online Reference Shelf 2, Thomas J. Ahrens, Editor, 29-44

Fortin, J., Schubnel, A., Gueguen, Y. (2005): Elastic wave velocities and permeability evolution during compaction of Bleurswiller sandstone, International Journal of Rock Mechanics & Mining Sciences, 42, 873-889

Gurevich, B., (2004): A simple derivation of the effective stress coefficient for seismic velocities in porous rocks, Geophysics, Vol. 69, No. 2, 393-397

Hill, R. (1952): The elastic behavior of crystalline aggregate, Proc. Physical Soc., London, A65, 349-354

Lachenbruch, AH (1980): Frictional heating, fluid pressure and the resistance to fault motion. Journal of Geophysical Research, 85, 6097-6112

Lockner, D.A. and Stanchits, S.A. (2002): Undrained poroelastic response of sandstones to deviatoric stress change, Journal of Geophysical Research, Vol. 107, No. B12, 2353

McTigue, D. F. (1986): Thermoelastic response of fluid-saturated porous rock, Journal of Geophysical Research, 91(B9), 9533-9542

Mesri, G., Adachi, K., Ulrich, C.R. (1976): Pore-pressure response in rock to undrained change in all-around stress, Géotechnique 26, No. 2, 317-330

Palciauskas, V.V. and Domenico, P.A. (1982): Characterization of drained and undrained response of thermally loaded repository rocks, Water Resources Research, Vol. 18, No. 2, 281-290

Rempel, A.W. and Rice, J.R. (2006): Thermal pressurization and onset of melting in fault zones, Journal of Geophysical Research, Vol. 111, B09314

Rice, J.R. and Cleary, M.P. (1976): Some basic stress diffusion solutions for fluid-saturated elastic porous media with compressible constituents, Review of geophysics and space physics, Vol. 14, No. 2, 227-240

Rice, J.R. (2006): Heating and weakening of faults during earthquake slip, Journal of Geophysical Research, Vol. 111, B05311

Skempton, A.W. (1954): The Pore Pressure Coefficients A and B, Géotechnique, 4, 143-147

Skempton, A.W. (1960): Effective stress in soils, concrete and rocks, Conference on pore pressure and suction in soils, 4-16, London, Butterworths

Spang, B. (2002): Excel Add-In for Properties of Water and Steam in SI-Units, http://www.cheresources.com/ iapwsif97.shtml

Sulem, J. Vardoulakis, I. Papamichos, E. Oulahna, A. Tronvoll, J. (1999): Elasto-plastic Modelling of Red Wildmoor Sandstone, Mechanics of Cohesive-frictional Materials, Vol 4, Number 3, 215-246

Sulem, J., Vardoulakis, I., Ouffroukh, H., Boulon, M., Hans, J. (2004) Experimental characterization of the thermo-poro-mechanical properties of the Aegion fault gouge, Comptes Rendus Geosciences, 336, 4-5, 455-466

Sulem, J. and Ouffroukh, H. (2006): Hydromechanical Behaviour of Fontainebleau Sandstone, Rock Mechanics and Rock Engineering, Volume 39, Number 3, 185-213

Sulem, J., Lazar, P. and Vardoulakis, I. (2007): Thermo-Poro-Mechanical Properties of Clayey Gouge and Application to Rapid Fault Shearing, Int. J. Num. Anal. Meth. Geomechanics, Volume 31, Issue 3, 523-540

Sultan, N. (1997): Etude du comportement thermo-mécanique de l'argile de Boom : expériences et modélisation, PhD thesis, CERMES, Ecole Nationale des Ponts et Chaussées, France

Vardoulakis, I., (2002): Dynamic thermo-poro-mechanical analysis of catastrophic landslides, Géotechnique, Vol. 52, No. 3, 157-171

Walsh, J.B. (1973): Theoretical bounds for thermal expansion, specific heat and strain energy due to internal stresses, Journal of Geophysical Research, 78, 7636-7647.

Wissa, A.E.Z. (1969): Pore pressure measurement in saturated stiff soils, Jnl Soil Mech. Fdn Div. Am. Soc. Civ. Engrs 95, SM4, 1063-1073

Zaoui, A. (2000): Matériaux hétérogènes et composites, Ecole Polytechnique

Zimmerman, R.W. (1991): Compressibility of sandstones, Elsevier, Amsterdam

4.3 Effet de chauffage sur la pâte de ciment durcie

Dans cette partie, l'influence d'un changement de température en conditions drainées et non-drainées sur la pâte de ciment durcie est étudiée expérimentalement en réalisant des essais de chauffage et de refroidissement drainés et non-drainés. Le coefficient d'expansion thermique drainé α_d du ciment étudié est trouvé constant, égal à $6\times10^{-5}(°C)^{-1}$. Au cours de la vie d'un puits pétrolier, le ciment peut être soumis à des changements de température suffisamment rapides pour exclure la possibilité de drainage du fluide interstitiel. L'effet d'un changement rapide de température est étudié ici à partir d'un essai de chauffage non-drainé. La surpression interstitielle mesurée dans cet essai est corrigée pour tenir compte de l'effet des déformations du système de drainage de la cellule triaxiale en utilisant la méthode présentée dans la section 4.2. Les résultats obtenus montrent que le coefficient de pressurisation thermique est sensiblement constant, égal à 0,6MPa/°C. Ce coefficient de pressurisation thermique est relativement important, comparé à d'autres géomatériaux (Ghabezloo et Sulem, 2008), ce qui montre l'importance des changements de contraintes effectives que peut occasionner un brusque changement de température dans un puits pétrolier. La mesure d'un coefficient de pressurisation thermique qui ne varie pas avec la température semble d'être en contradiction avec la variation du coefficient d'expansion thermique de l'eau avec la température et les discussions présentées dans la section 4.2. L'analyse des résultats de l'essai de chauffage non-drainé montre que ce phénomène peut être attribué à l'anomalie du comportement thermique du fluide interstitiel du ciment due à son confinement dans des pores de très petite taille et aussi à la présence des ions dans le fluide interstitiel. Les résultats de l'analyse montrent que le coefficient d'expansion thermique du fluide interstitiel du ciment est plus important que celui de l'eau pure. De plus, le coefficient d'expansion thermique du fluide interstitiel du ciment semble d'être moins sensible aux variations de la température que celui de l'eau pure.

Cement and Concrete Research 39 (2009) 54–64

Contents lists available at ScienceDirect

Cement and Concrete Research

journal homepage: http://ees.elsevier.com/CEMCON/default.asp

The effect of undrained heating on a fluid-saturated hardened cement paste

Siavash Ghabezloo [a,*], Jean Sulem [a], Jérémie Saint-Marc [b]

[a] Université Paris-Est, UR Navier, CERMES, Ecole Nationale des Ponts et Chaussées, Marne la Vallée, France
[b] TOTAL, Management of Residual Gases Project, Pau, France

Abstract

The effect of undrained heating on volume change and induced pore pressure increase is an important point to properly understand the behaviour and evaluate the integrity of an oil well cement sheath submitted to rapid temperature changes. This thermal pressurization of the pore fluid is due to the discrepancy between the thermal expansion coefficients of the pore fluid and of the solid matrix. The equations governing the undrained thermo-hydro-mechanical response of a porous material are presented and the effect of undrained heating is studied experimentally for a saturated hardened cement paste. The measured value of the thermal pressurization coefficient is equal to 0.6MPa/°C. The drained and undrained thermal expansion coefficients of the hardened cement paste are also measured in the heating tests. The anomalous thermal behaviour of cement paste pore fluid is back analysed from the results of the undrained heating test.

***Keywords*:** hardened cement paste, thermo-poro-elasticity, thermal pressurization, pore pressure, thermal expansion

1 Introduction

Temperature increase in saturated porous materials under undrained condition leads to volume change and pore fluid pressure increase. This thermal pressurization of the pore fluid is due to the discrepancy between the thermal expansion coefficients of the pore fluid and of the solid phase. This increase of the pore fluid pressure induces a reduction of the effective mean stress, and can lead to shear failure or hydraulic fracturing. This phenomenon is important in petroleum engineering where the reservoir rock and the well cement lining undergo sudden temperature changes. This is for example the case when extracting heavy oils by steam injection methods where steam is injected into the reservoir to heat the oil to a temperature at which it flows. This rapid increase of temperature could damage cement sheath integrity of wells and lead to loss of zonal isolation. As a consequence, its impact on cement behaviour should be properly understood to be pro-active when designing cement sheath integrity.

The phenomenon of thermal pressurization is also important in environmental engineering for radioactive (exothermal) waste disposal in deep clay geological formations as well as in geophysics in the studies of rapid fault slip events when shear heating tends to increase the pore pressure and to decrease the effective compressive stress and the shearing resistance of the fault material [1].

The values of the thermal pressurization coefficient, defined as the pore pressure increase due to a unit temperature increase in undrained condition, is largely dependent upon the nature of the material, the state of stress, the range of temperature change, the induced damage. The large variability of the thermal pressurization coefficient reported in the literature for different porous materials with values from 0.01MPa/°C to 1.5MPa/°C (see Ghabezloo and Sulem [2] for a review) highlights the necessity of laboratory studies.

The aim of this paper is to study the effect of undrained heating and the phenomenon of thermal pressurization for a fluid-saturated hardened cement paste. Using the framework of thermo-poro-mechanics, the response of hardened cement paste to heating is modelled. An experimental program of drained and undrained heating tests is performed and the tests results are critically discussed.

A better understanding of the effect of undrained heating and induced thermal pressurization phenomenon is an important point to properly understand the behaviour and evaluate the integrity of an oil well cement sheath submitted to rapid temperature changes.

2 Thermo-Poro-Mechanical background

We present here the framework used to describe the thermo-elastic volumetric behaviour of a porous material which can be heterogeneous and anisotropic at the micro-scale. The theoretical basis of the formulation has been presented in many earlier studies. Among them, one can refer to the milestone papers and textbooks of Biot and Willis [3], Brown and Korringa [4], Rice and Cleary [5], Palciauskas and Domenico [6], McTigue [7], Zimmerman [8], Detournay and Cheng [9], Vardoulakis and Sulem [10], Coussy [11]. This framework is recalled here in a comprehensive manner in order to clarify the mathematical and physical significance of the different parameters which are measured in our experimental program. We extend here the presentation made in Ghabezloo *et al*. [12] to account for the effect of temperature.

A fluid saturated porous material can be seen as a mixture of two phases: a solid phase and a fluid phase. The solid phase may be itself made up of several constituents. The porosity ϕ is defined as the ratio of the volume of the porous space V_ϕ to the total volume V in the actual (deformed) state.

$$\phi = \frac{V_\phi}{V} \tag{1}$$

For a saturated material, the volume of the pore space is equal to the volume of the fluid phase. We consider a saturated sample under an isotropic state of stress σ (positive in compression). We choose three independent variables for characterizing the volumetric response of a porous material: the pore pressure p_f, the differential pressure σ_d as defined below and the temperature T.

$$\sigma_d = \sigma - p_f \tag{2}$$

The expression of the variations of the total volume V and of the pore volume V_ϕ introduces six parameters:

$$\frac{dV}{V} = \frac{1}{V}\left(\frac{\partial V}{\partial \sigma_d}\right)_{p_f,T} d\sigma_d + \frac{1}{V}\left(\frac{\partial V}{\partial p_f}\right)_{\sigma_d,T} dp_f + \frac{1}{V}\left(\frac{\partial V}{\partial T}\right)_{p_f,\sigma_d} dT$$

$$\frac{dV_\phi}{V_\phi} = \frac{1}{V_\phi}\left(\frac{\partial V_\phi}{\partial \sigma_d}\right)_{p_f,T} d\sigma_d + \frac{1}{V_\phi}\left(\frac{\partial V_\phi}{\partial p_f}\right)_{\sigma_d,T} dp_f + \frac{1}{V_\phi}\left(\frac{\partial V_\phi}{\partial T}\right)_{p_f,\sigma_d} dT \tag{3}$$

$$\frac{1}{K_d} = -\frac{1}{V}\left(\frac{\partial V}{\partial \sigma_d}\right)_{p_f,T} \quad , \quad \frac{1}{K_p} = -\frac{1}{V_\phi}\left(\frac{\partial V_\phi}{\partial \sigma_d}\right)_{p_f,T} \tag{4}$$

$$\frac{1}{K_s} = -\frac{1}{V}\left(\frac{\partial V}{\partial p_f}\right)_{\sigma_d,T} \quad , \quad \frac{1}{K_\phi} = -\frac{1}{V_\phi}\left(\frac{\partial V_\phi}{\partial p_f}\right)_{\sigma_d,T} \tag{5}$$

$$\alpha_d = \frac{1}{V}\left(\frac{\partial V}{\partial T}\right)_{p_f,\sigma_d} \quad , \quad \alpha_\phi = \frac{1}{V_\phi}\left(\frac{\partial V_\phi}{\partial T}\right)_{p_f,\sigma_d} \tag{6}$$

Equation (4) corresponds to an isotropic and isothermal drained compression test in which the pore pressure is controlled to remain constant in the sample. The variations of the total volume of the sample V and of the volume of the pore space V_ϕ with respect to the applied confining pressure give the (isothermal) drained bulk modulus K_d and the modulus K_p. Equation (5) corresponds to the so-called unjacketed isothermal compression test, in which equal increments of confining pressure and pore pressure are simultaneously applied to the sample, as if the sample is submerged, without a jacket, into a fluid under the pressure p_f. The differential pressure σ_d in this condition remains constant. Neglecting the deformation of the jacket, the measured volumetric strain with the applied pressure gives the unjacketed modulus K_s. The variation of the pore volume of the sample in this test, evaluated from the quantity of fluid exchanged between the sample and the pore pressure generator when applying equal increments of confining pressure and pore pressure could in principle give the modulus K_ϕ. However experimental evaluation of this parameter is very difficult as the volume of the exchanged fluid has to be corrected for the effect of fluid compressibility and also for the effect of the deformations of the pore pressure generator and drainage system in order to access to the variation of the pore volume of the sample. In the case of a porous material which is homogeneous and isotropic at the micro-scale, the sample would deform in an unjacketed test as if all the pores were filled with the solid component. The skeleton and the solid component experience a uniform volumetric strain with no change of the porosity [9]. For such a material $K_s = K_\phi = K_m$, where K_m is the bulk modulus of the single solid constituent of the porous material. In the case of a porous material which is composed of two or more solids and

therefore is heterogeneous at the micro-scale, the unjacketed modulus K_s is some weighted average of the bulk moduli of solid constituents [13]. The modulus K_ϕ for such a material has a complicated dependence on material properties. Generally it is not bounded by the elastic moduli of the solid components and can even have a negative sign if the bulk moduli of the individual solid components are greatly different one from another [14][15].

Equation (6) corresponds to a drained heating test in which the pore pressure is controlled to remain constant in the sample while the thermal loading is applied. The variations of the total volume of the sample V and of the volume of the pore space V_ϕ with respect to the applied thermal loading give the volumetric drained thermal expansion coefficient α_d and pore volume thermal expansion coefficient α_ϕ. According to Palciauskas and Domenico [6], the coefficient α_d measured in a heating test also takes into account the non-reversible thermal deformations which can be produced by the microfracture generation due to the discrepancy between the thermal expansions of different constituents of the porous material, but the experimental study of Walsh [16] on rocks showed that the microfracture generation is only initiated at elevated temperatures. Like for K_ϕ, the experimental evaluation of α_ϕ is very difficult as the volume of the exchanged fluid has to be corrected for the effect of thermal expansion of the fluid and also for the effect of the thermal deformations of the pore pressure generator and of the drainage system in order to access to the variation of the pore volume of the sample. In the case of a micro-homogeneous and micro-isotropic porous material, $\alpha_d = \alpha_\phi = \alpha_m$, where α_m is the thermal expansion coefficient of the single solid constituent of the porous material. For such a material, there is no change of porosity during a drained thermal loading because an isotropic thermal expansion would cause a proportional change in every linear dimension of the body. In the general case, the difference between the expansion coefficients α_d and α_m reflects the difference between the thermal response of the bulk porous medium and that of the solid phase alone [7].

Using Betti's reciprocal theorem the following relation between the elastic moduli is obtained [4]:

$$\frac{1}{K_p} = \frac{1}{\phi}\left(\frac{1}{K_d} - \frac{1}{K_s}\right) \tag{7}$$

Using equation (7), the number of the required parameters to characterize the volumetric thermo-elastic behaviour of a porous material is reduced to five.

The variations of the total volume V and of the pore volume V_ϕ (equation (3)) can be rewritten as follows:

$$\begin{aligned} \frac{dV}{V} &= -\frac{d\sigma_d}{K_d} - \frac{dp_f}{K_s} + \alpha_d dT \\ \frac{dV_\phi}{V_\phi} &= -\frac{d\sigma_d}{K_p} - \frac{dp_f}{K_\phi} + \alpha_\phi dT \end{aligned} \tag{8}$$

The incremental volumetric strain $d\varepsilon = -dV/V$ is thus expressed as:

$$d\varepsilon = -\frac{dV}{V} = \frac{d\sigma_d}{K_d} + \frac{dp_f}{K_s} - \alpha_d dT \tag{9}$$

Using the definition of the porosity presented in equation (1), the following equation is obtained for the variation of the porosity:

$$\frac{d\phi}{\phi} = \frac{dV_\phi}{V_\phi} - \frac{dV}{V} \tag{10}$$

Replacing equations (8) and (7) in equation (10), the expression of the variation of porosity is obtained:

$$\frac{d\phi}{\phi} = -\frac{1}{\phi}\left(\frac{1-\phi}{K_d} - \frac{1}{K_s}\right) d\sigma_d + \left(\frac{1}{K_s} - \frac{1}{K_\phi}\right) dp_f - \left(\alpha_d - \alpha_\phi\right) dT \tag{11}$$

Equation (11) clearly shows that in the case of an ideal porous material ($\alpha_d = \alpha_\phi, K_s = K_\phi$) there would be no change of porosity during an isotropic thermal loading or during an unjacketed loading ($d\sigma_d = 0$).

The undrained condition is defined as a condition in which the mass of the fluid phase is constant ($dm_f = 0$). Under this condition we choose three different independent variables: the total stress σ, the fluid mass m_f, and the temperature T. The measured quantities are the total volume V and the pore pressure p_f. Writing the expression of the variation of these quantities, we can define four new parameters to describe the response of the porous material in undrained condition:

$$B = \left(\frac{\partial p_f}{\partial \sigma}\right)_{m_f,T} \quad , \quad \frac{1}{K_u} = -\frac{1}{V}\left(\frac{\partial V}{\partial \sigma}\right)_{m_f,T} \tag{12}$$

$$\Lambda = \left(\frac{\partial p_f}{\partial T}\right)_{m_f,\sigma} \quad , \quad \alpha_u = \frac{1}{V}\left(\frac{\partial V}{\partial T}\right)_{m_f,\sigma} \tag{13}$$

The parameter K_u is the undrained bulk modulus and B is the so-called Skempton coefficient [17]. α_u is the undrained volumetric thermal expansion coefficient and Λ is the thermal pressurization coefficient. Fluid mass conservation under undrained condition leads to the following expression for variation of the volume of the fluid:

$$-\frac{dV_\phi}{V_\phi} = \frac{dp_f}{K_f} - \alpha_f dT \tag{14}$$

where K_f and α_f are respectively the fluid compression modulus and thermal expansion coefficient. Replacing equation (14) in equation (8) and using equations (2) and (7) the following expression is found for the variation of pore pressure with the confining pressure and temperature in undrained condition:

$$dp_f = \frac{\left(1/K_d - 1/K_s\right)}{\left(1/K_d - 1/K_s\right) + \phi\left(1/K_f - 1/K_\phi\right)} d\sigma + \frac{\phi\left(\alpha_f - \alpha_\phi\right)}{\left(1/K_d - 1/K_s\right) + \phi\left(1/K_f - 1/K_\phi\right)} dT \tag{15}$$

Comparing equation (15) with the definitions of the Skempton coefficient B and of the thermal pressurization coefficient Λ (equations (12) and (13)), we obtain:

$$B = \frac{\left(1/K_d - 1/K_s\right)}{\left(1/K_d - 1/K_s\right) + \phi\left(1/K_f - 1/K_\phi\right)} \tag{16}$$

$$\Lambda = \frac{\phi\left(\alpha_f - \alpha_\phi\right)}{\left(1/K_d - 1/K_s\right) + \phi\left(1/K_f - 1/K_\phi\right)} \tag{17}$$

Equation (17) clearly highlights that the thermal pressurization of porous materials is caused by the discrepancy between the thermal expansion of the pore fluid and the one of the pore volume.

The variation of the total volume in undrained condition is given by the undrained bulk modulus K_u and the undrained thermal expansion coefficient α_u as presented in equations (12) and (13). Replacing $dV/V = -d\sigma/K_u + \alpha_u dT$, $d\sigma_d = d\sigma - dp_f$ and $dp_f = Bd\sigma + \Lambda dT$ in equation (9), the following relationships are found between the various coefficients:

$$K_u = \frac{K_d}{1 - B\left(1 - K_d/K_s\right)} \tag{18}$$

$$\alpha_u = \alpha_d + \Lambda\left(1/K_d - 1/K_s\right) \tag{19}$$

Using equations (16) and (17) in equation (19) the following expression as presented by McTigue [7] for the undrained thermal expansion coefficient is retrieved:

$$\alpha_u = \alpha_d + \phi B\left(\alpha_f - \alpha_\phi\right) \tag{20}$$

2.1 Influence of non-elastic strains

The above framework can be extended to account for the effect of non-elastic strains. These strains can be plastic, viscoelastic or viscoplastic and induce non-elastic porosity changes. The non-elastic changes of the total volume, pore volume and solid volume are defined by:

$$dV^{ne} = dV - dV^e \; ; dV_\phi^{ne} = dV_\phi - dV_\phi^e \; ; dV_s^{ne} = dV_s - dV_s^e \tag{21}$$

The non-elastic increment of pore volume dV_ϕ^{ne} can be calculated from the definition of the porosity (equation (1)) and knowing that $V_\phi = V - V_s$.

$$dV_\phi^{ne} = dV_\phi - dV_\phi^e = V\left[-d\varepsilon^{ne} + (1-\phi)d\varepsilon_s^{ne}\right] \tag{22}$$

From (22) we obtain:

$$\frac{dV_\phi^{ne}}{V_\phi} = \frac{-1}{\phi}\left[d\varepsilon^{ne} - (1-\phi)d\varepsilon_s^{ne}\right] \tag{23}$$

Using equation (23), equation (8) is re-written with the additional contribution of the non-elastic volume changes:

$$\begin{aligned} -\frac{dV}{V} &= \frac{d\sigma_d}{K_d} + \frac{dp_f}{K_s} - \alpha_d dT + d\varepsilon^{ne} \\ -\frac{dV_\phi}{V_\phi} &= \frac{d\sigma_d}{K_p} + \frac{dp_f}{K_\phi} - \alpha_\phi dT + \frac{d\varepsilon^{ne}}{\phi} - \frac{1-\phi}{\phi} d\varepsilon_s^{ne} \end{aligned} \tag{24}$$

Using equations (10) and (24) the following relation is obtained for the variations of the porosity:

$$\frac{d\phi}{\phi} = -\frac{1}{\phi}\left(\frac{1-\phi}{K_d} - \frac{1}{K_s}\right)d\sigma_d + \left(\frac{1}{K_s} - \frac{1}{K_\phi}\right)dp_f - \left(\alpha_d - \alpha_\phi\right)dT - \frac{1-\phi}{\phi}\left(d\varepsilon^{ne} - d\varepsilon_s^{ne}\right) \tag{25}$$

Replacing equation (14) in equation (24) and using equations (2) and (7), the following expression is found for the variation of pore pressure with the confining pressure and temperature in undrained condition, in presence of non-elastic volume changes:

$$dp_f = Bd\sigma + \Lambda dT + \frac{d\varepsilon^{ne} - (1-\phi)d\varepsilon_s^{ne}}{(1/K_d - 1/K_s) + \phi(1/K_f - 1/K_\phi)} \tag{26}$$

Equation (26) shows that non-elastic volume changes add an additional term in the generated pore pressure. In the case of a material for which the solid phase is elastic ($d\varepsilon_s^{ne} = 0$), equation (26) can be rewritten as:

$$dp_f = Bd\sigma + \Lambda dT + \frac{d\varepsilon^{ne}}{(1/K_d - 1/K_s) + \phi(1/K_f - 1/K_\phi)} \tag{27}$$

2.2 Cement paste porosity to be used for poromechanical calculations

The size of pores in the microstructure of hardened cement paste covers an impressive range, from nanometre-sized gel pores, to micro-metre sized capillary pores and millimetre-sized air voids [18]. From the different microstructural models of C-S-H, it can be seen that a part of the water in the pore structure of cement paste is interlayer structural water. Feldman and Sereda [19] propose a model for multilayer structure of C-S-H that postulates the existence of interlayer space containing strongly adsorbed water. According to Feldman [20], the interlayer water behaves as a solid bridge between the layers and consequently the interlayer space can not be included in the porosity and the interlayer water must be regarded as a part of the solid structure of hydrated cement paste. Feldman's experiments show that the interlayer water evaporates at very low relative humidity, below 11%. This can be seen also in Jennings' [21][22] microstructural model of C-S-H, in which the amorphous colloidal structure of the C-S-H is organized in elements, called 'globules'. In Jennings' [22] model, the globule is composed of solid C-S-H sheets, intra-globule porosity and a monolayer of water on the surface. For relative humidities below 11%, a part of the water filling the intra-globule porosity is evaporated. In a porosity measurement procedure in which the sample is dried at 105°C until a constant mass is achieved, a part of the interlayer water is evaporated and is thus included in the measured porosity [18][23]. Consequently, the porosity measured by oven-drying at 105°C should not be used in poromechanical formulation, as it includes a part of the interlayer porosity. The free-water porosity is defined and measured by equilibrating the cement paste at 11% relative humidity [18][23]. Some measurements of the free-water porosity, which is obviously smaller than the total porosity measured by drying at 105°C, from Feldman [24] are presented by Jennings *et al*. [18]. From the above discussion it appears that the free-water porosity is the cement paste porosity that should be used in the poromechanical formulations. This is in accordance with the assumption made by Ulm *et al*. [25] in their multi-scale microstructural model for the evaluation of the poromechanical properties of hardened cement paste. These authors use the Jennings' [21] model and exclude the intra-globule porosity from the cement paste porosity used in the calculations. According to Ulm *et al*. [25], considering the characteristic size of the interlayer space, which is less than ten water molecules in size, it is recognized that the water in this space can not be regarded as a bulk water phase. On the other hand, Scherer *et al*. [26] consider that the pores with a diameter less than 2nm, which corresponds to the size of 8 water molecules, can participate in water transfer phenomenon for the permeabilities in the range of nanodarcy (10-21m2). According to these authors, on the surface of the solid, the thickness of the layer of immobile water is about 0.5nm which corresponds to two water molecules. Accordingly, these authors reduce the total porosity of the cement paste for the effect of the thickness of the immobile water (see equation 17 in Scherer *et al*. [26]).

In Ghabezloo *et al*. [12], the analysis of the experimentally evaluated poroelastic parameters of the hardened cement paste clearly shows that the porosity that should be used in poromechanical calculations is smaller than the total porosity. This statement is based on the following inequality [13]:

$$\frac{1}{K_\phi} \leq \frac{1-K_d/K_s}{\phi K_s} \tag{28}$$

Replacing this inequality in the expression of $1/K_\phi$ obtained from equation (16) the following upper limit is obtained for the cement paste porosity:

$$\phi \leq K_f \left(\frac{1}{K_d} - \frac{1}{K_s} \right) \left(\frac{K_d}{K_s} + \frac{1-B}{B} \right) \tag{29}$$

Replacing the values of poroelastic parameters, $K_d = 8.7\text{GPa}$, $K_s = 21\text{GPa}$ and $B = 0.4$ evaluated in experimental study of Ghabezloo *et al*. [12], and taking $K_f = 2.2\text{GPa}$, from equation (29) we obtain $\phi \leq 0.28$ which is smaller than the total porosity of the tested cement paste, measured by oven drying at 105°C equal to 0.35. This analysis is in accordance with the discussion presented above and confirms that the porosity of the cement paste that should be used in poromechanical calculations is smaller than the total porosity.

Taylor [23] (in his Fig. 8.5) presents the values of total and free-water porosity derived from calculated phase compositions of mature ordinary cement paste with varying w/c ratio. The comparison of the calculated free-water porosity with the porosity measured by mercury intrusion shows that for w/c ratios smaller than 0.5, the free-water porosity can be approximated by the mercury porosity. For higher w/c ratios, the free-water porosity is somewhat higher than the mercury porosity. This approximation of the free-water porosity with the mercury porosity is made in Ghabezloo *et al*. [12] and a very good compatibility of the experimental results is obtained.

3 Experimental program

In order to evaluate the effect of temperature on the behaviour of hardened cement paste a drained and an undrained heating test are performed and presented in the following.

3.1 Sample preparation

A class G oil well cement was used to prepare the cement paste with a water to cement ratio $w/c = 0.44$. Two additives, a dispersant and an anti-foaming agent were used in the paste. The fresh paste is conserved in 14cm cubic moulds for four days in lime saturated water at 90°C temperature. After this period the temperature is reduced slightly to prevent the cracking of the blocs due to a sudden temperature change. Then, the blocs were cored and cut to obtain cylindrical samples with 38mm diameter and 76mm length. The two ends of the cylindrical samples were rectified to obtain horizontal surfaces. After the preparation of the samples, the geometry and the weight of the samples were measured. To insure the homogeneity and the integrity of the samples, measurements of wave velocity and dynamic elastic modulus were performed on all of them. These measurements were performed in ambient temperature.

After the sample preparation phase, the samples have been submerged in a fluid which is neutral regarding to the pore fluid of the cement paste to prevent chemical reactions during the period of curing. The composition of the natural fluid, presented in Table (1), is provided by TOTAL and is commonly

used in the laboratory experiments of the company. The samples were cured for at least three months at 90°C in the neutral fluid with pH=13 before performing the tests. Before doing each test, the temperature of the sample was reduced slowly to prevent any thermal cracking.

Material	**Quantity (g) in 1kg pure water**
$Al(OH)_3$	7.8
$Ca(OH)_2$	7.4
NaCl	0.3
NaOH	5.93
Na_2SO_4	7.6
SiO_2	1.2
pH ≈	**13**

Table 1- Composition of neutral fluid

The porosity of the samples is studied by two methods: oven drying and mercury intrusion porosimetry. The total porosity is measured by drying the samples at 105°C until a constant mass is achieved, and an average value equal to $\phi = 0.35$ is obtained. As mentioned in section 2.2, this porosity includes a part of the interlayer space of the cement paste. The mercury intrusion porosimetry is performed on the samples which are dried before the tests with the freeze-drying technique using liquid nitrogen which is, according to Gallé [27], the most suitable drying procedure to investigate the pore structure of cement-based materials. With a maximum intruding pressure of 200MPa the average mercury porosity of the samples is obtained equal to $\phi = 0.26$ (Figure (1)). Using the Washburn-Laplace equation ($P = -4\gamma\cos\theta/d$) and assuming a contact angle θ of 130° and a surface tension of mercury γ of 0.483N/m from Ref.[23], the maximum intruding pressure P of 200MPa corresponds to a minimum pore diameter of about 6nm. Based on the discussions of section 2.2, this value of $\phi = 0.26$ will be used as an approximation of the free-water porosity of the studied cement paste in the following poromechanical calculations, as we did also in the study of poromechanical properties of the studied hardened cement paste, presented in Ghabezloo *et al*. [12].

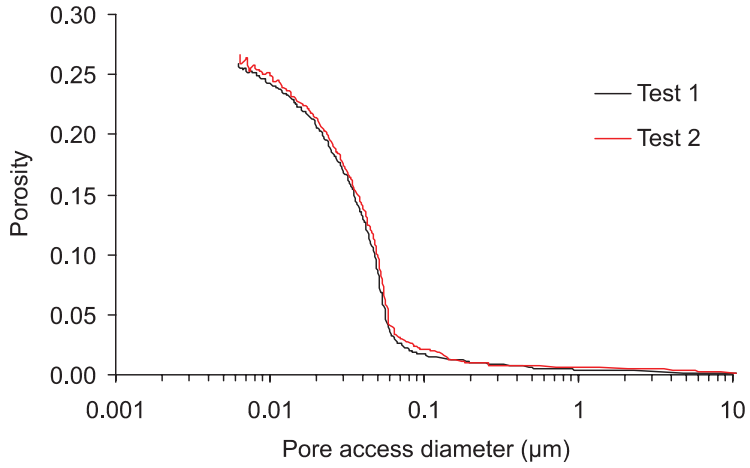

Figure 1- Mercury intrusion porosimetry tests

3.2 Experimental setting

The triaxial cell used in this study can sustain a confining pressure up to 60MPa. It contains a system of hydraulic self-compensated piston. The loading piston is then equilibrated during the confining pressure build up and directly applies the deviatoric stress. The axial and radial strains are measured directly on the sample inside the cell with two axial transducers and four radial ones of LVDT type. The confining pressure is applied by a servo controlled high pressure generator. Hydraulic oil is used as confining fluid. The pore pressure is applied by another servo-controlled pressure generator with possible control of pore volume or pore pressure.

The heating system consists of a heating belt around the cell which can apply a temperature change with a given rate and regulate the temperature, and a thermocouple which measures the temperature of the heater. In order to limit the temperature loss, an insulation layer is inserted between the heater element and the external wall of the cell. A second insulation element is also installed beneath the cell. The heating system heats the confining oil and the sample is heated consequently. Therefore there is a discrepancy between the temperature of the heating element in the exterior part of the cell and that of the sample. In order to control the temperature in the centre of the cell, a second thermocouple is placed at the vicinity of sample. The temperature given by this transducer is considered as the sample temperature in the analysis of the test results. Further details and a schematic view of this triaxial cell are presented in Ghabezloo and Sulem [2] and Sulem and Ouffroukh [28].

3.2.1 Effect of mechanical and thermal deformation of the drainage system

The undrained condition is defined as a condition in which there is no change in the fluid mass of the porous material. Achieving this condition in a conventional triaxial system is very difficult. In these systems an undrained test is usually performed by closing the valves of the drainage system. As the drainage system is compressible, it experiences volume changes with pressure and temperature changes. A variation of the volume of the drainage system induces a fluid flow into or out of the sample to achieve pressure equilibrium between the sample and the drainage system. This fluid mass exchange between the sample and the drainage system and more generally the mechanical and thermal deformations of the drainage system modify the measured pore pressure during the test.

Ghabezloo and Sulem [2] have presented an extension of the formulation of Bishop [29] and have proposed a simple method for the correction of pore pressure measurements during an undrained heating test. This method requires only two simple calibration tests to determine the needed parameters. The resulting equation which links the corrected value Λ_{cor} of the thermal pressurization coefficient to the measured value Λ_{mes} can be written as:

$$\Lambda_{cor} = \frac{\Lambda_{mes}}{1 + \dfrac{\beta\left(V_L\alpha_{fL} - \alpha_L\right)}{\phi V\left(\alpha_f - \alpha_\phi\right)} - \Lambda_{mes}\dfrac{V_L c_{fL} + c_L}{\phi V\left(\alpha_f - \alpha_\phi\right)}} \tag{30}$$

In equation (30), V_L is the volume of fluid in the drainage system, V is the total volume of the sample, c_L and α_L are the compressibility and the thermal expansion coefficient of the drainage system respectively defined as the variation of the volume of drainage system due to a unit variation in pore pressure and temperature. $\beta = \Delta T_L / \Delta T$ where ΔT is the temperature change of the sample and ΔT_L is the equivalent temperature change of the drainage system. α_{fL} and c_{fL} are the thermal expansion coefficient and the compressibility of fluid in the drainage system. As the physical properties of water

are temperature and pressure dependent, the effect of temperature and pressure changes on these coefficients has to be taken into account in the analysis of the tests results. Detailed evaluation of these parameters in the calibration tests are presented in Ghabezloo and Sulem [2]. The evaluated parameters for the triaxial system used in this study are:

$$\begin{aligned} V_L &= 2300\,\mathrm{mm}^3 \\ c_L &= 0.27\,\mathrm{mm}^3/\mathrm{MPa} \\ \alpha_L &= 0.31\,\mathrm{mm}^3/^\circ\mathrm{C} \\ \beta &= 0.46 \end{aligned} \tag{31}$$

3.3 Drained heating test

In order to measure the drained thermal expansion coefficient α_d of the hardened cement paste, a drained heating test was carried out under a constant confining pressure of 1.5MPa and a constant pore fluid pressure of 1.0MPa. During the test, the temperature was increased from 18°C to 87°C at a rate of 0.08°C/min and the drained thermal expansion coefficient is evaluated as the slope of the temperature-volumetric strain response (Figure 2).

A kinetics analysis of the used heating rate, presented in Appendix 1, shows that with the applied heating rate, the homogeneity of temperature in the sample is quasi instantaneous and the homogeneity of pore pressure along the height of the sample is satisfactory to guaranty that the performed heating test is indeed in drained condition. For drained heating tests performed in the triaxial cell, the test is done using a constant imposed pore pressure and a confining pressure which is greater than the pore pressure. When using a slow rate of temperature change, the duration of the test is large (more than 14 hours in the performed test) and creep may influence the test results. The effect of creep is reduced by choosing small values of imposed confining pressure and pore pressure and a small difference, equal to 0.5MPa, between them. The drained thermal expansion coefficient of hardened cement paste in the performed test is found equal to $6\times10^{-5}\left(^\circ C\right)^{-1}$ (Figure 2).

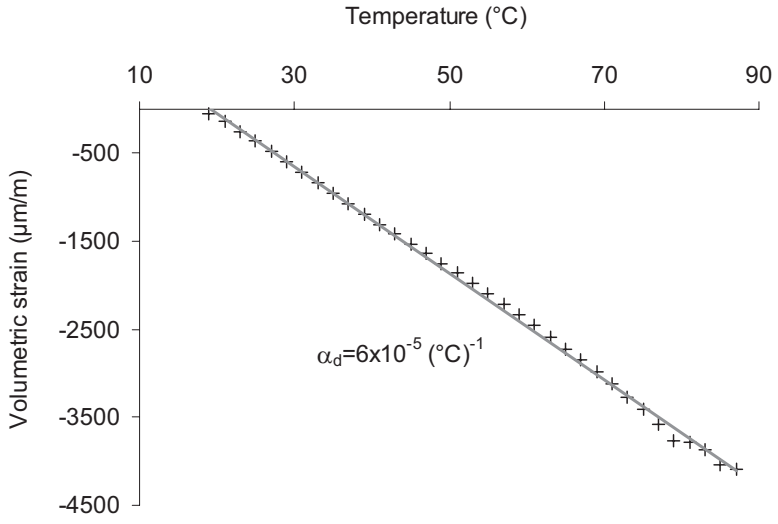

Figure 2- Drained heating test, temperature - volumetric strain response

3.4 Undrained heating test

The phenomenon of thermal pressurization was studied in an undrained heating test under a constant isotropic stress equal to 19MPa. After the saturation phase, the confining pressure is increased up to 19MPa in drained condition at a rate of 0.025MPa/min. In Ghabezloo *et al*. [12] the effect of creep of hardened cement paste under isotropic loading was mentioned. According to equation (26), creep deformations can influence the measured pore pressure variation during the undrained heating test. In order to minimize these effects, the sample was kept under constant load at ambient temperature during about two days before starting the undrained heating test. The volumetric response of the sample during this period is presented in Figure (3) and one can see that the creep strains are stabilized. However, it is well-known that the cement paste creep increases with temperature [30], consequently some additional creep strains may occur during the test due to the temperature increase.

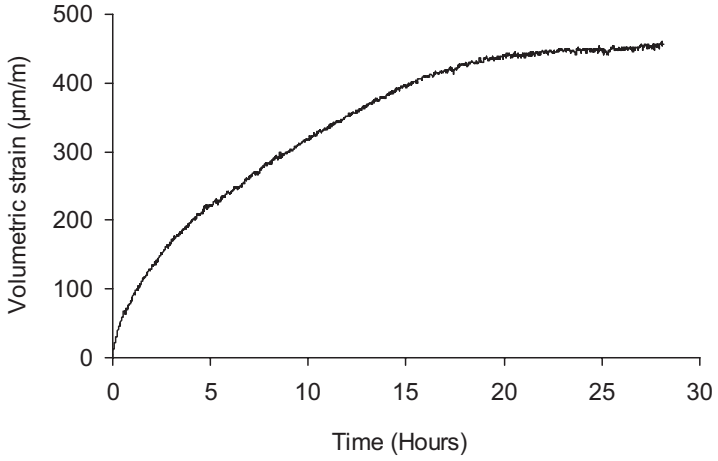

Figure 3- Creep phase of the tested sample before the undrained heating test

After the stabilization of the creep strains the temperature was increased at a rate equal to 0.1°C/min and the pore pressure change was monitored during the test. As it can be seen in Appendix 1, with the applied heating rate, the homogeneity of the temperature and consequently the homogeneity of the generated pore pressure in the sample is quasi instantaneous. As in a triaxial device the pore pressure cannot exceed the confining pressure, the heating phase was stopped when the pore pressure reached the confining pressure and the temperature was then decreased. The test results are shown on Figures (4) and (5) where the measured pore pressure variation and the volumetric strain are plotted versus the temperature change.

As can be seen in Figure (4), for a pore pressure close to the confining pressure, the pressurization curve becomes almost horizontal and no more fluid pressurization is observed. This phenomenon is due to the presence of fluid between the sample and the rubber membrane when the difference between the confining pressure and the pore pressure is too small. For the same reason, the pore pressure reduction is delayed at the beginning of the cooling phase.

The measured volumetric strains, presented in Figure (5), show the expansion and the contraction of the sample during the heating and cooling phases respectively.

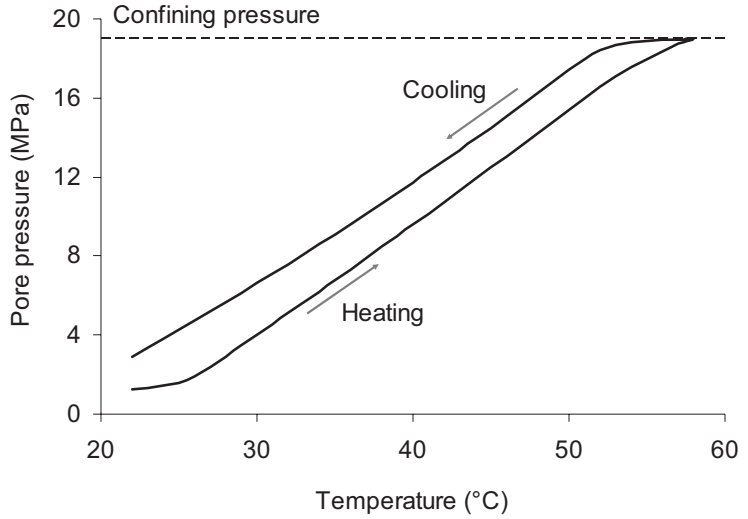

Figure 4- Undrained heating test, temperature-pore pressure response

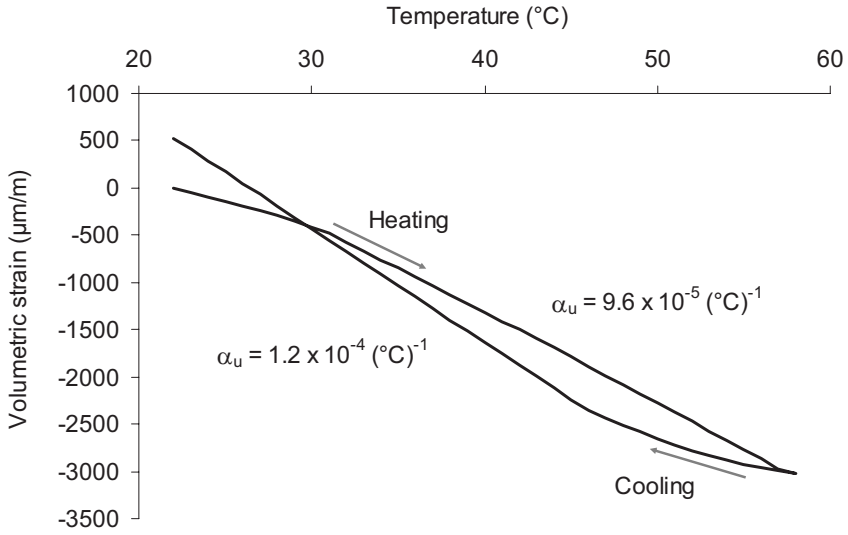

Figure 5- Undrained heating test, temperature-volumetric strain response

We can see in Figure (4) that the measured pore pressure at the end of the cooling phase is larger than the one measured at the beginning of the test. The difference between these two values is equal to 1.7MPa. As it can be seen in Figure (5), at the end of the cooling phase a small positive irreversible volumetric strain, equal to 530µm/m is observed. This irreversible volumetric strain can be attributed to creep and may be responsible for the difference between the pore pressures at the beginning and at the end of the undrained heating test. This can be examined quantitatively by introducing the effect of this irreversible volumetric strain (530µm/m) on the pore pressure in equation (27). Based on the results of Ghabezloo *et al*. [12], the following values are considered: $K_d = 8.7\,\text{GPa}$, $K_s = 21\text{GPa}$ and $K_\phi = 16.9\,\text{GPa}$. At 40°C which is the average temperature at which the undrained heating test is performed, the compression modulus of the pore fluid can be taken equal to the one of pure water: $K_f = 2.27\text{GPa}$ [31]. Inserting these values in equation (27) and with $\phi = 0.26$, the value of pore pressure increase due to the measured irreversible strain is found equal to 3.2MPa which is a bit higher than the measured pore pressure difference between the beginning and the end of the heating cycle, equal to 1.7MPa. This difference can be explained by the leakage of a small quantity of the pore fluid at the end of the heating test when the pore pressure approaches the confining pressure as mentioned

above. From simple poroelastic calculations, one can evaluate the quantity of the leaked fluid sufficient to obtain this pore pressure difference, equal to about 17mm3, which is a very small quantity.

3.4.1 Heating phase

The undrained thermal expansion coefficient for the heating phase is found equal to $9.6\times10^{-5}\,(°C)^{-1}$ (Figure (5)).

The measured pore pressure change with the temperature increase during the heating phase, presented in Figure (6), is corrected for the effect of the deformation of the drainage and pressure measurement systems, as explained in section 3.2.1, using equation (30) and the parameters presented in equation (31). The corrected thermal pressurization coefficient is evaluated as the slope of this curve and is equal to 0.62MPa/°C. The pressurization is stopped at the end of the heating phase, when the pore pressure approaches the confining pressure and the fluid leaks between the sample and the membrane. The comparison of the slopes of measured and corrected curves in Figure (6) shows that the corrected thermal pressurization coefficient is greater than the measured one. We also observe that this correction is more significant for the hardened cement paste than for example the Rothbach sandstone (Ghabezloo and Sulem [2]). The corrected curves are cut when the corrected pore pressure equals the confining pressure, at 54°C.

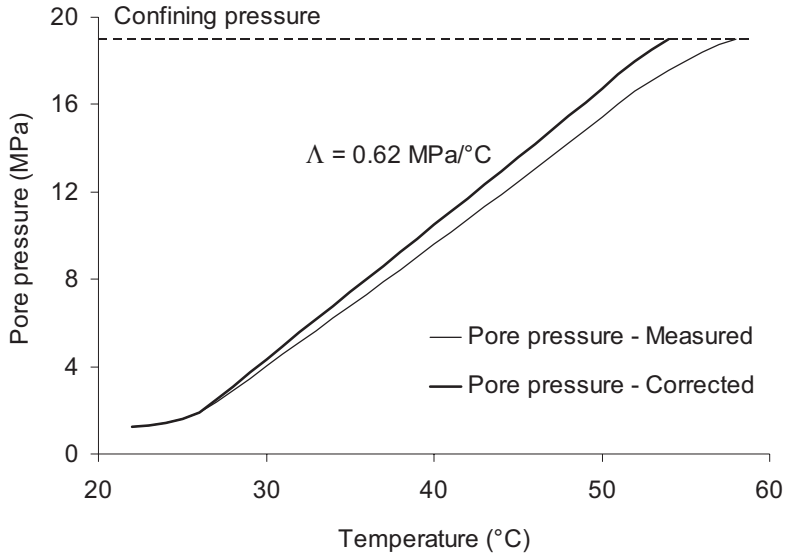

Figure 6- Heating phase of the undrained heating test, measured and corrected pore pressure

3.4.2 Cooling phase

The measured volumetric strain during cooling is presented on Figure (5). The measured thermal expansion at the beginning of the cooling phase is influenced by the presence of fluid between the sample and the membrane, as explained above. The undrained thermal expansion coefficient, which is the slope of the temperature-volumetric strain curve, then increases and remains constant during the test, equal to $1.2\times10^{-4}\,(°C)^{-1}$ which is slightly greater than the measured value during the heating phase.

Figure (7) presents the measured pore pressure during the cooling phase with the temperature. The corrected pore pressure curve is also presented on the same figure along with the calculated thermal pressurization coefficient. Due to the fluid leakage between the sample and the membrane at the end of

the heating phase, the pore pressure decrease at the beginning of the cooling phase is not visible. The correction of the effect of the deformation of the drainage and pressure measurement systems resulted in a thermal pressurization coefficient which is here again greater than the measured one. The corrected thermal pressurization coefficient measured in the cooling phase is equal to 0.57MPa/°C.

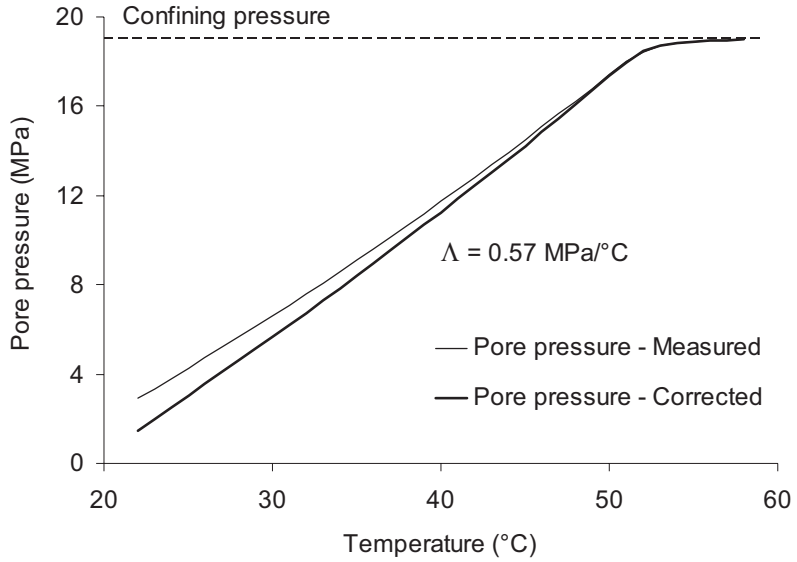

Figure 7- Cooling phase of the undrained heating test, measured and corrected pore pressure

4 Discussion of the results

In the tests results presented above, it is found that the thermal pressurization curve during heating and cooling is almost a straight line so that the thermal pressurization coefficient of the hardened cement paste can be considered as a constant, equal to 0.6MPa/°C. It has been checked that this value is retrieved when the test is repeated.

From equation (17) we can see that Λ depends on the physical properties of water and on the thermal and mechanical properties of the porous material considered. Stress and temperature dependency of these parameters can thus lead to a variation of the thermal pressurization coefficient with the temperature and the level of stress. The variations of physical properties of pure water, α_f and K_f with temperature and pressure are shown in Figure (8) [31]. We can see that α_f varies significantly with temperature but is less sensitive to pressure variations. On the other hand, in the range of temperature and pressure of our tests, K_f does not vary much and takes values between 2.2GPa and 2.4GPa. The experimental study of Ghabezloo *et al*. [12] has shown the stress dependent character of the mechanical properties of the hardened cement paste. In this previous study, we have obtained that the elastic bulk modulus is reduced when the effective stress is increased as the result of microcracking. On the other hand, the degradation of the elastic modulus of the hardened cement paste with temperature increase is shown in the experimental studies of Dias *et al*. [32], Masse *et al*. [33] and Farage *et al*. [34]. DeJong [35] has also shown the degradation of the elastic properties of the hardened cement paste by performing nanoindentation tests at different temperatures. Then one can ask the question why is it found that the thermal pressurization coefficient is constant during the undrained heating test?

One possible explanation can be found in the anomalies of the thermal expansion of cement paste pore fluid, as presented by Valenza and Scherer [36]. They evaluated the permeability of the hardened cement paste using two different methods: thermopermeametry and beam bending. According to these

authors, the comparison of the measurements using these methods showed that to bring the two measurements into agreement, the pore fluid in the fine pores of the hardened cement paste should have a thermal expansion coefficient about one and a half times larger than the one of the bulk liquid. Indeed, thermal expansion of water, when confined in nanopores is higher than that of bulk water. This phenomenon is showed experimentally by Derjaguin *et al*. [37] who studied the thermal expansion of water in nanopores of silica gel (5nm) and observed that the thermal expansion of water in small pores is anomalously higher than that of bulk water. The results presented by these authors also show that the rate of increase of the thermal expansion of water confined in nanopores with temperature is smaller than the one of bulk water. The ratio of the thermal expansion of water in nanopores to that of bulk water decreases with temperature. For temperatures higher than 70°C no more difference is observed between the thermal expansion coefficients. Xu *et al*. [38] also studied the thermal expansion and viscosity of water and salt solutions in porous silica glasses with two different pore sizes and found that the value of the thermal expansion of confined water is greater than that of bulk water. Additionally, the thermal expansion of water in smaller pores (5.0nm) is found to be higher than that in larger pores (7.4nm).

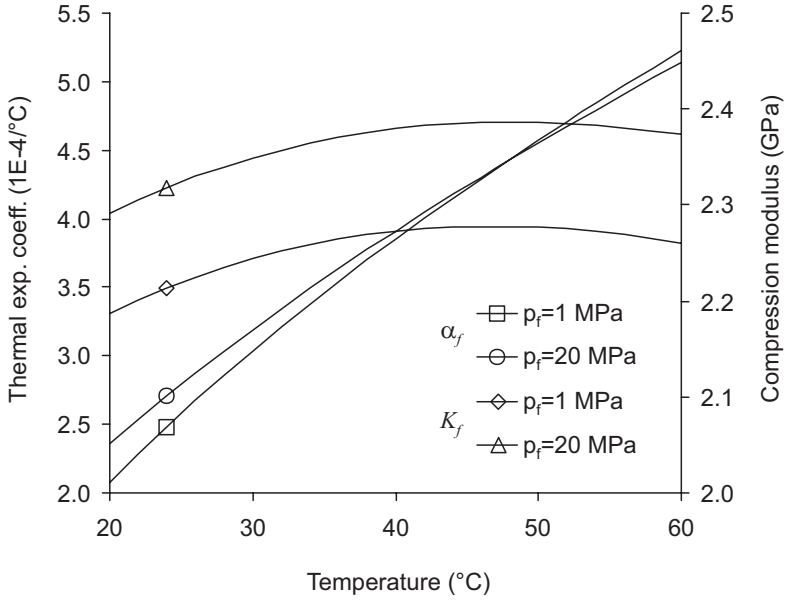

Figure 8- Variations of the thermal expansion coefficient and of the compression modulus of pure water with temperature and pressure

The possible effect of the anomalies of thermal expansion of water on our test results can be investigated by analysing the performed undrained heating test. In this test the confining pressure remains constant, $d\sigma = 0$, so that $d\sigma_d = -dp_f$. Inserting this expression in equation (9), the following expression is obtained:

$$dp_f = \frac{-1}{\left(1/K_d - 1/K_s\right)}\left(d\varepsilon + \alpha_d dT\right) \tag{32}$$

Inserting the term $1/K_d - 1/K_s$ from equation (32) in equation (15), with $d\sigma = 0$, we get

$$\alpha_f dT = \alpha_\phi dT - \frac{1}{\phi}\left(d\varepsilon + \alpha_d dT\right) + dp_f\left(\frac{1}{K_f} - \frac{1}{K_\phi}\right) \tag{33}$$

Replacing $d\varepsilon = -\alpha_u dT$ and $dp_f = \Lambda dT$ in equation (33) the following expression is obtained for the thermal expansion coefficient of the pore fluid:

$$\alpha_f = \alpha_\phi + \frac{1}{\phi}\left(\alpha_u - \alpha_d\right) + \Lambda\left(\frac{1}{K_f} - \frac{1}{K_\phi}\right) \tag{34}$$

Based on the results of Ghabezloo *et al*. [12], we take $K_\phi = 16.9\,\text{GPa}$ and we assume that this value does not vary during the test. Furthermore, in the absence of any information on the value of α_ϕ, we assume that $\alpha_\phi = \alpha_d = 6\times10^{-5}\left(°\text{C}\right)^{-1}$. In the analysis we take $\phi = 0.26$, $\Lambda = 0.6$ and $\alpha_u = 1.08\times10^{-4}\left(°\text{C}\right)^{-1}$ which are average values obtained from the heating and the cooling phase (Figures 5-7). The compression modulus K_f of the pore fluid is taken equal to the one of pure water which as seen before does not vary significantly for the range of pressures and temperatures of the test $K_f = 2.27\text{GPa}$. With this set of values, from equation (34) we obtain $\alpha_f = 4.7\times10^{-4}(°\text{C})^{-1}$. On the other hand, we can also evaluate α_f by using equation (20). The value of the Skempton coefficient *B* is taken from the undrained compression tests of Ghabezloo *et al*. [12] at ambient temperature: $B = 0.4$. We obtain $\alpha_f = 5.2\times10^{-4}(°\text{C})^{-1}$ which is in accordance with the one obtained above. These calculations give a constant value for the thermal expansion coefficient of the cement pore fluid which is obtained as an average value of the heating and cooling phases. A more detailed calculation can be done using equation (33) and the data of the performed undrained heating test. By doing so, the value of the thermal expansion coefficient of the cement pore fluid can be calculated for each data point during the test. The analysis is applied here for the cooling phase where the creep effects are of less importance. Moreover, the first part of the cooling phase in which the pore pressure reduction is delayed due to the presence of water between the sample and the membrane, is excluded from the analysis and only the temperatures below 45°C are considered. The result is shown in Figure (9). On the same graph the evolution of the thermal expansion coefficients of pure bulk water and of 0.5 mol/l NaOH bulk solution (data from Ref. [39]) are also plotted. On Figure (9), we observe that the thermal expansion of cement pore fluid is larger than the one of pure bulk water which is compatible with the results of Valenza and Scherer [36].

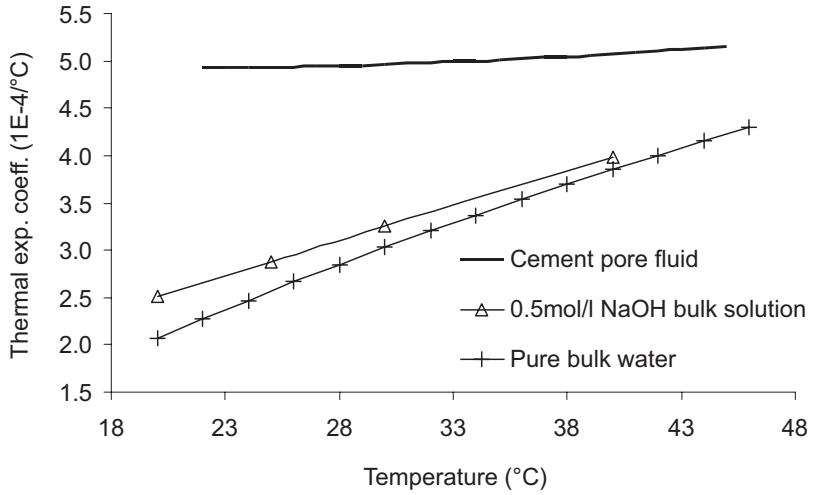

Figure 9- Evaluated thermal expansion coefficient of cement pore fluid compared with the thermal expansion coefficients of pure water, and of 0.5 mol/l NaOH solution (data from [40])

We observe also that the rate of increase of the thermal expansion of cement pore fluid with temperature is lower. This is compatible with the experimental results of Derjaguin *et al*. [37] and Xu *et al*. [38] who found that the rate of increase of the thermal expansion of water confined in nanopores of silica with temperature is smaller than the one of bulk water, as explained above. On the other hand this lower rate of increase with temperature is probably also due to the presence of dissolved ions in cement pore fluid. It is well-known that the presence of ions in water can influence its thermal expansion. Comparing the thermal expansion of pure bulk water with the one of 0.5mol/l NaOH bulk solution, we can see that the presence of ions increases the thermal expansion coefficient and decreases its rate of change with temperature. Additional results with various concentrations can be found in Valenza and Scherer [36] (their Figure 8). According to Taylor [23], typical concentrations after 180 days for pastes of w/c ratio 0.5 for Na^+, K^+ and OH^- are respectively 0.08mol/l, 0.24mol/l and 0.32mol/l for low-alkali cement. The values for high-alkali cement are respectively equal to 0.16mol/l, 0.55mol/l and 0.71mol/l. Considering these concentrations, we use the thermal expansion of 0.5mol/l NaOH solution presented in Figure (9) as the thermal expansion of the bulk fluid in the cement paste. By doing so, we can evaluate the effect of the anomaly of pore fluid thermal expansion as ratio between the thermal expansion of the (confined) pore fluid and the one of the bulk fluid. This ratio reflects the effect of cement pore structure on the thermal expansion of pore fluid and is almost independent of presence of dissolved ions in the case of cement pore fluid which is mainly composed of univalent ions. According to experimental results of Xu *et al*. [38], the presence of dissolved ions in water can increase the anomaly of thermal expansion, but this influence is very small in the case of univalent ions. These authors measured the thermal expansion of the pure water and a 1.0mol/l NaCl solution for bulk fluids and when confined in silica pores (7.4nm). From their results we can evaluate the confined/bulk ratio of the thermal expansion of the NaCl solution which is only 2% larger than that of pure water. This result shows that the confined/bulk ratio of the thermal expansion of cement paste pore fluid is almost independent of the presence of dissolved ions and can be compared with that of pure water confined in silica pores. The comparison is presented in Figure (10) and shows a good accordance with the experimental results of Xu *et al*. [38]. This good accordance, when the effect of the dissolved ions is excluded from the results by using the confined/bulk thermal expansion ratio, clearly shows the effect of cement pore structure on the anomaly of cement paste pore fluid.

The above analysis shows several competing effects: (a) the increase of the thermal expansion coefficient with temperature, (b) the anomalous thermal behaviour of the confined pore fluid, (c) the decrease of this effect with temperature increase, (d) the effect of dissolved ions in the cement pore fluid. The combination of these effects may be a possible explanation for obtaining a thermal expansion coefficient of the pore fluid which does not vary significantly with temperature and consequently a constant thermal pressurization coefficient, as measured in the performed undrained heating test. We should also emphasized that the present analysis is based also on a set of assumptions: the variations of the poromechanical parameters of the hardened cement paste with the temperature and stress state are ignored, the thermal expansion coefficients α_ϕ and α_d are assumed to be equal and the compression modulus K_f of cement pore fluid is assumed to be equal to the one of pure bulk water. We would like also to point out that the low temperature dependency of cement paste pore fluid obtained from the back analysis of the results of the undrained heating test is not in agreement with some measurements of Xu *et al*., presented by Valenza and Scherer [36] (Figure 9 in [36]). Although the thermal expansion coefficient of the cement fluid presented by these authors is of the same range of our results, they obtain a stronger temperature dependency similar to that of pure bulk water. We believe that the experimental

evaluation of the thermal properties of the cement paste fluid is still an open question which requires future investigation as it can only be addressed through indirect methods.

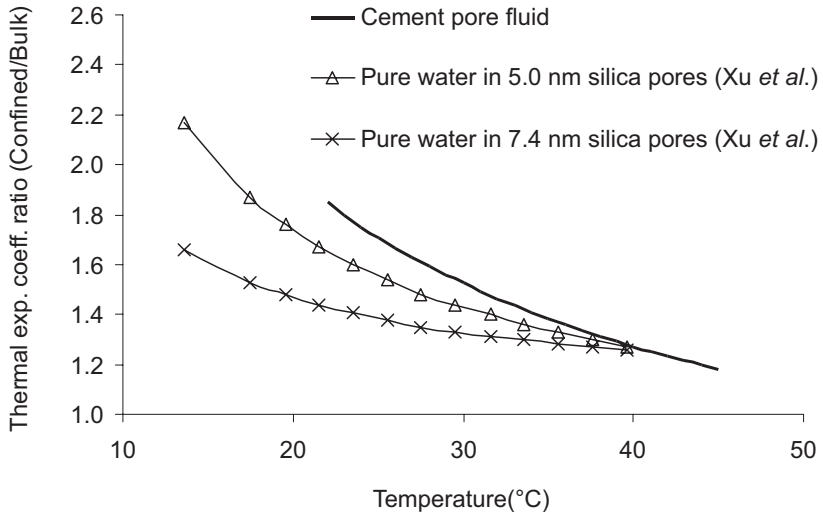

Figure 10- Anomaly of the thermal expansion of cement pore fluid compared with pure water confined in silica pores of different size (data from Xu et al. [39])

5 Conclusions

A better understanding of the effect of rapid temperature changes is an important point to properly evaluate the integrity of an oil well cement sheath submitted to such a variation. With this objective in mind, in this paper the effect of undrained heating on induced thermal pressurization and thermal expansion is formulated theoretically within the framework of thermo-poro-mechanics and is studied experimentally for a fluid-saturated hardened cement paste. The experimental study is performed on a hardened class G oilwell cement paste prepared with $w/c = 0.44$.

In the analysis of test results, special care is taken to the effect of the deformation of the drainage and pore pressure measurement systems and appropriate corrections are brought to the raw data. It is shown that these corrections can be significant and that the errors induced by the compressibility and the thermal deformation of the drainage systems should not be neglected. The drained thermal expansion coefficient of the hardened cement paste is measured in a drained heating test and found equal to $6\times10^{-5}\left(°\mathrm{C}\right)^{-1}$. An undrained heating test with a heating-cooling cycle is performed and shows a proportional change of pore fluid pressure with temperature change. This linear response is described by a constant thermal pressurization coefficient equal to 0.6MPa/°C. It is expected that this coefficient varies during the heating and cooling phases due to the variations of the thermal expansion of water with temperature. The analysis of the results of the undrained heating test showed that this phenomenon may be attributed to the anomalies of the thermal expansion of cement paste pore fluid. The results of the undrained heating test are thus used to back analyse the thermal behaviour of cement pore fluid on the basis of the observation of a constant thermal pressurization coefficient in the range of temperature of the test. The evaluated thermal expansion of pore fluid is larger than the one of pure bulk water and its rate of increase with temperature is smaller. These anomalies are mainly attributed to the thermal behaviour of water when confined in small pores and also to the presence of dissolved ions in the cement paste pore fluid.

6 Appendix 1: Heating rate for drained and undrained heating tests

When performing elementary tests in the laboratory, the response of the sample should reproduce the response of a representative volume of the considered continuum. Thus, constitutive tests must be performed in such a way that temperature, strain and stress inside the sample can be assumed homogeneous. The choice of the loading rate is crucial to insure the homogeneity condition and preclude all kinetic effects.

For the undrained heating test, the rate of temperature change should be slow enough to ensure the homogeneity of temperature in the sample. Consequently, the induced pore pressure change inside the sample is quasi instantaneously homogeneous. For the drained heating test, in addition to the temperature homogeneity, the rate of temperature change should be slow enough to allow for the dissipation of the generated pore pressure change.

The rate of temperature change necessary for homogeneity of temperature in the sample can be analysed using the solution of temperature diffusion in an infinite cylinder of radius *R*. The initial condition at $t = 0^-$ is $T = T_0$ for $r \le R$, where t is the time and r is the radial coordinate. At $t = 0^+$ the boundary condition is $T = T_1$ at $r = R$. Considering the dimensionless variable $\theta = \left(T - T_1\right)/\left(T_0 - T_1\right)$, the diffusion of temperature in the cylinder is given by the following differential equation:

$$\frac{\partial \theta}{\partial t} = C_T \left(\frac{\partial^2 \theta}{\partial r^2} + \frac{1}{r} \frac{\partial \theta}{\partial r} \right) \tag{35}$$

where C_T is the thermal diffusivity. The solution of this differential equation can be expressed in terms of a series of Bessel functions *r* and exponential functions for *t*:

$$\theta\left(r,t\right) = 2\sum_{n=1}^{\infty} e^{-C_T \lambda_n^2 t} \frac{J_0\left(\lambda_n r\right)}{\lambda_n J_1\left(\lambda_n\right)} \tag{36}$$

where J_0 and J_1 are respectively Bessel functions of the first kind of order 0 and 1, and λ_n are the roots of J_0. This solution is presented and used in a slightly different form also by Ciardullo *et al*. [40]. Taking $R = 19\text{mm}$, $T_0 = 20°\text{C}$ and $C_T = 0.33\,\text{mm}^2/\text{s}$ from Ref. [40], we consider an instantaneous temperature increase of 0.1°C at the exterior of the cylinder, $T_1 = 20.1°\text{C}$. Using equation (36) one finds that after only one second, the temperature at the centre of the sample is equal to 20.096°C. So one can see that the homogeneity of temperature in the sample is quasi instantaneous, and consequently the homogeneity of the pore pressure in the undrained heating test is also quasi instantaneous. Therefore, in order to have a good homogeneity of the temperature between the heating element at the exterior part of the triaxial cell and the sample's temperature, a heating rate of 0.1°C/min is chosen for the undrained heating test.

Now assuming instantaneous temperature homogeneity in the sample, the rate of temperature change for the drained heating test can be analysed using the problem of one dimensional pressure diffusion along the axis of the sample. In order to derive this equation, the fluid mass conservation in a deforming elementary volume reads:

$$\frac{dm_f}{dt} + m_f \frac{dV/V}{dt} + \frac{\partial q}{\partial z} = 0 \tag{37}$$

where m_f is the fluid mass per unit volume of the porous material, $m_f = \rho_f \phi$ and q is the fluid mass flux per surface area (orthogonal to flow direction z). Knowing that $dm_f = \phi d\rho_f + \rho_f d\phi$, $d\rho_f = \rho_f \left(dp_f / K_f - \alpha_f dT \right)$ and equation (10) one obtains:

$$dm_f = \phi \rho_f \left(\frac{dp_f}{K_f} - \alpha_f dT + \frac{dV_\phi}{V_\phi} - \frac{dV}{V} \right) \tag{38}$$

Inserting equation (38) and $m_f = \rho_f \phi$ in equation (37) the following expression is obtained:

$$\phi \rho_f \left(\frac{1}{K_f} \frac{dp_f}{dt} - \alpha_f \frac{dT}{dt} + \frac{dV_\phi / V_\phi}{dt} \right) + \frac{\partial q}{\partial z} = 0 \tag{39}$$

Replacing equation (8) and then equation (7) in equation (39) the following relation is found:

$$\left[\phi \left(\frac{1}{K_f} - \frac{1}{K_\phi} \right) + \left(\frac{1}{K_d} - \frac{1}{K_s} \right) \right] \frac{dp_f}{dt} - \left(\frac{1}{K_d} - \frac{1}{K_s} \right) \frac{d\sigma}{dt} - \phi \left(\alpha_f - \alpha_\phi \right) \frac{dT}{dt} + \frac{1}{\rho_f} \frac{\partial q}{\partial z} = 0 \tag{40}$$

Using equations (16) and (17), equation (40) can be written in the following form:

$$\frac{dp_f}{dt} = B \frac{d\sigma}{dt} + \Lambda \frac{dT}{dt} - \frac{\beta_u}{\rho_f} \frac{\partial q}{\partial z} \tag{41}$$

where

$$\beta_u = \frac{1}{\phi \left(1/K_f - 1/K_\phi \right) + \left(1/K_d - 1/K_s \right)} \tag{42}$$

The fluid mass flux q in equation (41) is given by Darcy's law:

$$q = -k \frac{\rho_f}{\mu_f} \frac{\partial p_f}{\partial z} \tag{43}$$

where k is the permeability and μ_f is the fluid viscosity. Replacing equation (43) in equation (41) the following expression is obtained:

$$\frac{dp_f}{dt} = B \frac{d\sigma}{dt} + \Lambda \frac{dT}{dt} + \frac{\beta_u}{\rho_f} \frac{\partial}{\partial z} \left(k \frac{\rho_f}{\mu_f} \frac{\partial p_f}{\partial z} \right) \tag{44}$$

Equation (44) can be extended to take into account the effect of non-elastic strains as presented in section 2.1. The effect of creep is also presented in Ref. [41]. By doing so, in the case of a material for which the solid phase is elastic ($d\varepsilon_s^{ne} = 0$), one obtains:

$$\frac{dp_f}{dt} - \beta_u \frac{d\varepsilon^{ne}}{dt} = B \frac{d\sigma}{dt} + \Lambda \frac{dT}{dt} + \frac{\beta_u}{\rho_f} \frac{\partial}{\partial z} \left(k \frac{\rho_f}{\mu_f} \frac{\partial p_f}{\partial z} \right) \tag{45}$$

The drained heating test is performed under constant confining pressure, so that $d\sigma / dt = 0$. In order to exclude the effect of creep deformations during the test, the test is performed under a low confining pressure, so that $d\varepsilon^{ne} / dt = 0$. From equation (45) one can see that the diffusion of pressure in the sample depends directly on the permeability k, the thermal pressurization coefficient Λ of the tested sample and the length of the drainage path. The permeability of the tested sample is evaluated equal to $1.1 \times 10^{-19}\ \mathrm{m}^2$ [42]. The elastic moduli required for evaluation of β_u in equation (42) are evaluated

experimentally by Ghabezloo *et al*. [12] at ambient temperature: $K_d = 8.7\text{GPa}$, $K_s = 21\text{GPa}$, $K_\phi = 16.9\text{GPa}$, $\phi = 0.26$. Based on some preliminary calculations, the heating rate of 0.08°C/min is chosen for the drained heating test. Compared to the rates of temperature change used by Helmuth [43] and Sabri and Illston [44], 0.25°C/min and 0.33°C/min respectively, the chosen rate of temperature change, 0.08°C/min, can be considered to be relatively slow. In the following, we show that this choice of the heating rate is satisfactory. In this analysis, we use the value of thermal pressurization coefficient Λ, equal to 0.6MPa/°C, which is obtained in the performed undrained heating test, as presented in section 3.4. A numerical simulation of drained heating test is performed in which the temperature of the sample is increased with different rates from 20°C to 50°C. Only one half of the tested sample is modelled which makes the model length equal to 38mm. At one end of the sample, a constant pore pressure equal to 1.0MPa is applied, while at the other end a no-flow condition is imposed. Equation (45) is solved using a finite difference scheme with the parameters presented above. The physical properties of water, density, compressibility and viscosity, are assumed equal to the ones of pure water and their variations with temperature are taken into account. Figure (11) presents the distribution of the pore pressure along the height of the sample at the end of the numerical heating test, for three different heating rates. One can see that for the heating rate used in this study, 0.08°C/min, a relatively small pressure difference equal to 0.43MPa remains along the axis of the sample. Using equation (9), $K_d = 8.7\text{GPa}$ and $K_s = 21\text{GPa}$, this pore pressure difference of 0.43MPa induces a difference of 30μm/m (0.003%) in the volumetric strains between the middle and the end of the sample. Obviously this small strain heterogeneity has a negligible effect in the evaluation of the thermal expansion coefficient. Notice that with $\Lambda = 0.6\,\text{MPa}/\text{°C}$, an undrained heating test from 20°C to 50°C would result in an excess pore pressure of 18MPa. This excess pore pressure in undrained conditions can be compared with the excess pore pressure obtained in the performed numerical drained heating test, equal to 0.43MPa, which shows that a heating rate, 0.08°C/min as used in our experiments guaranties that the heating test is performed in drained condition. It is interesting to note that, due to the relatively low permeability of the sample and the high value of Λ, even by using a r heating rate four times slower, 0.02°C/min, a pressure difference of 0.17MPa still remains inside the sample. This pressure difference increases to 1.14MPa for a heating rate of 0.20°C/min (Figure 11).

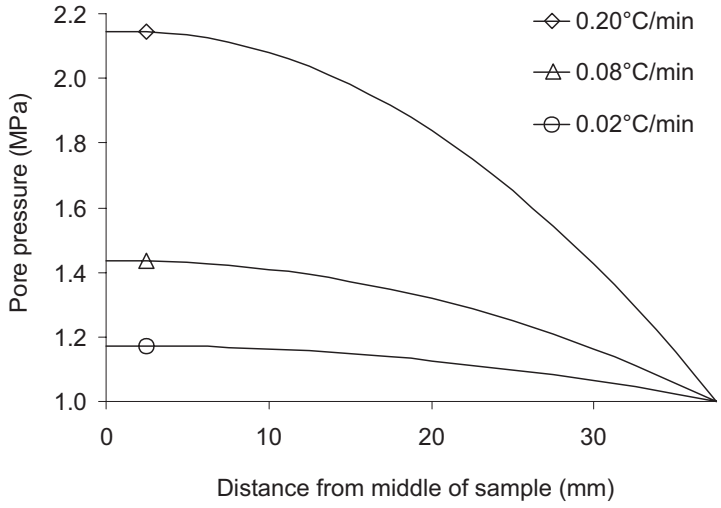

Figure 11- Numerical simulation of a drained heating test from 20°C to 50°C with different heating rates: Pore pressure along the height of the sample

7 Acknowledgments

The authors gratefully acknowledge TOTAL for supporting this research. They wish also to thank George W. Scherer for interesting discussions and François Martineau for his assistance in the experimental work.

8 References

[1] J. Sulem, P. Lazar, I. Vardoulakis, Thermo-Poro-Mechanical Properties of Clayey Gouge and Application to Rapid Fault Shearing, Int. J. Num. Anal. Meth. Geomechanics, 31(3) (2007), 523-540

[2] S. Ghabezloo, J. Sulem, Stress dependent thermal pressurization of a fluid-saturated rock, Rock Mech Rock Engng 42(1) (2009) 1-24.

[3] M.A. Biot, D.G. Willis, The elastic coefficients of the theory of consolidation, Journal of Applied Mechanics 24 (1957) 594-601.

[4] R.J.S. Brown, J. Korringa, On the dependence of the elastic properties of a porous rock on the compressibility of the pore fluid, Geophysics 40 (1975) 608-616.

[5] J.R. Rice, M.P. Cleary, Some basic stress diffusion solutions for fluid-saturated elastic porous media with compressible constituents, Review of geophysics and space physics, Vol. 14, No. 2 (1976) 227-240.

[6] V.V. Palciauskas, P.A. Domenico, Characterization of drained and undrained response of thermally loaded repository rocks. Water Resources Research, 18(1982), No. 2, 281-290.

[7] D.F. McTigue, Thermoelastic response of fluid-saturated porous rock. Journal of Geophysical Research, 91(B9) (1986), 9533-9542.

[8] R.W. Zimmerman, Compressibility of sandstones, Elsevier Sci., Amsterdam, 1991.

[9] E. Detournay, A.H.-D. Cheng, Fundamentals of Poroelasticity, Chap. 5 in Comprehensive Rock Engineering: Principles, Practice and Projects, Vol. II, Analysis and Design Method, ed. C. Fairhurst, Pergamon, (1993) 113-171

[10] I. Vardoulakis, J. Sulem, Bifurcation Analysis in Geomechanics. Blackie Academic and Professional, 1995.

[11] O. Coussy, Poromechanics, John Wiley and Sons, 2004.

[12] S. Ghabezloo, J. Sulem, S. Guedon, F. Martineau, J. Saint-Marc, Poromechanical behaviour of hardened cement paste under isotropic loading. Cement and Concrete Research 38(12) (2008), 1424-1437.

[13] J.G. Berryman, Effective stress for transport properties of inhomogeneous porous rock, Journal of Geophysical Research 97 (1992) 17409-17424.

[14] P.A. Berge, J. G. Berryman, Realizability of Negative Pore Compressibility in Poroelastic Composites, Journal of Applied Mechanics 62 (4) (1995) 1053-1062.

[15] P.A. Berge, Pore Compressiblity in Rocks, Biot Conference on Poromechanics, Louvain-la-Neuve, Belgium, September 14-16, 1998.

[16] J.B. Walsh, Theoretical bounds for thermal expansion, specific heat and strain energy due to internal stresses, Journal of Geophysical Research, 78 (1973), 7636-7647.

[17] A.W. Skempton, The Pore Pressure Coefficients A and B, Géotechnique 4 (1954) 143-147.

[18] H.M. Jennings, J.J. Thomas, J.J. Chen, D. Rothstein, Cement as a Porous Materials, Chapter 6.11 in Handbook of Porous Solids, ed. F. Schuth, K. Sing, J. Weitkamp. Wiley-VCH, 5, 2971-3028, 2002.

[19] R.F. Feldman, P.J. Sereda, A model for hydrated Portland cement paste as deduced from sorption-length change and mechanical properties, Materials and Structures 1(6) (1968) 509-520.

[20] R.F. Feldman, Factors affecting young's modulus - porosity relation of hydrated portland cement compacts, Cement and Concrete Research 2 (4) (1972) 375-386.

[21] H.M. Jennings, A model for the microstructure of calcium silicate hydrate in cement paste, Cement and Concrete Research 30 (1) (2000) 101-116.

[22] H.M. Jennings, Refinements to colloid model of C-S-H in cement: CM-II, Cement and Concrete Research 38(3) (2008) 275-289.

[23] H.F.W. Taylor, Cement chemistry, Thomas Telford, London, 1997.

[24] R.F. Feldman, Helium flow and density measurement of the hydrated tricalcium silicate-water system, Cement and Concrete Research 2 (1) (1972) 123-136.

[25] F.-J. Ulm, G. Constantinides, F.H. Heukamp, Is concrete a poromechanics material? - A multiscale investigation of poroelastic properties, Materials and Structures 37 (265) (2004) 43-58.

[26] G.W. Scherer, J.J. Valenza II, G. Simmons, New methods to measure liquid permeability in porous materials, Cement and Concrete Research 37 (2007) 386–397.

[27] C. Gallé, Effect of drying on cement-based materials pore structure as identified by mercury intrusion porosimetry: A comparative study between oven-, vacuum-, and freeze-drying, Cement and Concrete Research 31 (10) (2001) 1467-1477.

[28] J. Sulem, H. Ouffroukh, Hydromechanical Behaviour of Fontainebleau Sandstone, Rock Mechanics and Rock Engineering 39 (3) (2006) 185-213.

[29] A.W. Bishop, The influence of system compressibility on the observed pore pressure response to an undrained change in stress in saturated rock. Géotechnique 26 (1976), No 2, 371-375.

[30] Z.P. Bazant, G. Cusatis, L. Cedolin, Temperature effect on concrete creep modeled by microprestress-solidification theory. J. of Engrg. Mechanics ASCE 130(6) (2004) 691-699.

[31] B. Spang, Excel Add-In for Properties of Water and Steam in SI-Units, http://www.cheresources.com/ iapwsif97.shtml, 2002.

[32] W.P.S. Dias, G.A. Khoury, P.J.E. Sullivan, Mechanical Properties of Hardened Cement Paste Exposed to Temperatures up to 700 C (1292 F), ACI Materials Journal, 87(2) (1990), 160-166.

[33] S. Masse, G. Vetter, P. Boch, C. Haehnel, Elastic modulus changes in cementitious materials submitted to thermal treatments up to 1000°C, Advances in Cement Research, 14(4) (2002), 169-177.

[34] M.C.R. Farage, J. Sercombe, C. Galle, Rehydration of microstructure of cement paste after heating at temperatures up to 300°C, Cement and Concrete Research, 33 (2003), 1047-1056.

[35] M.J. DeJong, Sources of high temperature degradation of cement-based materials: nanoindentation and microporoelastic analysis, PhD thesis, Massachusetts Institute of Technology. Dept. of Civil and Environmental Engineering, 2005.

[36] J.J. Valenza II, G.W. Scherer, Evidence of anomalous thermal expansion of water in cement paste, Cement and Concrete Research 35 (2005) 57–66.

[37] B.V. Derjaguin, V.V. Karasev, E.N. Khromova, Thermal expansion of water in fine pores, J. Colloid Interface Sci. 109 (2) (1986) 586–587.

[38] S. Xu, G.C. Simmons, G.W. Scherer, Thermal expansion and viscosity of confined liquids, Mat. Res. Soc. Symp. Proc., vol. 790, Materials Res. Soc, Warrendale, 2004, P6.8.1– P6.8.7.

[39] J.M. Simonson, R.J. Ryther, Volumetric properties of aqueous sodium hydroxide from 273.15 to 348.15 K, J. Chem. Eng. Data 34 (1989) 57–63.

[40] J.P. Ciardullo, D.J. Sweeney, G.W. Scherer, Thermal expansion kinetics: Method to measure permeability of cementitious materials, IV. Effect of thermal gradients and viscoelasticity, J. Am. Ceram. Soc. 88(5) (2005) 1213-1221.

[41] G.W. Scherer, Thermal expansion kinetics: Method to measure permeability of cementitious materials, III. Effect of viscoelasticity, J. Am. Ceram. Soc. 87(8) (2004) 1509-1516.

[42] S. Ghabezloo, J. Sulem, J. Saint-Marc, Evaluation of a permeability-porosity relationship in a low permeability creeping material using a single transient test. International Journal of Rock Mechanics and Mining Sciences 46(4) (2009), 761-768.

[43] R.A. Helmuth, Dimensional changes of hardened Portland cement pastes caused by temperature changes, Highway Research Board, Proc. Highway Research Record 40 (1967) 315-366.

[44] S. Sabri, J.M. Illston, Immediate and delayed thermal expansion of hardened cement paste, Cement and Concrete Research 12 (1982) 192–208.

4.4 Conclusions

En résumé, nous pouvons tirer les conclusions suivantes sur l'effet d'un changement de température en conditions drainées et non drainées sur les matériaux poreux saturés et en particulier sur le ciment :

1- Le phénomène de pressurisation thermique dans les milieux poreux saturés est contrôlé par la différence entre les expansions thermique de l'eau et de la phase solide, et aussi par les variations du volume poreux du matériau.

2- Une méthode simple est présentée pour la correction de la pression interstitielle mesurée lors d'un essai de chauffage non-drainé pour prendre en compte l'effet des déformations thermiques et mécaniques du système de drainage de la cellule triaxiale.

3- Les paramètres thermoélastiques du ciment étudié sont les suivants :

$\Lambda = 0,6\,\mathrm{MPa/°C}$; coefficient de pressurisation thermique

$\alpha_d = 6\times10^{-5}\,(\mathrm{°C})^{-1}$; coefficient d'expansion thermique drainé

$\alpha_u^{moyen} = 1,1\times10^{-4}\,(\mathrm{°C})^{-1}$; coefficient d'expansion thermique non-drainé

4- Pour la gamme de températures étudiées dans l'essai de chauffage non-drainé réalisé, entre 20°C et 60°C, le coefficient de pressurisation thermique du ciment étudié ne varie pas significativement avec les variations de la température et de l'état de contraintes. Ceci peut être attribué aux anomalies du comportement thermique du fluide interstitiel du ciment confiné dans pores de très petite taille.

5- L'analyse des résultats de l'essai de chauffage non-drainé permet d'évaluer le comportement volumique du fluide interstitiel du ciment. Le coefficient d'expansion thermique du fluide interstitiel du ciment est plus grand et moins sensible aux variations de la température que celui de l'eau pure. Cette anomalie est attribuée au confinement du fluide dans des pores de très petite taille de la microstructure du ciment et aussi à la présence des ions dans le fluide interstitiel.

4.5 Perspectives

L'étude expérimentale de l'effet de chauffage sur la pâte de ciment durcie, présentée dans ce chapitre, peut être complétée en réalisant le même essai de chauffage non-drainé dans des gammes de températures différentes. Cela permettra d'évaluer le coefficient de pressurisation thermique du ciment, et par conséquent le coefficient d'expansion thermique du fluide interstitiel du ciment à des températures plus élevées. Les résultats de Derjaguin *et al*. (1986) sur l'expansion thermique de l'eau dans les nanopores de gel de silice montrent que l'anomalie du comportement thermique de l'eau diminue avec la température et il n'y a plus d'anomalie pour les températures supérieure à 70°C. Les essais de chauffage non-drainés à des températures plus élevées permettront ainsi de vérifier ce point pour le fluide interstitiel du ciment.

CHAPITRE 5. ETUDE PRELIMINAIRE DU COMPORTEMENT DU CIMENT PETROLIER SOUS CHARGEMENT DEVIATORIQUE

5.1 Introduction

Les résultats des études du comportement poromécanique isotherme et du comportement thermique sous l'état de contraintes isotropes du ciment pétrolier présentées respectivement dans les chapitres 3 et 4 nous ont permis d'avoir une connaissance de base du comportement du ciment en tant que matériau poreux. Dans ce cinquième chapitre on étend cette étude au comportement du ciment sous chargement déviatorique. L'étude du comportement poromécanique du ciment sous chargement déviatorique permet d'évaluer les autres paramètres poroélastiques du ciment tels que le module d'Young E, le coefficient de Poission ν et le module de cisaillement G. Elle permet également d'étudier l'endommagement et la dégradation des modules élastiques du ciment sous l'effet de chargement déviatorique. Cette partie de l'étude est toutefois préliminaire, car elle est limitée à trois essais de compression déviatoriques réalisés à 90°C.

5.2 Résultats des essais déviatoriques

Trois essais de compression déviatoriques drainés ont été réalisés à 90°C sous une pression interstitielle constante $p_f = 1,0\text{MPa}$. Les détails des essais sont présentés dans le Tableau 5-1. Trois cycles de charge-décharge à différents niveaux de contrainte déviatorique ont été réalisés dans les essais DV-1 et DV-2. Une phase de chargement jusqu'à la rupture est aussi réalisée dans l'essai DV-1. A cause d'un problème du dispositif expérimental, la phase de rupture n'a pas pu être mise en œuvre dans l'essai DV-2 et celle-ci a été réalisée dans l'essai DV-3 où la rupture de l'échantillon a été atteinte en une seule phase de chargement sans cycles de charge-décharge. Dans les essais réalisés, les cycles de charge-décharge sont contrôlés en force. Le même taux de chargement utilisé dans les essais de compression isotrope drainés, 0,025MPa/min, est utilisé pour les essais déviatoriques pour le contrôle de la contrainte moyenne. Afin d'avoir un meilleur contrôle des conditions de la rupture, la phase de chargement jusqu'à la rupture est contrôlée en déplacement axial à une vitesse de $1,2\times10^{-4}\,\text{mm/s}$ qui est équivalent d'une vitesse en déformation de $1,6\times10^{-6}\,\text{s}^{-1}$.

Les invariants des contraintes (contrainte moyenne effective p' et deuxième invariant du tenseur des contraintes déviatorique τ), et des déformations (déformation volumique ε et déformation déviatorique γ) sont calculés en conditions axisymmétriques par les relations suivantes :

$$\tau = \frac{\left|\sigma_{ax} - \sigma_{rad}\right|}{\sqrt{3}} \tag{5-1}$$

$$p' = \frac{\sigma_{ax} + 2\sigma_{rad}}{3} - p_f \tag{5-2}$$

$$\varepsilon = \varepsilon_{ax} + 2\varepsilon_{rad} \tag{5-3}$$

$$\gamma = \frac{2}{\sqrt{3}}\left|\varepsilon_{ax} - \varepsilon_{rad}\right| \tag{5-4}$$

	Température (°C)	Cycle	Contrainte de confinement (MPa)	Contrainte déviatorique (MPa)	Vitesse de chargement (MPa/min)
DV-1	90	1	10	8,6	0,025 (Contrainte moyenne)
		2		19,2	
		3		28,0	
		4		43,7 (Rupture)	Contrôle en déplacement axial
DV-2	90	1	25	8,9	0,025 (Contrainte moyenne)
		2		23,8	
		3		49,0	
DV-3	90	1	25	58,2 (Rupture)	Contrôle en déplacement axial

Tableau 5-1-Détailles des essais réalisés

Etant donné que seuls des essais de compression triaxiale ont été réalisés, il ne nous est pas possible d'étudier l'effet du troisième invariant des contraintes sur la réponse du matériau.

Les résultats obtenus sont présentés dans les figures suivantes. La Figure 5-1 présente la variation de la contrainte déviatorique $\Delta\left(\sigma_{ax} - \sigma_{rad}\right)$ avec la déformation axiale. Les modules d'Young E sont évalués dans les cycles de décharge-recharge et dans les phases de décharge après la rupture. La Figure 5-2 présente le deuxième invariant du tenseur des contraintes déviatoriques τ avec la déformation déviatorique γ. Ce graphe est utilisé pour évaluer le module de cisaillement G. Dans la Figure 5-3 les déformations radiales sont présentées en fonction des déformations axiales. Les coefficients de Poisson sont évalués sur ce graphe. Les modules élastiques et les déformations plastiques mesurés dans les essais sont présentés dans le Tableau 5-2.

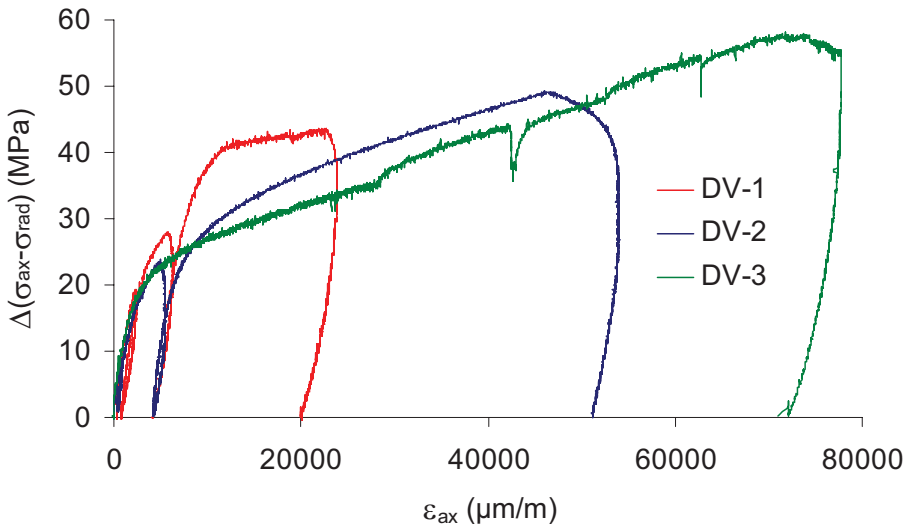

Figure 5-1- Déformations axiales - contrainte déviatorique

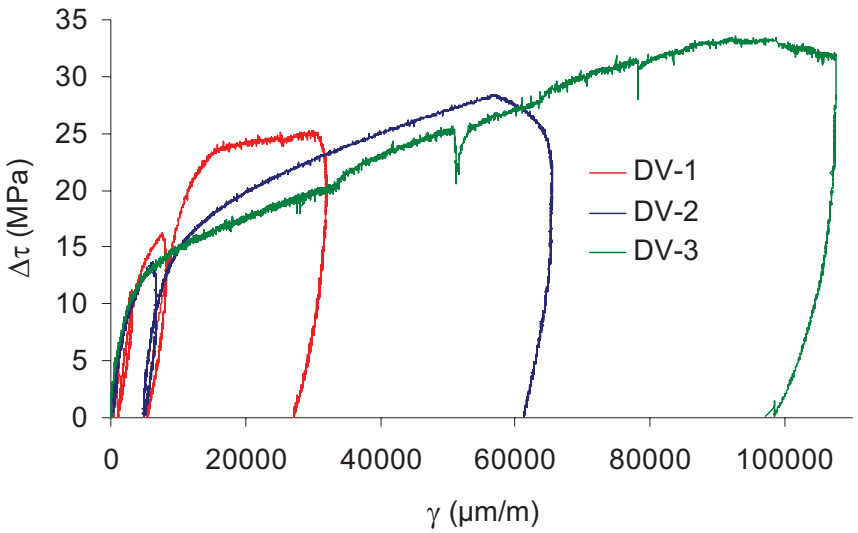

Figure 5-2- Déformations déviatoriques – deuxième invariant du tenseur des contraintes déviatoriques

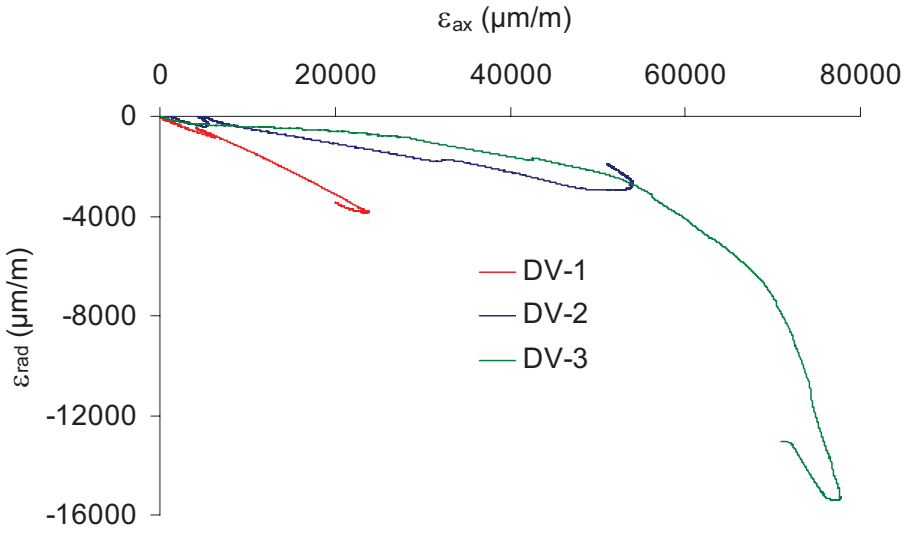

Figure 5-3- Déformations axiales – déformations radiales

Essai	τ (MPa)	p' (MPa)	γ^p (µm/m)	ν	E (GPa)	G (GPa)
DV-1	5,0	12,5	460	0,10	12,9	5,9
	10,8	16,0	1132	0,16	9,4	4,1
	16,2	19,0	5410	0,15	8,6	3,8
	25,0	24,0	27085	0,13	7,6	3,4
DV-2	5,1	27,0	493	0,12	11,6	5,1
	13,7	32,0	4820	0,16	9,8	4,3
	28,3	40,3	61249	0,23	8,0	3,3
DV-3	33,6	43,7	98363	0,44	7,0	2,4

Tableau 5-2- Les modules élastiques et les déformations plastiques mesurés

Afin de vérifier la compatibilité des données mesurées dans les essais on peut calculer le module de cisaillement pour chaque point en fonction du module d'Young et du coefficient de Poisson en utilisant la relation suivante :

$$G = \frac{E}{2(1+\nu)} \tag{5-5}$$

La comparaison des modules de cisaillement mesurés et évalués, est présentée sur la Figure 5-4 ; elle montre la très bonne compatibilité des données mesurées dans les essais réalisés.

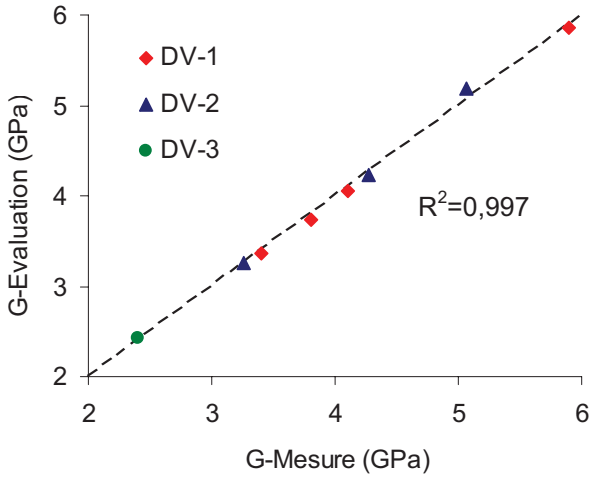

Figure 5-4- Comparaison des modules de cisaillement mesurés et évalués

Les Figures 5-5, 5-6 et 5-7 montrent respectivement les variations de module d'Young, module de cisaillement et coefficient de Poisson en fonction de la déformation déviatorique plastique. Sur la Figure 5-5 et la Figure 5-6 on peut observer la dégradation des modules élastique du ciment au cours des essais déviatoriques. Cette dégradation résulte en une augmentation de coefficient de Poisson.

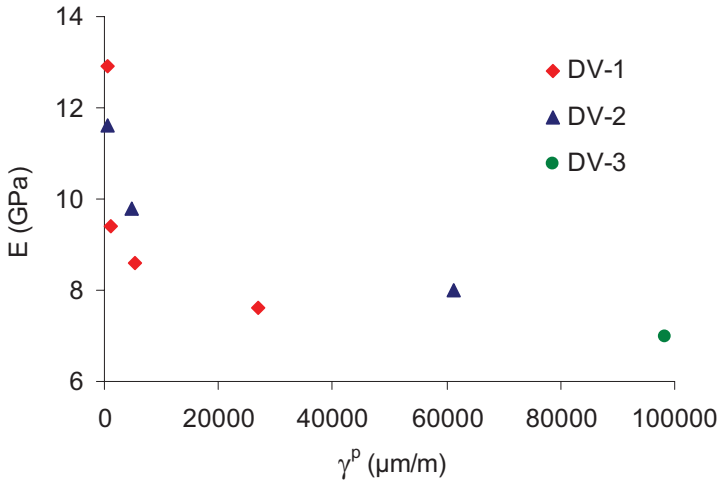

Figure 5-5- Dégradation de module d'Young avec la déformation déviatorique plastique

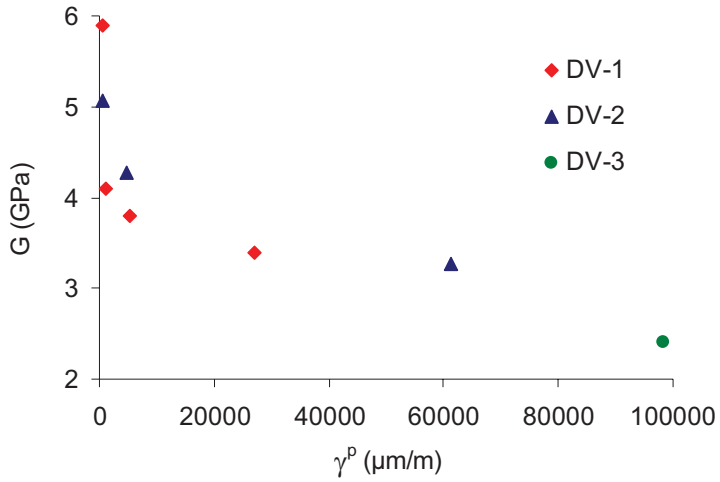

Figure 5-6- Dégradation de module de cisaillement avec la déformation déviatorique plastique

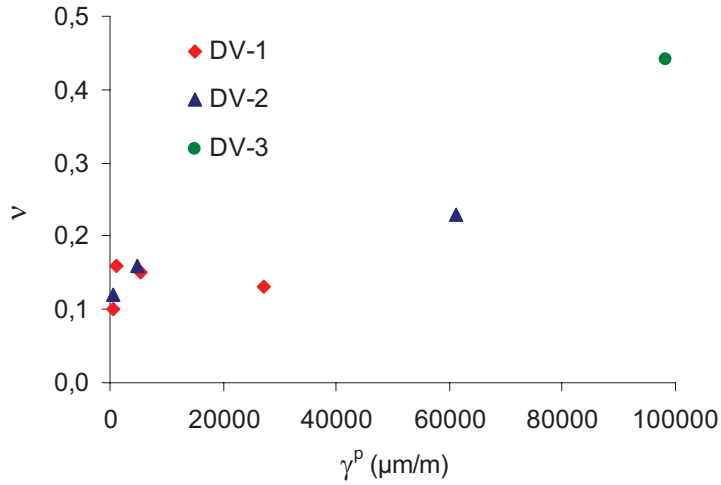

Figure 5-7- Dégradation de coefficient de Poisson avec la déformation déviatorique plastique

5.3 Modèle d'endommagement

Les résultats obtenus dans les essais déviatoriques réalisés peuvent être utilisés pour le développement d'un modèle d'endommagement des modules élastiques du matériau. Etant donné le nombre limité des résultats, on est considère ici un modèle très simple avec un nombre minimum des paramètres. Pour cela on suppose que l'endommagement des modules élastiques est uniquement fonction de la déformation déviatorique plastique γ^p. La fonction suivante est considérée pour la variation de module d'Young avec la déformation déviatorique plastique :

$$E = E^* \left(1 - \frac{a\gamma^p}{b + \gamma^p} \right) \tag{5-6}$$

où a et b sont deux paramètres de modèle qui doivent être évalués à partir des résultats des essais et E^* peut être considéré comme un module d'Young initial moyen. Les résultats des essais de compression isotropes, présentés dans le chapitre 3, ont montré la dégradation de module de compression avec la contrainte moyenne effective de Terzaghi due à la microfissuration du matériau. Logiquement on peut considérer que le même mécanisme de dégradation va aussi influencer le module

d'Young. Afin de simplifier le modèle d'endommagement, l'effet de la contrainte moyenne sur le module d'Young est négligé ici. L'évaluation des trois paramètres de modèle, E^*, a et b, est réalisée à l'aide d'un algorithme des moindres carrés et l'expression suivante est trouvée :

$$E = 13,0\left(1 - \frac{0,43\gamma^p}{1633 + \gamma^p}\right) \qquad \left(E\text{:GPa}\ ,\ \gamma^p\text{:}\mu\text{m/m}\right) \tag{5-7}$$

La Figure 5-8 présente une comparaison des modules d'Young mesurés et ceux évalués par le modèle et montre une reproduction satisfaisante des résultats expérimentaux par le modèle.

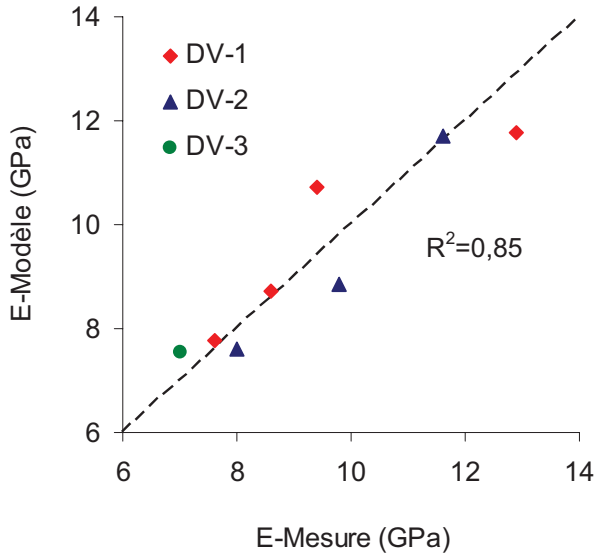

Figure 5-8- La comparaison des modules d'Young mesurés et évalués par le modèle

Une relation similaire à celle présentée dans l'équation (5-7) peut être trouvée pour la dégradation du module de cisaillement G dans la forme suivante :

$$G = 5,7\left(1 - \frac{0,49\gamma^p}{2522 + \gamma^p}\right) \qquad \left(G\text{:GPa}\ ,\ \gamma^p\text{:}\mu\text{m/m}\right) \tag{5-8}$$

La comparaison des modules de cisaillement mesurés et évalués par le modèle, présentée dans la Figure 5-9, montre encore une reproduction satisfaisante des résultats expérimentaux par le modèle.

Les expressions du module d'Young et du module de cisaillement, présentées respectivement dans les équations (5-7) et (5-8), permettent d'évaluer le coefficient de Poisson en fonction de la déformation déviatorique plastique en utilisant l'équation (5-5). Cette évaluation permet de faire une analyse complémentaire de la compatibilité des modèles d'endommagement proposés avec les données expérimentales. Dans la Figure 5-10, les coefficients de Poisson évalués sont comparés avec les valeurs mesurées. On observe que mis à part le point de l'essai DV-3 pour lequel un coefficient de Poisson élevé, égal à 0,44 est mesuré, la reproduction des autres résultats par les modèles d'endommagement est acceptable. En résumé, le modèle d'endommagement proposé donne des résultats acceptables pour exprimer la dégradation des modules élastiques du ciment sous chargement déviatorique. Etant donné de nombre limité des résultats expérimentaux, le modèle proposé est très simple, mais donne quand même une première idée de l'évolution des paramètres élastiques du ciment pétrolier en fonction de la déformation déviatorique plastique.

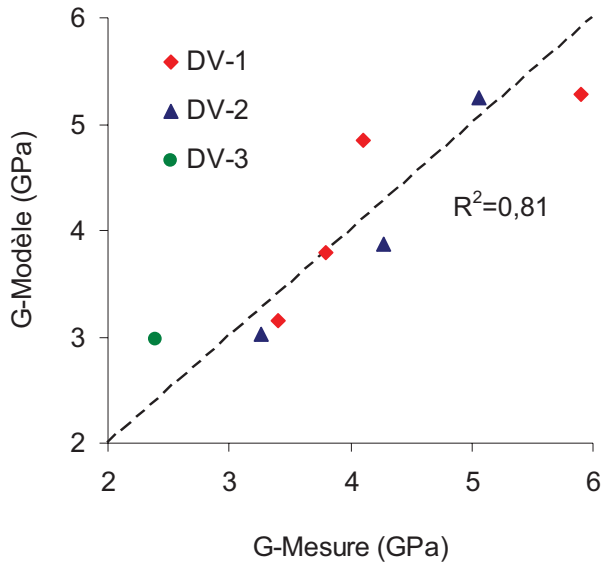

Figure 5-9- La comparaison des modules de cisaillement mesurés et évalués par le modèle

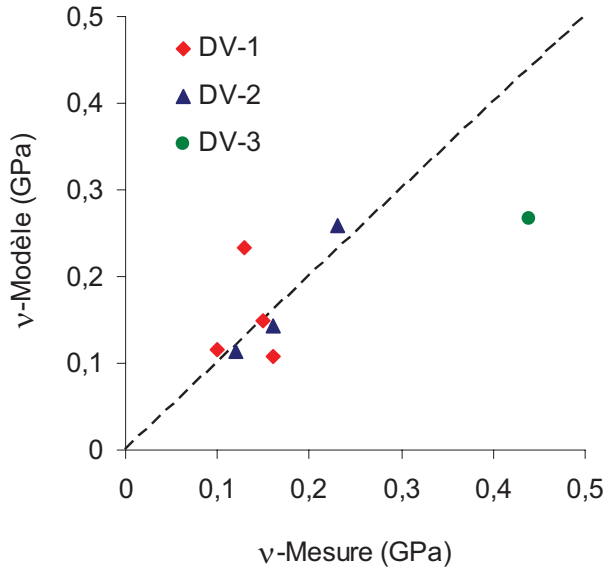

Figure 5-10- La comparaison des modules de cisaillement mesurés et évalués par le modèle

5.4 Caractérisation des échantillons après la rupture

Le Tableau 5-3 présente les dimensions, la vitesse des ondes longitudinales et le module d'élasticité dynamique des échantillons avant les essais et après la rupture. La comparaison des dimensions montre la contraction importante des échantillons due au chargement. Le diamètre des échantillons est resté à peu près constant. On observe également une diminution de la vitesse des ondes longitudinales et du module d'élasticité dynamique. La diminution du module d'élasticité dynamique est d'environ 5% pour l'essai DV-1 et 20% pour l'essai DV-3. Cette diminution est plus faible que celle évaluée pour le module d'Young statique qui est d'environ 40% (Tableau 5-2 et équation (5-7)). Cela peut être attribué au fait que le module d'élasticité dynamique correspond à des niveaux de déformation très faibles.

Afin de mieux comprendre le mécanisme de l'endommagement et de la rupture de l'échantillon sous le chargement déviatorique, des observations microscopiques ont été réalisées. Pour une meilleure observation des microfissures de l'échantillon DV-1, un matériel colorant est utilisé sur la surface de

l'échantillon. L'échantillon préparé est présenté sur la Figure 5-11. On peut observer les petites fissures diffuses sur la surface de l'échantillon et aussi deux fissures longues.

Mesure	Unité	DV-1		DV-3	
		Avant Essai	Après Essai	Avant Essai	Après Essai
Diamètre	mm	37,85	37,90	38,00	38,00
Hauteur	mm	75,05	70,47	73,31	69,91
Vitesse des ondes	m/sec	3389	3293	2903	2605
Module d'élasticité dynamique	GPa	16,37	15,53	16,14	13,33

Tableau 5-3- Caractérisation de l'échantillon avant et après la rupture

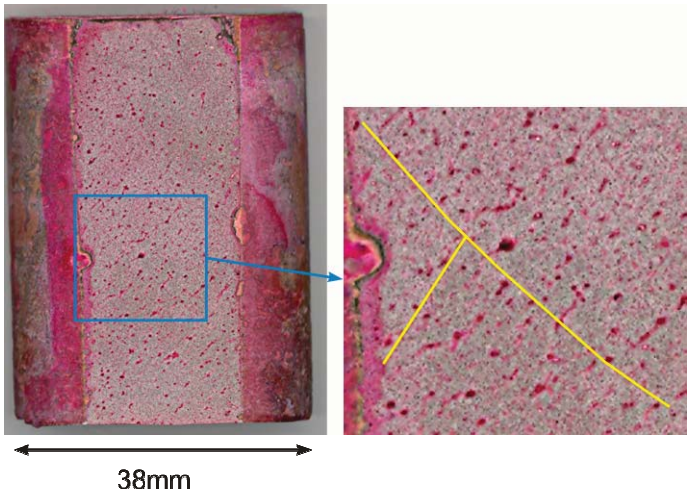

Figure 5-11- Surface polie de l'échantillon DV-1 après la rupture

L'observation microscopique de l'échantillon DV-1 à l'aide de microscope électronique à balayage (MEB) montre une direction préférentielle de la fissuration. Les photos présentées sur la Figure 5-12 et la Figure 5-13 sont prises avec un agrandissement 50X. Les fissures observées sur ces images ont des longueurs entre 0,5 et 2,5mm.

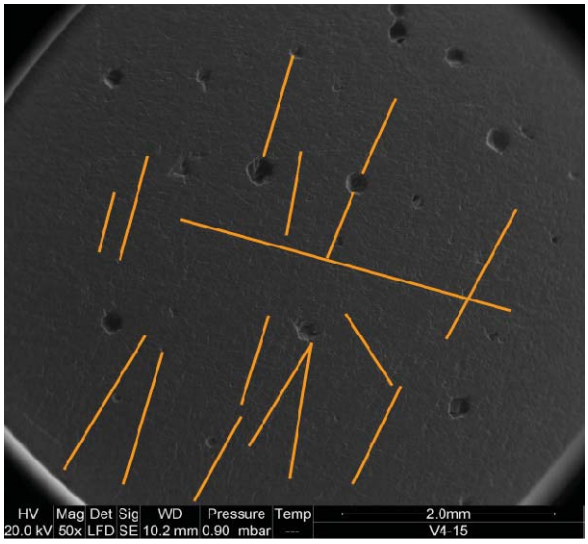

Figure 5-12- Observation microscopique de la surface polie de l'échantillon DV-1 après la rupture

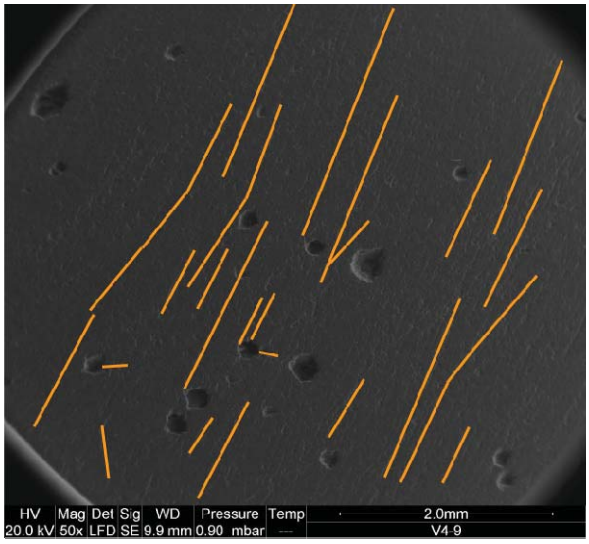

Figure 5-13- Observation microscopique de la surface polie de l'échantillon DV-1 après la rupture

La comparaison des photos prises avec différents agrandissements montre un effet d'échelle dans l'observation des fissures. Etant donné que différents chemins de contrainte sont appliqués sur cet échantillon avant la rupture, différentes familles de fissure sont produites et peuvent être observées. Le chargement isotrope produit des fissures diffuses, sans direction préférentielle, avec une longueur typique de 100 à 200 µm, tandis que le chargement déviatorique et la rupture de l'échantillon induisent des fissures avec une longueur plus importante, entre 1 et 2 mm avec une direction préférentielle (Figure 5-14).

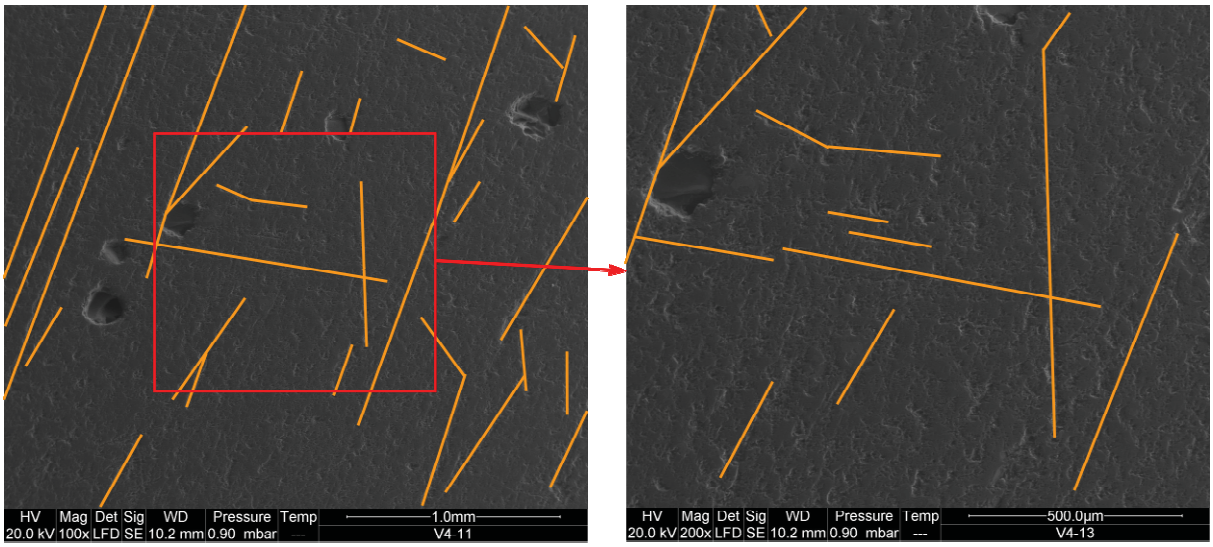

Figure 5-14- Observation microscopique de la surface polie de l'échantillon DV-1 après la rupture – Effet de l'échelle de l'observation

L'observation microscopique de la surface polie de l'échantillon DV-3 après la rupture (Figure 5-15 et Figure 5-16) montre une fissuration sensiblement plus légère que l'échantillon DV-1. Les fissures observées sont moins nombreuses et de plus faible longueur. Ceci peut être attribué à la pression de confinement plus importante appliquée dans l'essai DV-3, 25MPa contre 10MPa dans l'essai DV-1.

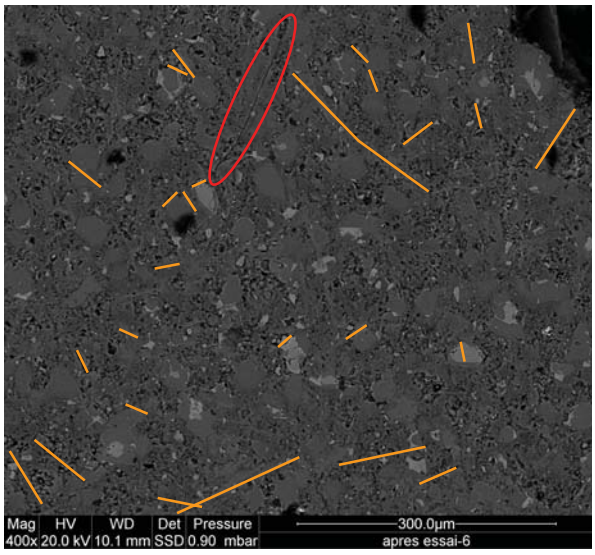

Figure 5-15- Observation microscopique de l'échantillon DV-3 après la rupture

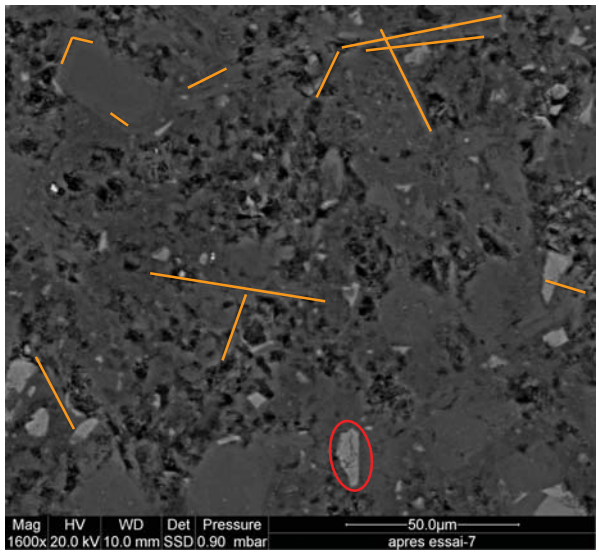

Figure 5-16- Observation microscopique de l'échantillon DV-3 après la rupture

La Figure 5-17 présente les détails des microfissures générées dans l'échantillon DV-3. On peut observer que la zone de contact entre les différents constituants de la microstructure du ciment est un

endroit favorable pour la génération des microfissures en raison de leur déformabilité différente. On observe des fissures générées au contact entre les grains anhydres et le C-S-H (a,b,d,i,k,l) et aussi au contact entre les C-S-H haute densité et basse densité (e,f,h). On peut aussi observer des fissures qui sont entièrement situées à l'intérieur du C-S-H haute densité (g) ou basse densité (c,j).

La compaction des échantillons sous l'effet de chargement peut être observée sur la Figure 5-18, ou des cristaux de portlandite formé dans un macropore sont comparés dans deux photos prises sur un échantillon sain et sur un échantillon après la rupture. Notons que les photos n'ont pas la même échelle. Ces photos ainsi que le raccourcissement très important des échantillons, présenté dans le Tableau 5-3, montrent la compaction très importante du ciment sous l'effet du chargement.

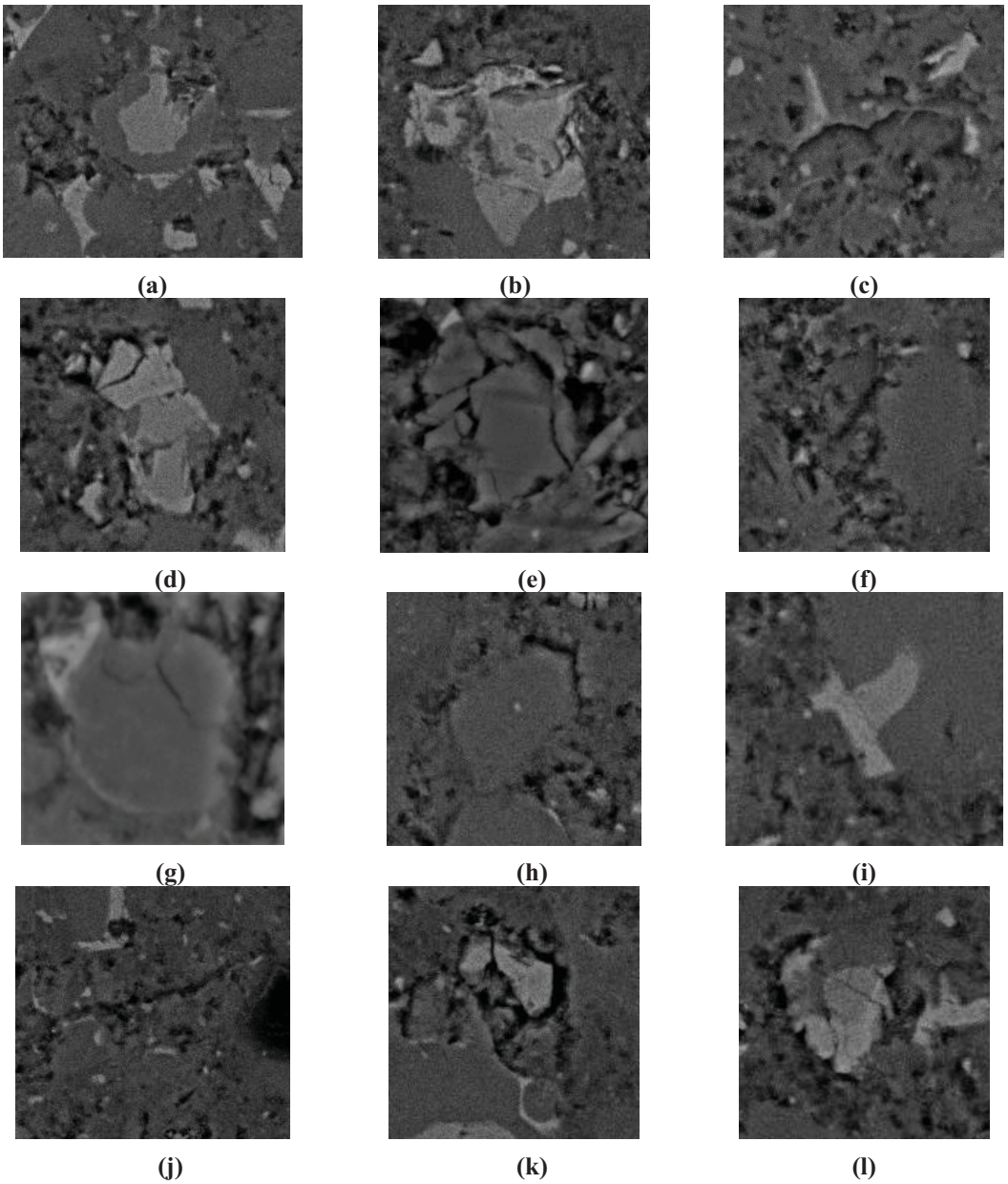

Figure 5-17- Observation microscopique de l'échantillon DV-3 après la rupture

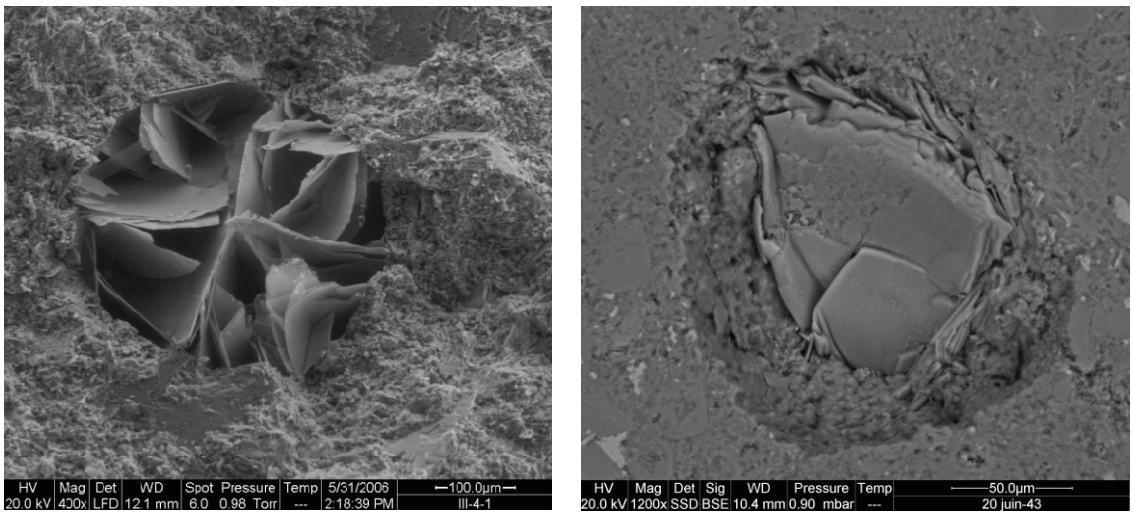

(a) échantillon sain (b) après la rupture

Figure 5-18- Effet de compaction de l'échantillon sur des cristaux de portlandite

5.5 Conclusions

1- Trois essais de compression déviatoriques drainés ont été réalisés à 90°C et les modules élastiques et les coefficients de Poisson ont été évalués dans les cycles de décharge-recharge et dans les phases de décharge après la rupture. Une bonne compatibilité entre les résultats obtenus est observée.

2- Les résultats des essais montrent la dégradation du module d'Young et du module de cisaillement au cours des essais déviatoriques. Cette dégradation résulte en une augmentation de coefficient de Poisson sous chargement déviatorique.

3- Les observations microscopiques des échantillons après la rupture montrent la fissuration des échantillons et également la compaction des échantillons sous l'effet du chargement. Ceci est compatible avec le raccourcissement important des échantillons sous chargement déviatorique. Les fissures observées dans l'échantillon DV-1 (pression de confinement 10MPa) sont plus nombreuses et plus longues que celles observées dans l'échantillon DV-3 (pression de confinement 25MPa).

4- Les observations microscopiques montrent que la zone de contact entre les différents constituants de la microstructure du ciment est un endroit favorable pour la génération des microfissures en raison de leur déformabilité différente. Ainsi on observe des fissures au contact des grains anhydres et du C-S-H ou au contact entre le C-S-H haute densité et le C-S-H basse densité.

5- On observe une diminution de la vitesse des ondes longitudinales et du module d'élasticité dynamique. Cette diminution du module d'élasticité dynamique est plus faible que celle évaluée pour le module d'Young statique, ce qui peut être attribué au fait que le module d'élasticité dynamique correspond à des niveaux de déformation très faibles

6- Un modèle d'endommagement très simple est proposé sur la base des résultats obtenus. Ce modèle décrit la diminution du module d'Young et du module de cisaillement en fonction de la déformation déviatorique plastique accumulée. Malgré le nombre limité des données expérimentales, les résultats du modèle proposé pour la description de l'endommagement du ciment sous chargement déviatorique sont acceptables.

5.6 Perspectives

L'étude préliminaire du comportement du ciment pétrolier sous chargement déviatorique présentée dans ce chapitre doit être complétée afin d'établir un critère de rupture. Cela nécessite de:

1- Poursuivre le programme des essais déviatoriques à 90°C en réalisant les essais sous des pressions de confinement plus importantes.
2- Réaliser les essais déviatoriques à d'autres températures afin d'étudier l'effet de la température sur les paramètres du critère de rupture.

Le modèle d'endommagement présenté dans ce chapitre peut aussi être amélioré et complété à l'aide des données de ces essais.

CHAPITRE 6. **CONCLUSIONS ET PERSPECTIVES GENERALES**

6.1 Conclusions générales

L'étude du comportement thermo-poro-mécanique d'un ciment pétrolier présenté dans mémoire nous permet de tirer les conclusions suivantes:

1- **La pâte de ciment durcie est un matériau poromécanique**. Le comportement de ce matériau peut être effectivement décrit par la théorie des milieux poreux.
2- L'analyse des résultats expérimentaux montre que la porosité de ciment qui doit être utilisée dans les formulations poromécanique est inférieure à la porosité totale du ciment, mesurée en séchant l'échantillon à 105°C. La porosité qui doit être utilisée, est vraisemblablement la porosité de l'eau libre qui peut être mesurée en mettant le ciment en équilibre à 11% humidité relative. Cette porosité pour les pâtes du ciment avec w/c<0,5 peut être approximée par la porosité mesurée au porosimètre à mercure.
3- Les résultats expérimentaux montrent la dégradation des modules élastiques de la pâte de ciment durcie sous l'effet du chargement mécanique et de la température. Sous chargement isotrope, cette dégradation se manifeste dans la diminution des modules de compression et l'augmentation du coefficient de Biot avec la contrainte effective et avec la température. Sous chargement déviatorique, les résultats des essais montrent la diminution du module d'Young et du module de cisaillement et l'augmentation du coefficient de Poisson. Les observations microscopiques des échantillons montrent que ce phénomène est dû à la microfissuration du ciment y compris sous chargement isotrope. Cette microfissuration peut être expliquée par la microstructure fortement hétérogène du matériau. Sous chargement déviatorique, le nombre et la longueur des fissures générées diminuent avec l'augmentation de la pression de confinement. Ces observations montrent aussi que la zone de contact entre les différents constituants de la microstructure du ciment est un endroit favorable pour la génération des microfissures, ce qui peut être expliqué par la concentration de contrainte associée à la déformabilité différente des constituants.
4- Les coefficients de contrainte effective correspondants aux variations du volume total, du volume poreux, du volume solide, de porosité et du module de compression drainé du ciment sont évalués. Le module de compression drainé K_d du ciment varie avec la contrainte effective de *Terzaghi*. Ceci est compatible avec la mesure d'un module de compression de la phase solide K_s constant pour le ciment étudié.
5- Le fluage du ciment sous chargement isotrope augmente sensiblement avec la température.
6- La perméabilité du ciment diminue sous chargement isotrope. Ceci montre que la compaction de la matrice poreuse de ciment a un effet plus important sur la perméabilité que la microfissuration, étant donné que les fissures peuvent rester fermées sous l'effet du chargement. Une loi puissance est établie pour la diminution de la perméabilité du ciment en fonction de sa porosité. La puissance égale à 11 est une caractéristique du processus de compaction de ciment sous chargement isotrope et ne peut pas être utilisée pour la variation de la porosité dans un autre processus d'évolution de la porosité.

$$k = 1{,}14 \times 10^{-19} \left(\frac{\phi}{0{,}26} \right)^{11} \qquad \left(k : \mathrm{m}^2 \right)$$

7- Une méthode simple est présentée pour la correction de la pression interstitielle mesurée lors d'un essai de chauffage non-drainé pour prendre en compte l'effet des déformations thermiques et mécaniques du système de drainage de la cellule triaxiale.

8- Pour la gamme de températures étudiées dans l'essai de chauffage non-drainé réalisé, entre 20°C et 60°C, le coefficient de pressurisation thermique du ciment étudié ne varie pas significativement avec les variations de la température et de l'état de contraintes. Ceci peut être attribué aux anomalies du comportement thermique du fluide interstitiel du ciment confiné dans pores de très petite taille.

9- L'analyse des résultats de l'essai de chauffage non-drainé montre que le coefficient d'expansion thermique du fluide interstitiel du ciment est plus grand et moins sensible aux variations de la température que celui de l'eau pure. Cette anomalie est attribuée au confinement du fluide dans des pores de très petite taille de la microstructure du ciment et aussi à la présence des ions dans le fluide interstitiel.

10- L'ensemble des paramètres thermo-poro-mécanique de la pâte de ciment étudiée (w/c=0,44, hydratée à 90°C) sont présentés dans le tableau suivante :

Paramètres poroélastiques				
Paramètre	**Description**	**Unité**	**Valeur**	
			Température ambiante	**90°C**
K_s	Module de compression des grains solides	GPa	21,0	17,5
K_d^{sec}	Module de compression drainé	GPa	$8,69-0,087\sigma_d$ (a)	$5,26-0,034\sigma_d$ (a)
K_u^{sec}	Module de compression non-drainé	GPa	$11,25-0,099\sigma_d$ (a)	8,5(b)
K_ϕ	Module de compression de l'espace poreux	GPa	16,9	-
B	Coefficient de Skempton	-	0,4	0,55(b)
α^{sec}	Coefficient de Biot	-	$0,586+0,004\sigma_d$ (a)	$0,7+0,002\sigma_d$ (a)
E	Module d'Young	GPa	-	$13,0\left(1-\frac{0,43\gamma^p}{1633+\gamma^p}\right)$ (d)
G	Module de cisaillement	GPa	-	$5,7\left(1-\frac{0,49\gamma^p}{2522+\gamma^p}\right)$ (d)
Paramètres thermiques				
α_d	Coefficient d'expansion thermique drainé	$(°C)^{-1}$	6×10^{-5}	
α_u	Coefficient d'expansion thermique non-drainé	$(°C)^{-1}$	$1,1\times10^{-4}$ (c)	
Λ	Coefficient de pressurisation thermique	MPa/°C	0,6 (c)	
Propriétés du transport				
k	Perméabilité	m^2	$1,14\times10^{-19}\left(\frac{\phi}{0,26}\right)^{11}$ (e)	

(a) σ_d contrainte effective de Terzaghi en MPa , (b) Evalué indirectement pour $\sigma_d = 0$, (c)Valeur moyenne pour les températures entre 20 et 60°C , (d) γ^p déformation déviatorique plastique en µm/m , (e) Evolution de la perméabilité sous chargement isotrope

6.2 Perspectives générales

L'étude du comportement thermo-poro-mécanique du ciment pétrolier présentée dans cette thèse nécessite d'être complétée en poursuivant les travaux expérimentaux et en développant l'analyse sur les points suivants. Une description plus détaillée de ces études est présentée à la fin des chapitres 3, 4 et 5.

a. Prendre en compte les effets du fluage de ciment dans l'analyse des résultats des essais de compression isotrope.
b. Réaliser quelques essais supplémentaires spécialement programmés afin d'étudier l'effet de fluage sous contraintes isotropes sur les paramètres poroélastiques du ciment.
c. Compléter l'étude sur la réponse en compression isotrope à 90°C en réalisant des essais non-drainés.
d. Etudier l'influence de la température sur la relation perméabilité-porosité du ciment sous contraintes isotropes.
e. Réaliser les essais de compression isotrope à une température intermédiaire, e.g. 50°C.
f. Réaliser des essais de chauffage non-drainés dans une gamme de température entre 60 et 90°C afin d'évaluer le coefficient de pressurisation thermique et le coefficient d'expansion thermique du fluide interstitiel du ciment dans cette gamme de température.
g. Poursuivre la caractérisation de la réponse du ciment sous chargement déviatorique à 90°C en réalisant des essais sous pressions de confinement plus importantes et réaliser également des essais déviatoriques à d'autres températures..

Les dispositifs expérimentaux du Laboratoire Central des Ponts et Chaussées (LCPC) permettront prochainement la réalisation d'essais à des contraintes beaucoup plus importantes pouvant atteindre 200MPa de pression de confinement et 1000MPa de contrainte axiale. Le phénomène de diminution du module de compression du ciment sous contrainte isotrope observé jusqu'à 60MPa dans notre étude, pourra ainsi être exploré dans une gamme de contraintes permettant d'atteindre éventuellement l'effondrement poreux du matériau et le renforcement par compaction.

Le ciment coulé dans un puits pétrolier est hydraté et durci à températures différentes, selon la profondeur à laquelle le ciment est situé. Comme mentionné dans le chapitre 1, la température d'hydratation à une influence très importante sur les propriétés mécanique du ciment. Il est donc nécessaire d'étudier l'effet de la température d'hydratation sur les propriétés thermo-poro-mécaniques du ciment pétrolier. Pour ce faire, il faut réaliser un programme expérimental similaire à celui présenté dans cette étude, sur des ciments hydratés à différentes températures.

De plus, les ciments situés à différentes profondeurs dans un puits pétrolier sont hydratés sous des pressions différentes. Cette pression peut également influencer les propriétés thermo-poro-mécaniques de la pâte de ciment durcie, ce qui peut être étudié en réalisant des essais poromécaniques sur des ciments hydratés sous différentes pressions.

Au cours de la vie d'un puits, la gaine de ciment d'un puits pétrolier est soumise à de nombreux cycles de sollicitations mécaniques et thermiques. Il est donc intéressant d'étudier l'effet des cycles de chargements mécaniques et thermiques sur les propriétés et le comportement thermo-poro-mécanique du ciment et explorer ainsi la réponse en fatigue du matériau.

Il est également intéressant et très utile d'associer les études expérimentales des propriétés poromécaniques du ciment, comme la présente étude, avec les modélisations micromécaniques et les méthodes d'homogénéisation existantes pour l'évaluation des propriétés poromécaniques de ce

matériau. Les résultats des essais poromécaniques peuvent être utilisés pour l'étalonnage d'un modèle micromécanique. Un avantage significatif de ces modèles est leur capacité à produire des résultats pour les ciments préparés avec différents rapports w/c ou différentes degrés d'hydratation. D'autre part, ce couplage entre les approches expérimentales macroscopiques et les modélisations micromécanique peut également fournir des informations sur les propriétés mécaniques des constituants de la microstructure du ciment.

A plus long terme, le but de ces études sur le comportement des ciments pétroliers est l'établissement d'un modèle de comportement pouvant être introduit dans un outil de calcul. En effet, seul une approche numérique permet de prévoir la réponse de la gaine de ciment aux chemins complexes de chargements mécaniques et thermiques auxquels elle est soumise au cours de la vie du puits dans la phase d'exploitation du réservoir et dans la phase éventuelle de stockage des gaz à effet de serre. La composition du ciment, le rapport eau/ciment, les conditions d'hydratation (température, pression), déterminent le matériau initial. A ce matériau initial, on doit associer un modèle de comportement suffisamment complet pour prendre en compte l'effet des contraintes, de la température, du temps dans un cadre thermo-poro-visco-elasto-plastique. Le stockage de gaz acides induit de plus un effet de dégradation chimique sur un ciment qui a subi déjà de nombreux chemins de chargements mécaniques et thermiques. On voit donc toute la complexité du problème et le nombre important d'études expérimentales nécessaires qui doivent être couplées à une bonne connaissance de la microstructure du matériau et à une modélisation micro-mécanique.

ANNEXE 1. **LOI DE CONTRAINTE EFFECTIVE POUR LA PERMEABILITE D'UN CALCAIRE**

Dans le chapitre 1 nous avons discuté l'existence d'une contrainte effective qui contrôle une propriété donnée d'un matériau poreux. Dans cette annexe, nous développons un exemple relatif à la perméabilité à partir d'une étude expérimentale menée sur un calcaire. Cet exemple est présenté sous la forme d'un article intitulé « Effective stress law for the permeability of a limestone » qui est publié dans la revue « International Journal of Rock Mechanics and Mining Sciences ». Un résumé des principaux résultats est présenté ci-dessous.

La perméabilité de la roche dépend à la fois de la contrainte totale et de la pression interstitielle et donc on peut toujours exprimer la perméabilité comme une fonction de ces deux variables. Si la perméabilité peut aussi être exprimée en fonction d'une seule variable, combinaison linéaire de la contrainte totale et de la pression interstitielle, on peut dire que la perméabilité suit une loi de contrainte effective. Afin d'évaluer la loi de la contrainte effective correspondant à la variation de la perméabilité de la roche étudiée, des essais de perméabilité en régime permanent ont été réalisés avec différentes combinaisons des valeurs de la contrainte totale et la pression interstitielle. Les résultats montrent que la perméabilité diminue avec la pression de confinement et augmente avec la pression interstitielle, mais l'effet de la pression interstitielle est plus important que l'effet de la pression de confinement. Les résultats de ces essais permettent de définir une contrainte effective pour la variation de la perméabilité pour laquelle le coefficient de contrainte effective augmente avec la contrainte différentielle (contrainte de Terzaghi) et devient supérieur à un dès que la contrainte différentielle dépasse quelques bars. Une loi de puissance est proposée pour la variation de la perméabilité avec la contrainte effective. Des observations microscopiques ont été réalisées afin d'étudier le rôle de la microstructure de la roche dans les variations de la perméabilité. Sur la base de ces observations, un modèle conceptuel, appelé « pore-shell model », est proposé pour la microtexture de la roche. Ce modèle est capable de produire des coefficients de contrainte effective pour la perméabilité qui sont plus grands que un et qui augmentent avec le rapport des modules de compression des différents constituants de la roche. Ce rapport a été étudié expérimentalement en réalisant des essais de microdureté et on a trouvé effectivement des valeurs supérieures à un. Selon le modèle proposé, ce résultat conduit à un coefficient de contrainte effective pour la perméabilité qui est supérieur à un. Par conséquent, l'approche microtexturale est compatible avec les résultats des essais réalisés.

International Journal of Rock Mechanics & Mining Sciences 46 (2009) 297–306

Contents lists available at ScienceDirect

International Journal of Rock Mechanics & Mining Sciences

journal homepage: www.elsevier.com/locate/ijrmms

Effective stress law for the permeability of a limestone

Siavash Ghabezloo [a,*], Jean Sulem [a], Sylvine Guédon [b], François Martineau [b]

[a] Université Paris-Est, UR Navier, CERMES, Ecole Nationale des Ponts et Chaussées, 6-8 avenue Blaise Pascal, Cité Descartes, 77455 Champs-sur-Marne, Marne la Vallée cedex 2, France

[b] Université Paris-Est, LCPC, MSRGI, 58, boulevard Lefebvre, 75015 Paris Cedex 15, France

Abstract

The effective stress law for the permeability of a limestone is studied experimentally by performing constant head permeability tests in a triaxial cell with different conditions of confining pressure σ and pore pressure p_f. Test results have shown that a pore pressure increase and a confining pressure decrease both result in an increase of the permeability, and that the effect of the pore pressure change on the variation of the permeability is more important than the effect of a change of the confining pressure. A power law is proposed for the variation of the permeability with the effective stress ($\sigma' = \sigma - n_k p_f$). The permeability effective stress coefficient n_k increases linearly with the differential pressure and is greater than one as soon the differential pressure exceeds few bars. The test results are well reproduced using the proposed permeability-effective stress law. A conceptual pore-shell model based on a detailed observation of the microstructure of the studied limestone is proposed. This model is able to explain the experimental observations on the effect of the total stress and of the pore pressure on the permeability of the limestone. Effective stress coefficients for the stress-dependent permeability which are greater than one are obtained. It is shown that the important factor is the ratio of the different bulk moduli of the various constituents of the rock. This ratio is studied experimentally by performing microhardness tests.

Keywords: permeability, effective stress, limestone, microstructure, microhardness test

1 Introduction

The determination of the permeability of a rock and its variation with changes of total stress and pore pressure has a great interest in petroleum reservoir engineering. The pore pressure decrease during the oil or gas production from a reservoir causes the reduction of the permeability of the reservoir and consequently the reduction of the production rate. The variations of permeability with the state of stress is also important in geophysics in the studies of rapid fault slip events when shear heating tends to increase the pore pressure and to decrease the effective compressive stress and the shearing resistance of the fault material (Rempel and Rice [1], Sulem et al. [2]). The increase of the permeability of the fault material with the pore pressure increase can lead to a faster dissipation of the excess pore pressure and consequently can decelerate the weakening of the shearing resistance of the fault material.

If a single variable can be defined as a linear combination of the total stress and the pore pressure to express the variations of the permeability, then we can say that the permeability follows an effective stress law. The concept of effective stress was first introduced by Terzaghi [3] who defined it as the difference between the total stress σ and pore pressure p_f and attributed all measurable effects of a change in stress exclusively to changes in the effective stress:

$$\sigma_d = \sigma - p_f \tag{1}$$

In equation (1) σ_d is the Terzaghi effective stress, which is also called the differential pressure. More generally, the effective stress $\sigma' = \sigma'\left(\sigma, p_f\right)$ can be defined as a stress quantity which can be used as a single variable to express the stress dependency of a property Q of a porous material (Equation (2)). Reducing the number of independent variables from two to one by using the concept of effective stress greatly simplifies the analysis of total stress and pore pressure dependency of the porous material properties.

$$Q = Q\left(\sigma, p_f\right) = Q\left(\sigma'\right) \tag{2}$$

If the total stress and the pore pressure vary in such a way that the effective stress remains constant, then no variation in the corresponding property Q is expected. Thus the expression of the effective stress can be obtained from the evaluation of the isolines of $Q(\sigma, p_f)$.

Since different material properties may depend on total stress and pore pressure in different ways, there is not a unique effective stress which would be appropriate for all properties of the material, and consequently different effective stress expressions should be defined for the different properties.

Assuming that the function $Q(\sigma, p_f)$ is smooth enough so that its derivatives can be defined, the incremental variation of Q can be written as:

$$dQ = \frac{\partial Q}{\partial \sigma} d\sigma + \frac{\partial Q}{\partial p_f} dp_f \tag{3}$$

We can re-write equation (3) in the following form:

$$dQ = \frac{\partial Q}{\partial \sigma}\left[d\sigma - \left(-\frac{\partial Q / \partial p_f}{\partial Q / \partial \sigma} \right) dp_f \right] \tag{4}$$

The above expression shows that the variation of the property Q can be expressed as a function of a single incremental quantity $d\sigma'$:

$$dQ = \frac{\partial Q}{\partial \sigma} d\sigma' \tag{5}$$

with

$$d\sigma' = d\sigma - n_Q dp_f \tag{6}$$

The coefficient n_Q is the effective stress coefficient corresponding to the property Q defined as:

$$n_Q(\sigma, p_f) = -\frac{\partial Q / \partial p_f}{\partial Q / \partial \sigma} \tag{7}$$

The isolines of Q are obtained by the integration of the following differential equation:

$$d\sigma' = 0 \tag{8}$$

In the close vicinity of a given state of stress (σ, p_f), the isolines are generally approximated with parallel straight lines (e.g. Bernabé [4]) which is equivalent to the assumption that n_Q is a constant. Under this assumption, equation (6) can be easily integrated and a linear expression for the effective stress is obtained:

$$\sigma' = \sigma - n_Q p_f \tag{9}$$

The linear expression presented in equation (9) is the most common expression for the effective stress as it is usually used in the mechanics of porous media. The effective stress coefficient n_Q is equal to one in Terzaghi's definition which means that the total stress and the pore pressure have similar, but inverse, effects on the variation of the property Q. A value of the coefficient n_Q smaller (respectively greater) than unity means that the effect of pore pressure change on the variation of the property Q is less (respectively more) important than the effect of a change in total stress.

Zimmerman [5] and Berryman [6] have derived general effective stress rules for various physical properties of rocks and presented the expressions of the effective stress coefficients n_Q corresponding to different physical properties together with some bounds and general relations among these coefficients.

As mentioned earlier, the great advantage of the effective stress concept is the simplification of the analysis by using one single variable σ' instead of two independent variables, σ and p_f. The resulted simplification is significant when the effective stress coefficient is constant, but the variability of this coefficient adds new difficulties to the problem. In this case, if the effective stress coefficient is a simple function of the pore pressure and the confining pressure, for example a linear function of the differential pressure σ_d, then the use of the effective stress concept may be still advantageous. Obviously, if the effective stress coefficient involves a complicated relation between the pore pressure and the confining pressure, it may be more appropriate to abandon the effective stress concept and to analyse the problem using the two independent variables.

The effective stress corresponding to the variations of the permeability of the rocks has been studied theoretically and experimentally by different researchers. Berryman [6] has studied the problem theoretically and has derived the expressions of the effective stress coefficient for the permeability of the rocks constituted by one single and two different minerals. His approach resulted in an effective stress coefficient which is smaller than one for a micro-homogeneous material made up of one single mineral and which may be greater than one for a porous material constituted by two different minerals. This is for example the case in clay-rich sandstones as the grains modulus of the pore-filling material is much smaller than the one of the sand grains. Experimental studies on both sedimentary and crystalline rocks

can be found in the literature. Most of the studies on sedimentary rocks have been conducted on clay-rich sandstones (Zoback [7], Zoback and Byerlee [8], Walls and Nur [9], Nur et al. [10], Walls [11], Al-Wardy [12], Al-Wardy and Zimmerman [13]) and resulted in effective stress coefficients which are greater than one and which increase with the clay content. The evaluated effective stress coefficient by Walls [11] varies from 1.2 for clean sandstone to 7.1 for sandstone containing 20% clay. These results show that the permeability of the studied rock is more sensitive to variations of the pore pressure than to the changes of the total stress. To explain these results, Zoback and Byerlee [8] have proposed a conceptual clay-shell model in which the rock consists of quartz, permeated with cylindrical pores that are lined with an annular layer of clay which is more compliant than the outer quartz layer. Such a model is more sensitive to changes in pore pressure than to changes in total stress, and therefore results in an effective stress coefficient greater than one. Al-Wardy and Zimmerman [13] have proposed a different microstructural model in which the clay is distributed in the form of particles that are weakly coupled to the pore walls and have obtained results that are more compatible with the experimental results. Kwon et al. [14] have studied the permeability of illite-rich shale with a clay content of about 45% and found an effective stress coefficient equal to one which differs from the results obtained for clay-bearing sandstones with low clay content. They concluded that this is due to the contiguity of clays throughout the rock which support the applied confining pressure as well as the pore pressure.

As opposed to the results obtained for porous sedimentary rocks, the experimental studies performed on crystalline and jointed rocks resulted in effective stress coefficients which are smaller than or very close to one. Walsh [15] examined the experimental results of Kranz et al. [16] for flow through joints with polished surfaces and joints with jagged surfaces formed by a tensile fracture. The estimated effective stress coefficients are equal to 0.9 for the polished surfaces and 0.56 for the tension fractures. Experimental studies of Coyner [17] and Morrow et al. [18] on two granites resulted in permeability effective stress coefficients very close to one. Bernabé [4],[19] studied the permeability of several crystalline rocks and found effective stress coefficients which are smaller than one and which decrease with increasing confining pressure due to the changes in the geometry of the cracks during closure. He also reported the strong loading path dependency of the effective stress coefficient. This stress path dependency decreases rapidly with the number of cycles and the effective stress coefficient approaches one after a few cycles.

In this paper an experimental study for determining the effective stress law for the permeability of a limestone is presented. A drained hydrostatic compression test is performed in order to evaluate the drained bulk modulus of the rock. Constant head permeability tests are performed with different conditions of confining pressure and pore pressure and the effective stress coefficient for the variations of the permeability of the rock is determined. The results enable us to compare the sensitivity of the permeability of the rock to the variations of the total stress and of the pore pressure. Microscopic observations have been performed in order to study the microstructure of the limestone and to better understand the mechanism of permeability evolution with total stress and pore pressure variations. On the basis of these observations, a conceptual model is proposed for the microstructure of the material in order to determine the effective stress coefficient for the permeability of the rock and to interpret the experimentally measured values of this coefficient. This model accounts for the relative compliance of the constituents of the rock which is studied by performing microhardness tests.

2 Description of the studied rock

The rock studied in this paper is an oolitic limestone of Neocomian age (–135 to –127 million years), collected near Nîmes in south of France. This white limestone is homogeneous at the scale of the quarry, at the scale of the blocs and also at the scale of the samples observed under a microscope.

The observations are performed using a polarizing optical microscope and an environmental scanning electron microscope (ESEM). These two observation methods are complementary for this study, as they provide two different magnification scales.

The ESEM is equipped by two types of detectors: A detector of secondary electrons (SE) and a detector of backscattered electrons (BSE). The SE detector results in images which emphasize the topographical contrasts on the observed sample and have a three-dimensional appearance. In these images, steep surfaces and edges tend to be brighter than flat surfaces. The BSE detector can detect the contrast between areas with different chemical compositions, especially when the average atomic number of the various regions is different. The brightness of the images taken by this detector tends to increase with the atomic number.

The studied limestone is entirely composed of calcite, with calcite crystals of different sizes depending on the period and the dynamics of the crystallization. An image using the optical microscope under polarized light is presented in Figure (1a). This microphotograph shows that the studied rock is constituted of quasi spherical oolites, with a size of 100 to 400 µm, cemented by a sparitic calcite. An other image taken with the ESEM using the SE detector is presented in Figure (1b) and shows the details of the microstructure and the interface between oolites and sparitic calcite cement. The geological formation of this limestone can be summarized in three steps:

- Formation of concentric oolites in a high-energy marine environment at high temperature, low depth waters; these oolites are constituted from micro-crystallized calcite (micrite)
- Sedimentation of oolitic sand and crystallization of a palissadic calcite ore around the oolites; this sedimentation has also a marine origin
- Cementation of the oolites by precipitation of crystalline calcite of sparite type

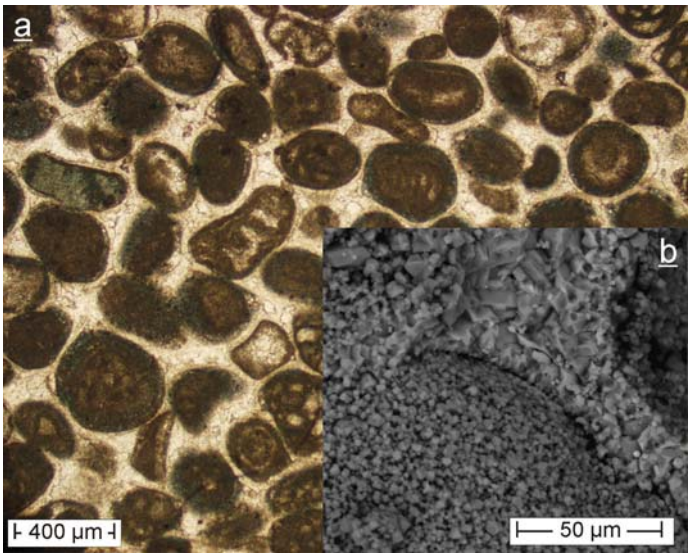

Figure 1- Microstructure of the studied limestone observed with (a) optical microscope, (b) ESEM

Figure (2a) presents the details of the micrite crystals forming the oolites. We can see that the microstructure of the oolites is similar to a granular material with grains diameters varying from 2 to 5

µm and with a fine porosity between the grains. The sparite crystals which constitute the cement connecting the oolites are shown in Figure (2b). We can see clearly the difference between the microstructure of the oolites and the one of the sparitic cement. This latter is composed of interlocked grains with a bigger size than the micrite grains of the oolites. Both sparite and micrite are entirely composed of calcite.

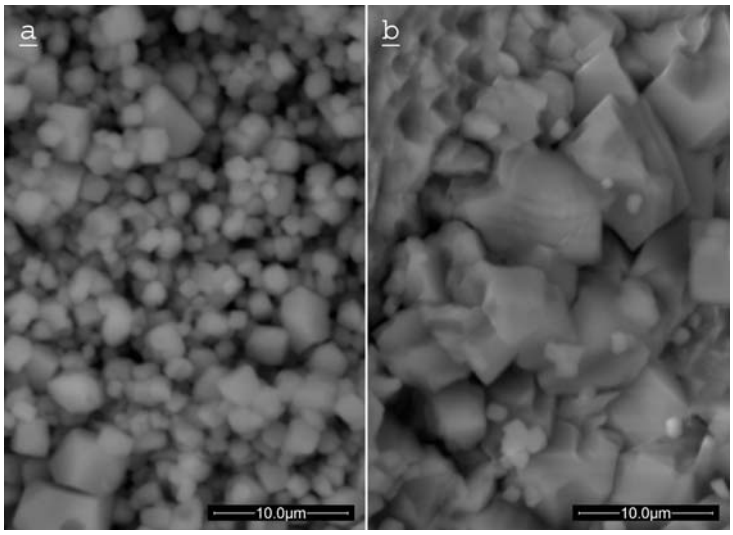

Figure 2- Details of (a) an oolite and (b) the sparitic cement observed with the ESEM

The measured connected porosity of the studied limestone is between 13.4% and 17.6% with the average value equal to 15.7%. The measured apparent density of the skeleton is equal to $2.22\,g/cm^3$ and the measured absolute density of the grains is equal to $2.70\,g/cm^3$ which is compatible with the value $2.71\,g/cm^3$ given by Bass [20] for calcite. From these values the total porosity of the rock is evaluated equal to 17.7%. The difference between the connected and the total porosity reveals the presence of 2.0% occluded porosity in the rock matrix.

The porosity of the rock is studied using the optical microscope on a sample which was injected with a blue resin (Figure (3a)). The blue areas, which correspond to the pores, are mostly concentrated around the oolites in a layer with a thickness of 10 to 20 µm. The porosity of the rock can also be studied using the ESEM images taken with the BSE detector. In these images the porous space appears as in black areas. An image is shown in Figure (3b) and shows clearly that the porosity is concentrated around the oolites. Comparing this porosity with the one observed in Figures (2a) and (2b) we can conclude that there are two types of porosity in the studied limestone: a macro-porosity and a micro-porosity. The macro-porosity as seen in Figure (3) is mostly concentrated around the oolites while the micro-porosity corresponds to the intergranular voids between the grains of micrite in the oolite and between the grains of sparite in the cement. The analysis of several images showed that the blue areas, which represent the macro-porosity, fill about 13% of the total area of the images. Comparing this value to the average connected porosity of the rock, 15.7%, one can deduce that most of the connected porosity is located around the oolites. Comparing the evaluated macro porosity, about 13%, and the total porosity, 17.7%, we can estimate the micro-porosity of the rock equal to 4.7%. As mentioned above, 2.0% of the porosity of the rock is occluded. Comparing this value with the micro-porosity, we can infer that about 42% of the micro-porosity of the rock is occluded.

The analysis of the image presented in Figure (1a) shows that about 28% of the area of this image is filled with the sparitic cement and thus the remaining 72% is filled with the oolites and the macro

porosity. Knowing that the macro porosity is equal to 13% as presented above, the volumetric fraction of the oolites is found equal to 59%.

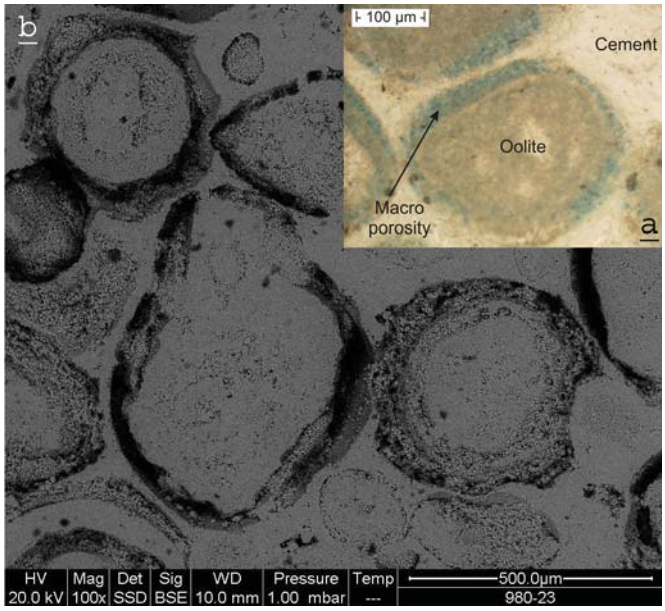

Figure 3- Porous space of the limestone-concentration of the main porosity around the oolites, (a) optical microscope (b) ESEM

3 Laboratory tests

Laboratory tests in this study consist of a drained hydrostatic compression test for the evaluation of the compressibility of the rock and constant head permeability tests with different values of pore pressure and confining pressure in order to study their individual effect on the variations of the permeability. Note that all the tests are performed on the same sample. The drained compression test with a loading-unloading cycle is performed before the permeability tests. This guaranties that the sample behaves elastically during the permeability tests. The tests are performed on a 40mm diameter and 80mm length saturated sample in a triaxial cell as described in Ghabezloo and Sulem [21]. The saturation procedure is the following: The sample is first dried at a temperature of 60°C until the measured mass remains constant and then it is put in a vacuum chamber during 24 hours to eliminate the remaining air bubbles. Water is then introduced in the chamber and the sample is kept immerged under water during 48 hours. The sample is then put in a rubber jacket with a grease layer inside the jacket and installed inside the triaxial cell. An initial confining pressure is applied and water is circulated using a pressure generator.

3.1 Drained hydrostatic compression test

The bulk modulus of the rock is evaluated in a drained hydrostatic compression test with a loading and unloading cycle. In this test, a fluid back pressure of 1.0MPa was maintained constant inside the sample. In Figure (4) the volumetric strain response is shown versus the applied total stress. The observed non-linear response reflects the stress-dependent character of the rock compressibility (Zimmerman [5], Sulem et al. [22][23]). Moreover this curve exhibits a different response in loading and unloading and irreversible deformation. Therefore the elastic tangent drained compression modulus K_d is evaluated on the unloading curve. The slope of this curve is directly evaluated of the experimental

data using the method used in Ghabezloo and Sulem [21] where the slope of the tangent at each point is calculated as a difference quotient of N data points centred around the corresponding point. The evaluated bulk modulus is presented as a function of Terzaghi effective stress on Figure (5). This curve can be approximated by the following linear expression:

$$K_d = 6.22 + 1.035\sigma_d \qquad \left(K_d : \text{GPa}\,,\ \sigma_d : \text{MPa}\right) \tag{10}$$

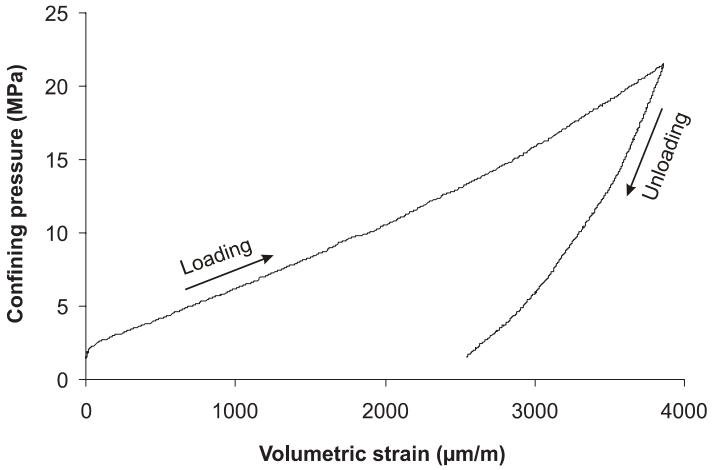

Figure 4- Drained hydrostatic compression test with a loading-unloading cycle

This expression shows the linear increase of the drained bulk modulus with Terzaghi effective stress in the limit of the applied pressures. The non linear elastic response in hydrostatic compression can be attributed to the closure of the regions of imperfect bounding between grains (Zimmerman [5]) and the compaction of the porous space of the rock. Figure (3b) exhibits limited contact areas between the oolites and the surrounding cement, which can cause the compressibility of the microstructure of the rock. More contacts can be formed under stress leading thus to a strengthening of the rock. This strengthening effect will be limited at higher stress due to saturation of the network of contact points and possible grains breakage. Thus the linear increase of the bulk modulus is only valid at low stress.

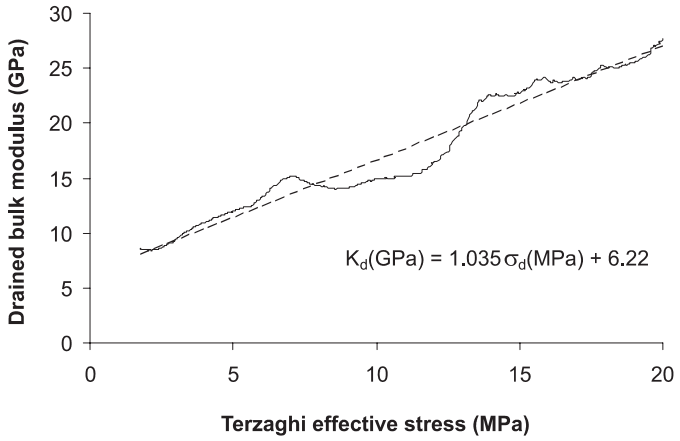

Figure 5- Drained bulk modulus of the studied limestone as a function of Terzaghi effective stress

3.2 Permeability tests

Constant head permeability tests have been performed in a triaxial cell on a water saturated limestone sample under isotropic loading. After the saturation, two pore pressure generators were used to keep a

constant pore pressure difference of 300 kPa between the two ends of the sample. The confining pressure was always kept about 2MPa higher than the pore pressure to prevent the fluid infiltration between the sample and the jacket. The permeability tests have been performed with different combinations of pore pressure and confining pressure. The mean value of the two pore pressures imposed at the ends of the sample is taken as the sample average pore pressure for the evaluation of the effective stress inside the sample. After the saturation of the sample under the initial confining pressure, the pore pressure at each end of the sample was maintained constant and the confining pressure was increased by steps of 1.0MPa. At each step the flow rate was recorded after the stabilization of the fluid flow and the permeability of the sample was calculated using the Darcy's law. This procedure was repeated for three different pore pressure levels with eight confining pressure steps for each level. Thus, 24 permeability tests have been performed with various combinations of pore pressure and confining pressure. The results, presented in Figure (6), show the measured permeability as a function of the confining pressure for different average pore pressures. These results show that the permeability decreases with the confining pressure increase for a constant average pore pressure. Moreover, under a constant confining pressure, the permeability increases with the pore pressure increase. These experimental results can be explained by the pore diameter changes under the effect of the confining pressure and the pore pressure variations. The shape of the permeability curves and its reduction with the confining pressure increase is similar to the results reported in the literature for porous sedimentary rocks (Coyner [17], Yale [24], David et al. [25], Schutjens et al. [26]) as well as for crystalline rocks (Kranz et al. [16], Coyner [17], Bernabé [19]). As mentioned by David et al. [25], the compaction mechanism in crystalline rocks is related to the closure of microcracks and the pressure sensitivity of permeability decreases with confining pressure increase. This pressure sensitivity of the permeability is more important in crystalline rocks than in porous sedimentary rocks for which the compaction is related to the relative movement of grains. Vairogs et al. [27] showed that the pressure sensitivity is more important for the rocks with lower permeability.

On Figure (6), for the range of the applied confining pressures, the variation of the permeability with the confining pressure follows a power law. Even though this power law cannot be accepted as a general permeability-stress relationship due to the infinite value at zero stress, it can be accepted to express the permeability variations with the variations of the confining pressure in the limit of the applied pressures.

4 Analysis of test results

The easiest way to determine the effective stress coefficient for the variations of the permeability based on the obtained experimental results is to draw a contour plan of the permeability as a function of pore pressure and confining pressure. The slope of the isolines gives the effective stress coefficient corresponding to the variations of the permeability. Parallel isolines would mean that the effective stress coefficient is constant. The contour plan is shown in Figure (7). In this figure, the same scale is used for the pore pressure and the confining pressure axes so that the slope of the isolines can be calculated directly on the graph. We can clearly see that the isolines are not parallel and that the effective stress coefficient calculated as the average slope of the isolines decreases with increasing values of the permeability. The effective stress coefficients evaluated on this graph varies between 0.9 and 2.4. Considering the limited number of data points on Figure (7), it should be mentioned that most of the fine details of the isolines on this figure are just artefacts. Moreover, considering the small difference between the measured permeabilities at higher confining pressures, the evaluated effective stress

coefficients should be seen as approximate values. Nevertheless, these data clearly show the general trend for the evolution of the effective stress coefficient as described above.

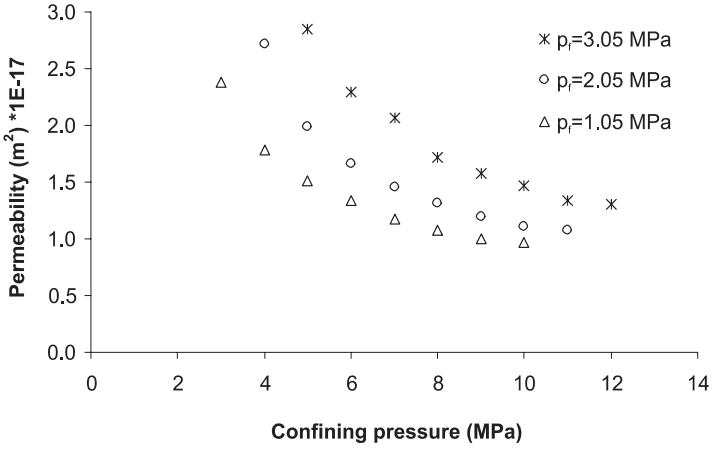

Figure 6- Results of permeability tests performed with different conditions of pore pressure and confining

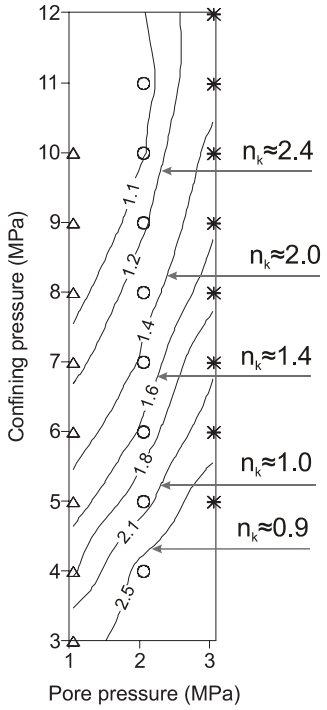

Figure 7- Permeability contour plan and the approximate effective stress coefficient corresponding to each isoline

In order to represent the effect of total stress and pore pressure on the permeability and on the effective stress coefficient, a power law for the variation of the permeability with the effective stress as defined by equation (9) is assumed:

$$k = a\sigma'^{b} \tag{11}$$

The effective stress coefficient n_k is assumed to vary linearly with the differential stress (i.e. Terzaghi effective stress):

$$n_k = c\sigma_d + d \tag{12}$$

The coefficients a and b in equation (11) and c and d in equation (12) are evaluated using a least square algorithm by fitting the experimental data. The following expressions for the effective stress coefficient and for the permeability-effective stress dependency are found:

$$n_k = 0.89 + 0.17\sigma_d \qquad \left(\sigma_d : \text{MPa}\right) \tag{13}$$

$$\sigma' = \sigma - n_k p_f \tag{14}$$

$$k = 3.37 \times 10^{-17} \sigma'^{-0.65} \qquad \left(k : \text{m}^2 , \sigma' : \text{MPa}\right) \tag{15}$$

The results of the curve fitting procedure are shown on Figure (8). We can observe that the experimental permeability measurements are well superposed when plotted against the obtained effective stress. Figure (9) shows the simulation of the permeability tests using the above permeability law. This graphs show that the experimental data are well reproduced and that the contour plans of the measured and computed permeability are very well superposed.

As mentioned earlier, the main advantage of the effective stress concept is its simplicity. Thus, one could simplify the stress-dependent permeability law given by equations (13) and (15) by neglecting the variations of the effective stress coefficient and take a mean value for n_k, equal to 1.3.

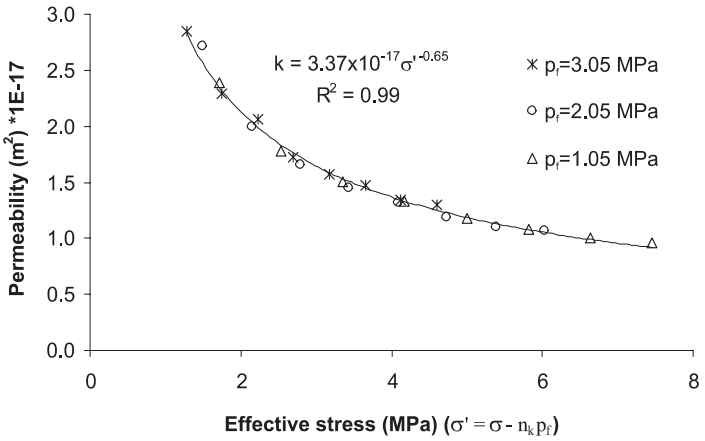

Figure 8- Relation between permeability and effective stress

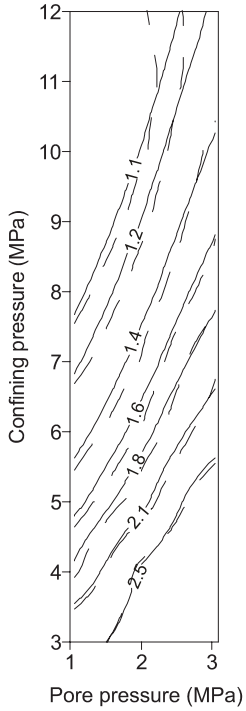

Figure 9- Comparison of the contour plans of the experimental results (dashed lines) and the proposed permeability-effective stress model (solid lines)

An effective stress coefficient which is greater than unity means that the effect of pore pressure variation on the permeability of the limestone is more important than the effect of the variation of the total stress. This result is similar to the ones presented by Zoback and Byerlee [8], Walls and Nur [9], Walls [11] and Al-Wardy and Zimmerman [13] for clay-rich sandstone. In the clay-shell and clay-particle models proposed by Zoback and Byerlee [8] and Al-Wardy and Zimmerman [13], an effective stress coefficient greater than one is interpreted by the presence of the clay in the rock and the great difference between the elastic moduli of the clay and the quartz. For the studied limestone a simple conceptual model for the microstructure is proposed in the following section in order to understand the mechanism of the variation of the permeability and of the corresponding effective stress coefficient with the confining pressure and the pore pressure.

5 Pore-shell model

Based on the microscopic observations of the limestone, a simplified model for the microstructure of the studied rock is proposed in this section. This model is presented in Figure (10) and consists of a central oolite circular core that is covered by a pore shell and in the external part by a cement shell. Following the observation that an important portion of the connected porosity of the studied limestone is concentrated around the oolites, it is assumed that the porosity of the rock is entirely situated around the central oolite core. Consequently the micro-porosity of the rock observed between the micrite and sparite grains is neglected and oolite and cement are considered as non-porous elastic materials. This

assumption is supported by the fact that about 42% of the micro-porosity of the rock, situated in the oolites and in the sparitic cement, is occluded. This model is in its principles similar to the clay-shell model and to the clay-particle model proposed respectively by Zoback and Byerlee [8] and Al-Wardy and Zimmerman [13]. Similarly to the assumption of non porous cement and oolites in the proposed pore-shell model, a mechanism is needed to prevent the penetration and distribution of the pore pressure inside the clay phase in the clay-shell and clay-particle models. Indeed, as mentioned by Coyner [17], the compressibility of clay particles and of the rock solid grains are comparable so that if the pore pressure freely infiltrates into the clay pore space, the resulting effect will be equivalent of an 'unjacketed' compression test and will lead to a very small deformation caused by the compressibility of clay particles, and consequently the permeability change will be much less sensitive to the pore pressure variations.

The oolites in the studied limestone are quasi-spherical. Moreover, as can be seen in Figure (3), the macro-porosity situated around the oolites is interconnected. Therefore we can consider a spherical geometry for the proposed pore-shell model. The problem can also be solved using a cylindrical geometry, as it is derived for the clay-shell and clay-particle models. In order to compare the results obtained with these two geometries, the solution for cylindrical geometry is presented in Appendix 1. As shown by Al-Wardy [12], it is expected that the results obtained from cylindrical and spherical geometries do not differ much.

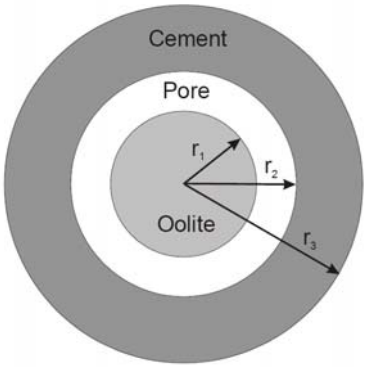

Figure 10- Pore-Shell model

5.1 Model formulation

The permeability of the proposed model is a function of the pore-shell geometry and thus a function of the pore-shell thickness:

$$k = f\left(r_2 - r_1\right) \tag{16}$$

Assuming the permeability k as the property Q in equation (7) and using equation (16), the expression of the effective stress coefficient n_k for the permeability of the model is written as:

$$n_k = -\frac{\left(\dfrac{\partial\left(r_2 - r_1\right)}{\partial p_f}\right)_\sigma}{\left(\dfrac{\partial\left(r_2 - r_1\right)}{\partial \sigma}\right)_{p_f}} \tag{17}$$

The radius of the central oolite core (r_1) is independent of the confining pressure σ, thus the following expression is obtained for n_k :

$$\frac{\partial r_1}{\partial \sigma} = 0 \quad \Rightarrow \quad n_k = \frac{-\dfrac{\partial r_2}{\partial p_f} + \dfrac{\partial r_1}{\partial p_f}}{\dfrac{\partial r_2}{\partial \sigma}} \tag{18}$$

The confining pressure is applied on the external boundary of the model and the pore pressure is applied inside the pore-shell. The elastic solution of the problem and the variations of the model geometry parameters with the applied pressures are obtained from the solution of a hollow sphere problem.

Considering a hollow sphere with the inner radius a and the outer radius b, the radial stresses at the inner and outer boundaries are respectively $-p_i$ and $-p_o$. Compressive stresses are taken negative. The well-known Lamé solution holds for the radial displacement $u(r)$:

$$u(r) = Ar + \frac{B}{r^2} \tag{19}$$

The integration constants A and B are obtained from the boundary conditions:

$$A = \frac{p_i a^3 - p_o b^3}{\left(3\lambda + 2\mu\right)\left(b^3 - a^3\right)} \tag{20}$$

$$B = \frac{\left(p_i - p_o\right) a^3 b^3}{4\mu\left(b^3 - a^3\right)} \tag{21}$$

where λ and μ are the Lamé coefficients of the elastic cylinder.

For the central oolite core $a = 0$, $b = r_1$ and $p_o = p_f$ and let's denote by λ_o and μ_o the Lamé coefficients of the oolite core. Using equations (19), (20) and (21) the expression of the displacement is found as:

$$u\left(r\right) = \frac{-p_f}{3\lambda_o + 2\mu_o} r \tag{22}$$

The term $\partial r_1 / \partial p_f$ in equation (18) is thus given by:

$$\frac{\partial r_1}{\partial p_f} = \frac{-r_1}{3\lambda_o + 2\mu_o} \tag{23}$$

For the outer cement shell $a = r_2$, $b = r_3$, $p_i = p_f$ and $p_o = \sigma$ and let's denote by λ_c and μ_c the Lamé coefficients of the cement shell. Using equations (19), (20) and (21) the expression of the displacement is found as:

$$u\left(r\right) = \frac{p_f r_2^3 - \sigma r_3^3}{\left(3\lambda_c + 2\mu_c\right)\left(r_3^3 - r_2^3\right)} r + \frac{\left(p_f - \sigma\right) r_2^3 r_3^3}{4\mu_c\left(r_3^3 - r_2^3\right) r^2} \tag{24}$$

The terms $\partial r_2 / \partial p_f$ and $\partial r_2 / \partial \sigma$ in equations (18) are given by:

$$\frac{\partial r_2}{\partial p_f} = \frac{r_2^4}{\left(3\lambda_c + 2\mu_c\right)\left(r_3^3 - r_2^3\right)} + \frac{r_2 r_3^3}{4\mu_c\left(r_3^3 - r_2^3\right)} \tag{25}$$

$$\frac{\partial r_2}{\partial \sigma} = -\frac{r_2 r_3^3}{\left(3\lambda_c + 2\mu_c\right)\left(r_3^3 - r_2^3\right)} - \frac{r_2 r_3^3}{4\mu_c\left(r_3^4 - r_2^4\right)} \tag{26}$$

Introducing (23), (25) and (26) in equation (18) with some algebraic re-arrangements, the following expression is obtained for the effective stress coefficient corresponding to the variations of the permeability of the model:

$$n_k = 1 + \frac{4\mu_c\left(1 - \left(r_2/r_3\right)^3\right)}{3\lambda_c + 6\mu_c}\left(\frac{\left(3\lambda_c + 2\mu_c\right)r_1}{\left(3\lambda_o + 2\mu_o\right)r_2} - 1\right) \tag{27}$$

Equation (27) can be re-written using the bulk modulus K and of the Poisson's ratio ν ($\lambda = \frac{3K\nu}{1+\nu}$, $\mu = \frac{3K\left(1-2\nu\right)}{2\left(1+\nu\right)}$):

$$n_k = 1 + \left(1 - \left(r_2/r_3\right)^3\right)\frac{2\left(1-2\nu_c\right)}{3\left(1-\nu_c\right)}\left(\frac{K_c r_1}{K_o r_2} - 1\right) \tag{28}$$

Note that only the Poisson's ratio of the cement appears in the above relation, whereas the Poisson's ratio of both the oolites and the cement appear for the cylindrical geometry as shown in equation (40) in Appendix 1.

The range of variations of the Poisson's ratio of rocks is relatively narrow. In order to simplify equation (28), we assume that $\nu_c = 0.3$ which is the value of the Poisson's ratio of calcite presented by Bass [20]. Using this assumption equation (28) is reduced to the following form:

$$n_k = 1 + \frac{8}{21}\left(1 - \left(r_2/r_3\right)^3\right)\left(\frac{K_c r_1}{K_o r_2} - 1\right) \tag{29}$$

Based on the microscopic observations and the porosity measurements presented in the previous section, the following values are considered for the geometry of the model:

$$r_1 = 125\,\mu\text{m}\,,\ r_2 = 135\,\mu\text{m}\,,\ r_3 = 150\,\mu\text{m} \tag{30}$$

With these dimensions, the porosity of the model is equal to 15.0% which is approximately equal to the average measured connected porosity of the studied limestone, equal to 15.7%. Moreover, the volumetric fractions of different constituents of the microstructure of the rock, evaluated by image analysis and presented in the previous section, 59% oolite and 28% cement, are approximately retrieved with these values. In doing so, the following simple linear variation of the effective stress coefficient with the K_c/K_o ratio is obtained:

$$n_k = 0.9 + 0.1\frac{K_c}{K_o} \quad \text{(spherical geometry)} \tag{31}$$

In case of a microscopically homogeneous material, $K_c = K_o$, the coefficient n_k is found equal to one. Note that for the cylindrical geometry, as presented in Appendix 1, we obtain a very close expression for the effective stress coefficient:

$$n_k = 0.92 + 0.07\,K_c/K_o \quad \text{(cylindrical geometry)} \tag{32}$$

We can see that the proposed pore-shell model, which is based on a detailed study of the microstructure of the limestone, is able to produce permeability effective stress coefficients that are

greater than one and vary with the relative bulk moduli of the different constituents of the rock. The observations of the microstructure of the cement and of the oolites have shown that the interlocking of the particles in the cement can indeed lead to higher bulk modulus than for the oolites ($K_c / K_o > 1$). The K_c/K_o ratio will be studied experimentally in the following section by performing microhardness tests.

5.2 Microhardness testing of the limestone

In the previous section it was shown that the permeability effective stress coefficient obtained from the proposed pore-shell model is a linear function of the K_c/K_o ratio. The mechanical properties of the different constituents of the microstructure of the studied rock (mainly oolites and sparitic cement) are studied experimentally by performing Vickers microhardness tests. The Vickers hardness test consists of indenting the material with a diamond indenter, in the form of a right pyramid with a square base and an angle of 136° between opposite faces. The average length d of the two diagonals of the indentation left on the surface of the material is measured. Obviously this length is smaller for a harder material. The Vickers hardness, H_V, is determined by the ratio of the load p over the surface area of indentation and is calculated using the following simple equation:

$$H_V = 1.8544 \frac{p}{d^2} \tag{33}$$

The microhardness tests are performed on the oolites and cements separately and the tested sample is observed using an ESEM with the backscattered electron detector. From equation (33), the ratio of the hardness H_{Vc} of the cement to the hardness H_{Vo} of the oolites is given by:

$$\frac{H_{Vc}}{H_{Vo}} = \left(\frac{d_c}{d_o} \right)^{-2} \tag{34}$$

where d_c and d_o are the diagonals of the indentation on the cement and on the oolite respectively.

The Vickers hardness is defined with reference to the area of the permanent impression (Das [28]), so it measures in some lumped way a combination of elastic, plastic, and fracture properties. There is, however, no unique relation between the hardness number and the primary parameters, but empirical relations may be obtained for certain classes of materials. For example, for a wide range of metals, the ratio of the hardness to uniaxial yield strength is a constant value between 2.7 and 3.0, but this relation does not hold for frictional materials, for which the hardness is a function of at least two variables: the cohesion and the friction angle of the material (Ganneau [29]). Only few empirical relations can be found in the literature between the Vickers hardness and the macroscopic elastic and strength properties of rocks. Das and Hucka [30] performed penetration tests on coal and showed a linear relation between the penetration strength and penetration modulus. They also presented a result from Honda and Sanada [31] which shows that the ratio of the Vickers hardness of coal to its Young's modulus is a constant. In absence of such data for limestone, we assume that the same type of relation holds for the constituents of the studied rock. Assuming also that the Poisson's ratio of the oolite and of the cement are equal, we obtain $K_c/K_o = H_{Vc}/H_{Vo}$.

The observation of the indentations of several performed microhardness tests resulted in a H_{Vc}/H_{Vo} ratio which is greater than one and varies between 1.6 and 4.0. Figure (11) shows an image of an indentation situated on an oolite. Figure (12) shows two adjacent indentations situated on the sparitic cement. Both images are taken with the same magnification, so that the size of indented zones can be

directly compared. This comparison clearly shows that the indentation on the oolite has a greater area and consequently that the hardness of the oolite is smaller than the hardness of the cement.

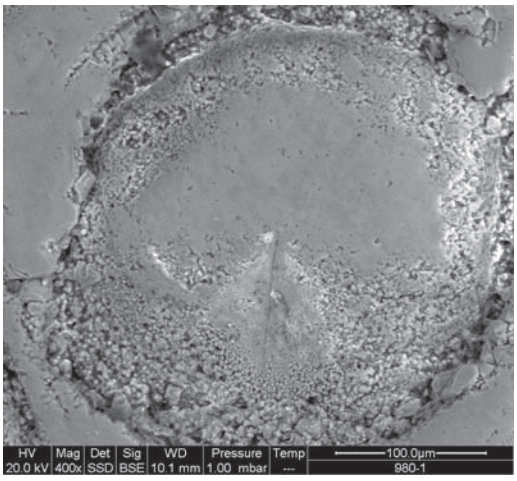

Figure 11- Microhardness test: view of an indentation situated on an oolite

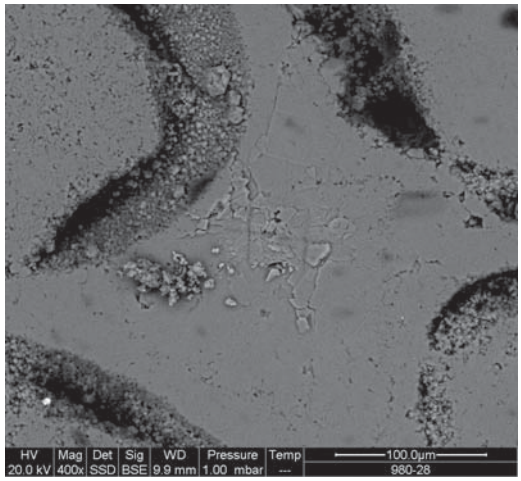

Figure 12- Microhardness test: view of two adjacent indentations situated on the sparitic cement

5.3 Discussion of model results

Inserting the values of K_c/K_o ratio evaluated by microhardness tests in equation (31), we obtain that the effective stress coefficient is between 1.0 and 1.2. This is compatible with the result obtained using equation (13) for small differential pressures.

It should be noted that the K_c/K_o ratio is obtained in the microhardness tests for zero confining pressure. It is expected that the bulk moduli K_c and K_o increase with the confining pressure due to the compaction of the pore space. This increase of the bulk moduli should be more important for the cement due to the interlocking of the particles and the greater coordination number than for the oolites. The ratio K_c/K_o is thus expected to increase with the confining pressure which results in an increase of the permeability effective stress coefficient (equation (31)). In the absence of experimental data on the stress dependency of the bulk moduli K_c and K_o, we can try to have a rough estimation from the drained bulk modulus of the rock (equation (10)) and considerations from homogenization theory. It is reasonable to assume that only the bulk modulus K_c of the cement increases with confining pressure whereas the bulk modulus K_o of the oolites remains constant. In the proposed pore-shell model, the confining pressure is applied only on the outer cement shell and has no effect on the oolite core. This may be realistic to some extent for low confining pressures. As can be seen in Figure (3), the oolites are connected to the surrounding cement with a few contact areas. The Voigt upper bound of a homogenized medium constituted by spherical oolites surrounded in a matrix of sparitic cement is given by:

$$K_d \le f_o K_o + f_c K_c \tag{35}$$

where f_o and f_c are the volume fractions of the oolites and of the cement ($f_o + f_c = 1$). Considering the macro-porosity of the rock as a part of the oolite fraction, we get $f_o = 0.72$ and $f_c = 0.28$. For $\sigma_d = 0$ (unloaded state), equation (10) gives $K_d = 6.22\,\text{GPa}$ and for $\sigma_d = 8.95\,\text{MPa}$ (maximum applied differential pressure), $K_d = 15.5\,\text{GPa}$. From the results of microhardness tests we can take an average value for the ratio $K_c/K_o \simeq 3$ corresponding to the unloaded state. From equation (35) we obtain an upper bound for K_o in the unloaded state equal to 4GPa. Keeping this value constant,

the variation of K_c is found from equation (35) to be between 12 and 34 GPa when σ_d increases from 0 to 8.95MPa. Using equation (31), this results in an effective stress coefficient n_k which varies between 1.2 and 2.0. This is comparable to the experimental results where n_k was found to vary between 0.9 and 2.4.

It should be emphasized that this simple pore-shell model for the studied limestone is based on strong assumptions and is only used here for a better understanding of the mechanism of the evolution of the permeability with the pore pressure and the confining pressure without trying to obtain quantitative predictions.

6 Conclusion

The effective stress law for the permeability of a limestone is studied in an approach which combines laboratory testing and microstructural observations and modelling. 24 constant head permeability tests have been performed in a triaxial cell with various conditions of confining pressure and pore pressure. The experimental results have shown that the pore pressure increase and the confining pressure decrease both result in an increase of the permeability, but the effect of the pore pressure change on the variation of the permeability is more important that the effect of a change in the confining pressure. It is shown that an effective stress law can be defined for the permeability and that the corresponding effective stress coefficient increases linearly with the differential pressure and is greater than one as soon the differential pressure exceeds few bars. A power law is proposed for the variation of the permeability with the effective stress. The test results are well reproduced using the proposed permeability-effective stress law.

The microscopic observations of the microstructure of the rock shows that the studied limestone is entirely composed of calcite and is constituted of quasi spherical oolites cemented by sparitic calcite. The observations have shown that the main porosity of the rock is concentrated around the oolite cores. Based on the microscopic observations, a conceptual pore-shell model is proposed to study the effective stress law for the permeability of the studied limestone. The proposed model is able to reproduce permeability effective stress coefficients that are greater than one and which vary with the ratio of the bulk moduli of the two constituents of the rock. The ratio of the bulk moduli of the sparitic cement to the one of the oolites is studied experimentally by performing microhardness tests and is found to be greater than one. According to the proposed pore-shell model, this results in an effective stress coefficient which is greater than one. The microstructural approach is thus consistent with the experimental results of the permeability tests.

7 Appendix 1

In this appendix we present the equations of the pore-shell model for cylindrical plane strain geometry. All of the parameters are the same as the ones used in section 5.1. Considering a hollow cylinder with the inner radius a and the outer radius b, and the radial stresses $-p_i$ and $-p_o$ respectively at the inner and outer boundaries, the radial displacement $u(r)$ is given by the following equation:

$$u(r) = Ar + \frac{B}{r} \tag{36}$$

With the integration constants A and B given by:

$$A = \frac{p_i a^2 - p_o b^2}{2(\lambda + \mu)(b^2 - a^2)} \tag{37}$$

$$B = \frac{(p_i - p_o) a^2 b^2}{2\mu(b^2 - a^2)} \tag{38}$$

Following the same procedure presented in section 5.1 for spherical geometry, the effective stress coefficient for the permeability of the cylindrical geometry is obtained as:

$$n_k = 1 + \frac{\mu_c \left(1 - (r_2/r_3)^2\right)}{\lambda_c + 2\mu_c} \left(\frac{(\lambda_c + \mu_c) r_1}{(\lambda_o + \mu_o) r_2} - 1 \right) \tag{39}$$

Equation (39) can be re-written using the bulk modulus K and of the Poisson's ratio ν of the material:

$$n_k = 1 + \left(1 - (r_2/r_3)^2\right) \frac{(1 - 2\nu_c)}{2(1 - \nu_c)} \left(\frac{\left(K_c/(1+\nu_c)\right) r_1}{\left(K_o/(1+\nu_o)\right) r_2} - 1 \right) \tag{40}$$

Taking $\nu_c = \nu_o = 0.3$, equation (40) is reduced to the following form:

$$n_k = 1 + \frac{2}{7}\left(1 - (r_2/r_3)^2\right) \left(\frac{K_c r_1}{K_o r_2} - 1 \right) \tag{41}$$

Based on the microscopic observations and the porosity measurements presented in the previous section, the following values are considered for the geometry of the cylindrical model:

$$r_1 = 125\,\mu\text{m}\,,\ r_2 = 141\,\mu\text{m}\,,\ r_3 = 165\,\mu\text{m} \tag{42}$$

With these dimensions, the porosity of the model is equal to 15.6% which is approximately equal to the average measured connected porosity of the studied limestone, equal to 15.7%. Moreover, the volumetric fractions of different constituents of the microstructure of the rock, evaluated by image analysis are approximately retrieved with these values. Inserting these dimensions in equation (41), the following linear variation of the effective stress coefficient with the K_c/K_o ratio is obtained:

$$n_k = 0.92 + 0.07 \frac{K_c}{K_o} \tag{43}$$

8 References

[1] Rempel AW, Rice JR. Thermal pressurization and onset of melting in fault zones. Journal of Geophysical Research 2006;111:B09314

[2] Sulem J, Lazar P, Vardoulakis I. Thermo-Poro-Mechanical Properties of Clayey Gouge and Application to Rapid Fault Shearing. Int. J. Num. Anal. Meth. Geomechanics. 2007;31(3):523-540

[3] Terzaghi K. The shearing resistance of saturated soils and the angle between the planes of shear, First Int. Conf. Soil Mech., Vol. 1, Harvard Univ., Cambridge, Mass. 1936:54-56

[4] Bernabé Y. The effective pressure law for permeability in Chelmsford granite and Barre granite. Int J Rock Mech Min Sci & Geomech Abstr 1986;23-3:267-275.

[5] Zimmerman RW. Compressibility of sandstones. Amsterdam: Elsevier, 1991.

[6] Berryman JG. Effective stress for transport properties of inhomogeneous porous rock. Journal of Geophysical Research 1992;97:17409-17424.

[7] Zoback MD. High pressure deformation and fluid flow in sandstone, granite, and granular materials. Ph.D. thesis, Stanford Univ., Stanford, Calif. 1975.

[8] Zoback MD, Byerlee JD. Permeability and effective stress. Bull. Am. Assn. Petr. Geol. 1975;59:154-158

[9] Walls JD, Nur A. Pore pressure and confining pressure dependence of permeability in sandstone. In: proceedings of the 7th Formation Evaluation Symposium of the Canadian Well Logging Society. 1979; Paper O, Can. Well Logging Soc., Alberta, Calgary.

[10] Nur AM, Walls JD, Winkler K, DeVilbiss J. Effects of fluid saturation on waves in porous rock and relation to hydraulic permeability. Soc. Petr. Eng. 1980;J.20:450-458.

[11] Walls JD. Effects on pore pressure, confining pressure and partial saturation on permeability of sandstones. Ph.D. Thesis, Department of Geophysics, Stanford Univ., Stanford, Calif. 1982.

[12] Al-Wardy W. Analytical and experimental study of the poroelastic behaviour of clean and clay-rich sandstones, Ph.D. thesis, Imp. Coll., London. 2003.

[13] Al-Wardy W, Zimmerman RW. Effective stress law for the permeability of clay-rich sandstones. Journal of Geophysical Research 2004;109:B04203

[14] Kwon O, Kronenberg AK, Gangi AF, Johnson B. Permeability of Wilcox shale and its effective stress law. Journal of Geophysical Research 2001;106,B9:19339-19353.

[15] Walsh JB. Effect of pore pressure and confining pressure on fracture permeability, Int J Rock Mech Min Sci & Geomech. Abstr. 1981;18:429-435.

[16] Kranz RL, Frankel SD, Engelder T, Scholz CH. The permeability of whole and jointed Barre granite, Int J Rock Mech Min Sci & Geomech. Abstr. 1980;16:225-234.

[17] Coyner KB. Effects of stress, pore pressure, and pore fluids on bulk strain, velocity, and permeability in rocks. Ph.D. thesis, Massachusetts Institute of Technology, Dept. of Earth, Atmospheric and Planetary Sciences, 1984.

[18] Morrow C, Bo-Chong Z, Byerlee J. Effective Pressure Law for Permeability of Westerly Granite Under Cyclic Loading, Journal of Geophysical Research 1986;91,B3: 3870-3876.

[19] Bernabé Y. The effective pressure law for permeability during pore pressure and confining pressure cycling of several crystalline rocks, Journal of Geophysical Research 1987;92,B1:649-657.

[20] Bass JD. Elasticity of Minerals, Glasses, and Melts, In: Mineral Physics and Crystallography: A Handbook of Physical Constants, American Geophysical Union Online Reference Shelf 2, TJ Ahrens, ed, 1995, pp 45-63.

[21] Ghabezloo S, Sulem J. Stress dependent thermal pressurization of a fluid-saturated rock. Rock Mechanics and Rock Engineering 2009;42(1):1-24.

[22] Sulem J, Vardoulakis I, Papamichos E, Oulahna A, Tronvoll J. Elasto-plastic Modelling of Red Wildmoor Sandstone, Mechanics of Cohesive-frictional Materials 1999;4(3):215-246.

[23] Sulem J, Ouffroukh H. Hydromechanical Behaviour of Fontainebleau Sandstone. Rock Mechanics and Rock Engineering 2006;39(3):185-213.

[24] Yale DP. Network Modeling of Flow, Storage and Deformation in Porous Rocks. Ph.D. thesis, Stanford University, 1994.

[25] David C, Wong T-F, Zhu W, Zhang J. Laboratory measurement of compaction-induced permeability change in porous rocks: Implications for the generation and maintenance of pore pressure excess in the crust, Pure and Applied Geophysics 1994;143(1-3):425-456.

[26] Schutjens PMTM, Hanssen TH, Hettema MHH, Merour J, de Bree P, Coremans JWA, Helliesen G. Compaction-Induced Porosity/Permeability Reduction in Sandstone Reservoirs: Data and Model for Elasticity-Dominated Deformation, SPE Reservoir Evaluation & Engineering (2004);7(3):202-216, SPE 88441-PA.

[27] Vairogs J, Hearn CL, Dareing DW, Rhoades VW. Effect of rock stress on gas production from low-permeability reservoirs. J. Pet. Technol. 1971;23:1161-1167.

[28] Das B. Vickers hardness concept in the light of Vickers impression, Int J Rock Mech Min Sci & Geomech. Abstr. 1974;11:85-89.

[29] Ganneau FP. From nanohardness to strength properties of cohesive-frictional materials-application to shale materials, Master thesis, Massachusetts Institute of Technology, 2004.

[30] Das B, Hucka V. Laboratory investigation of penetration properties of the complete coal series, Int J Rock Mech Min Sci & Geomech. Abstr. 1975;12:213-217.

[31] Honda H, Sanada Y. Hardness of coal, Fuel 1956;35:451.

REFERENCES

1. Acker P., (2001) Micromechanical analysis of creep and shrinkage mechanisms, in F.-J. Ulm, Z.P. Bažant and F.H. Wittmann, editors, Creep, Shrinkage and Durability Mechanics of Concrete and other quasi-brittle Materials, Cambridge, MA, August 2001 (Elsevier, Oxford UK), 15-25.
2. Ai H., Young J.F., Scherer G.W., (2004) Thermal expansion kinetics: method to measure permeability of cementitious materials: II, application to hardened cement paste. J Am Ceram Soc 84(2), 385–391, Erratum, J. Am. Ceram. Soc. 87(8), 1611.
3. Al-Wardy W., (2003) Analytical and experimental study of the poroelastic behaviour of clean and clay-rich sandstones, Ph.D. thesis, Imp. Coll., London.
4. Al-Wardy W., Zimmerman R.W., (2004) Effective stress law for the permeability of clay-rich sandstones. Journal of Geophysical Research 109, B04203
5. Anson, M., Newman, E., (1966) The effect of mix proportions and method of testing on Poisson's ratio for mortars and concretes, Mag. Concr. Res. 18(56), 115-129
6. Bass, J.D., (1995) Elasticity of Minerals, Glasses, and Melts, in Mineral Physics and Crystallography: A Handbook of Physical Constants, American Geophysical Union Online Reference Shelf 2, Thomas J. Ahrens, Editor, 45-63
7. Bazant Z.P., Cusatis G., Cedolin L., (2004) Temperature effect on concrete creep modeled by microprestress-solidification theory. J. of Engrg. Mechanics ASCE 130(6), 691-699.
8. Berge P.A., (1998) Pore Compressiblity in Rocks, Biot Conference on Poromechanics, Louvain-la-Neuve, Belgium, September 14-16.
9. Berge P.A., Berryman J.G., (1995) Realizability of Negative Pore Compressibility in Poroelastic Composites, Journal of Applied Mechanics 62(4), 1053-1062.
10. Bernabé Y., Brace WF, Evans B. (1982) Permeability, porosity and pore geometry of hot-pressed calcite. Mechanics of Materials 1, 173-183.
11. Bernabé Y., (1986) The effective pressure law for permeability in Chelmsford granite and Barre granite, Int J Rock Mech Min Sci & Geomech Abstr 23(3), 267-275.
12. Bernabé Y., (1987) The effective pressure law for permeability during pore pressure and confining pressure cycling of several crystalline rocks, Journal of Geophysical Research 92(B1), 649-657.
13. Bernabé Y., Mok U., Evans B., (2003) Permeability-porosity Relationships in Rocks Subjected to Various Evolution Processes. Pure and Applied Geophysics 160, 937-960.
14. Berryman J.G., (1992) Effective stress for transport properties of inhomogeneous porous rock, Journal of Geophysical Research, 97, 17409-17424
15. Berryman J., (1995) Mixture Theories for Rock Properties, in Rock physics & phase relations: A Handbook of Physical Constants, American Geophysical Union Online Reference Shelf 3, Thomas J. Ahrens, Editor, 205-228
16. Biot M.A., (1941) General theory of three-dimensional consolidation, J. Appl. Phys. 12, 155-164.
17. Biot M.A., Willis D.G., (1957) The elastic coefficients of the theory of consolidation, Journal of Applied Mechanics 24, 594-601.
18. Bishop A.W., Eldin A.K.G., (1950) Undrained triaxial tests on saturated sands and their significance in the general theory of shear strength, Géotechnique 2, No. 1, 13-32

19. Bishop A.W., (1973) The influence of an undrained change in stress on the pore pressure in porous media of low compressibility, Géotechnique 23(3).

20. Bishop A.W., (1976) The influence of system compressibility on the observed pore pressure response to an undrained change in stress in saturated rock, Géotechnique 26, No 2, 371-375

21. Boutéca M.J., Bary D., Piau J.M., Kessler N., Boisson M., Fourmaintraux, D., (1994) Contribution of Poroelasticity to Reservoir Engineering: Lab Experiments, Application to Core Decompression and Implication in HP-HT Reservoirs Depletion, Proceedings of the Eurock'94, Delft, Balkema, Rotterdam, Paper SPE/ISRM 28093

22. Brace W., Walsh J., Frangos W., (1968) Permeability of Granite under High Pressure. Journal of Geophysical Research 73(6), 2225-2236.

23. Breysse D., Gérard B., (1997) Modelling of permeability in cement-based materials: Part 1-Uncracked medium. Cement and Concrete Research 27(5), 761-775.

24. Brown R.J.S., Korringa J., (1975) On the dependence of the elastic properties of a porous rock on the compressibility of the pore fluid, Geophysics 40, 608-616.

25. Campanella R.G. and Mitchell J.K., (1968) Influence of temperature variations on soil behaviour, Jnl Soil Mech. Fdn Div., Am. Soc. Civ. Engrs, 94, SM3, 709-734

26. Ciardullo J.P., Sweeney D.J., Scherer G.W., (2005) Thermal expansion kinetics: Method to measure permeability of cementitious materials, IV. Effect of thermal gradients and viscoelasticity, J. Am. Ceram. Soc. 88(5), 1213-1221.

27. Constantinides G., Ulm F.-J., (2004) The effect of two types of C-S-H on the elasticity of cement-based materials: Results from nanoindentation and micromechanical modelling, Cement and Concrete Research 34, 67-80.

28. Constantinides G., Ulm F.-J., (2007) The nanogranular nature of C–S–H. Journal of the Mechanics and Physics of Solids 55, 64-90.

29. Coussy O., (1991) Mécanique des milieux poreux, Technip, Paris.

30. Coussy O., (2004) Poromechanics, John Wiley & Sons

31. Coyner K.B., (1984) Effects of stress, pore pressure, and pore fluids on bulk strain, velocity, and permeability in rocks. PhD thesis, Massachusetts Institute of Technology, Dept. of Earth, Atmospheric and Planetary Sciences.

32. Das B., (1974) Vickers hardness concept in the light of Vickers impression, Int J Rock Mech Min Sci & Geomech. Abstr. 11, 85-89.

33. Das B., Hucka V., (1975) Laboratory investigation of penetration properties of the complete coal series, Int J Rock Mech Min Sci & Geomech. Abstr. 12, 213-217.

34. David C, Wong T-F, Zhu W, Zhang J. (1994) Laboratory measurement of compaction-induced permeability change in porous rocks: Implications for the generation and maintenance of pore pressure excess in the crust. Pure and Applied Geophysics 143(1-3), 425-456.

35. DeJong M.J., (2005) Sources of high temperature degradation of cement-based materials: nanoindentation and microporoelastic analysis, PhD thesis, Massachusetts Institute of Technology. Dept. of Civil and Environmental Engineering.

36. DeJong M.J., Ulm F.-J., (2007) The nanogranular behavior of C-S-H at elevated temperatures (up to 700 °C), Cement and Concrete Research 37, 1-12.

37. Derjaguin B.V., Karasev V.V., Khromova E.N., (1986) Thermal expansion of water in fine pores, J. Colloid Interface Sci. 109(2), 586–587.

38. Detournay E., Cheng A.H.-D., (1993) Fundamentals of Poroelasticity, Chap. 5 in Comprehensive Rock Engineering: Principles, Practice and Projects, Vol. II, Analysis and Design Method, ed. C. Fairhurst, Pergamon, 113-171

39. Diamond S., (2004) The microstructure of cement paste and concrete - a visual primer, Cement & Concrete Composites 26, 919–933.

40. Dias W.P.S., Khoury G.A., Sullivan P.J.E., (1990) Mechanical Properties of Hardened Cement Paste Exposed to Temperatures up to 700 C (1292 F), ACI Materials Journal, 87(2),160-166.

41. Dormieux L., Molinari A., Kondo D., (2002) Micromechanical approach to the behavior of poroelastic materials, Journal of the Mechanics and Physics of Solids, 50, 2203-2231

42. Dropek R.K., Johnson J.N., Walsh J.B., (1978) The influence of pore pressure on the mechanical properties of Kayenta sandstone, Journal of Geophysical Research, Vol. 83, No. B6, 2817-2824

43. Escoffier S., Homand F., Giraud A., Hoteit N., Kun Su. (2005) Under stress permeability determination of the Meuse/Haute-Marne mudstone. Engineering Geology, 81(3), 329-340.

44. Farage M.C.R., Sercombe J., Galle C., (2003) Rehydration of microstructure of cement paste after heating at temperatures up to 300°C, Cement and Concrete Research 33, 1047-1056.

45. Fei Y., (1995) Thermal Expansion, in Mineral Physics and Crystallography: A Handbook of Physical Constants, American Geophysical Union Online Reference Shelf 2, Thomas J. Ahrens, Editor, 29-44

46. Feldman R.F., (1972) Factors affecting young's modulus - porosity relation of hydrated portland cement compacts, Cement and Concrete Research 2(4), 375-386.

47. Feldman R.F., (1972) Helium flow and density measurement of the hydrated tricalcium silicate-water system, Cement and Concrete Research 2(1), 123-136.

48. Feldman R.F., Sereda P.J., (1968) A model for hydrated Portland cement paste as deduced from sorption-length change and mechanical properties, Materials and Structures 1(6), 509-520.

49. Fortin J., Schubnel A., Gueguen Y., (2005) Elastic wave velocities and permeability evolution during compaction of Bleurswiller sandstone, International Journal of Rock Mechanics & Mining Sciences, 42, 873-889

50. Fredrich J.T., Martin J.W., Clayton R.B., (1995) Induced pore pressure response during undrained deformation of tuff and sandstone, Mechanics of Materials 20, 95-104.

51. Gallé C., (2001) Effect of drying on cement-based materials pore structure as identified by mercury intrusion porosimetry: A comparative study between oven-, vacuum-, and freeze-drying, Cement and Concrete Research 31(10), 1467-1477.

52. Ganneau F.P., (2004) From nanohardness to strength properties of cohesive-frictional materials-application to shale materials, Master thesis, Massachusetts Institute of Technology.

53. Gassmann F., (1951) Über die elastizität poröser medien, Veirteljahrsschrift der Naturforschenden Gesellschaft Zürich, 96, 1–23. (English translation: http://sepwww.stanford.edu/sep/berryman/PS/gassmann.pdf)

54. Geertsma J., (1957) The effect of fluid pressure decline on volumetric changes of porous rocks, Trans. AIME 210, 331-340

55. Ghabezloo S., Sulem J., (2009) Stress dependent thermal pressurization of a fluid-saturated rock, Rock Mechanics and Rock Engineering, 42(1), 1-24.

56. Ghabezloo S, Sulem J, Guedon S, Martineau F. (2009) Effective stress law for the permeability of a limestone. Int. J. Rock Mech. Min. Sci., 46(2), 297-306.

57. Ghabezloo S., Sulem J., Guedon S., Martineau F., Saint-Marc J., (2008) Poromechanical behaviour of hardened cement paste under isotropic loading. Cement and Concrete Research 38(12), 1424-1437.

58. Ghabezloo S, Sulem J, Saint-Marc J., (2009) The effect of undrained heating on a hardened cement paste. Cement and Concrete Research 39(1), 54-64.

59. Ghabezloo S., Sulem J., Saint-Marc J., (2009) Evaluation of a permeability-porosity relationship in a low permeability creeping material using a single transient test, Int. J. Rock Mech. and Mining Sci., 46(4), 761-768.

60. Gibson L.J., Ashby M.F., (1998) Cellular Solids, Structure and Properties, Pergamon Press.

61. Grasley Z.C., Valenza II J.J., Scherer G.W., Lange D.A., (2007) Dynamic pressurization method for measuring permeability and modulus: II. cementitious materials. Materials & Structures 40, 711-721

62. Green D.H., Wang H.F., (1986) Fluid pressure response to undrained compression in saturated sedimentary rock, Geophysics 51(4), 948-956.

63. Gurevich, B., (2004) A simple derivation of the effective stress coefficient for seismic velocities in porous rocks, Geophysics, Vol. 69, No. 2, 393-397

64. Haecker C.-J., Garboczi E.J., Bullard J.W., Bohn R.B., Sun Z., Shah S.P., Voigt T., (2005) Modeling the linear elastic properties of Portland cement paste, Cement and Concrete Research 35, 1948-1960.

65. Hart D.J., Wang H.F., (2001) A single test method for determination of poroelastic constants and flow parameters in rocks with low hydraulic conductivities, Int. J. Rock Mech. and Mining Sci. 38, 577-583.

66. Hashin Z., Shtrikman S., (1961) Note on a variational approach to the theory of elastic composite materials, J. Franklin Inst. 271, 336-341.

67. Helmuth R.A., D.H. Turk, (1966) Elastic moduli of hardened Portland cement and tricalcium silicate pastes: effect of porosity, Symposium on Structure of Portland Cement Paste and Concrete (Special Report 90), Highway Research Board, Washington, 135–144.

68. Helmuth R.A., (1967) Dimensional changes of hardened Portland cement pastes caused by temperature changes, Highway Research Board, Proc. Highway Research Record 40, 315-366.

69. Heukamp F.H., Ulm F.-J., Germaine J.T., (2001) Mechanical properties of calcium-leached cement pastes ,Triaxial stress states and the influence of the pore pressure, Cement and Concrete Research 31, 767-774.

70. Heukamp F.H., (2003) Chemomechanics of calcium leaching of cement-based materials at different scales: The role of CH-dissolution and C-S-H degradation on strength and durability performance of materials and structures, PhD Dissertation, Massachusetts Institute of Technology.

71. Heukamp F.H., Ulm F.-J., Germaine J.T., (2003) Poroplastic properties of calcium-leached cement-based materials, Cement and Concrete Research 33, 1155–1173.

72. Hill R. (1952) The elastic behavior of crystalline aggregate, Proc. Physical Soc., London, A65, 349-354

73. Honda H., Sanada Y. (1956) Hardness of coal, Fuel 35, 451.

74. Jennings H.M., Tennis P.D., (1994) Model for the Developing Microstructure in Portland Cement Pastes, J. Am. Ceram. Soc. 77(12), 3161-72; Correction in J. Am. Ceram. Soc. 78(9), 1995.

75. Jennings H.M., (2000) A model for the microstructure of calcium silicate hydrate in cement paste, Cement and Concrete Research 30(1), 101-116.

76. Jennings H.M., Thomas J.J., Chen J.J., Rothstein D., (2002) Cement as a Porous Materials, Chapter 6.11 in Handbook of Porous Solids, ed. F. Schuth, K. Sing, J. Weitkamp. Wiley-VCH, 5, 2971-3028.

77. Jennings H.M., (2008) Refinements to colloid model of C-S-H in cement: CM-II, Cement and Concrete Research 38(3), 275-289.

78. Kendall K., Howard A.J., Birchall J.D., Pratt P.L., Proctor B.A., Jefferis S.A., (1983) The Relation between Porosity, Microstructure and Strength, and the Approach to Advanced Cement-Based Materials, Philosophical Transactions of the Royal Society of London. Series A, Mathematical and Physical Sciences 310(1511), 139-153.

79. Kjellsen K.O., Detwiler R.J., Gjørv O.E., (1990) Pore structure of plain cement pastes hydrated at different temperatures, Cement and Concrete Research 20, 927-933.

80. Kjellsen K.O., Monsøy A., Isachsen K., Detwiler R.J., (2003) Preparation of flat-polished specimens for SEM-backscattered electron imaging and X-ray microanalysis - importance of epoxy impregnation, Cement and Concrete Research 33, 611-616.

81. Kranz R.L., Frankel S.D., Engelder T., Scholz C.H., (1980) The permeability of whole and jointed Barre granite, Int J Rock Mech Min Sci & Geomech. Abstr., 16, 225-234.

82. Kwon O., Kronenberg A.K., Gangi A.F., Johnson B., (2001) Permeability of Wilcox shale and its effective stress law. Journal of Geophysical Research 106(B9), 19339-19353.

83. Lachenbruch A.H. (1980) Frictional heating, fluid pressure and the resistance to fault motion. Journal of Geophysical Research, 85, 6097-6112.

84. Lazar P.L., (2006) Etude expérimentale et modélisation du comportement thermo-hydro-mécanique de matériaux de failles rocheuse, Thèse de doctorat, Ecole Nationale des Ponts et Chaussées, France.

85. Le Bellego C., (2001) Couplage chimie-mécanique dans les structures en béton attaquées par l'eau: étude expérimentale et analyse numérique, PhD. Dissertation, ENS de Cachan, France.

86. Lockner D.A., Stanchits S.A., (2002) Undrained poroelastic response of sandstones to deviatoric stress change, Journal of Geophysical Research, Vol. 107, No. B12, 2353

87. Masse S., Vetter G., Boch P., Haehnel C., (2002) Elastic modulus changes in cementitious materials submitted to thermal treatments up to 1000°C, Advances in Cement Research, 14(4), 169-177.

88. McTigue D.F., (1986) Thermoelastic response of fluid-saturated porous rock, Journal of Geophysical Research, 91(B9), 9533-9542

89. Mesri G., Adachi K., Ulrich C.R., (1976) Pore-pressure response in rock to undrained change in all-around stress, Géotechnique 26, No. 2, 317-330

90. Meziani H., (2006) Gas permeability measurements of cement-based materials under hydrostatic test conditions using a low-transient method. Magazine of Concrete Research 58(8), 489-503.

91. Michaux M., Nelson E.B., Vidick B., (1990) Chemistry and characterization of portland cement, Chapter 2 in Nelson E.B. ed., Well Cementing, Schlumberger, Netherlands.

92. Mindess S., Young J.F., Darwin D., (2003) Concrete, Prentice Hall, Second edition.

93. Monteiro P.J.M., Chang C.T., (1995) The elastic moduli of calcium hydroxide, Cement and Concrete Research 25(8), 1605-1609.

94. Morrow C., Bo-Chong Z., Byerlee J., (1986) Effective Pressure Law for Permeability of Westerly Granite Under Cyclic Loading, Journal of Geophysical Research 91(B3), 3870-3876.

95. Nur A.M., Walls J.D., Winkler K., DeVilbiss J., (1980) Effects of fluid saturation on waves in porous rock and relation to hydraulic permeability. Soc. Petr. Eng. J.20, 450-458.

96. Ouffroukh H., (2004) Comportement hydromécanique d'une roche granulaire et localisation des déformations, Thèse de doctorat, Ecole Nationale des Ponts et Chaussées, France.

97. Palciauskas V.V., Domenico P.A., (1982) Characterization of drained and undrained response of thermally loaded repository rocks, Water Resources Research, Vol. 18, No. 2, 281-290

98. Powers T.C., Brownyard, T.L., (1948) Studies of the physical properties of hardened Portland cement paste, PCA Bulletin 22.

99. Rempel A.W., Rice J.R., (2006) Thermal pressurization and onset of melting in fault zones, Journal of Geophysical Research, Vol. 111, B09314

100. Rice J.R., Cleary M.P., (1976) Some basic stress diffusion solutions for fluid-saturated elastic porous media with compressible constituents, Review of geophysics and space physics, Vol. 14, No. 2, 227-240

101. Rice J.R., (2006) Heating and weakening of faults during earthquake slip, Journal of Geophysical Research, Vol. 111, B05311

102. Sabri S., Illston J.M., (1982) Immediate and delayed thermal expansion of hardened cement paste, Cement and Concrete Research 12, 192–208.

103. Sanahuja J., Dormieux L., Chanvillard G., (2007) Modelling elasticity of a hydrating cement paste, Cement and Concrete Research 37, 1427-1439.

104. Scherer G.W., (1992) Bending of gel beams: method of characterizing mechanical properties and permeability, J. Non-Cryst. Solids, 142(1-2), 18-35.

105. Scherer G.W., (2004) Characterization of saturated porous bodies. Concr Sci Eng 37(265), 21-30.

106. Scherer G.W., (2004) Thermal expansion kinetics: Method to measure permeability of cementitious materials, III. Effect of viscoelasticity, J. Am. Ceram. Soc. 87(8), 1509-1516.

107. Scherer G.W, Valenza II J.J., Simmons G., (2006) New methods to measure liquid permeability in porous materials. Cement and concrete research 37, 386-397.

108. Scherer GW. (2006) Dynamic pressurization method for measuring permeability and modulus: I. Theory. Materials & Structures 39, 1041-1057.

109. Scherer G.W., Valenza II J.J., Simmons G., (2007) New methods to measure liquid permeability in porous materials, Cement and Concrete Research 37, 386–397.

110. Schutjens P.M.T.M., Hanssen T.H., Hettema M.H.H., Merour J., de Bree P., Coremans J.W.A., Helliesen G., (2004) Compaction-Induced Porosity/Permeability Reduction in Sandstone Reservoirs: Data and Model for Elasticity-Dominated Deformation, SPE Reservoir Evaluation & Engineering 7(3), 202-216, SPE 88441-PA.

111. Sellevold E.J., Bjontegaard Ø. (2006) Coefficient of thermal expansion of cement paste and concrete, Materials and Structures 39, 809-815.

112. Simonson J.M., Ryther R.J., (1989) Volumetric properties of aqueous sodium hydroxide from 273.15 to 348.15 K, J. Chem. Eng. Data 34, 57–63.

113. Skempton A.W., (1954) The Pore Pressure Coefficients A and B, Géotechnique, 4, 143-147

114. Skempton A.W., (1960) Effective stress in soils, concrete and rocks, Conference on pore pressure and suction in soils, 4-16, London, Butterworths

115. Spang B., (2002) Excel Add-In for Properties of Water and Steam in SI-Units, http://www.cheresources.com/ iapwsif97.shtml

116. Stutzman P.E., Clifton J.R., (1999) Specimen preparation for scanning electron microscopy. In: Proceedings of the 21st International Conference on Cement Microscopy, Las Vegas, 10-22.

117. Sulem J., Vardoulakis I., Papamichos E., Oulahna A., Tronvoll J., (1999) Elasto-plastic Modelling of Red Wildmoor Sandstone, Mechanics of Cohesive-frictional Materials 4(3), 215-246.

118. Sulem J., Vardoulakis I., Ouffroukh H., Boulon M., Hans J., (2004) Experimental characterization of the thermo-poro-mechanical properties of the Aegion fault gouge, Comptes Rendus Geosciences, 336, 4-5, 455-466

119. Sulem, J. and Ouffroukh, H. (2006) Hydromechanical Behaviour of Fontainebleau Sandstone, Rock Mechanics and Rock Engineering, Volume 39, Number 3, 185-213

120. Sulem J., Lazar P. and Vardoulakis I., (2007) Thermo-Poro-Mechanical Properties of Clayey Gouge and Application to Rapid Fault Shearing, Int. J. Num. Anal. Meth. Geomechanics, Volume 31, Issue 3, 523-540

121. Sultan N., (1997) Etude du comportement thermo-mécanique de l'argile de Boom : expériences et modélisation, PhD thesis, CERMES, Ecole Nationale des Ponts et Chaussées, France

122. Taylor H.F.W., (1997) Cement chemistry, Thomas Telford, London.

123. Terzaghi K., (1936) The shearing resistance of saturated soils and the angle between the planes of shear, First Int. Conf. Soil Mech., Vol. 1, Harvard Univ., Cambridge, Mass. 54-56.

124. Todd T., Simmons G., (1972) Effect of pore pressure on the velocity of compressional waves in low porosity rocks, Journal of Geophysical Research, 77, 3731-3743.

125. Ulm F.-J., Constantinides G., Heukamp F.H., (2004) Is concrete a poromechanics material? - A multiscale investigation of poroelastic properties, Materials and Structures 37(265), 43-58.

126. Vairogs J., Hearn C.L., Dareing D.W., Rhoades V.W., (1971) Effect of rock stress on gas production from low-permeability reservoirs. J. Pet. Technol. 23, 1161-1167.

127. Valenza II J.J., Scherer G.W., (2005) Evidence of anomalous thermal expansion of water in cement paste, Cement and Concrete Research 35, 57-66.

128. Vardoulakis I., Sulem J., (1995) Bifurcation Analysis in Geomechanics. Blackie Academic and Professional.

129. Vardoulakis, I., (2002) Dynamic thermo-poro-mechanical analysis of catastrophic landslides, Géotechnique, Vol. 52, No. 3, 157-171

130. Velez K., Maximilien S., Damidot D., Fantozzi G., Sorrentino F., (2001) Determination by nanoindentation of elastic modulus and hardness of pure constituents of Portland cement clinker, Cement and Concrete Research 31(4), 555-561.

131. Verbeck G.J., Helmuth R.A., (1968) Structures and physical properties of cement paste, Proceeding of fifth international symposium on chemistry of cement, Tokyo, Vol 3, 1-32.

132. Walder J., Nur A., (1984) Porosity reduction and crustal pore pressure development. Journal of Geophysical Research 89, 11539-11548.

133. Walls J.D., (1982) Effects on pore pressure, confining pressure and partial saturation on permeability of sandstones. Ph.D. Thesis, Department of Geophysics, Stanford Univ., Stanford, Calif.

134. Walls J.D., Nur A., (1979) Pore pressure and confining pressure dependence of permeability in sandstone. In: proceedings of the 7th Formation Evaluation Symposium of the Canadian Well Logging Society. Paper O, Can. Well Logging Soc., Alberta, Calgary.

135. Walsh J.B., (1973) Theoretical bounds for thermal expansion, specific heat and strain energy due to internal stresses, Journal of Geophysical Research, 78, 7636-7647.

136. Walsh J.B., (1981) Effect of pore pressure and confining pressure on fracture permeability, Int J Rock Mech Min Sci & Geomech. Abstr. 18, 429-435.

137. Wissa, A.E.Z. (1969) Pore pressure measurement in saturated stiff soils, Jnl Soil Mech. Fdn Div. Am. Soc. Civ. Engrs 95, SM4, 1063-1073

138. Xi Y., Jennings H.M., (1997) Shrinkage of cement paste and concrete modelled by a multiscale effective homogeneous theory, Materials and Structures 30, 329-339.

139. Xu S., Simmons G.C., Scherer G.W., (2004) Thermal expansion and viscosity of confined liquids, Mat. Res. Soc. Symp. Proc., vol. 790, Materials Res. Soc, Warrendale, P6.8.1– P6.8.7.

140. Yale D.P. (1994) Network Modeling of Flow, Storage and Deformation in Porous Rocks. Ph.D. thesis, Stanford University.

141. Zaoui A., (2000) Matériaux hétérogènes et composites, Ecole Polytechnique

142. Zhu W., Wong T.-f., (1997) The transition from brittle faulting to cataclastic flow: Permeability evolution, Journal of Geophysical Research 102(B2), 3027-3041.

143. Zimmerman R.W., Somerton W.H., King M.S., (1986) Compressibility of porous rocks, Journal of Geophysical Research 91(B12), 12765-12777.

144. Zimmerman R.W., (1991) Compressibility of sandstones, Elsevier, Amsterdam

145. Zoback M.D., (1975) High pressure deformation and fluid flow in sandstone, granite, and granular materials. Ph.D. thesis, Stanford Univ., Stanford, Calif.

146. Zoback M.D., Byerlee J.D., (1975) Permeability and effective stress. Bull. Am. Assn. Petr. Geol. 59, 154-158